Aus dem Institut für Biomedizinische Technik
Friedrich-Barnewitz-Straße 4, 18119 Rostock

Prozessierung und Modifikation polymerbasierter Biomaterialsysteme für Implantatanwendungen

kumulative Habilitationsschrift zur Erlangung des akademischen Grades
doctor rerum naturalium habilitatus (Dr. *rer*. *nat*. *habil*.)
der Universitätsmedizin Rostock

vorgelegt von:

Dr. *rer*. *nat*. Stefan Thomas Oschatz,

geboren am 20.11.1985 in Berlin,

wohnhaft in Rostock

Rostock, den 30.06.2025

https://doi.org/10.18453/rosdok_id00005143

1. Gutachter:	Prof. Dr.-Ing. Niels Grabow Institut für Biomedizinische Technik Universitätsmedizin Rostock
2. Gutachter:	Prof. Dr.-Ing. Marc Kraft Institut für Maschinenkonstruktion und Systemtechnik Fachgebiet Medizintechnik Technische Universität Berlin
3. Gutachter:	Univ.-Prof. Dr. med. Stefan Jockenhövel NRW Schwerpunktprofessur Biohybrid & Medical Textiles (BioTex) Helmholtz Institut für Angewandte Medizintechnik Center for Biohybrid Medical Systems RWTH Aachen

Jahr der Einreichung:	2025
Jahr der Verteidigung:	2025
Jahr der Probevorlesung:	2025

Inhalt

Liste der Publikationen, die für die vorliegende kumulative Habilitationsschrift zusammengefasst wurden iii

1. Einleitung 1

1.1. Klinische Relevanz von Poly-L-lactid-basierten Polymeren in Implantatanwendungen 2

1.2. PLLA - Prozessierung und Modifikationen 4

1.3. Fragestellungen in Forschung und Anwendung 8

2. Zielsetzung der Arbeit 16

3. Zusammenfassung der inkludierten Publikationen 17

Publikation 1: PLLA/Polyurethan-Hybridmaterialien zur Verbesserung der Biomaterialeigenschaften 17

Publikation 2: PLLA/PEO-Blend als selbstverfestigendes Material für Stentanwendungen in der Eustachi‘schen Tube. 18

Publikation 3: Korrelation des beschleunigten *in vitro*-Abbauverhaltens von PLLA und P3HB zur prozessbegleitenden Materialcharakterisierung 20

Publikation 4: Einfluss von polymerbasierten Beschichtungen auf die Korrosionsrate von Magnesium unter physiologischen *in vitro* Bedingungen 21

Publikation 5: Einfluss der Inkorporation von Wirkstoffen auf die Materialeigenschaften der PLLA-Trägermatrix im Kontext kardiovaskulärer DES-Anwendungen 22

Publikation 6: PLLA-co-PEG-Hybrid-Fasermembranen zur Verbesserung der Biomineralisation 24

4. Literaturverzeichnis 26

5. Vollständige Publikationsliste I

6. Patente IX

7. Vorträge und Posterpräsentationen XI

8. Danksagung XIII

9. Eidesstattliche Erklärung XIV

10. Publikationen der Habilitationsschrift XV

Liste der Publikationen, die für die vorliegende kumulative Habilitationsschrift zusammengefasst wurden

Publikation 1: **Oschatz S**, Schultz S, Fiedler N, Senz V, Schmitz KP, Grabow N and Koper D. Melt blending of poly(lactic acid) with biomedically relevant polyurethanes to improve mechanical performance. *Heliyon*, 2024, 10, e26268, https://doi.org/10.1016/j.heliyon.2024.e26268, IF: 3,6

Publikation 2: **Oschatz S**, Schultz S, Fiedler N, Markhoff J, Teske M, Koper D, Senz V, Brandt-Wunderlich C, Schmitz KP, Grabow N and Lebahn K. PLLA/PEO blend as self-curing material for a biodegradable Eustachian tube stent. *Mater. Des.*, 2025, 256, 114255, https://doi.org/10.1016/j.matdes.2025.114255, IF: 7,9

Publikation 3: Arbeiter D, Lebahn K, Reske T, Senz V, Eickner T, Schmitz KP, Grabow N and **Oschatz S**. Comparison of accelerated and enzyme-associated real-time degradation of HMW PLLA and HMW P3HB films, *Polym. Test.*, 2022, 107471, https://doi.org/10.1016/j.polymertesting.2021.107471, IF: 5,1

Publikation 4: Fiedler N, Teske M, Nelz SC, Flügge J, Senz V, Bajer D, Grabow N and **Oschatz S**. In vitro corrosion of polyester coated magnesium alloy under pH-static conditions, *ACS Biomater. Sci. Eng.*, 2024, 10, 9, 5844-5855 https://doi.org/10.1021/acsbiomaterials.4c00835, IF: 5,5

Publikation 5: Arbeiter D, Reske T, Teske M, Bajer D; Senz V, Schmitz KP, Grabow N and **Oschatz S**. Influence of Drug Incorporation on the Physico-Chemical Properties of Poly(L-Lactide) Implant Coating Matrices - A Systematic Study. *Polymers*, 2021, 13, 292, https://doi.org/10.3390/polym13020292, IF: 4,967

Publikation 6: **Oschatz S**, Teske M, Burmeister U, Illner S, Lang H, Senz V, Grabow and Markhoff J. Fetuin A functionalisation of biodegradable PLLA-co-PEG nonwovens towards enhanced biomineralisation and osteoblastic growth behavior, *Biomater. Sci.*, 2023, 11, 5240-5250, https://doi.org/10.1039/d3bm00141e, IF: 5,8

1. Einleitung

Im Kontext biomedizintechnischer Entwicklungen, insbesondere im Hinblick auf innovative Implantatanwendungen, sind polymere Materialien aufgrund ihrer Vielseitigkeit in Materialeigenschaften und Verarbeitungsmöglichkeiten von enormer Relevanz [1,2]. In Abbildung 1 sind ausgewählte Beispiele für polymerbasierte Implantate dargestellt.

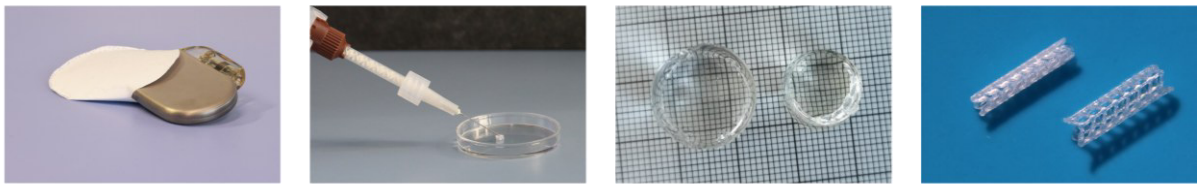


Abbildung 1: Ausgewählte Implantatentwicklungen am Institut für Biomedizinische Technik der Universitätsmedizin Rostock auf Basis polymerer Biomaterialien (v.l.n.r.): Implantattasche auf Basis elektrogesponnener Faservliese, *in situ*-polymerisierendes Wirkstoffdepotsystem, Hydrogelkörper auf Basis eines Polyelektrolyten und Prototyp eines polymerbasierten Stents für die Anwendung in der Eustachi‘schen Tube.

Vor diesem Hintergrund war das Ziel der vorliegenden Arbeit, Methoden für Prozessierung und Modifikation von Poly-L-lactid (PLLA)-basierten biodegradierbaren Materialsystemen als Implantatvollmaterial sowie als Implantatbeschichtung zu entwickeln und damit zu einem erweiterten Materialverständnis und zukünftigen Anwendungsperspektiven beizutragen.

Ein Forschungsthema waren PLLA-Blendmaterialien zur Einstellung mechanischer Eigenschaften für innovative Stentanwendungen (Publikation 1). Darauf folgt die Entwicklung und Testung selbstverfestigenden Stents auf Basis eines Blends bestehend aus PLLA und Polyethylenoxid (PEO) vor dem Hintergrund der Anwendung in der Eustachi‘schen Tube (Publikation 2).

Ein weiterer Schwerpunkt lag auf der Entwicklung eines beschleunigten *in vitro* Degradationsprotokolls und die Untersuchung der Echtzeitkorrelation, für polymerbasierte Implantatmaterialien (Publikation 3), sowie auf der Untersuchung der korrosionsschützenden Wirkung polyesterbasierter Beschichtungen auf Magnesiumsubstrat (Publikation 4).

Weiterhin wurde der Einfluss inkorporierter Wirkstoffe auf die Stabilität von PLLA als Beschichtungs- und Trägermatrix untersucht (Publikation 5). Eine weitere berücksichtigte Arbeit behandelt die kovalente Anbindung eines Calcium-affinen Proteins zur Förderung der Biomineralisation auf Faservliesen realisiert (Publikation 6).

Damit leistet die vorliegende Arbeit einen Beitrag zum besseren Verständnis von PLLA-basierten Biomaterialien im Hinblick auf deren Einsatz in innovativen Implantaten, vorwiegend im Rahmen von Stententwicklungen, auch über den Einsatz im kardiovaskulären Bereich hinaus.

1.1. Klinische Relevanz von Poly-L-lactid-basierten Polymeren in Implantatanwendungen

In der modernen klinischen Praxis sind Implantatanwendungen als Therapiemöglichkeit fester Bestandteil, dennoch bleibt jedes Implantat ein Fremdkörper, mit den damit assoziierten Negativeffekten und Risiken. Dazu zählen beispielsweise eine gestörte Vasomotorik bei kardiovaskulären Implantaten [3], eine veränderte mechanische Belastbarkeit im Fall von Knochenimplantaten [4], oder allgemein Infektionen und fibrotische Reaktionen [5,6]. Hinzu kommt, dass viele Implantate, z.B. stentbasierte Systeme, nach Implantation nicht problemlos entfernt werden können [7].

Daraus ergibt sich für geeignete Anwendungen das Idealkonzept, dass ein Implantat nach Erfüllung seiner Funktion vollständig vom Körper abgebaut und wieder durch natürliches körpereigenes Gewebe ersetzt wird. Für die Herstellung biodegradierbarer Implantate steht ein breites Materialspektrum (Tabelle 1), sowohl aus Metallen, Keramiken und Polymeren sowie Kombinationen der Materialien, zur Verfügung [8]. Allerdings müssen mit der Degradierbarkeit der Materialien auch immer Kompromisse eingegangen werden [9]. Die Materialauswahl ist zudem eingeschränkt, da viele Materialien keine oder nicht die gewünschte Degradation zeigen, und so können z.B. die mechanischen Eigenschaften, wie etwa bezuigen auf Stents oder anderen lasttragenden Strukturen, weniger optimal im Vergleich zu permanenten Materialien sein [10]. Außerdem muss die Standzeit mit der Heilungszeit harmonisiert werden, und es dürfen sich während der Implantatdegradation, insbesondere bei kardiovaskulären Anwendungen, in der Spätphase keine Fragmente oder sogar das gesamte Implantat selbst lösen [7].

Tabelle 1: Übersichtstabelle zu Biomaterialklassen, biologische Schlüsseleigenschaften von Biomaterialien, sowie für Biomaterialanwendungen relevante ausgewählte Material- und Halbzeugformen [8,11].

Biomaterialklassen	Biomaterial-Eigenschaften	Materialformen
▪ Metalle	▪ zytokompatibel	▪ Fasern
▪ Keramiken	▪ nicht-thrombogen	▪ Folien
▪ Polymere	▪ nicht-immunogen	▪ poröse Strukturen
▪ Verbundstoffe	▪ bioresponsiv	▪ Hydrogele
	▪ bioaktiv	▪ …
	▪ bioresorbierbar vs. biostabil	

Zu beachten ist auch, dass die Degradation des Biomaterials das lokale Gewebe im Körper stark beeinflussen kann [12]. Im Fall der Degradation von Magnesium, als verbreitetem Vertreter temporärer metallischer Implantatmaterialien, ist die Korrosion mit einer starken Erhöhung des lokalen pH-Wertes verbunden [13]. Diese kann zwar vom körpereigenen Puffersystem abgefangen werden, örtlich begrenzte pH-Spitzen bei unzureichender

Pufferkapazität können allerdings negative Effekte im umliegenden Gewebe hervorrufen. Zudem entsteht bei der Mg-Korrosion eine relevante Menge an Wasserstoffgas, welches zur Hohlraumbildung führen kann und damit die Gewebeheilung stört [14,15].

Die beiden genannten Effekte können allerdings auch positive Effekte zeigen. So ist die Erhöhung des pH-Wertes auch mit einer Verbesserung des Heilungsprozesses verbunden, insbesondere im Kontext von Knochenregeneration [16], und freigesetztes Wasserstoffgas reduziert freie Sauerstoffspezies, was zu einem antiinflammatorischen Effekt führt [17]. Dies zeigt, dass häufig Dualismen existieren und, insbesondere bezogen auf Implantat-entwicklungen, die Materialauswahl mit der vorgesehenen Zielanwendung präzise abgestimmt werden muss.

Bezogen auf die Entwicklung polymerbasierter biodgradierbarer Implantate befindet sich eine Vielzahl an Materialien in klinischer Anwendung [18]. Dazu zählen vor allem Polyester, aber auch Polycarbonate, Polyanhydride, Polyorthoester, Polysaccharide, Polyphosphazene sowie diverse Copolymere und Blends [19]. Die biodegradierbaren Polyester - Polylactide, Polyglycolide, Polydioxanon, Polycaprolacton oder Polyhydroxyalkanoate - nehmen dabei eine besondere Rolle ein, da sie bereits umfassend klinisch erprobt und zugelassen sind [20].

In diesem Zusammenhang sind besonders Polylactid-basierte Materialien relevant [21]. Sie finden Verwendung in biodegradierbaren Implantatbeschichtungen zur lokalen Wirkstoff-freisetzung, als Nahtmaterialien, Basismaterial für Gerüststrukturen zur gesteuerten Geweberegeneration sowie in abbaubaren, vollständig aus einem Polmyer bestehenden, Implantaten, wie Knochenschrauben oder bioresorbierbaren Stents (BRS) [22].

Dabei lässt sich das Konzept eines bioresorbierbaren Implantats etwa für Nahtmaterial sehr gut realisieren, ist aber im Fall von z.B. Stentanwendungen komplex. Ein prominentes Beispiel ist der bioresorbierbare Polymerstent *Absorb* der Firma Abbott [23]. Klinische Studien zeigten, dass dieser Stent innerhalb von zwei Jahren nach Implantation mit einer signifikant höheren Rate an In-Stent-Thrombosen einherging. Zwar wurde keine signifikante Erhöhung der kardialen Mortalität festgestellt, jedoch wies der BRS auch keine klare Überlegenheit gegenüber etablierten Metallstents auf. Aufgrund der folgenden niedrigen Verkaufszahlen wurde der *Absorb*-Stent schließlich vom Markt genommen [24].

Trotz solcher Rückschläge bleibt das Konzept des bioresorbierbaren Polymerstents ein wichtiges Thema aktueller Forschung, auch für innovative Anwendungen außerhalb des kardiovaskulären Anwendungsfeldes [25–27]. So machen neue Fertigungstechnologien, wie etwa additive Verfahren, neue Strukturen und Funktionen zugänglich, was den anhaltenden Forschungsbedarf für ein tieferes Verständnis des Materialverhaltens unter den komplexen Bedingungen im Körper zur Entwicklung innovativer Implantate für bioresorbierbare Polymere unterstreicht [28,29].

Im regulatorischen Umfeld der Biomedizintechnik müssen alle polymeren Basismaterialien, welche für Implantatanwendungen vorgesehen sind, anhand der *United States Pharmacopeia* (USP) Klassifizierung von Kunststoffen bewertet, getestet und als sicher eingestuft werden müssen, wobei die Klassen IV und VI für Materialien vorgesehen sind, die für die Verwendung in Implantaten und Medizinprodukten bestimmt sind [30,31]. Zu den nach USP durchzuführenden Tests gehören die intravenöse und intraperitoneale Injektion von Probenextrakten und die intramuskuläre Implantation von Probenstreifen, sowie Prüfungen zur akuten systemischen Toxizität, zur intrakutanen Reaktivität und zur Gewebereaktion nach Implantation nach DIN EN ISO 10993 [32]. Diese Tests sollten darüber hinaus den Grundsätzen der Guten Laborpraxis (GLP) entsprechen. Daneben, und vor allem für Implantathersteller herausfordernd, gelten in der EU noch die Bestimmungen der *Medical Device Regulation*, welche einen umfangreichen Anforderungskatalog an die Dokumentation und Testung von Medizinprodukten, insbesondere Implantate, vorsehen [33].

Damit liegt nahe, dass Biomaterialinnovationen in diesem hoch regulierten Umfeld äußerst zeitaufwändig und kostenintensiv sind, und die Auswahl an Materialien zur Herstellung innovativer Implantate oft auf klinisch etablierte medizinisch zugelassene Polymere beschränkt ist, um aufwändige Zulassungsstudien zu vermeiden oder zu reduzieren [34–36]. Dies hat zur Folge, dass, trotz wachsender Materialvielfalt, die Forschung an etablierten Polymeren, wie Polylactid (PLA), von hoher Bedeutung bleibt, nicht zuletzt wegen der zentralen Rolle von PLA in zahlreichen zugelassenen Medizinprodukten [37,38].

PLA, einschließlich Poly-L-lactid (PLLA), ist seit Jahrzehnten in resorbierbaren Implantaten etabliert und dominiert weiterhin den Markt mit einem geschätzten Marktanteil unter den bioresorbierbaren Polymeren von knapp 30% im Jahr 2025 [39], deutlich vor weiteren Vertretern, wie Polyglycolsäure (~20%) und Polycaprolacton (~15%). Insgesamt wird der globale Markt für bioresorbierbare Polymere im Medizinsektor auf 1,3 Mrd. USD [39] bis 1,8 Mrd. USD [40] geschätzt und soll, je nach Quelle, auf über 3,5 Mrd. USD (bis 2033 [39]) bzw. 6 Mrd. USD (bis 2030 [40]) anwachsen. Die größten Anwendungsfelder sind Orthopädie (ca. 50 - 55 %) und *Drug Delivery* (ca. 40 %) [39,40], mit regionalem Schwerpunkt der Marktverteilung in Nordamerika mit >30 % gegenüber >25% in Europa [41].

Die damit verbundene große wirtschaftliche Relevanz sowie des nachgewiesenen klinischen Nutzens PLA-basierter Systeme bilden die Grundlage für die in dieser Arbeit adressierten Forschungsfragen zu Prozessierung, Modifikation und umfangreicher Charakterisierung polymerbasierter Biomaterialien.

1.2. PLLA - Prozessierung und Modifikationen

PLLA zeichnet sich durch ein breites Anwendungs- und Verarbeitungsspektrum aus [42]. Dieses Polymer lässt sich sowohl durch thermische Verfahren (z.B. Schmelzformen,

Extrusion, Schmelzschichtverfahren bzw. *Fused Filament Fabrication* [43], *Melt Electro Writing* [44]), sowie durch lösemittelbasierte Verfahren (z.B. *Spray Coating* [45], Lösemitteltauchen und -gießen, *Freeze Casting* [46], Elektrospinning [47], Direktes Tintenschreiben bzw. *Direct Ink Writing* [48]) verarbeiten (Abbildung 2).

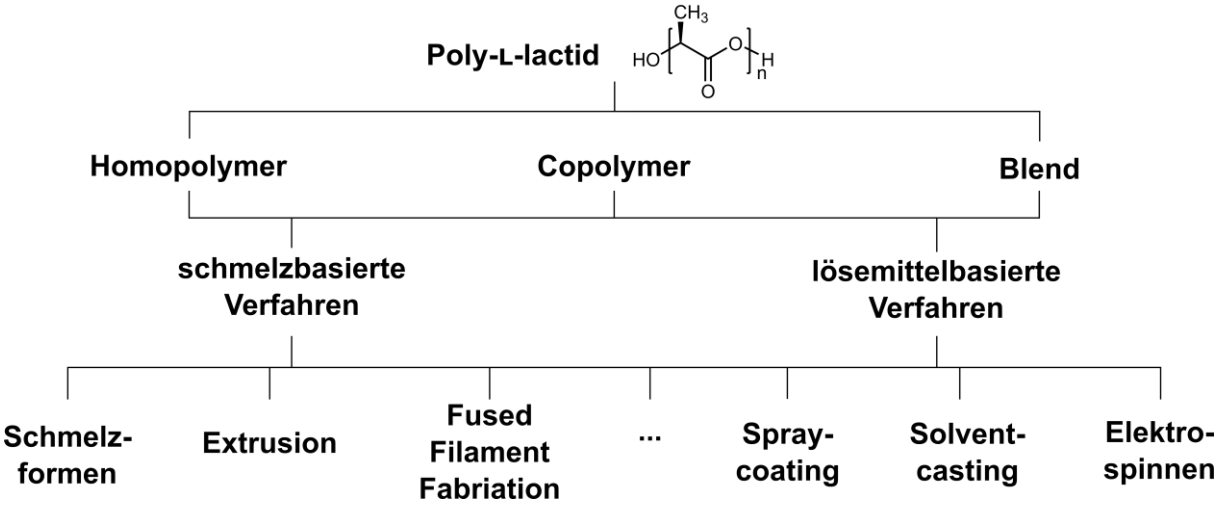


Abbildung 2: Übersicht zu den wichtigsten Verarbeitungskategorien und -formen von PLLA sowie PLLA-basierten Copolymeren und Blends.

Generell weist PLLA, in Abhängigkeit vom Molekulargewicht, eine hohe Festigkeit, verbunden mit einer Glasübergangstemperatur T_g >45 °C und einer Schmelztemperatur T_m >150 °C auf, die eine vielfältige Verarbeitung erlauben [20]. Beide Verfahrenstypen, schmelz- und lösemittelbasiert, haben spezifische Vor- und Nachteile (Tabelle 2).

Tabelle 2: Vergleich von lösemittelbasierten und schmelzbasierten Verarbeitungsformen am Beispiel von PLLA.

schmelzbasiert		**lösemittelbasiert**	
Vorteile	**Nachteile**	**Vorteile**	**Nachteile**
▪ Prozesskontrolle ▪ Inkorporation unlöslicher APIs* ▪ keine chemischen Rückstände ▪ bessere Skalierbarkeit	▪ thermische Degradation ▪ anspruchsvolles (teures) Equipment ▪ Feinstrukturierung schwierig	▪ feinere Strukturen ▪ Inkorporation temperatur-empfindlicher Zusätze/APIs ▪ z.T. einfacher im Labormaßstab umsetzbar	▪ Entfernung des Lösemittels notwendig ▪ Lösemittel oft teuer ▪ Produktion von chemischem Abfall ▪ teils schwer skalierbar

*API: *Active Pharmaceutical Ingredient*, Wirkstoff

Ein klinisch relevantes Anwendungsbeispiel sind PLLA-basierte Beschichtungen für Stentanwendungen. Neben Polymer-freien wirkstofffreisetzenden Stents (*Drug Eluting Stent*, DES) ist eine der gängigsten Technologien die Inkorporation von Medikamenten in eine auf den Stent aufgebrachte Polymerbeschichtung (Abbildung 3). Eine breite Palette von Polymeren ist als wirkstofftragende Matrix für DES im klinischen Einsatz [49]. Neben chemisch inerten Polymeren, wie z.B. fluorierten Polymeren, werden hauptsächlich Polylactide (PLA)

und dessen Derivate aufgrund ihrer leichten Verarbeitbarkeit und ihrer biologischen Abbaubarkeit als Wirkstoffträgermatrix verwendet [50].

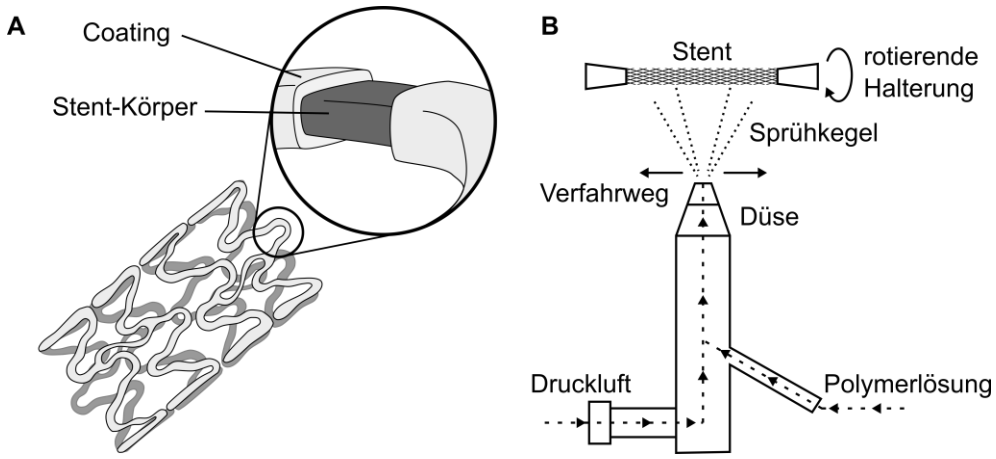


Abbildung 3: A: Darstellung eines Stents mit korrosionsschützender und/oder wirkstofffreisetzender Beschichtung (eigene Abbildung). B: Schematische Darstellung des Beschichtungsprozesses eines Stents, modifiziert nach [51].

Die Verwendung von reinem PLLA kann jedoch für bestimmte Implantatanwendungen aufgrund der Abbauzeit des Materials von 2-5 Jahren nachteilig sein [52]. Weitere Nachteile von PLLA als Werkstoff sind, in starker Abhängigkeit von der thermischen Vorgeschichte des Materials, seine hohe Sprödigkeit bzw. geringe Bruchdehnung und das Auftreten von Spannungs-induzierten Kristallisationsvorgängen (*Strain Induced Crystallization*) [53]. Auch ist PLLA stark anfällig gegenüber thermischen Degradationsvorgängen während der Verarbeitung, welche bereits beim Vorhandensein bereits geringer Mengen an Restfeuchte im Material auftreten können. Weiterhin nachteilig ist die Bildung saurer Abbauprodukte während der Biodegradation, welche im umliegenden Gewebe Entzündungsreaktionen hervorrufen können [54].

Entsprechend der Zielanwendung können die Eigenschaften von PLLA über die Wahl der Kettenlänge, sowie über die Verwendung von PLLA-basierten Copolymeren oder Blends verbessert und an die Zielanwendung angepasst werden [55]. PLLA-co-PEG Copolymere kombinieren beispielsweise die mechanischen Eigenschaften von PLLA mit einer erheblich verkürzten Degradationszeit [56]. Diese wird durch die Inkorporation von Poly(ethylenglykol)-Blöcken (PEG) erreicht, die zur verbesserten Hydratisierungsfähigkeit der Polymerketten führen. Dies erleichtert den Transport abgebauter Kettenfragmente durch das umgebende Medium bzw. Körperflüssigkeit. Über den Anteil an PEG-Ketten im Polymer kann so die Abbauzeit im Bereich von Monaten bis hin zu Wochen eingestellt werden.

Eine weitere relevante Modifikation zur Verbesserung der Eigenschaften von Polymermaterialien hinsichtlich des biomechanischen Verhaltens ist das Verblenden [57,58]. PEG und Polyethylenoxid (PEO), strukturell identische aliphatische Polyester mit unterschiedlicher Kettenlänge ($M_{n,PEG}$ < 20 000 g/mol < $M_{n,PEO}$), sind sehr gute geeignete Blendpartner für PLLA.

Durch die Einlagerung von Fremdpolymeren wird die molekulare Ordnung verändert, z.B. durch die Bildung von Wasserstoffbrücken, was wiederum Kristallisations- und Phasenübergangsprozesse beeinflusst, wodurch sich die Materialeigenschaften verändern [59]. So ist eine Erhöhung der Plastizität mit einhergehender Steigerung der Bruchdehnung von erheblichem Vorteil für lasttragende Implantate, welche häufig zyklischen Verformungen ausgesetzt sind. Dabei muss allerdings auf einen möglichst geringen Einfluss auf die Festigkeit des Materials in Abhängigkeit von der PEG-Konzentration geachtet werden [60]. In Abbildung 4 sind die kristallinen Eigenschaften von reinem PLLA gegenüber einem PLLA/PEG-Blend sowie einem PLLA-PEG-Copolymer nach Kristallisation aus der Schmelze gegenübergestellt.

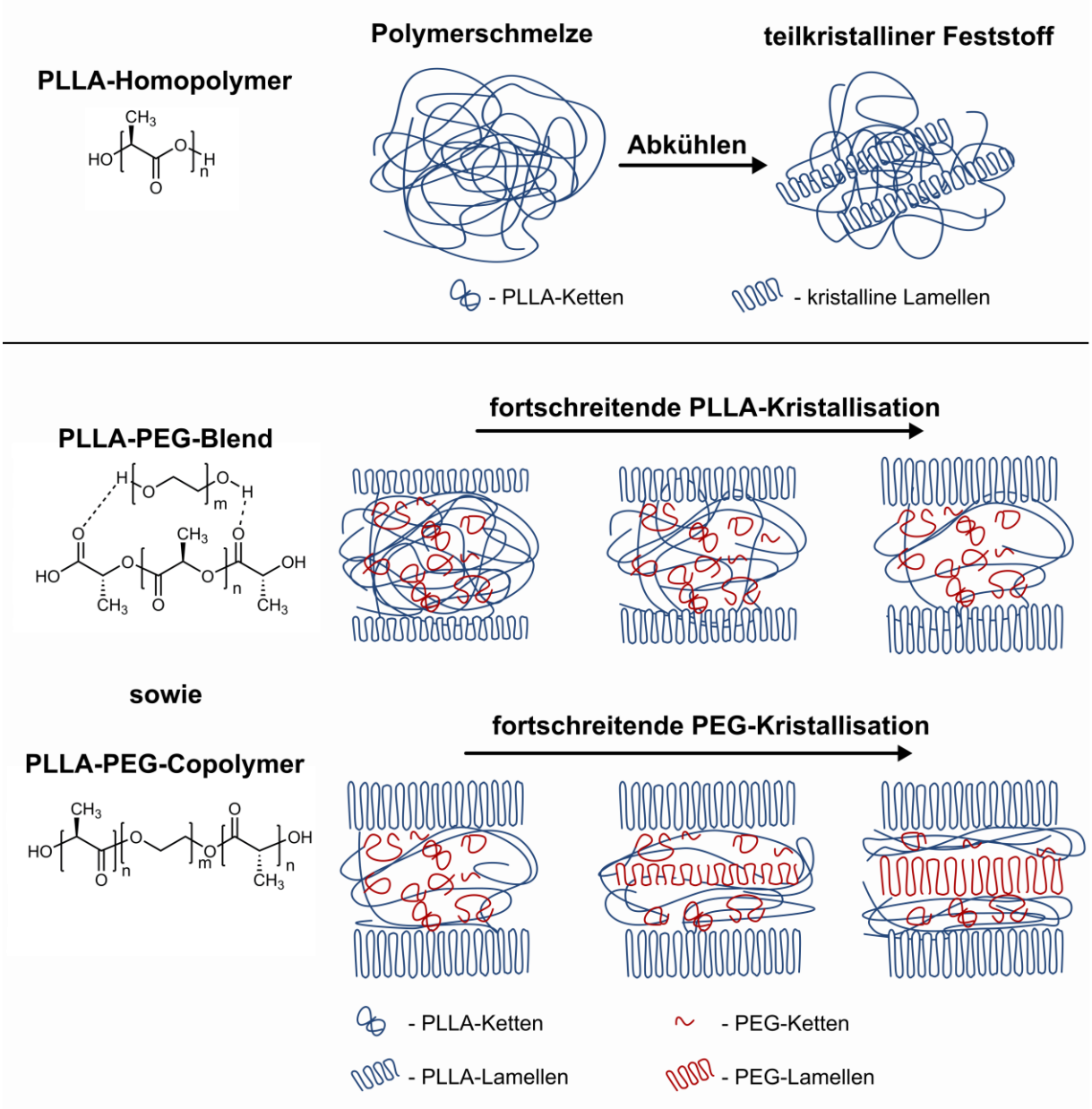


Abbildung 4: Übersicht zur chemischen Struktur sowie molekularer Wechselwirkungen im Polymer mit Auswirkungen auf die Kristallisation aus der Schmelze für PLLA (Abbildung modifiziert nach [61]), sowie PLLA/PEG-Blends und Copolymere (Abbildung modifiziert nach [62]).

Dabei wird ersichtlich, wie die Interaktion, zum Beispiel durch die Ausbildung von Wasserstoffbrücken, und damit die molekulare Anordnung, durch die chemische Beschaffenheit des Materials, insbesondere bei Gegenwart von Fremdpolymeren, wie PEG, entweder im *Backbone* oder als Blendpartner, beeinflusst wird. So entsteht beim Abkühlen von PLLA eine alternierende Zweiphasenstruktur, die aus kristallinen Lamellen und amorphen Schichten besteht, was zur Bildung von gefalteten Kettenkristalliten führt [60,62,63].

Bei PLLA/PEG- bzw. PLLA/PEO-Blends und Copolymeren hingegen, welche in der Schmelze sehr gut miteinander mischbar sind, erhöht sich während des Wachstums der PLLA-Lamellen in der amorphen Phase der PEG-Anteil [64] und es kommt zur Mikrophasentrennung [65]. Beim anschließenden thermische Nachbehandeln, welches notwendig ist um Kaltkristallisationsvorgänge zu eliminieren und das Material thermisch zu stabilisieren, kann es anschließend zur Bildung von PEG-Lamellen kommen, welche sich in der amorphen Schicht zwischen den PLLA-Lamellen bilden, was wiederum erheblichen Einfluss auf die Materialeigenschaften, wie Mechanik, Wirkstofffreisetzungsverhalten und Abbauzeit hat. Dies verdeutlicht das zur Verfügung stehenden umfangreiche Methodenspektrum, aber auch die Komplexität, in der Anpassung der Materialeigenschaften hin zu langzeitsicheren und funktionalen Implantaten.

1.3. Fragestellungen in Forschung und Anwendung

Mechanische und physiko-chemische Werkstoffeigenschaften

Bioresorbierbare Stents auf Polymerbasis gewinnen nach der Abbott *Absorb* Problematik [66] wieder an Interesse, auch für Anwendungen neben der klassischen kardiovaskulären Intervention [29,67,68]. Aufgrund der minimalinvasiven Implantation besteht hinsichtlich Stentanwendung ein hoher Bedarf an gegensätzlichen mechanischen Materialeigenschaften, wie einem ausreichenden plastischen Verformungsvermögen (für Crimp- und Expansionsvorgänge), einem hohen Elastizitätsmodul und einer hohen Streckspannung (hohe radiale Stützkraft) sowie einer ausreichenden strukturellen und mechanischen Widerstandsfähigkeit gegenüber zyklischen Wechselbelastungen. So kann die mechanische Belastung während des Expansionsprozesses zu einem unmittelbaren Implantatversagen führen, wenn das Material nicht ausreichend duktil ist. Daher sind für die Herstellung funktioneller Implantate auf PLLA-Basis oft Folgeverarbeitungsschritte, wie Blasformen, Ziehen oder Tempern, erforderlich [69,70]. Durch diese Postprozessierungen können Kettenorientierung und Kristallinität des Polymers und so die erforderlichen mechanischen Eigenschaften eingestellt werden.

Vor allem die Verarbeitungsmethoden haben einen erheblichen Einfluss auf die Eigenschaften des entstehenden Materials, z.B. Oberflächenmorphologie, Kristallinität, Ausrichtung der Polymerketten und Verteilung kristalliner und amorpher Bereiche. Auch können, je nach Prozess, Phasenseparationseffekte auftreten. Im Vergleich zur thermischen Verarbeitung erfordern lösemittelbasierte Verfahren eine zusätzliche Nachbehandlung der Halbzeuge, die entweder aus Waschen, Tempern oder einer Kombination aus beiden bestehen kann, um Lösungsmittelrückstände zu entfernen. Diese können einerseits die Materialeigenschaften verändern [71,72], andererseits aber auch toxische Wirkungen (z.B. Chloroform als gängiges Lösemittel für PLLA) zeigen [73,74]. Darüber hinaus beeinflusst das Molekulargewicht des Polymermaterials die Materialeigenschaften.

Neben der Postprozessierung ist die Verwendung von Copolymeren sowie PLLA-Blends, sowohl mit Polymeren als auch mit kleinen Molekülen (z.B. Weichmachern, Wirkstoffen) als Blendpartner, ein geeignetes Mittel, um die Grundeigenschaften des Materials anzupassen [57,58]. Allerdings stellt sich dabei immer die Frage nach der Kompatibilität der Materialien, der Verarbeitbarkeit sowie der Entwicklung der Materialeigenschaften über einen längeren Zeitraum nach Implantation, unter Einfluss der Körperbedingungen und in Abhängigkeit vom Implantationsort.

Im Zusammenhang der Blendherstellung beschreibt das Flory-Huggins-Gittermodell die Wechselwirkungen und Thermodynamik von Polymerlösungen und Polymermischungen [75]. So führt bei vielen Blend-Systemen, wie z.B. PLLA/PCL, die unvollständige Mischbarkeit der Polymere zu einer komplexen Situation mit der Ausbildung verschiedener Phasen und Mischkristallisationsprozessen, auch unter Berücksichtigung der Lösemittel, welche die einzelnen Blendpartner unterschiedlich beeinflussen [76,77].

Die resultierende Phasenmorphologie und die Art der Phaseninteraktion ist für die Eignung als Implantatmaterial entscheidend, da unkontrollierte Phasenseparation und eine schwache Phasengrenze zu einer Verschlechterung mechanischer Materialeigenschaften und damit zur Untauglichkeit für biomedizinische Anwendungen führen. Das komplexe Materialverhalten von PLLA erfordert eine präzise Abstimmung der Werkstoffeigenschaften auf spezifische biomedizintechnische Anwendungen, verbunden mit umfangreicher biomechanischer und physikochemischer Materialcharakterisierung und Prozessoptimierung. Die Untersuchung der Verbesserung der Werkstoffeigenschaften PLLA-basierter Biomaterialien sind Gegenstand der dieser Arbeit zugrundeliegenden Publikationen zu PLLA/Polyurethan-Hybridmaterialien, sowie PLLA/PEO-Blends als selbstverfestigendes Material für Stentanwendungen in der Eustachi‘schen Tube.

Degradation

Eine charakteristische Eigenschaft von PLLA ist seine Biodegradierbarkeit. Temporäre Implantatmaterialien ermöglichen, dass die natürlichen Gewebeeigenschaften wiederhergestellt werden können, Reoperationen zur Implantatentfernung aufgrund der Biodegradation unnötig werden und Langzeitfolgen, ausgelöst durch eine späte negative Implantat-Gewebe-Wechselwirkung, vermieden werden können [78]. In Abbildung 5 ist schematisch die hydrolytische Biodegradation für den Anwendungsfall eines PLLA-basierten Stents mit den drei Phasen Wirkstoffelution, Regeneration und Resorption gezeigt.

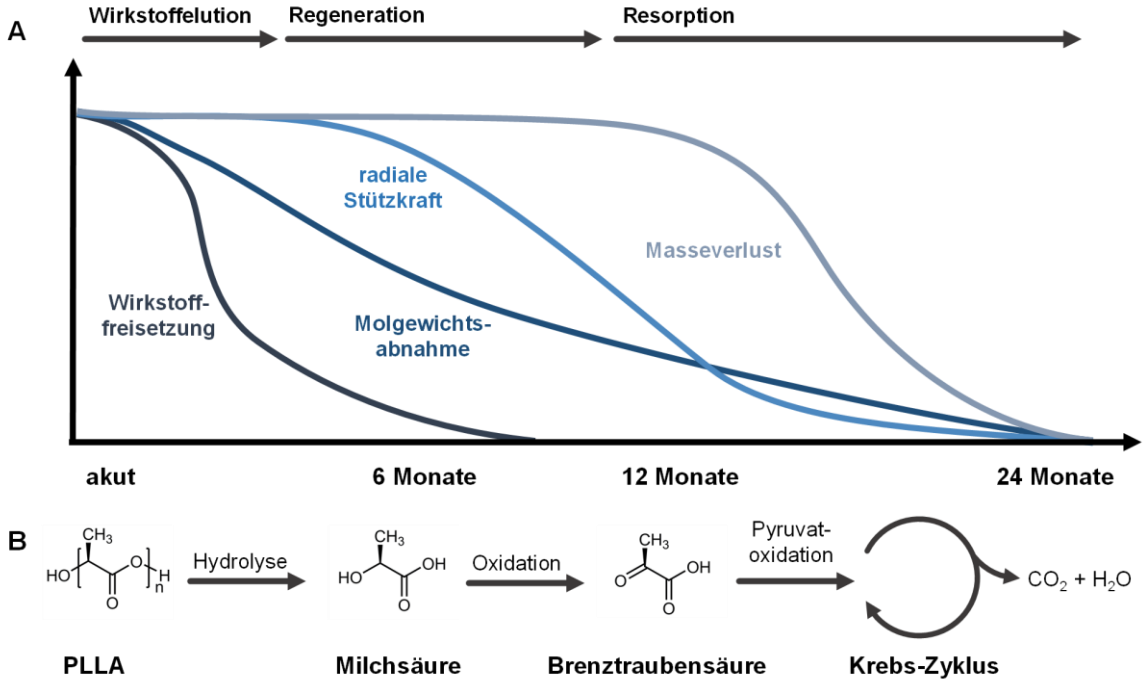


Abbildung 5: A: Schematische Darstellung des Verlaufs von Wirkstofffreisetzung und Verlauf der Implantatdegradation am Beispiel eines wirkstofffreisetzenden PLLA-Stents, modifiziert nach [78]. Zunächst wird der Wirkstoff aus der Trägermatrix diffusionsgesteuert freigesetzt, gefolgt von einer degradationsgesteuerten Freisetzung während des Polymerabbaus. Anschließend erfolgt die Verringerung des Molekulargewichts und nach ca. 6 Monaten die Abnahme der radialen Stützwirkung. Nach ca. 12 Monaten erfolgt der Masseverlust. Nach etwa 24 Monaten ist die Resorption abgeschlossen. B: Schematische Übersicht über den chemischen Abbau von PLLA im Körper über die Umwandlung zu Milchsäure, Brenztraubensäure und letztlich der Pyruvatoxidation zu Acetyl-CoA, gefolgt vom vollständigen Abbau zu CO_2 und H_2O im Krebs-Zyklus.

Um die Degradationseigenschaften eines Materials über die Lebenszeit des Implantats zu bewerten, muss letztlich immer ein Tierversuch durchgeführt werden, da im *in vitro*-Modell naturgemäß Vereinfachungen und Modellannahmen getroffen werden müssen, wodurch die komplexe *in vivo*-Situation nur näherungsweise abgebildet werden kann [52,79]. Allerdings gilt es, während der Entwicklungskaskade, auch nach dem 3R-Prinzip (*Replace*, *Reduce* und *Refine*), unnötige Tierversuche zu vermeiden. Außerdem ermöglicht die *in vitro*-Darstellung des *in vivo*-Abbaus die prozessbegleitende Analyse von Biomaterialien, z.B. hinsichtlich Veränderungen der Ermüdungseigenschaften unter Last, Auswirkungen auf die

Oberflächenmorphologie oder Fragmentierung und Partikelbildung. Über *in vitro*-Modelle lassen sich gut die physiko-chemischen Materialveränderungen während der Degradation untersuchen, wie Kristallinität und Phasenverhalten, beides wichtige Eigenschaften zur Einschätzung der Sicherheit biodegradierbarer Implantate bei längerer Standzeit [79–82]. Dies setzt jedoch eine hinreichende *in vivo*-Korrelation der verwendeten *in vitro*-Modelle voraus.

Da Degradationsstudien lange, teilweise über mehrere Jahre hinweg, andauern, ist es in der Biomaterialentwicklung von hoher Relevanz, beschleunigte Protokolle zu entwickeln, welche die Echtzeiteffekte prozessbegleitend möglichst gut abbilden und damit die Basis für Vorhersagemodelle bilden [83]. Üblich ist es dabei, entsprechend der van-'t-Hoff'schen Regel, die Medientemperatur für die Degradationsstudie zu erhöhen [82]. Alternativ kann der pH-Wert des Mediums ins Alkalische verschoben werden, da PLLA bei hohem pH-Wert erheblich schneller abbaut [84]. Es ist auch eine Kombination aus beidem gängige Praxis.

Aufgrund möglicher erheblicher Einflüsse auf die Materialeigenschaften, muss berücksichtigt werden, dass eine Erhöhung der Medientemperatur an oder über den Glasübergangsbereich des Materials in einer erhöhten Diffusion des Mediums in das Polymer resultiert, was dazu führt, dass die Echtzeitbedingungen, bei denen eine andere Diffusionsbarrierewirkung des Materials vorliegt, nicht mehr hinreichend gut abgebildet werden. Auch können z.B. Kettenfragmente, welche langsam aus dem Polymer heraus diffundieren, bei beschleunigten Bedingungen im Material verbleiben und damit als Weichmacher agieren. Damit wiederum ändert sich das Verhältnis von kristallinen und amorphen Bereichen, was letztlich einen erheblichen Einfluss auf Degradationsprozesse hat [52,54,79,82].

Enzyme, wie Proteinasen oder Lipasen, spielen darüber hinaus auch eine wichtige Rolle bei der Biodegradation, sind aber unter den Bedingungen einer beschleunigten Degradation meist inaktiv, denaturiert oder selbst chemisch abgebaut [85]. Der Enzym-assoziierte Abbau erfolgt bei Polymeren, wie PLLA, an der Oberfläche, da das Enzym aufgrund seiner molekularen Ausdehnung nicht in das Material eindringen kann [86]. Im Gegensatz dazu erfolgt die rein hydrolytische Degradation bedingt durch die Diffusion des Wassers zusätzlich zur Oberfläche auch im Bulk des Materials, was bei der Interpretation beschleunigter Degradationsstudien berücksichtigt werden muss. Auch ist der Einfluss der Autokatalyse, bedingt durch die Bildung saurer Gruppen durch die Esterspaltung im Polymerkörper, relevant, da sich so ein selbstverstärkender Effekt einstellen kann [83].

Die Fragestellung, in wieweit der Enzym-assoziierte Echtzeitabbau mit dem beschleunigten Abbau bei erhöhten Temperaturen verglichen werden kann, war Gegenstand der dieser Arbeit zugrundeliegenden Publikation zur Korrelation des beschleunigten *in vitro*-Abbauverhaltens von PLLA und P3HB. Die erzielten Ergebnisse zeigen, dass für beschleunigte Experimente vor allem identische Randbedingungen in Form von Molekulargewicht, Anfangskristallinität

und Abbauparametern erforderlich sind, um die Abbauprozesse realistischer abzubilden. Zudem konnte gezeigt werden, dass das Molekulargewicht des Polymers einen erheblichen Einfluss auf die Anfälligkeit gegenüber dem enzymatischen Abbau an der Oberfläche hat, wobei ein höheres Molekulargewicht mit einer schnelleren Enzym-assoziierten Degradation einhergeht.

Bezogen auf degradierbare Biomaterialien ist auch die Entwicklung und Testung polymerbasierter Beschichtungen auf Magnesium zur Verlangsamung und Modulation der Biokorrosion des metallischen Implantatgrundkörpers ein aktueller Forschungsbereich. Reines Magnesium wird in physiologischen Medien sehr schnell zu löslichen Mg^{2+}-Ionen oxidiert, begleitet von einer starken H_2-Entwicklung und der Bildung einer alkalischen Umgebung [87]. Dies führt zu Risiken, wie Dislokation aufgrund der Gasbildung, in Verbindung mit lokalen potentiell zelltoxischen Effekten. Zur Einstellung der Korrosionsgeschwindigkeit kommen daher vorwiegend Mg-Legierungen zum Einsatz, wobei die Legierungspartner so gewählt sind, dass der Korrosionsprozess verlangsamt wird. Eine weitere Methode zur Verzögerung der Korrosion ist die Aufbringung schützender polymerer Beschichtungen, welche die Mg-Oxidation aufgrund ihrer Wirkung als Diffusionsbarriere verlangsamen. Dabei können durch den Einsatz klinisch etablierter wirkstofftragender Beschichtungen auch synergistische Effekte genutzt werden.

Die Entwicklung von Prüfprotokollen zur *in vitro*-Korrosion Mg-basierter Implantate ist besonders anspruchsvoll, da bereits innerhalb kürzester Zeit ein erheblicher Anstieg des pH-Wertes aufgrund der $Mg(OH)_2$-Bildung erfolgt, mit Auswirkungen auf die sich bildenden Redox- und Löslichkeitsgleichgewichte [88]. Die Stabilisierung des pH-Wertes mit organischen Systemen, wie TRIS (Tris(hydroxymethyl)aminomethan) oder HEPES (2-(4-(2-Hydroxyethyl)-1-piperazinyl)-ethansulfonsäure), ist aufgrund begrenzter Pufferkapazität sowie des Einflusses der Puffer auf die Ausbildung typischer Korrosionsprodukte, z.B. durch chelatisierende oder abschirmende Effekte, mit daraus resultierender Destabilisierung der Korrosionsschicht und Beeinflussung der Korrosionsrate, nicht geeignet [89–91].

Eine Alternative ist die Stabilisierung des pH-Wertes durch die kontrollierte Zugabe von gasförmigem CO_2, zumal dies der Wirkung des Carbonatpuffersystems im menschlichen Körper näherungsweise entspricht. Damit kann ein pH-stabiler Versuchsaufbau zur Evaluation der Schutzwirkung und Degradation/Korrosion von mit polymeren Dünnfilmbeschichtungen versehenen Mg-Implantaten realisiert werden, welcher kontinuierliche Testung mit anpassbaren Probenahmezeiten ermöglicht.

Die Entwicklung eines entsprechenden Prüfstands inklusive Prüfprotokoll war Gegenstand der in dieser Arbeit berücksichtigten Publikation zum Einfluss von polymerbasierten

Beschichtungen auf die Korrosionsrate von Magnesiumsubstraten unter physiologischen *in vitro*-Bedingungen.

Wirkstofffunktionalisierungen

In der Implantattechnologie sind funktionale Materialien, beispielsweise mit Wirkstoffen oder Wachstumsfaktoren, ein wesentlicher Bestandteil der Entwicklungen. So sind medikamentenbeschichtete Stents (DES) bei der Behandlung von Koronararteriienstenosen Stents aus reiner Metalllegierung (*Bare Metal Stents*) überlegen [92,93]. Dabei werden in der klinischen Praxis häufig Medikamente aus der Limus-Familie eingesetzt [94], speziell Sirolimus [95], aber auch Zytostatika, wie Paclitaxel [49]. Bei der Entwicklung und Optimierung wirkstofftragender Materialien spielen neben dem Freisetzungsverhalten, zum Erreichen einer pharmakologisch wirksamen Konzentration, auch die Auswirkungen auf die grundlegenden Materialeigenschaften eine erhebliche Rolle. Dabei sind besonders die thermischen und mechanischen Eigenschaften relevant, sowie die Langzeitstabilität (*shelf life*) des Materials.

Dieses Verhalten hängt von der Chemie des Wirkstoffs und intermolekularer Wechselwirkungen mit der Polymermatrix ab. Verschiedene Wirkstoffe besitzen aufgrund ihrer Strukturunterschiede stark unterschiedliche chemische Eigenschaften, so dass der Einfluss auf die Polymermatrix nicht ohne Weiteres vorhergesagt werden kann. Im einfachsten Fall vermischen sich Polymer und Wirkstoff vollständig, ohne dass Änderungen der Materialeigenschaften beobachtbar sind. Andere pharmakologisch aktive Substanzen wiederum können zu einer Erhöhung der Zugfestigkeit des Implantatmaterials führen, oder aber zur Phasentrennung zwischen PLLA und Wirkstoff, bis hin zur thermischen Destabilisierung des Polymers. Letzteres bedingt damit die Notwendigkeit einer zielgerichteten thermischen Nachbehandlung, um Haltbarkeit und mechanische Belastbarkeit des Implantats zu gewährleisten [72].

Diese komplexen Wechselwirkungen machen es notwendig, vor dem Hintergrund der Fortschritte in etablierten *Drug Eluting*-Anwendungen und der Entwicklung neuartiger Polymer/Wirkstoff-Kombinationen die Interaktion zwischen PLLA und verschiedenen Wirkstoffen individuell zu untersuchen. Während die Kinetik der Wirkstofffreisetzung eindeutig wichtig ist und im Mittelpunkt umfangreicher Forschungsarbeiten steht, ist der Einfluss der Wirkstoffe von hoher Relevanz bezogen auf die Werkstoffeigenschaften gegenwärtiger Implantatentwicklungen. Diese Fragestellung war Gegenstand der in dieser Arbeit berücksichtigten Publikation 5 zum Einfluss der Inkorporation von Wirkstoffen auf die Materialeigenschaften der PLLA-Trägermatrix.

Oberflächenfunktionalisierungen

Neben der Wirkstoffinkorporation ist die Oberflächenmodifikation, von Strukturierungen bis hin zu chemischen Funktionalisierungen, wichtiger Gegenstand in der Biomaterialforschung [96]. Vor allem bei Implantaten, welche als Gerüststruktur zur Geweberegeneration dienen sollen, sind Oberflächenmodifikationen wichtige Werkzeuge zur Sicherstellung der Langzeitfunktionalität des Biomaterials [97].

Naturgemäß ist bei einem Implantat das Material immer in direktem Kontakt mit Gewebe und Körperflüssigkeiten und ruft dementsprechend eine Fremdkörperreaktion hervor. Daher spielt für Implantatanwendungen neben grundsätzlicher Werkstoffeigenschaften, wie Verarbeitbarkeit, Mechanik oder Degradation, die Oberflächenbeschaffenheit eine zentrale Rolle, um eine suffiziente Integration in das Gewebe, sowie eine ausreichende Zellbesiedlung ohne schwerwiegende Nebenwirkungen oder Abstoßungen zu gewährleisten [11].

Eine vielseitige Technologie zur Herstellung poröser Membranstrukturen ist das Elektrospinning [98]. Dieser Prozess nutzt ein elektrisches Feld aus, um kontinuierlich Fasern aus einer viskosen Polymerlösung zu erzeugen (Abbildung 6).

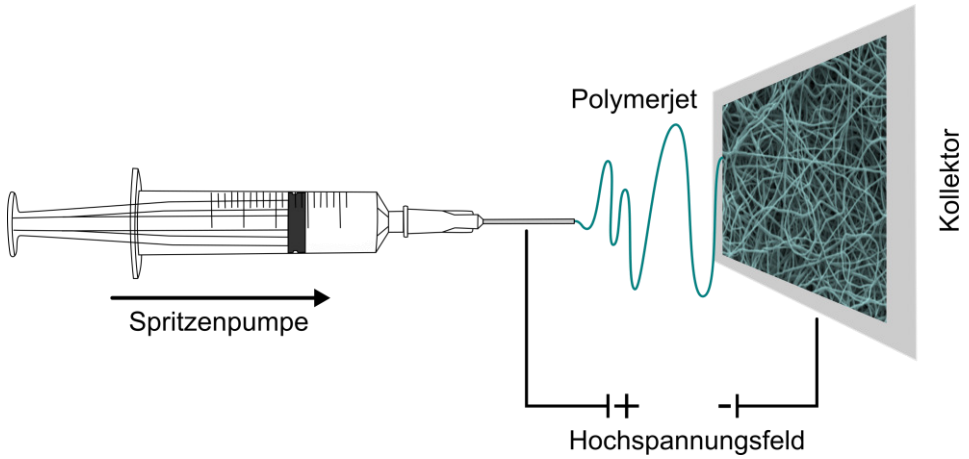


Abbildung 6: Schematische Darstellung des Elektrospinningprozesses zur Erzeugung polymerer Fasermatten. Eine viskose Polymerlösung wird mittels Spritzenpumpe kontinuierlich durch eine elektrisch kontaktierte Kanüle gefördert. Im elektrischen Feld wird an der Kanülenspitze ein Taylor-Konus erzeugt, aus dem ein Polymerjet austritt, welcher auf dem geerdeten Kollektor durch Verdampfen des Lösemittels als Fasermatte abgeschieden wird.

Die auf diesem Wege zugänglichen Materialien ahmen durch den Faseraufbau die fibrilläre Struktur natürlichen Gewebes nach, wodurch Fremdkörperreaktionen verringert und die Zellantwort verbessert werden können [99]. Üblicherweise werden mittels Elektrospinning Faserdurchmesser im Submikrometerbereich erreicht, aber es sind auch Faserdurchmesser im Nanometerbereich zugänglich [100]. Im Vergleich zu alternativen Verfahren, wie z.B. Weben oder Wirken, weist das Elektrospinning bezogen auf die Prozesskette eine wesentlich verringerte Komplexität auf, was Faser- oder Porenstrukturen kosteneffizient und in großem

Maßstab zugänglich macht. Die Technologie des Elektrospinnings erlaubt es darüber hinaus, Wirkstoffe in die gesponnenen Fasern zu inkorporieren [101].

Die auf diesem Wege zugänglichen Faserstrukturen sind z.B. als Gewebescaffold interessant, etwa im Bereich der gesteuerten Knochenregeneration. Die Therapie von großflächigen Knochendefekten ist nach wie vor eine große Herausforderung, da Schädigungen des Knochengewebes nur bis zu einer gewissen Größe (< 2,5 cm) spontan regeneriert werden können [102].

Abbaubare Faserscaffolds können in diesem Kontext als temporäres implantierbares Gerüst eingesetzt werden, um zur Geweberegeneration beizutragen. Um die Oberflächeneigenschaften des Biomaterials weiter zu verbessern und für die Gewebeintegration zu optimieren, müssen allerdings weitere Modifikationen vorgenommen werden. So können über etablierte chemische Aktivierung, etwa nasschemisch oder auf Plasmabasis, über die oberflächliche Spaltung der Polymerketten auf dem Material funktionelle Gruppen erzeugt werden, an die wiederum mittels Ankergruppen aktive Moleküle angebunden werden können [103]. Auf diesem Weg sind Oberflächenfunktionalisierungen mit Wachstumsfaktoren zugänglich , wie VEGF oder BMP, Enzymen und Proteinen oder chemisch abspaltbaren Wirkstoffen (Abbildung 7).

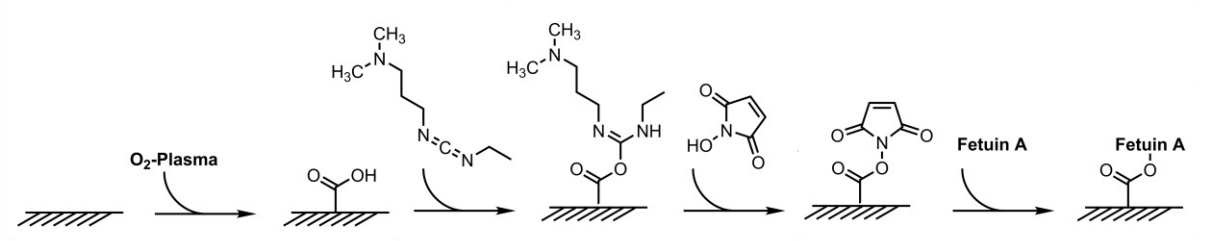


Abbildung 7: Schematische Darstellung der kovalenten Anbindung von Biomolekülen mittels EDC/NHS-Kopplung nach Plasmaaktivierung der Materialoberfläche am Beispiel von Fetuin A.

In diesem Zusammenhang war die kovalente Ankopplung von Fetuin A, welches aufgrund seiner distinktiven Calciumaffinität das Wachstum von Calciumphosphat auf der Materialoberfläche initiiert [104], sowie die Zytokompatibilität im Direktkontakttest nach beschleunigter *in vitro*-Biomineralisation Gegenstand der in dieser Arbeit betrachteten Publikation zu Fetuin A-funktionalisierten PLLA-co-PEG-Hybrid-Fasermembranen.

2. Zielsetzung der Arbeit

Die vorliegende Arbeit konzentriert sich auf Untersuchungen zu Prozessierung und Modifikation PLLA-basierter Biomaterialien im Kontext der Implantatanwendungen und des Einflusses von Verarbeitung und Modifikation auf die Materialeigenschaften.

Der erste dargestellte Themenkomplex fokussierte sich auf PLLA-basierte Blendmaterialien. Das Ziel war die Einstellung grundlegender Materialeigenschaften, insbesondere für innovative Stentanwendungen (Publikation 1). Dabei wurden schließlich basierend auf PLLA/Polyethylenoxid-Blends Prototypen von Stents zur Implantation in der Eustachi‘schen Tube hergestellt und umfangreich getestet (Publikation 2).

Ein weiteres Thema dabei war die prozessbegleitende Charakterisierung des Abbauverhaltens, welches mit der Korrelation der beschleunigten *in vitro*-Degradation mit der Echtzeitdegradation höchste Relevanz für die Entwicklung biodegradierbarer Implantate hat, vor allem vor dem Hintergrund PLLA-basierter Beschichtungen (Publikation 3). Es stellte sich auch die Frage nach der Bewertung der Korrosionsschutzwirkung verschiedener polyesterbasierter Beschichtungen auf Magnesiumsubstraten als klinisch relevantem temporären Implantatmaterial (Publikation 4). Dazu stellte sich die Aufgabe, ein Prüfprotokoll zur pH-statischen Mg-Korrosion mit der Möglichkeit der Echtzeitkontrolle zu entwickeln.

In das Anwendungsgebiet der Stenttechnologie ordnet sich auch die durchgeführte Studie zum Einfluss von inkorporierten Wirkstoffen auf die Eigenschaften der PLLA-Trägermatrix ein (Publikation 5). Darin wurden Studien bezüglich des Einflusses von in der Stenttechnologie etablierten Wirkstoffen auf die thermischen und mechanischen Eigenschaften der Polymermatrix durchgeführt.

Im Forschungsfeld der Oberflächeninteraktion wurden weiterhin Untersuchungen zur kovalenten Ankopplung eines Ca-affinen Proteins auf der Oberfläche von PLLA-basierten Faservliesen durchgeführt (Publikation 6). Mit diesem Ansatz ist es möglich, im Anwendungsfeld der Hartgeweberegeneration Biomineralisationsprozesse unter Erhalt der Oberflächenmorphologie zu beschleunigen und dabei die Nachteile von etablierten Ansätzen, wie dem Animpfen mit Kristallisationskeimen, zu umgehen.

Die Arbeiten leisten damit einen Beitrag zum erweiterten Verständnis PLLA-basierter Biomaterialien als klinisch höchst relevanter Materialklasse. Dabei wurden umfangreiche interdisziplinäre Untersuchungen an der Schnittstelle physiko-chemischer Materialanalytik, biomechanischer Testung und zellbiologischer Untersuchung durchgeführt, um Perspektiven hin zu innovativen Implantatentwicklungen zu schaffen.

3. Zusammenfassung der inkludierten Publikationen

Publikation 1: PLLA/Polyurethan-Hybridmaterialien zur Verbesserung der Biomaterial-eigenschaften

Oschatz S, Schultz S, Fiedler N, Senz V, Schmitz KP, Grabow N und Koper D. Melt blending of poly(lactic acid) with biomedically relevant polyurethanes to improve mechanical performance. *Heliyon*, 2024, 10, e26268.

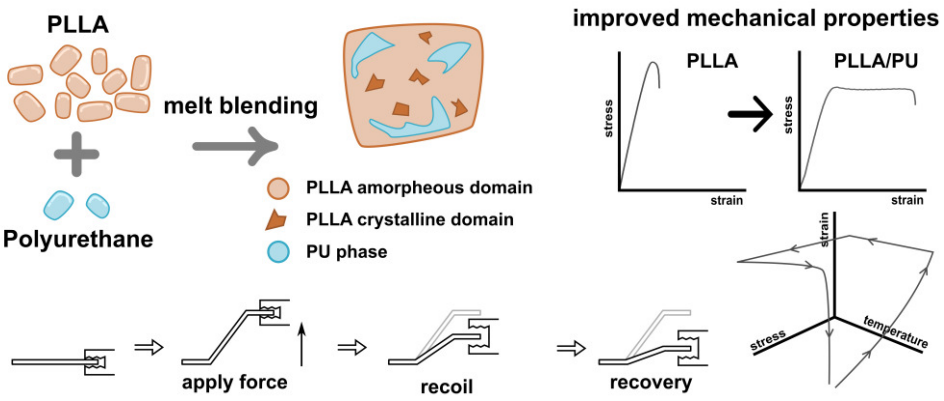


Abbildung 8: Graphische Kurzzusammenfassung der Publikation 1.

Die minimalinvasive Implantation von Stentsystemen bedingt konträre mechanische Materialanforderungen. Die radiale Verformbarkeit sollte sowohl kleine Stentdurchmesser während der Applikation als auch eine ausreichende Verformungsreserve für die Stentaufweitung auf den benötigten Zieldurchmesser gewährleisten. Zur sicheren Offenhaltung eines stenosierten Gefäßes ist weiterhin eine hohe radiale Stützkraft erforderlich. Aufgrund der inhärenten Sprödigkeit und geringen Elastizität sowie Duktilität ist PLLA für eine Reihe biomedizinischer Anwendungen ohne aufwändige Nachbehandlung weniger geeignet [105]. Ein Ansatz ist die Beimischung kleiner Moleküle (als Härter oder Weichmacher) oder eines anderen Polymers [57,58]. Bezüglich eines klinischen Transfers ist die Auswahl geeigneter Blendpartner allerdings durch regulatorische Anforderungen stark begrenzt.

Diese Arbeit befasst sich mit durch Schmelzen hergestellten Blends aus PLLA mit biomedizintechnisch relevanten Polyurethanen (PU), um die plastische Verformbarkeit und Bruchdehnung zu erhöhen, bei möglichst geringem Einfluss auf Streckgrenze und thermischer Stabilität. Dazu wurde PLLA mit 10 Gew.-% an folgendenden Polyurethanen verblendet: Pellethane 2363 80A, Tecothane TT 1055D, Chronothane P75D, Adiamat und ElastEon. Diesen Polyurethanen ist gemeinsam, dass sie seit langem für Implantate, wie künstlichen Herzklappen, Blutgefäßersatz und als Isoliermaterial für Herzschrittmacherelektroden, eingesetzt werden [106–110].

Morphologische Analysen der hergestellten Materialien nach Kryo-Bruch und NaOH-Ätzen zeigten für PLLA eine homogene, sphärolithische Kristallstruktur, während die Blends PU-Domänen, teils mit Hohlräumen aufwiesen. Die Ergebnisse der Zugversuche zeigten, dass der PLLA/Pellethane-Blend eine im Vergleich zu reinem PLLA signifikant erhöhte Bruchdehnung aufweist, bei ähnlich hoher Streckgrenze. Das Verblenden mit Tecothane und ElastEon zeigte ähnliche, aber weniger ausgeprägte Effekte, während Chronothane und Adiamat die Duktilität und Bruchdehnung kaum beeinflussten. In den weiterführenden Untersuchungen konnte für PLLA/Pellethane-Blends (90:10, 80:20 und 70:30) zudem eine thermisch induzierte Formrückstellung beobachtet werden. Der Rückstellgrad war im Vergleich zu reinem PLLA zwar schwächer ausgeprägt, doch könnte diese in Verbindung mit der Verbesserten Duktilität für Stentanwendungen vorteilhaft sein.

Durch das Verblenden von PLLA mit Polyurethanen wird eine der vorteilhaften Eigenschaften für Stentanwendungen, die biologische Abbaubarkeit, in Teilen aufgehoben. Da der Polyurethananteil im Vergleich zu PLLA jedoch gering ist, verbleiben lediglich kleinste Fragmente. Ob diese Fragmente langfristig negative Auswirkungen auf das umgebende Gewebe haben, muss in weiterführenden Studien untersucht werden, um die Vorteile des Schmelzblendens gegenüber dem teilweisen Verlust der Abbaubarkeit zu bewerten.

Publikation 2: PLLA/PEO-Blend als selbstverfestigendes Material für Stent-anwendungen in der Eustachi‘schen Tube.

Oschatz S, Schultz S, Fiedler F, Markhoff J, Teske M, Koper D, Senz V, Brandt-Wunderlich C, Schmitz KP, Grabow N and Lebahn K. PLLA/PEO blend as self-curing material for a biodegradable Eustachian tube stent. *Materials & Design*, 2025, 256, 114255.

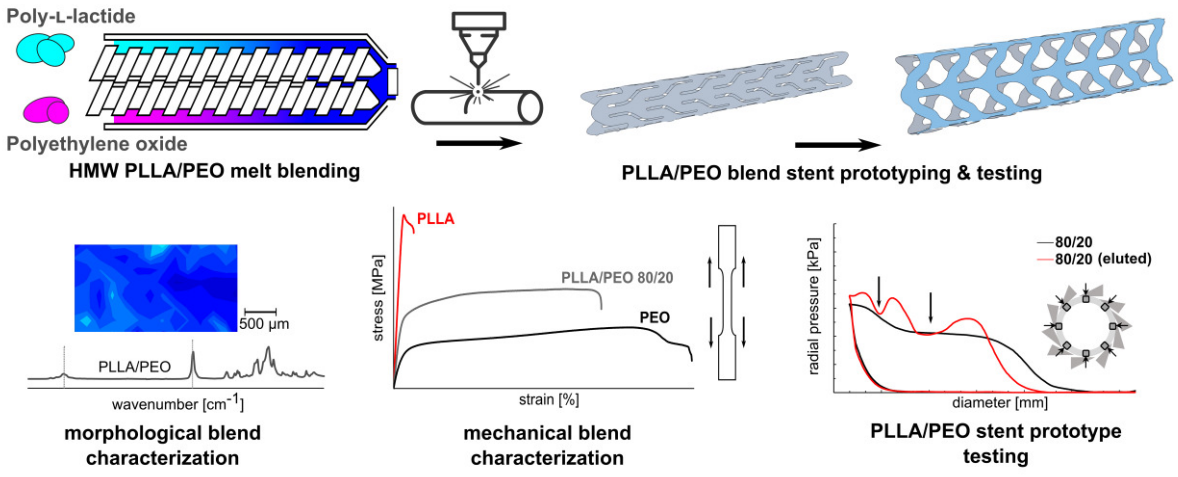


Abbildung 9: Graphische Kurzzusammenfassung der Publikation 2.

Belüftungsstörungen der Eustachi‘schen Tube können zu dauerhaften Schäden, bis hin zur Taubheit, führen [111]. Neben der Tuboplastie [112] ist eine innovative Behandlungsoption der Einsatz eines bioabbaubaren Stents [67,113], welcher die Tubenfunktion wiederherstellt. Ziel dieser Arbeit war die Entwicklung und Testung eines selbstverfestigenden, bioabbaubaren Stents auf Basis eines PLLA/PEO-Blends. Durch das Verblenden mit Polyethylenoxid (PEO) können die mechanischen Eigenschaften des Materials, Duktilität und Bruchdehnung, so angepasst werden, dass sich der Stent besser an die unregelmäßige Form der Eustachi‘schen Tube anpassen kann.

Dazu wurde zunächst untersucht, welche Verhältnisse von PLLA und PEO kompatibel sind, um ungewünschte Effekte auszuschließen, bei gleichzeitiger Verbesserung der biomechanischen Materialeigenschaften. Die Evaluation erfolgte an über aus der Schmelze hergestellten Blends, welche schließlich im Spritzguss zu Prüfkörpern verarbeitet wurden. Bis 20 Gew.-% PEO traten keine Phasentrennungen oder morphologischen Veränderungen auf.

Anschließend wurden über thermische Extrusion Röhrenhalbzeuge aus reinem PLLA, sowie PLLA/PEO 90/10 und 80/20, hergestellt, welche durch CO_2-Laserschneiden zu Stentprototypen auf Basis eines bereits entwickelten geschlitzten Designs [114] verarbeitet wurden. Die hergestellten Stents wurden anschließend hinsichtlich ihres Aufweitverhaltens sowie dem Verhalten unter radialer Last getestet. Dabei hat sich gezeigt, dass die verbesserten plastischen Eigenschaften der Blends gegenüber reinem PLLA eine problemlose Expansion des Stents ohne Bruch ermöglichten.

Weiterhin wird im Kontakt mit Wasser das PEO aus dem Stent herausgelöst, wodurch sich weitgehend die ursprünglichen mechanischen Eigenschaften des PLLA wiederherstellen und eine langfristige Öffnung der Eustachi‘schen Tube gewährleistet werden kann. In der mechanischen Testung wiesen die hergestellten Stentprototypen eine im Vergleich zu kommerziellen Vergleichsstents [115] geringere Radialkraft auf, übertrafen diese jedoch nach Herauslösen des PEO. Auch die Radialsteifigkeit der Stents stieg nach der PEO-Elution erheblich an, was die Stützfunktion verbesserte.

In vitro-Zytokompatibilitätstests mit relevanten Zelllinien zeigten nach PEO-Elution keine zytotoxischen Effekte, was auf Biokompatibilität hinweist. Damit liefert die Arbeit die Grundlage für weiterführende Studien mit primären Zellen (z. B. Fibroblasten, Endothelzellen), zudem sind weiterführende präklinische Studien unter realer Lastsituation erforderlich, um die klinische Translation vorzubereiten.

Publikation 3: Korrelation des beschleunigten *in vitro*-Abbauverhaltens von PLLA und P3HB zur prozessbegleitenden Materialcharakterisierung

Arbeiter D, Lebahn K, Reske T, Senz V, Eickner T, Schmitz KP, Grabow N and **Oschatz S**. Comparison of accelerated and enzyme-associated real-time degradation of HMW PLLA and HMW P3HB films, *Polymer Testing*, 2022, 107, 107471.

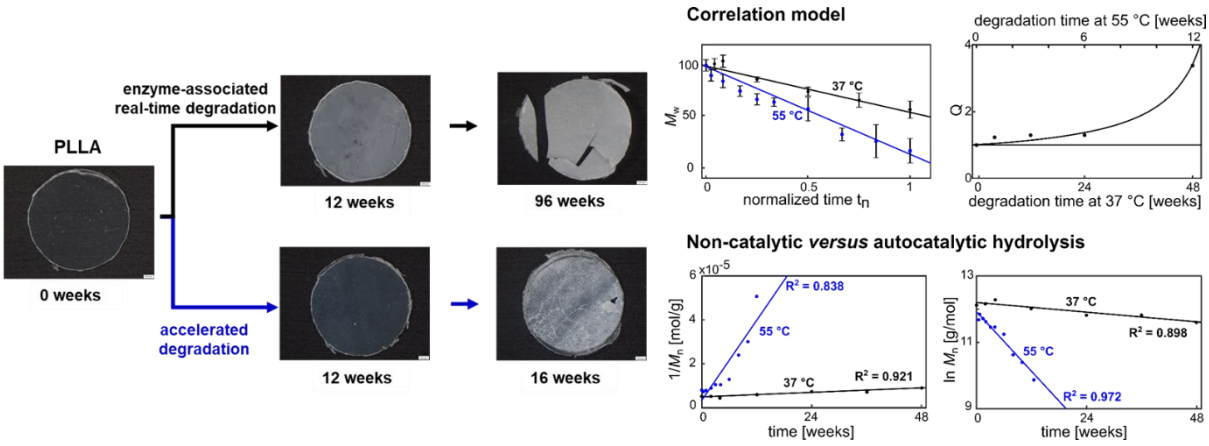


Abbildung 10: Graphische Kurzzusammenfassung der Publikation 3.

Beim *in vivo*-Abbau bioresorbierbarer Polymere spielt eine Vielzahl an Faktoren eine Rolle, wie etwa die Beteiligung von Enzymen. Beschleunigte *in vitro*-Abbauprotokolle sind für die Entwicklung und Testung innovativer Implantatsysteme essenziell und ermöglichen es, das Langzeitverhalten, z.B. hinsichtlich mechanischer Ermüdung, Veränderungen der Oberflächenrauheit oder Fragmentierung und Partikelbildung, in einem relativ kurzen Experiment entwicklungsbegleitend zu reproduzieren [116]. Allerdings kann die komplexe *in vivo*-Situation durch *in vitro*-Experimente nur begrenzt dargestellt werden.

Ziel dieser Arbeit war es, die *in vitro*-Degradation von hochmolekularem (HMW) PLLA und P3HB unter Echtzeitbedingungen mit Verwendung von Proteinase K, Pseudomonas-Lipase und Aspergillus-Lipase vergleichend zu beschleunigten Bedingungen bei 55 °C zu untersuchen, um so Beiträge zur Entwicklung beschleunigter Degradationsprotokolle zu leisten [117,118]. Die Daten der beschleunigten Studie wurden weiterhin mit denen der Echtzeitstudie verglichen, um eine Aussage hinsichtlich der Korrelation von beschleunigtem Experiment zur Echtzeitstudie zu treffen.

Die Ergebnissen zeigen, dass Herstellungsprozesse nur einen geringen Einfluss auf das Abbauverhalten haben, ganz im Gegensatz zu den Ausgangseigenschaften, wie der Kristallinität des Materials, welche das Degradationsverhalten erheblich stärker beeinflussen. Die Molekulargewichtsabnahme im Echtzeitversuch sowie unter beschleunigten Bedingungen zeigte, dass Echtzeitstudien durch beschleunigte Studien bis zu einem gewissen Maß abgebildet werden können.

Im Fall von PLLA L210 korrelieren 6 Wochen bei 55 °C mit einer 26-wöchigen Echtzeitdegradation, und für PLLA L214 bilden 16 Wochen bei 55 °C eine 48-wöchige Echtzeitdegradation ab. Im Falle von P3HB kann ein 16-wöchiger beschleunigter Abbau eine 108-wöchige Degradation in Echtzeit abbilden. Bezüglich der Entwicklung der Kristallinität, welche ebenfalls stark durch die Degradation beeinflusst wird und wiederum einen erheblichen Einfluss auf das Materialverhalten hat, konnte gezeigt werden, dass der wellenförmige Verlauf der Kristallinitätsentwicklung einem beschleunigten Degradationsmodell Grenzen setzt.

Zwei wichtige Ergebnisse dieser Arbeit sind, dass die ausgewählten Lipasen den Abbau von P3HB nicht beeinflussen, jedoch die Oberflächendegradation von PLLA. Auf die Bulkdegradation haben die Enzyme keinen Einfluss, da sie aufgrund ihrer Molekülgröße nicht in das Material hinein diffundieren können [86]. Darüber hinaus konnten beobachtet werden, dass beim beschleunigten PLLA-Abbau bei 55 °C im Vergleich zur Enzym-assoziierten Echtzeitdegradation erhebliche Veränderungen der Kristallinität auftreten. Daraus lässt sich schließen, dass für beschleunigte Experimente die Randbedingungen in Form von identischem Molekulargewicht, Anfangskristallinität und Abbauparametern essentiell sind, um aussagefähige Degradationsprotokolle zu entwickeln.

Publikation 4: Einfluss von polymerbasierten Beschichtungen auf die Korrosionsrate von Magnesium unter physiologischen *in vitro* Bedingungen

Fiedler N, Teske M, Nelz SC, Flügge J, Senz V, Bajer D, Grabow N and **Oschatz S**. *In vitro* corrosion of polyester coated magnesium alloy under pH-static conditions, *ACS Biomaterials Science & Engineering*, 2024, 10, 9, 5844-5855.

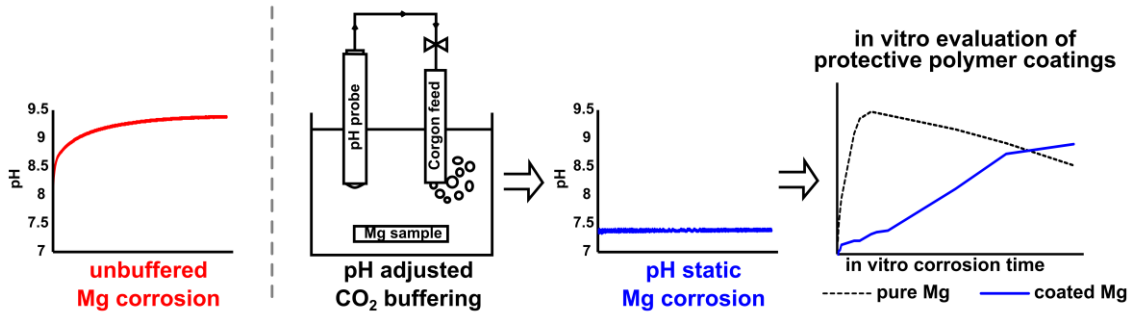


Abbildung 11: Graphische Kurzzusammenfassung der Publikation 4.

Neben der Anwendung als Wirkstoffträger können Polymerschichten auch die *in vivo*-Korrosionsraten von abbaubaren Metallimplantaten, z.B. auf Basis von Magnesium, regulieren. Insgesamt gilt, dass die Korrosionsrate von bioresorbierbaren Mg-Implantaten auf den gewünschten Anwendungsbereich abgestimmt werden muss. Da eine dauerhafte Beschichtung den Vorteilen der Verwendung von Mg als temporäres Implantatmaterial

entgegenwirken würde, stehen abbaubare Polymere, vorrangig Polyester, die sich in der klinischen Praxis langfristig bewährt haben, im Fokus der Entwicklung [119]. Die fortschreitende Oxidation von Mg zu verschiedenen MgO_x-Spezies führt innerhalb kürzester Zeit zu einem erheblichen Anstieg des pH-Wertes [120]. Damit würden sich die Korrosionsbedingungen während des Tests verändern. Aufgrund dessen ist eine pH-Regulierung des Korrosionsmediums unter Echtzeitkontrolle unerlässlich. Im Rahmen dieser Arbeit wurde ein Protokoll zur pH-gesteuerten CO_2-Pufferung entwickelt, das Testungen unter konstantem pH-Wert bei gleichzeitig zeitlich flexibler Probenahme erlaubt. Die Pufferung mit organischen Systemen ist aufgrund der begrenzten Pufferkapazität sowie der Beeinflussung der Bildung von Korrosionsprodukten mit der daraus resultierenden Destabilisierung der Korrosionsschicht und der Erhöhung der Korrosionsrate nur begrenzt zur *in vitro*-Testung geeignet.

Die kontrollierte Zugabe von gasförmigem CO_2 entspricht im Gegensatz zur Anwendung von Puffersalzen der Wirkung des Carbonatpuffersystems im menschlichen Körper und erlaubt auch im Versuchsaufbau die Bildung komplexer Mischkristallschichten auf der Oberfläche des Magnesiumprüfkörpers. Mittels eines photometrischen Mg-Assays konnte die Korrosion über das gelöste Mg in Echtzeit verfolgt werden, während der Prüfkörper unberührt blieb und für weitere morphologische Untersuchungen zur Verfügung stand. Der Prüfaufbau wurde dann für die Bewertung der degradationsverzögernden Wirkung von vier klinisch relevanten Beschichtungen, Poly-L-lactid (PLLA), Poly-L-lactid-co-Glycolid (PLGA), Poly(L-lactid-co-PEG)-Triblock-Copolymer (PLLA-co-PEG) und Polydioxanon (PDO), genutzt.

Alle Schichten zeigten dabei eine schützende Wirkung, wobei PLLA und PLLA-co-PEG die höchste korrosionsschützende Wirkung zeigten. Ebenso konnte die Bildung komplexer Mischkristalleinbettungen (wie Calcium und Phosphat) in die Passivschicht unter den Polymerbeschichtungen auf der Mg-Oberfläche abgebildet werden, welche gut mit *in vivo* beobachteten Vorgängen übereinstimmte [121,122]. Zwar schränkt die geringe Löslichkeit der Magnesiumcarbonate in Verbindung mit dem Volumenverlust durch die Luft-offene Konstruktion des Prüfstandes die Aussagekraft bei Langzeitstudien ein. Dennoch erlaubt die vorgestellte Methode relevante Daten, um die Wirksamkeit korrosionsschützender Beschichtungen auf degradierbaren Mg-Implantaten entwicklungsbegleitend zu bewerten.

Publikation 5: Einfluss der Inkorporation von Wirkstoffen auf die Materialeigenschaften der PLLA-Trägermatrix im Kontext kardiovaskulärer DES-Anwendungen

Arbeiter D, Reske T, Teske M, Bajer D; Senz V, Schmitz KP, Grabow N and **Oschatz S**. Influence of Drug Incorporation on the Physico-Chemical Properties of Poly(l-Lactide) Implant Coating Matrices - A Systematic Study. *Polymers*, 2021, 13, 292.

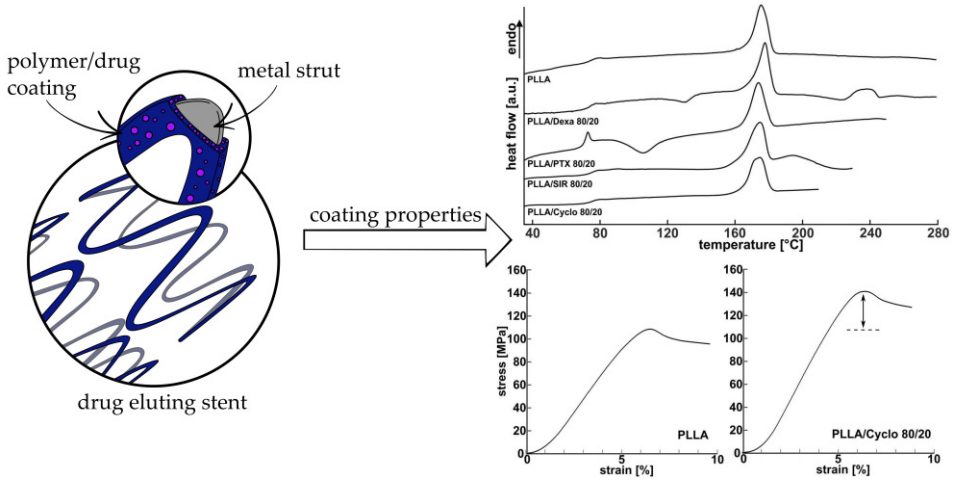


Abbildung 12: Graphische Kurzzusammenfassung der Publikation 5.

Drug-Eluting-Implantate sind in der Biomedizintechnik unverzichtbar geworden, z.B. über wirkstofftragende Polymerbeschichtungen, wie etwa unter Verwendung von PLLA als Trägermatrix. Dabei werden häufig Medikamente aus der Limus-Familie eingesetzt, vor allem Sirolimus, ein mTOR-Inhibitor welcher die Zellproliferation hemmt und damit das Risiko einer Restenose im Stent verringert. Weitere relevante Wirkstoffe sind Dexamethason, welches als Kortikosteroid wegen seiner immunsuppressiven und entzündungshemmenden Eigenschaften eingesetzt wird, oder Cyclosporin A, das die Calcineurin-Cyclophylin-Komplexbildung blockiert und somit die Proliferation und Migration von glatten Muskelzellen (*Smooth Muscle Cells*, SMCs) hemmt. Das Zytostatikum Paclitaxel (PTX) wurde in früheren Generationen der DES eingesetzt, ist aber mittlerweile aufgrund potentieller schwerwiegender Nebenwirkungen umstritten [123]. Aktuelle Studien versuchen, die Bedenken bezüglich der PTX-Anwendung zu widerlegen [124]. Diese Meinung wird aber (Stand 2025) noch nicht von der Europäischen Kommision bzw. dem BfARM übernommen [125,126].

In der vorliegenden Studie wurden dünne, mittels *Spray Coating* hergestellte PLLA/Wirkstoff-Folien vergleichend hinsichtlich des Einflusses der genannten Wirkstoffe auf die thermischen und mechanischen Eigenschaften der Polymermatrix untersucht. Dabei hat sich gezeigt, dass alle ausgewählten Wirkstoffe zu einer Erhöhung der Zugfestigkeit des Polymers führten. Weiterhin zeigte sich bei Sirolimus und Dexamethason eine Phasenseparation zwischen PLLA und Wirkstoff. Bei Paclitaxel und Dexamethason führte der Wirkstoffeinfluss zu einer ausgeprägten Kaltkristallisation des Polymers, was ein verändertes thermische Verhalten anzeigt. Hohe Mengen an Paclitaxel (20%) führten weiterhin zu einer starken Abnahme der Kristallinität des PLLA, was auf eine starke Wechselwirkung des Wirkstoffes mit dem Polymer schließen lässt.

Dies unterstreicht die Wichtigkeit von Nachprozessierungsschritten für die genannten Wirkstoffe, um eine stabile und dauerfeste wirkstofftragende Schicht zu erzeugen. Cyclosporin

A wiederum vermischte sich vollständig mit der PLLA-Matrix und beeinflusste die Polymereigenschaften nur wenig. Zusammenfassend konnte mit dieser Arbeit zum Verständnis der komplexen Wechselwirkung zwischen PLLA und Wirkstoffen beigetragen werden. Verschiedene Wirkstoffe weisen völlig unterschiedliche chemische Eigenschaften und damit Wechselwirkungen mit Polymeren auf, so dass der Einfluss auf die Polymermatrix nicht ohne weiteres vorhergesagt werden kann.

Publikation 6: PLLA-co-PEG-Hybrid-Fasermembranen zur Verbesserung der Biomineralisation

Oschatz S, Teske M, Burmeister U, Illner S, Lang H, Senz V, Grabow und Markhoff J. Fetuin A functionalisation of biodegradable PLLA-co-PEG nonwovens towards enhanced biomineralisation and osteoblastic growth behavior, *Biomaterials Science*, 2023, 11, 5240.

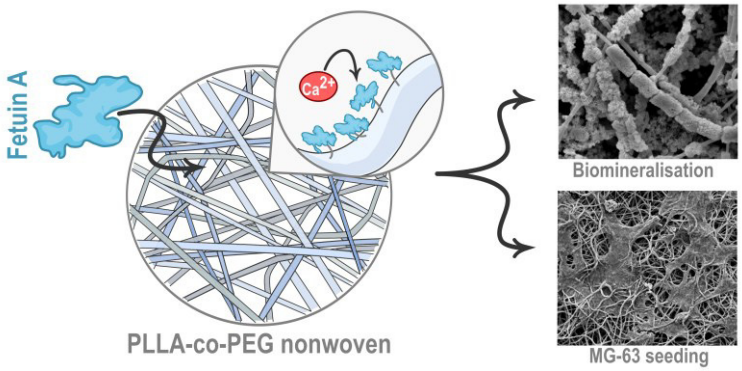


Abbildung 13: Graphische Kurzzusammenfassung der Publikation 6.

Neben der Wirkstoffinkorporation in Polymerbeschichtungen ist die Oberflächenfunktionalisierung von Biomaterialien, z.B. durch die Veränderung der Oberflächenhydrophilie oder die Immobilisierung von aktiven Verbindungen, ein höchst aktueller Forschungskomplex. Vor diesem Hintergrund ist das Thema dieser Arbeit die oberflächliche Ankopplung von Fetuin A zur Erzeugung von Hybrid-Fasermembranen zur Verbesserung der Biomineralisationseigenschaften des Materials.

Bei Hartgewebsdefekten, z.B. in der regenerativen Zahnmedizin, besteht die Gefahr, dass Bindegewebe und Gingivaepithel aufgrund der im Vergleich zum Knochengewebe höheren Proliferationsrate in den Knochendefekt einwachsen und ihn auffüllen, was die autologe Knochenregeneration hemmt [127]. Dies macht den Einsatz einer, im Idealfall temporären, Barriereschicht erforderlich, um die Infiltration des Weichgewebes zu verhindern, und gleichzeitig die Neubildung des Knochens zu unterstützen. Autogene Implantate sind dabei das Material der Wahl, allerdings ist ihre Verfügbarkeit begrenzt und die Gewinnung ist häufig mit Entnahmemorbiditäten verbunden [128]. Voll- oder teilsynthetische Materialien sind eine attraktive Option, aber oft unzureichend in Bezug auf Osteokonduktion, Osteoinduktion oder

Osteoneogenese. Zur Verbesserung knochenregenerativer Eigenschaften des Biomaterials werden oft elektrogesponnene Hybridmembranen, die mit Hydroxylapatit (HA)-Mikropartikeln als Kristallisationskeime beladen sind, erzeugt. Allerdings sind die mangelnde Stabilität und Homogenität der HA-Suspension vor und während des Herstellungsprozesses problematisch, da Phasenseparation zu ungleichmäßiger Verteilung der Kristallisationskeime führt [129].

Der verfolgte eigene Ansatz war die kovalente Immobilisierung von Fetuin A auf elektrogesponnenen Fasermembranen, bestehend aus biodegradierbarem PLLA-co-PEG Triblock-Copolymeren. Fetuin A ist ein Plasmaprotein von Wirbeltieren, das eine sehr hohe Calciumaffinität aufweist [130]. Ist dieses Protein auf der Oberfläche der Membran immobilisiert, so entzieht das Fetuin A Ca^{2+}-Ionen bzw. Calciumphosphat (CaP)-Cluster (Posner-Cluster) aus den umgebenden Körperflüssigkeiten, was wiederum die Biomineralisation initiiert und die Bildung einer biogenen CaP-Schicht ermöglicht. Dabei hat sich gezeigt, dass sich unter beschleunigten *in vitro*-Bedingungen eine flächendeckende CaP-Schicht auf und im Material unter Beibehaltung der ausgeprägten Morphologie der Fasermembran bildet.

Die derart biomineralisierten Hybridmembranen wurden anschließend hinsichtlich ihrer Wirkung auf das Zellwachstum von MG63-Osteoblasten, die Biosynthese von Typ-I-Kollagen-Propeptiden und die Ausbildung von Inflammationsmarkern untersucht. Dabei zeigte sich eine signifikant verbesserte Zelladhäsion und Ausbreitung auf mit Fetuin A funktionalisierten und anschließend biomineralisierten Hybridmembranen, bei vergleichbarer metabolischer Zellaktivität. Des Weiteren konnte keine signifikant erhöhte Biosynthese der ausgewählten Entzündungsmarker Interferon-alpha (IFN-α), Granulozyten-Monozyten-Kolonien-stimulierende Faktor (GM-CSF), sowie Interleukinen (IL-2, IL-4, IL-10 und IL-17) im Vergleich zu den Referenzmaterialien festgestellt werden.

Im Vergleich zur Referenz wurde eine verringerte Menge an Kollagen I-Vorstufen im Überstand gefunden. Da Fetuin A die intrafibrilläre Mineralisierung von Kollagen *in vitro* fördert, kann angenommen werden, dass synthetisierte Kollagenvorstufen an Fetuin A auf den modifizierten Vliesen gebunden wurden, was zu einer reduzierten Kollagen I-Vorstufen-konzentration im Überstand führte [131]. Die Bindung der Kollagenvorläufer an die Hybridmembranen konnte allerdings noch nicht untersucht werden.

Zusammenfassend lässt sich sagen, dass der vorgestellte Ansatz das Potenzial hat, als neuartiger Scaffold in der Knochenregeneration eingesetzt zu werden, da die Hybridmembran einfach zu handhaben ist und bequem an verschiedene Formen angepasst werden kann, um den individuellen Einsatzorten gerecht zu werden.

4. Literaturverzeichnis

[1] S. Todros, M. Todesco, A. Bagno, Biomaterials and Their Biomedical Applications: From Replacement to Regeneration, Processes 9 (2021) 1949. https://doi.org/10.3390/pr9111949.

[2] H.L. Ornaghi, F.M. Monticeli, L.D. Agnol, A Review on Polymers for Biomedical Applications on Hard and Soft Tissues and Prosthetic Limbs, Polymers 15 (2023) 4034. https://doi.org/10.3390/polym15194034.

[3] J.-S. Koh, B.D. Gogas, S. Kumar, J.J. Benham, S. Sur, N. Spilias, A. Kumar, D.P. Giddens, R. Rapoza, D.J. Kereiakes, G. Stone, H. Jo, H. Samady, Very late vasomotor responses and gene expression with bioresorbable scaffolds and metallic drug-eluting stents, Catheter. Cardiovasc. Interv. 98 (2021) 723–732. https://doi.org/10.1002/ccd.29819.

[4] X. Gao, M. Fraulob, G. Haïat, Biomechanical behaviours of the bone-implant interface: a review, J. R. Soc. Interface 16 (2019) 20190259. https://doi.org/10.1098/rsif.2019.0259.

[5] J.M. Morais, F. Papadimitrakopoulos, D.J. Burgess, Biomaterials/tissue interactions: possible solutions to overcome foreign body response, AAPS J 12 (2010) 188–196. https://doi.org/10.1208/s12248-010-9175-3.

[6] A. Josyula, K.S. Parikh, I. Pitha, L.M. Ensign, Engineering biomaterials to prevent post-operative infection and fibrosis, Drug. Deliv. Transl. Res. 11 (2021) 1675–1688. https://doi.org/10.1007/s13346-021-00955-0.

[7] J.S. Soares, J.E. Moore, Biomechanical Challenges to Polymeric Biodegradable Stents, Ann. Biomed. Eng. 44 (2016) 560–579. https://doi.org/10.1007/s10439-015-1477-2.

[8] Z. Morsada, M.M. Hossain, M.T. Islam, M.A. Mobin, S. Saha, Recent progress in biodegradable and bioresorbable materials: From passive implants to active electronics, App. Mater. Today 25 (2021) 101257. https://doi.org/10.1016/j.apmt.2021.101257.

[9] B. Parkinson, B. Sargent, C. Roubicek, S. Magleby, V. Garcia, L. Howell, Mechanical actuation via resorbable materials, Robotica 42 (2024) 3979–3993. https://doi.org/10.1017/S0263574723001534.

[10] M. Hussain, S.M. Khan, M. Shafiq, N. Abbas, U. Sajjad, K. Hamid, Advances in biodegradable materials: Degradation mechanisms, mechanical properties, and biocompatibility for orthopedic applications, Heliyon 10 (2024) e32713. https://doi.org/10.1016/j.heliyon.2024.e32713.

[11] N. Kasoju, A. Sunilkumar, Convergence of tissue engineering and sustainable development goals, Biotechnol. Sustain. Mater. 1 (2024) 1–16. https://doi.org/10.1186/s44316-024-00021-y.

[12] L. Yildirimer, A.M. Seifalian, Three-dimensional biomaterial degradation - Material choice, design and extrinsic factor considerations, Biotechnol. Adv. 32 (2014) 984–999. https://doi.org/10.1016/j.biotechadv.2014.04.014.

[13] A.R. Khan, N.S. Grewal, C. Zhou, K. Yuan, H.-J. Zhang, Z. Jun, Recent advances in biodegradable metals for implant applications: Exploring in vivo and in vitro responses, Results Eng. 20 (2023) 101526. https://doi.org/10.1016/j.rineng.2023.101526.

[14] A. Saberi, H.R. Bakhsheshi-Rad, S. Abazari, A.F. Ismail, S. Sharif, S. Ramakrishna, M. Daroonparvar, F. Berto, A Comprehensive Review on Surface Modifications of Biodegradable Magnesium-Based Implant Alloy: Polymer Coatings Opportunities and Challenges, Coatings 11 (2021) 747. https://doi.org/10.3390/coatings11070747.

[15] N.T. Kirkland, N. Birbilis, M.P. Staiger, Assessing the corrosion of biodegradable magnesium implants: a critical review of current methodologies and their limitations, Acta Biomater. 8 (2012) 925–936. https://doi.org/10.1016/j.actbio.2011.11.014.

[16] A.-M. Galow, A. Rebl, D. Koczan, S.M. Bonk, W. Baumann, J. Gimsa, Increased osteoblast viability at alkaline pH in vitro provides a new perspective on bone regeneration, Biochem. Biophys. Rep. 10 (2017) 17–25. https://doi.org/10.1016/j.bbrep.2017.02.001.

[17] Y. Yang, Y. Zhu, X. Xi, Anti-inflammatory and antitumor action of hydrogen via reactive oxygen species, Oncol. Lett. 16 (2018) 2771–2776. https://doi.org/10.3892/ol.2018.9023.

[18] C. Mukherjee, D. Varghese, J.S. Krishna, T. Boominathan, R. Rakeshkumar, S. Dineshkumar, C. Brahmananda Rao, A. Sivaramakrishna, Recent advances in biodegradable polymers – Properties, applications and future prospects, Eur. Polym. J. 192 (2023) 112068. https://doi.org/10.1016/j.eurpolymj.2023.112068.

[19] A. Ershad-Langroudi, N. Babazadeh, F. Alizadegan, S. Mehdi Mousaei, G. Moradi, Polymers for implantable devices, J. Ind. Eng. Chem. 137 (2024) 61–86. https://doi.org/10.1016/j.jiec.2024.03.030.

[20] I. Manavitehrani, A. Fathi, H. Badr, S. Daly, A. Negahi Shirazi, F. Dehghani, Biomedical Applications of Biodegradable Polyesters, Polymers 8 (2016) 20. https://doi.org/10.3390/polym8010020.

[21] N.G. Khouri, J.O. Bahú, C. Blanco-Llamero, P. Severino, V.O. Concha, E.B. Souto, Polylactic acid (PLA): Properties, synthesis, and biomedical applications – A review of the literature, J. Mol. Struct. 1309 (2024) 138243. https://doi.org/10.1016/j.molstruc.2024.138243.

[22] M. Oleksy, K. Dynarowicz, D. Aebisher, Advances in Biodegradable Polymers and Biomaterials for Medical Applications-A Review, Molecules 28 (2023). https://doi.org/10.3390/molecules28176213.

[23] D.A. Power, A. Camaj, D.J. Kereiakes, S.G. Ellis, R. Gao, T. Kimura, Z.A. Ali, K.A. Stockelman, O. Dressler, Y. Onuma, P.W. Serruys, G.W. Stone, Early and Late Outcomes With the Absorb Bioresorbable Vascular Scaffold: Final Report From the ABSORB Clinical Trial Program, JACC Cardiovasc. Interv. 18 (2025) 1–11. https://doi.org/10.1016/j.jcin.2024.08.050.

[24] W.A. Omar, D.J. Kumbhani, The Current Literature on Bioabsorbable Stents: a Review, Curr. Atheroscler. Rep. 21 (2019) 54. https://doi.org/10.1007/s11883-019-0816-4.

[25] G. Song, H.Q. Zhao, Q. Liu, Z. Fan, A review on biodegradable biliary stents: materials and future trends, Bioact. Mater. 17 (2022) 488–495. https://doi.org/10.1016/j.bioactmat.2022.01.017.

[26] Y. Yang, Y. Yang, Z. Hou, T. Wang, P. Wu, L. Shen, P. Li, K. Zhang, L. Yang, S. Sun, Comprehensive review of materials, applications, and future innovations in biodegradable esophageal stents, Front. Bioeng. Biotechnol. 11 (2023) 1327517. https://doi.org/10.3389/fbioe.2023.1327517.

[27] M. Zilberman, R.C. Eberhart, Drug-eluting bioresorbable stents for various applications, Annu. Rev. Biomed. Eng. 8 (2006) 153–180. https://doi.org/10.1146/annurev.bioeng.8.013106.151418.

[28] E. Gallinoro, M. Almendarez, R. Alvarez-Velasco, E. Barbato, P. Avanzas, Bioresorbable stents: Is the game over?, Int. J. Cardiol. 361 (2022) 20–28. https://doi.org/10.1016/j.ijcard.2022.05.024.

[29] J. Wright, A. Nguyen, N. D'Souza, J.M. Forbess, A. Nugent, S.R.V. Reddy, R. Jaquiss, T.R. Welch, Bioresorbable Stent to Manage Congenital Heart Defects in Children, Materialia 16 (2021) 101078. https://doi.org/10.1016/j.mtla.2021.101078.

[30] J.C.L. Schuh, K.A. Funk, Compilation of International Standards and Regulatory Guidance Documents for Evaluation of Biomaterials, Medical Devices, and 3-D Printed and Regenerative Medicine Products, Toxicol. Pathol. 47 (2019) 344–357. https://doi.org/10.1177/0192623318804121.

[31] X. Song, Z. Tang, W. Liu, K. Chen, J. Liang, B. Yuan, H. Lin, X. Zhu, Y. Fan, X. Shi, P. Zhao, L. Yang, K. Zhang, A.G. Mikos, X. Zhang, Biomaterials and regulatory science, Journal of Materials Science & Technology 128 (2022) 221–227. https://doi.org/10.1016/j.jmst.2022.04.018.

[32] DIN EN ISO 10993-1:2021-05, Biologische Beurteilung von Medizinprodukten_- Teil_1: Beurteilung und Prüfungen im Rahmen eines Risikomanagementsystems (ISO_10993-1:2018, einschließlich korrigierte Fassung 2018-10); Deutsche Fassung EN_ISO_10993-1:2020, DIN Media GmbH, Berlin.

[33] E. Bianchini, C.C. Mayer, Medical Device Regulation: Should We Care About It?, Artery Res. 28 (2022) 55–60. https://doi.org/10.1007/s44200-022-00014-0.

[34] K.M. Jurczak, T.A.B. van der Boon, R. Devia-Rodriguez, R.C.L. Schuurmann, J. Sjollema, L. van Huizen, J.-P.P.M. de Vries, P. van Rijn, Recent regulatory developments in EU Medical Device Regulation and their impact on biomaterials translation, Bioeng. Transl. Med. 10 (2025) e10721. https://doi.org/10.1002/btm2.10721.

[35] C. Amaral, M. Paiva, A.R. Rodrigues, F. Veiga, V. Bell, Global Regulatory Challenges for Medical Devices: Impact on Innovation and Market Access, Appl. Sci. 14 (2024) 9304. https://doi.org/10.3390/app14209304.

[36] G.D. Prestwich, S. Bhatia, C.K. Breuer, Shannon L. M. Dahl, C. Mason, R. Mcfarland, D.J. Mcquillan, J. Sackner-bernstein, J. Schox, W.E. Tente, A. Trounson, American Association for the Advancement of Science (14 November 2012), https://www.science.org/doi/full/10.1126/scitranslmed.3004915?, zuletzt geprüft am 27.06.2025.

[37] Z. Yang, G. Yin, S. Sun, P. Xu, Medical applications and prospects of polylactic acid materials, iScience 27 (2024) 111512. https://doi.org/10.1016/j.isci.2024.111512.

[38] M. Hussain, S.M. Khan, M. Shafiq, N. Abbas, A review on PLA-based biodegradable materials for biomedical applications, Giant 18 (2024) 100261. https://doi.org/10.1016/j.giant.2024.100261.

[39] Grand View Research, Bioresorbable Polymers Market Size, Share & Trends Analysis Report By Product (Proteins, PLA, Polysaccharides, Polyglycolic Acid, Polycaprolactone), By Application

(Orthopedics, Drug Delivery), By Region, And Segment Forecasts, 2023 - 2030, https://www.grandviewresearch.com/industry-analysis/bioresorbable-polymers-market, zuletzt geprüft am 05.06.2025.

[40] Verified Market Reports, Global Bioresorbable Medical Polymer and Material Market Size By Type of Polymer (Polylactic Acid (PLA), Polyglycolic Acid (PGA)), By Application (Drug Delivery Systems, sutures), By End-user (Hospitals, Ambulatory Surgical Centers), By Formulation Type (Injectable Forms, Pre-Molded Products), By Distribution Channel (Direct Sales, Distributors), By Geographic Scope And Forecast, 2025, https://www.verifiedmarketreports.com/product/bioresorbable-medical-polymer-and-material-market/,zuletzt geprüft am 05.06.2025.

[41] Predence Research, Bioresorbable Polymers Market Size, Share, and Trends 2025 to 2034, https://www.precedenceresearch.com/bioresorbable-polymers-market, zuletzt geprüft am 05.05.2025.

[42] L.-T. Lim, R. Auras, M. Rubino, Processing technologies for poly(lactic acid), Prog. Polym. Sci. 33 (2008) 820–852. https://doi.org/10.1016/j.progpolymsci.2008.05.004.

[43] M. Samykano, R. Kumaresan, J. Kananathan, K. Kadirgama, A.K. Pandey, An overview of fused filament fabrication technology and the advancement in PLA-biocomposites, Int J Adv Manuf Technol 132 (2024) 27–62. https://doi.org/10.1007/s00170-024-13394-1.

[44] K.L. O'Neill, P.D. Dalton, A Decade of Melt Electrowriting, Small Methods 7 (2023) e2201589. https://doi.org/10.1002/smtd.202201589.

[45] J.R. Smith, D.A. Lamprou, Polymer coatings for biomedical applications: a review, Trans. IMF 92 (2014) 9–19. https://doi.org/10.1179/0020296713Z.000000000157.

[46] H. Joukhdar, A. Seifert, T. Jüngst, J. Groll, M.S. Lord, J. Rnjak-Kovacina, Ice Templating Soft Matter: Fundamental Principles and Fabrication Approaches to Tailor Pore Structure and Morphology and Their Biomedical Applications, Adv. Mater. 33 (2021) e2100091. https://doi.org/10.1002/adma.202100091.

[47] H. Maleki, B. Azimi, S. Ismaeilimoghadam, S. Danti, Poly(lactic acid)-Based Electrospun Fibrous Structures for Biomedical Applications, Appl. Sci. 12 (2022) 3192. https://doi.org/10.3390/app12063192.

[48] M.A.S.R. Saadi, A. Maguire, N.T. Pottackal, M.S.H. Thakur, M.M. Ikram, A.J. Hart, P.M. Ajayan, M.M. Rahman, Direct Ink Writing: A 3D Printing Technology for Diverse Materials, Adv. Mater. 34 (2022) e2108855. https://doi.org/10.1002/adma.202108855.

[49] S. Hassan, M.N. Ali, B. Ghafoor, Evolutionary perspective of drug eluting stents: from thick polymer to polymer free approach, J. Cardiothorac. Surg. 17 (2022) 65. https://doi.org/10.1186/s13019-022-01812-y.

[50] J. Lv, L. Chen, X. Hu, R. Sun, B. Wang, J. Cheng, J. Lang, Z. Ni, G. Zhao, Systematically study the comprehensive performance of poly (L-lactic acid) drug-coated stent in vitro and in vivo during full degradation cycle, Mater. Today Commun. 42 (2025) 111441. https://doi.org/10.1016/j.mtcomm.2024.111441.

[51] N. Bege, S.O. Steinmüller, M. Kalinowski, R. Reul, S. Klaus, H. Petersen, C. Curdy, J. Janek, T. Kissel, Drug eluting stents based on Poly(ethylene carbonate): optimization of the stent coating process, Eur. J. Pharm. Biopharm. 80 (2012) 562–570. https://doi.org/10.1016/j.ejpb.2011.12.006.

[52] R. Suuronen, T. Pohjonen, J. Hietanen, C. Lindqvist, A 5-year in vitro and in vivo study of the biodegradation of polylactide plates, J. Oral. Maxillofac. Surg. 56 (1998) 604-14; discussion 614-5. https://doi.org/10.1016/S0278-2391(98)90461-X.

[53] J.S. Bergström, D. Hayman, An Overview of Mechanical Properties and Material Modeling of Polylactide (PLA) for Medical Applications, Ann. Biomed. Eng. 44 (2016) 330–340. https://doi.org/10.1007/s10439-015-1455-8.

[54] D. Da Silva, M. Kaduri, M. Poley, O. Adir, N. Krinsky, J. Shainsky-Roitman, A. Schroeder, Biocompatibility, biodegradation and excretion of polylactic acid (PLA) in medical implants and theranostic systems, Chem. Eng. J. 340 (2018) 9–14. https://doi.org/10.1016/j.cej.2018.01.010.

[55] V. Arias, A. Höglund, K. Odelius, A.-C. Albertsson, Tuning the degradation profiles of poly(L-lactide)-based materials through miscibility, Biomacromolecules 15 (2014) 391–402. https://doi.org/10.1021/bm401667b.

[56] Q. Breche, G. Chagnon, G. Machado, E. Girard, B. Nottelet, X. Garric, D. Favier, Mechanical behaviour׳s evolution of a PLA-b-PEG-b-PLA triblock copolymer during hydrolytic degradation, J. Mech. Behav. Biomed. Mater. 60 (2016) 288–300. https://doi.org/10.1016/j.jmbbm.2016.02.015.

[57] Alok Srivastava, Pooja Bhati, Shweta Singh, Mohit Agrawal, Nisha Kumari, Priya Vashisth, Pankaj Chauhan, Naresh Bhatnagar, A review on polylactic acid-based blends/composites and the role of compatibilizers in biomedical engineering applications, Polym. Eng. Sci. 64 (2024) 1003–1044. https://doi.org/10.1002/pen.26626.

[58] P. Saini, M. Arora, M.N.V.R. Kumar, Poly(lactic acid) blends in biomedical applications, Adv. Drug Deliv. Rev. 107 (2016) 47–59. https://doi.org/10.1016/j.addr.2016.06.014.

[59] N. Sundar, S.J. Stanley, S.A. Kumar, P. Keerthana, G.A. Kumar, 2021. Development of dual purpose, industrially important PLA–PEG based coated abrasives and packaging materials. J. Appl. Polym. Sci. 138, 50495. https://doi.org/10.1002/app.50495.

[60] J. Guo, X. Liu, M. Liu, M. Han, Y. Liu, S. Ji, Effect of molecular weight of Poly(ethylene glycol) on plasticization of Poly(L-lactic acid), Polymer 223 (2021) 123720. https://doi.org/10.1016/j.polymer.2021.123720.

[61] K. Nitta, On the Orientation-Induced Crystallization of Polymers, Polymers 8 (2016) 229. https://doi.org/10.3390/polym8060229.

[62] A. Banpean, H. Takagi, N. Shimizu, N. Igarashi, S. Sakurai, Small- and wide-angle X-ray scattering studies on confined crystallization of Poly(ethylene glycol) in Poly(L-lactic acid) spherulite in a PLLA/PEG blend, Polymer 229 (2021) 123971. https://doi.org/10.1016/j.polymer.2021.123971.

[63] P. Phuangthong, W. Li, J. Shen, M. Nofar, P. Worajittiphon, Y. Srithep, The Effect of Polyethylene Glycol on the Non-Isothermal Crystallization of Poly(L-lactide) and Poly(D-lactide) Blends, Polymers 16 (2024). https://doi.org/10.3390/polym16152129.

[64] D. Zhou, J. Sun, J. Shao, X. Bian, S. Huang, G. Li, X. Chen, Unusual crystallization and melting behavior induced by microphase separation in MPEG-b-PLLA diblock copolymer, Polymer 80 (2015) 123–129. https://doi.org/10.1016/j.polymer.2015.10.066.

[65] Q. Xie, L. Han, J. Zhou, G. Shan, Y. Bao, P. Pan, Homocrystalline mesophase formation and multistage structural transitions in stereocomplexable racemic blends of block copolymers, Polymer 189 (2020) 122180. https://doi.org/10.1016/j.polymer.2020.122180.

[66] S.B. King, B.D. Gogas, Can the Vanishing Stent Reappear?: Fix the Technique, or Fix the Device?, J. Am. Coll. Cardiol. 70 (2017) 2875–2877. https://doi.org/10.1016/j.jacc.2017.10.009.

[67] L. Rosenbusch, R. Schuon, T. Wilfling, P. Krüger, K. Lebahn, S. John, O. Sahmel, N. Grabow, M. Schulze, A. Wree, K.-P. Schmitz, T. Stein, T. Lenarz, G. Paasche, Investigation of Stent Prototypes for the Eustachian Tube in Human Donor Bodies, Bioeng. 10 (2023) 743. https://doi.org/10.3390/bioengineering10060743.

[68] N. Sethi, M. Agrawal, D. Dewani, L.S. Reddy, A. Dande, Navigating Fertility Challenges: A Comprehensive Review of Microsurgery for Fallopian Tubal Re-canalization in the Era of In Vitro Fertilization (IVF), Cureus 16 (2024) e54950. https://doi.org/10.7759/cureus.54950.

[69] N. Bink, V.B. Mohan, S. and Fakirov, Recent advances in plastic stents: a comprehensive review, Int. J. Polym. Mater. 70 (2021) 54–74. https://doi.org/10.1080/00914037.2019.1685519.

[70] S. McMahon, N. Bertollo, E.D.O. Cearbhaill, J. Salber, L. Pierucci, P. Duffy, T. Dürig, V. Bi, W. Wang, Bio-resorbable polymer stents: a review of material progress and prospects, Prog. Polym. Sci. 83 (2018) 79–96. https://doi.org/10.1016/j.progpolymsci.2018.05.002.

[71] M. Syazwan, T. Sasaki, Rapid crystallization and mesophase formation of poly(L-lactic acid) during precipitation from a solution, e-Polymers 18 (2018) 331–337. https://doi.org/10.1515/epoly-2017-0247.

[72] D. Vadas, Z.K. Nagy, I. Csontos, G. Marosi, K. Bocz, Effects of thermal annealing and solvent-induced crystallization on the structure and properties of poly(lactic acid) microfibres produced by high-speed electrospinning, J. Therm. Anal. Calorim. 142 (2020) 581–594. https://doi.org/10.1007/s10973-019-09191-8.

[73] M. Teske, D. Arbeiter, K. Schober, T. Eickner, N. Grabow, Systemic analysis about residual chloroform in PLLA films, Curr. Dir. Biomed. Eng. 2 (2016) 49–52. https://doi.org/10.1515/cdbme-2016-0014.

[74] T. Freier, C. Kunze, K.-P. Schmitz, J. Mater. Sci. Lett. 20 (2001) 1929–1931. https://doi.org/10.1023/A:1013174400236.

[75] G.A. Mannella, F. Carfì Pavia, V. La Carrubba, V. Brucato, Phase separation of polymer blends in solution: A case study, Eur. Polym. J. 79 (2016) 176–186. https://doi.org/10.1016/j.eurpolymj.2016.04.025.

[76] I. Fortelny, A. Ujcic, L. Fambri, M. Slouf, 2019. Phase Structure, Compatibility, and Toughness of PLA/PCL Blends: A Review. Front. Mater. 6, 206. https://doi.org/10.3389/fmats.2019.00206.

[77] E. Ivanov, R. Kotsilkova, V. Georgiev, T. Batakliev, V. Angelov, Advanced Rheological, Dynamic Mechanical and Thermal Characterization of Phase-Separation Behavior of PLA/PCL Blends, J. Manuf. Mater. Process. 9 (2025) 35. https://doi.org/10.3390/jmmp9020035.

[78] B. Tesfamariam, Bioresorbable Scaffold-Based Controlled Drug Delivery for Restenosis, J. Cardiovasc. Trans. Res. 12 (2019) 193–203. https://doi.org/10.1007/s12265-018-9841-x.

[79] N.A. Weir, F.J. Buchanan, J.F. Orr, G.R. Dickson, Degradation of poly-L-lactide. Part 1: in vitro and in vivo physiological temperature degradation, Proc. Inst. Mech. Eng. H 218 (2004) 307–319. https://doi.org/10.1243/0954411041932782.

[80] M. Haim Zada, A. Kumar, O. Elmalak, E. Markovitz, R. Icekson, A.J. Domb, In vitro and in vivo degradation behavior and the long-term performance of biodegradable PLCL balloon implants, Int. J. Pharm. 574 (2020) 118870. https://doi.org/10.1016/j.ijpharm.2019.118870.

[81] T. Beslikas, I. Gigis, V. Goulios, J. Christoforides, G.Z. Papageorgiou, D.N. Bikiaris, Crystallization study and comparative in vitro-in vivo hydrolysis of PLA reinforcement ligament, Int. J. Mol. Sci. 12 (2011) 6597–6618. https://doi.org/10.3390/ijms12106597.

[82] N.A. Weir, F.J. Buchanan, J.F. Orr, D.F. Farrar, G.R. Dickson, Degradation of poly-L-lactide. Part 2: increased temperature accelerated degradation, Proc. Inst. Mech. Eng. H 218 (2004) 321–330. https://doi.org/10.1243/0954411041932809.

[83] V. Chausse, C. Iglesias, E. Bou-Petit, M.-P. Ginebra, M. Pegueroles, Chemical vs thermal accelerated hydrolytic degradation of 3D-printed PLLA/PLCL bioresorbable stents: Characterization and influence of sterilization, Polym. Test. 117 (2023) 107817. https://doi.org/10.1016/j.polymertesting.2022.107817.

[84] P. Feng, J. Jia, M. Liu, S. Peng, Z. Zhao, C. Shuai, Degradation mechanisms and acceleration strategies of poly (lactic acid) scaffold for bone regeneration, Mater. Des. 210 (2021) 110066. https://doi.org/10.1016/j.matdes.2021.110066.

[85] A. Shalem, O. Yehezkeli, A. Fishman, Enzymatic degradation of polylactic acid (PLA), Appl. Microbiol. Biotechnol. 108 (2024) 413. https://doi.org/10.1007/s00253-024-13212-4.

[86] D. Cam, S.H. Hyon, Y. Ikada, Degradation of high molecular weight poly(L-lactide) in alkaline medium, Biomater. 16 (1995) 833–843. https://doi.org/10.1016/0142-9612(95)94144-A.

[87] S. Zhao, M. Tayyebi, Mahdireza Yarigarravesh, G. Hu, A review of magnesium corrosion in bio-applications: mechanism, classification, modeling, in-vitro, and in-vivo experimental testing, and tailoring Mg corrosion rate, J. Mater. Sci. 58 (2023) 12158–12181. https://doi.org/10.1007/s10853-023-08782-z.

[88] L. Xu, X. Liu, K. Sun, R. Fu, G. Wang, Corrosion Behavior in Magnesium-Based Alloys for Biomedical Applications, Materials (Basel) 15 (2022). https://doi.org/10.3390/ma15072613.

[89] J. Gonzalez, R.Q. Hou, E.P.S. Nidadavolu, R. Willumeit-Römer, F. Feyerabend, Magnesium degradation under physiological conditions - Best practice, Bioact. Mater. 3 (2018) 174–185. https://doi.org/10.1016/j.bioactmat.2018.01.003.

[90] Michael Schinhammer, Joëlle Hofstetter, Christian Wegmann, Frank Moszner, Jörg F. Löffler, Peter J. Uggowitzer, On the Immersion Testing of Degradable Implant Materials in Simulated Body Fluid: Active pH Regulation Using CO2, Adv. Eng. Mater. 15 (2013) 434–441. https://doi.org/10.1002/adem.201200218.

[91] K. Törne, A. Örnberg, J. Weissenrieder, The influence of buffer system and biological fluids on the degradation of magnesium, J. Biomed. Mater. Res. B Appl. Biomater. 105 (2017) 1490–1502. https://doi.org/10.1002/jbm.b.33685.

[92] N. Shafiq, S. Malhotra, P. Pandhi, A. Grover, A. Uboweja, A meta-analysis of clinical trials of paclitaxel- and sirolimus-eluting stents in patients with obstructive coronary artery disease, Br. J. Clin. Pharmacol. 59 (2005) 94–101. https://doi.org/10.1111/j.1365-2125.2005.02258.x.

[93] K. Matthews, Paclitaxel-eluting stents versus sirolimus-eluting stents in treatment of coronary vessels, Nat. Rev. Cardiol. 3 (2006) 236. https://doi.org/10.1038/ncpcardio0498.

[94] S. Windecker, A. Remondino, F.R. Eberli, P. Jüni, L. Räber, P. Wenaweser, M. Togni, M. Billinger, D. Tüller, C. Seiler, M. Roffi, R. Corti, G. Sütsch, W. Maier, T. Lüscher, O.M. Hess, M. Egger, B. Meier, Sirolimus-eluting and paclitaxel-eluting stents for coronary revascularization, N. Engl. J. Med. 353 (2005) 653–662. https://doi.org/10.1056/NEJMoa051175.

[95] S.J. Corbett, R. Babic, J. Cosgrave, G.M. Sangiorgi, A. Colombo, Is sirolimus better than paclitaxel? A review of the comparative data on drug-eluting stents, Cardiovasc. Revasc. Med. 7 (2006) 159–164. https://doi.org/10.1016/j.carrev.2006.03.106.

[96] X. Hu, T. Wang, F. Li, X. Mao, Surface modifications of biomaterials in different applied fields, RSC Adv. 13 (2023) 20495–20511. https://doi.org/10.1039/D3RA02248J.

[97] S. Jana, S. Jana (Eds.), Marine Biomaterials: Therapeutic Potential, 1st ed., Springer Nature Singapore; Imprint Springer, Singapore, 2022, ISBN-13. 978-9811653766.

[98] A. Repanas, S. Andriopoulou, B. Glasmacher, The significance of electrospinning as a method to create fibrous scaffolds for biomedical engineering and drug delivery applications, J. Drug Deliv. Sci. Technol. 31 (2016) 137–146. https://doi.org/10.1016/j.jddst.2015.12.007.

[99] G. Kathiresan, K. Adaikalam, H.-S. Kim, 2025. Advantages of Electrospinning Biomimetic Scaffolds for the Current Trend of Tissue Engineering Applications. J. Appl. Polym. Sci., e57309. https://doi.org/10.1002/app.57309.

[100] B. Cramariuc, R. Cramariuc, R. Scarlet, L.R. Manea, I.G. Lupu, O. Cramariuc, Fiber diameter in electrospinning process, J. Electrost. 71 (2013) 189–198. https://doi.org/10.1016/j.elstat.2012.12.018.

[101] R. CeCe, L. Jining, M. Islam, J.G. Korvink, B. Sharma, 2024. An Overview of the Electrospinning of Polymeric Nanofibers for Biomedical Applications Related to Drug Delivery. Adv. Eng. Mater. 26, 2301297. https://doi.org/10.1002/adem.202301297.

[102] M.J. Dewey, D.J. Milner, D. Weisgerber, C.L. Flanagan, M. Rubessa, S. Lotti, K.M. Polkoff, S. Crotts, S.J. Hollister, M.B. Wheeler, B.A.C. Harley, Repair of critical-size porcine craniofacial bone defects using a collagen-polycaprolactone composite biomaterial, Biofabrication 14 (2021). https://doi.org/10.1088/1758-5090/ac30d5.

[103] B.R. Coad, M. Jasieniak, S.S. Griesser, H.J. Griesser, Controlled covalent surface immobilisation of proteins and peptides using plasma methods, Surf. Coat. Int. 233 (2013) 169–177. https://doi.org/10.1016/j.surfcoat.2013.05.019.

[104] A. Heiss, V. Pipich, W. Jahnen-Dechent, D. Schwahn, Fetuin-A is a mineral carrier protein: small angle neutron scattering provides new insight on Fetuin-A controlled calcification inhibition, Biophys. J. 99 (2010) 3986–3995. https://doi.org/10.1016/j.bpj.2010.10.030.

[105] X. Jing, H.-Y. Mi, X.-F. Peng, L.-S. Turng, The morphology, properties, and shape memory behavior of polylactic acid/thermoplastic polyurethane blends, Polym. Eng. Sci. 55 (2015) 70–80. https://doi.org/10.1002/pen.23873.

[106] S.H. Daebritz, J.S. Sachweh, B. Hermanns, B. Fausten, A. Franke, J. Groetzner, B. Klosterhalfen, B.J. Messmer, Introduction of a flexible polymeric heart valve prosthesis with special design for mitral position, Circulation 108 Suppl 1 (2003) II134-9. https://doi.org/10.1161/01.cir.0000087655.41288.dc.

[107] S.D. Bruck, E.P. Mueller, Materials aspects of implantable cardiac pacemaker leads, Med. Prog. Technol. 13 (1988) 149–160.

[108] R.L. Li, J. Russ, C. Paschalides, G. Ferrari, H. Waisman, J.W. Kysar, D. Kalfa, Mechanical considerations for polymeric heart valve development: Biomechanics, materials, design and manufacturing, Biomater. 225 (2019) 119493. https://doi.org/10.1016/j.biomaterials.2019.119493.

[109] A. Mahomed, D.W. Hukins, S.N. Kukureka, D.E. Shepherd, Effect of accelerated aging on the viscoelastic properties of Elast-Eon™: A polyurethane with soft poly(dimethylsiloxane) and poly(hexamethylene oxide) segments, Mater. Sci. Eng. C 30 (2010) 1298–1303. https://doi.org/10.1016/j.msec.2010.07.014.

[110] B. Zhang, Y. Xu, S. Ma, L. Wang, C. Liu, W. Xu, J. Shi, W. Qiao, H. Yang, Small-diameter polyurethane vascular graft with high strength and excellent compliance, J. Mech. Behav. Biomed. Mater. 121 (2021) 104614. https://doi.org/10.1016/j.jmbbm.2021.104614.

[111] S. Schröder, U. Reineke, M. Lehmann, J. Ebmeyer, H. Sudhoff, Chronisch obstruktive Tubenfunktionsstörung des Erwachsenen: Langzeitergebnisse der Ballondilatation der Tuba Eustachii, HNO 61 (2013) 142–151. https://doi.org/10.1007/s00106-012-2573-3.

[112] S.-W. Choi, S.-J. Oh, Y. Kim, M.Y. Kwak, M.-W. Suh, M.K. Park, C.K. Lee, H.J. Park, S.-K. Kong, A multicenter, randomized, active-controlled, clinical trial study to evaluate the efficacy and safety of navigation guided balloon Eustachian tuboplasty, Sci. Rep. 11 (2021) 23296. https://doi.org/10.1038/s41598-021-02848-1.

[113] F. Pohl, R.A. Schuon, F. Miller, A. Kampmann, E. Bültmann, C. Hartmann, T. Lenarz, G. Paasche, Stenting the Eustachian tube to treat chronic otitis media - a feasibility study in sheep, Head Face Med. 14 (2018) 8. https://doi.org/10.1186/s13005-018-0165-5.

[114] N. Grabow, C.M. Bünger, K. Sternberg, S. Mews, K. Schmohl, K.-P. Schmitz, Mechanical Properties of a Biodegradable Balloon-expandable Stent From Poly(L-lactide) for Peripheral Vascular Applications, J. Med. Devices 1 (2007) 84–88. https://doi.org/10.1115/1.2355683.

[115] T.Y. Qiu, M. Song, L.G. Zhao, A computational study of crimping and expansion of bioresorbable polymeric stents, Mech. Time Depend. Mater. 22 (2018) 273–290. https://doi.org/10.1007/s11043-017-9371-y.

[116] J.E. Bergsma, F.R. Rozema, R.R.M. Bos, G. Boering, C.A.P. Joziasse, A.J. Pennings, In vitro predegradation at elevated temperatures of poly(lactide), J. Mater. Sci: Mater. Med. 6 (1995) 642–646. https://doi.org/10.1007/BF00123445.

[117] T. Freier, C. Kunze, C. Nischan, S. Kramer, K. Sternberg, M. Sass, U.T. Hopt, K.-P. Schmitz, In vitro and in vivo degradation studies for development of a biodegradable patch based on poly(3-hydroxybutyrate), Biomater. 23 (2002) 2649–2657. https://doi.org/10.1016/s0142-9612(01)00405-7.

[118] K. Herzog, R.-J. Müller, W.-D. Deckwer, Mechanism and kinetics of the enzymatic hydrolysis of polyester nanoparticles by lipases, Polym. Degrad. Stab. 91 (2006) 2486–2498. https://doi.org/10.1016/j.polymdegradstab.2006.03.005.

[119] Z.-Q. Zhang, Y.-X. Yang, J.-A. Li, R.-C. Zeng, S.-K. Guan, Advances in coatings on magnesium alloys for cardiovascular stents - A review, Bioact. Mater. 6 (2021) 4729–4757. https://doi.org/10.1016/j.bioactmat.2021.04.044.

[120] M. Esmaily, J.E. Svensson, S. Fajardo, N. Birbilis, G.S. Frankel, S. Virtanen, R. Arrabal, S. Thomas, L.G. Johansson, Fundamentals and advances in magnesium alloy corrosion, Prog. Mater. Sci. 89 (2017) 92–193. https://doi.org/10.1016/j.pmatsci.2017.04.011.

[121] M. Hayashi, A. Yamamoto, T. Aizawa, Y. Yusa, Y. Shimizu, Y. Imai, In vitroanalysis of insoluble salt formation mechanism associated with Mg corrosion-variations depending on the diffusion environment in model tissue, Biomed. Mater. 19 (2024). https://doi.org/10.1088/1748-605X/ad1d7f.

[122] B. Yavuzyegit, A. Karali, A. de Mori, N. Smith, S. Usov, P. Shashkov, R. Bonithon, G. Blunn, Evaluation of Corrosion Performance of AZ31 Mg Alloy in Physiological and Highly Corrosive Solutions, ACS Appl. Bio. Mater. 7 (2024) 1735–1747. https://doi.org/10.1021/acsabm.3c01169.

[123] K. Katsanos, S. Spiliopoulos, P. Kitrou, M. Krokidis, D. Karnabatidis, Risk of Death Following Application of Paclitaxel-Coated Balloons and Stents in the Femoropopliteal Artery of the Leg: A Systematic Review and Meta-Analysis of Randomized Controlled Trials, J. Am. Heart. Assoc. 7 (2018) e011245. https://doi.org/10.1161/JAHA.118.011245.

[124] T.T. Rissanen, Paclitaxel-coated balloons are safe for the treatment of arterial stenoses, Lancet 402 (2023) 1808–1809. https://doi.org/10.1016/S0140-6736(23)02300-0.

[125] Europäische Kommission, Generaldirektion Gesundheit und Lebensmittelsicherheit, Advice on the use of paclitaxel-coated devices in peripheral artery disease and potential association with higher mortality, 2024, https://health.ec.europa.eu/latest-updates/advice-use-paclitaxel-coated-devices-peripheral-artery-disease-and-potential-association-higher-2024-10-23_en, zuletzt geprüft am 28.06.2025.

[126] Bundesinstitut für Arzneimittel und Medizinprodukte, Empfehlung für die Verwendung von Paclitaxel-beschichteten Stents (DES) und Ballons (DCB) in der Behandlung der peripheren arteriellen Verschlusskrankheit (pAVK), 2024, https://www.bfarm.de/SharedDocs/Risikoinformationen/Medizinprodukte/DE/paclitaxel_stents_ballons_pavk.html, zuletzt geprüft am 28.06.2025.

[127] F. Yang, S.K. Both, X. Yang, X.F. Walboomers, J.A. Jansen, Development of an electrospun nano-apatite/PCL composite membrane for GTR/GBR application, Acta Biomater. 5 (2009) 3295–3304. https://doi.org/10.1016/j.actbio.2009.05.023.

[128] X. Cheng, F. Yang, More Than Just a Barrier—Challenges in the Development of Guided Bone Regeneration Membranes, Matter 1 (2019) 558–560. https://doi.org/10.1016/j.matt.2019.08.009.

[129] H.-W. Kim, H.-H. Lee, J.C. Knowles, Electrospinning biomedical nanocomposite fibers of hydroxyapatite/poly(lactic acid) for bone regeneration, J. Biomed. Mater. Res. A 79 (2006) 643–649. https://doi.org/10.1002/jbm.a.30866.

[130] E.S. Vasquez, J.L. Cunningham, J.B. McMahan, C.L. Simpson, K.B. Walters, Fetuin-A adsorption and stabilization of calcium carbonate nanoparticles in a simulated body fluid, J. Mater. Chem. B 3 (2015) 6411–6419. https://doi.org/10.1039/C5TB00565E.

[131] F. Nudelman, A.J. Lausch, N.A.J.M. Sommerdijk, E.D. Sone, In vitro models of collagen biomineralization, J. Struct. Biol. 183 (2013) 258–269. https://doi.org/10.1016/j.jsb.2013.04.003.

5. Vollständige Publikationsliste

Originalarbeiten mit Impact Factor:

Erscheinungsjahr	Impact Factor
2025	
Oschatz S, Schultz S, Fiedler N, Markhoff J, Teske M, Koper D, Senz V, Brandt-Wunderlich C, Schmitz KP, Grabow N and Lebahn K. PLLA/PEO blend as self-curing material for a biodegradable Eustachian tube stent. Mater. Des., 2025, 256, 114255.	7.9
Hlawa I, Reske T, Chabanovska O, Scholz M, Vasudevan P, **Oschatz S**, Grabow N, Lang H. In Vitro Release Dynamics of Atorvastatin-Loaded Alginate Particles for Enhanced Periodontal Treatment, Polymers (Basel), 2025, 17, 427.	4.9
2024	
Romischke J, Eickner T, Grabow N, Kragl U, **Oschatz S**. 3-Sulfopropyl acrylate potassium-based polyelectrolyte hydrogels: Sterilizable synthetic material for biomedical application, RSC Adv., 2024, 14, 28881-28888.	4,6
Fiedler N, Teske M, Nelz SC, Flügge J, Senz V, Bajer D, Grabow N, **Oschatz S**. In vitro corrosion of polyester coated magnesium alloy under pH-static conditions, ACS Biomater. Sci. Eng., 2024, 10, 9, 5844-5855.	5,5
Huling J, **Oschatz S**, Lange H, Sterenczak KA, Stahnke T, Markhoff J, Stachs O, Möller S, Undre N, Peil A, Jünemann A, Grabow N, Fuellen G, Eickner T. γ-Cyclodextrin hydrogel for the sustained release of josamycin for potential ocular application. Drug Deliv., 2024, 31, 2361168.	8,1
Oschatz S, Schultz S, Fiedler N, Senz V, Schmitz KP, Grabow N, Koper D. Melt blending of poly(lactic acid) with biomedically relevant polyurethanes to improve mechanical performance. Heliyon, 2024, 10, e26268.	3,6
2023	
Oschatz S, Teske M, Burmeister U, Illner S, Lang H, Senz V, Grabow and Markhoff J. Fetuin A functionalisation of biodegradable PLLA-co-PEG nonwovens towards enhanced biomineralisation and osteoblastic growth behavior, Biomater. Sci., 2023, 11, 5240-5250.	5,8
2022	
Arbeiter D, Lebahn K, Reske T, Senz V, Eickner T, Schmitz KP, Grabow N and **Oschatz S**. Comparison of accelerated and enzyme-associated real-time degradation of HMW PLLA and HMW P3HB films, Polym. Test., 2022, 107471.	5,1

Erscheinungsjahr	Impact Factor
2021	
Woitschach F, Kloss M, Schlodder K, Rabes A, Mörke C, **Oschatz S**, Senz V, Borck A, Grabow N, Reisinger EC and Sombetzki M. The Use of Zwitterionic Methylmethacrylat Coated Silicone Inhibits Bacterial Adhesion and Biofilm Formation of Staphylococcus aureus. Front. Bioeng. Biotechnol., 2021, 9:686192.	6,064
Arbeiter D, Reske T, Teske M, Bajer D; Senz V, Schmitz KP, Grabow N and **Oschatz S**. Influence of Drug Incorporation on the Physico-Chemical Properties of Poly(l-Lactide) Implant Coating Matrices - A Systematic Study. Polymers, 2021, 13, 292.	4,967
2020	
Arbeiter D, Eickner T, **Oschatz S**, Reske T, Specht O, Teske M, Senz V, Schmitz KP and Grabow N. Physico chemical and phase separation characterization of high molecular PLLA blended with low molecular PCL obtained from solvent cast processes. Mater. Res. Express, 2020, 7, 095302.	1,620
Claus J, Eickner T, Grabow N, Kragl U and **Oschatz S**. Ion Exchange Controlled Drug Release from Polymerized Ionic Liquids. Macromol. Biosci., 2020, 20, 2000152.	4,979
Claus J, Brietzke A, Lehnert C, **Oschatz S**, Grabow N and Kragl U. Swelling characteristics and biocompatibility of ionic liquid based hydrogels for biomedical applications. PLoS One, 2020 15(4):e0231421.	3,240
2015	
Wu XF. **Oschatz S**, Sharif M, Langer P. Palladium-Catalyzed Carbonylative Synthesis of N-Benzoylindoles with Mo(CO)(6) as the Carbon Monoxide Source. Synthesis, 2015, 47, 2641-2646.	2,652
Oschatz S, Brunzel T, Wu XF and Langer P. Catalyst-free synthesis of 2-aryl-1,2-dihydro-quinazolin-4(1*H*)-thiones from 2-aminobenzothio-amides and aldehydes in water. Org. Biomol. Chem., 2015, 13, 1150-1158.	3,559
2014	
Wu XF. **Oschatz S**, Sharif M, Beller M, Langer P. Palladium-catalyzed carbonylative synthesis of N-(2-cyanoaryl) benzamides and sequential synthesis of quinazolinones. Tetrahedron, 2014, 70, 23-29.	2,645
Wu XF, **Oschatz S**, Block A, Spannenberg A and Langer P. Base mediated synthesis of 2-aryl-2,3-dihydroquinazolin-4(1*H*)-ones from 2-aminobenzonitriles and aromatic aldehydes in water. Org. Biomol. Chem., 2014, 12, 1865-1870.	3,562

Erscheinungsjahr 2013	Impact Factor
Wu XF, **Oschatz S**, Sharif M, Flader A, Krey L, Beller M and Langer P. Palladium-Catalyzed Carbonylative Synthesis of Phthalimides from 1,2-Dibromoarenes with Molybdenum Hexacarbonyl as Carbon Monoxide Source. Adv. Synth. Catal., 2013, 355: 3581-3585.	5,542

Die angegebenen Impact-Faktoren entsprechen den in den Journal Citation Reports (JCR, Clarivate) der jeweiligen Fachzeitschrift für das Erscheinungsjahr der einzelnen Publikationen zugeordneten Impact-Faktoren. Für die Erscheinungsjahre 2025 wurden die zuletzt für das Jahr 2024 veröffentlichten Impact-Faktoren verwendet.

Sonstige Originalarbeiten:

[1] **Oschatz S**, Schultz S, Fiedler N, Grabow N. Temperature dependency of shape retention and shape recovery of HMW and UHMW poly-(l-lactide), Curr. Dir. Biomed. Eng., 10, 2024, 486-489, https://doi.org/10.1515/cdbme-2024-2119

[2] Fiedler N, **Oschatz S**, Ince H, Grabow N, Lebahn K. Bioresorbable Vascular Scaffolds for the Treatment of Aortic Coarctation in Pediatric Patients – Aspects of Dimensional and Mechanical Performance, Curr. Dir. Biomed. Eng., 10, 2024, 240-243. https://doi.org/10.1515/cdbme-2024-2058

[3] Eickner T, Huling J, **Oschatz S**, Lange H, Peil A, Undre N, Stachs O, Stahnke T, Grabow N, Jünnemann A, Füllen G. Antifibrotic Drug Delivery for Glaucoma Treatment – Determination of Josamycin in vivo, Curr. Dir. Biomed. Eng., 10, 2024, 224-227. https://doi.org/10.1515/cdbme-2024-2054

[4] **Oschatz S**, Koper D, Illner S, Senz V, Schmitz KP, Grabow N. Ceftriaxone-loaded PLLA-co-PEG nonwovens towards implant-associated infection prevention, Curr. Dir. Biomed. Eng., 9, 2023, 435-438. https://doi.org/10.1515/cdbme-2023-1109

[5] Götz A, Reske T, **Oschatz S**, Grabow N, Illner S. Post-modification of PLLA nanofiber nonwovens by various solvent treatments, Curr. Dir. Biomed. Eng., 9, 2023, 495-498. https://doi.org/10.1515/cdbme-2023-1124

[6] Fiedler N, **Oschatz S**, Grabow N, Lebahn K. Strain-rate dependence of mechanical characteristics of PLLA with different MW, Curr. Dir. Biomed. Eng., 9, 2023, 459-462. https://doi.org/10.1515/cdbme-2023-1115

[7] Koper D, Kaule S, Grabow N, Schmitz KP, **Oschatz S**. Fabrication of polymer-based stents: Impact of test specimen manufacturing protocol, Curr. Dir. Biomed. Eng., 9, 2023, 379-382. https://doi.org/10.1515/cdbme-2023-1095

[8] Arbeiter D, Grabow N and **Oschatz S**. PLLA crystallization kinetics in dependence of molecular weight, Curr. Dir. Biomed. Eng., 8, 2022, 372-375. https://doi.org/10.1515/cdbme-2022-1095

[9] **Oschatz S**, Arbeiter D, Schultz S, Fiedler N and Grabow N. “Thermal annealing of injection molded VHMW PLLA”, Curr. Dir. Biomed. Eng., 8, 2022, 356-359. https://doi.org/10.1515/cdbme-2022-1091

[10] Teske M, Lange H, Wulf K, Senz V, Grabow N, Eickner T and **Oschatz S**. Chemical characterization of plasma polymerized allylamine coatings with addition of ammonia and oxygen by XPS, Curr. Dir. Biomed. Eng., 8, 2022, 664-667. https://doi.org/10.1515/cdbme-2022-1169

[11] Teske M, Illner S, Markhoff J, Grabow N and **Oschatz S**. Ultrathin fibre coatings on nanofibrous nonwovens by plasma enhanced chemical vapor deposition, Curr. Dir. Biomed. Eng., 7, 2021, 535-538. https://doi.org/10.1515/cdbme-2021-2136

[12] Fiedler N, Arbeiter D, **Oschatz S**, Grabow N and Lebahn K. Definition of test parameters for dynamic mechanical testing of polymeric implant materials, Curr. Dir. Biomed. Eng., 7, 2021, 684-687. https://doi.org/10.1515/cdbme-2021-2174

[13] Arbeiter D, **Oschatz S**, Lebahn K, Illner S and Grabow N. Dry vs. wet testing: quasi-static tensile experiment setup for polymer based biomaterials, Curr. Dir. Biomed. Eng., 7, 2021, 637-639. https://doi.org/10.1515/cdbme-2021-2162

[14] Tautorat C, Lebahn K, **Oschatz S**, Arbeiter D, Schmitz K-P, Grabow N and Schmidt W. Thermal welding of polymeric biomaterials: Development of a novel device for temperature controlled local application, Curr. Dir. Biomed. Eng., 7, 2021, 660-663. https://doi.org/10.1515/cdbme-2021-2168

[15] **Oschatz S**, Illner S, Reske T, Schmitz K-P, Woitschach F, Sombetzki M, Reisinger E C and Grabow N. Antibiotic-loaded nonwovens as protection against implant-associated infection, Curr. Dir. Biomed. Eng., 7, 2021, 411-414. https://doi.org/10.1515/cdbme-2021-2104

[16] Lebahn K, Stöffler K, **Oschatz S**, Arbeiter D, Reske T, Schmitz K-P, Paasche G, Lenarz T and Grabow N. Polymer selection for Eustachian tube stent application based on mechanical, thermal and degradation behavior, Curr. Dir. Biomed. Eng., 7, 2021, 656-659. https://doi.org/10.1515/cdbme-2021-2167

[17] Finck J, Oldenburg J, Kuske T, Grabow N, Schmitz K-P, Siewert S, **Oschatz S**, Stiehm M and Kaule S. TAVI-Mimic for testing of heart valve leaflet materials in physiological loading situations, Curr. Dir. Biomed. Eng., 7, 2021, 570-573. https://doi.org/10.1515/cdbme-2021-2145

[18] Tuladhar RS, Teske M, **Oschatz S**, Illner S, Schilling T, Schmidt W, Grabow N, Haverich A and Schmitz K-P. Cell colonization potential of thermoplastic silicone-based polyurethane nonwovens for novel heart valve prosthesis, Curr. Dir. Biomed. Eng., 7, 2021, 13-16. https://doi.org/10.1515/cdbme-2021-2004

[19] Arbeiter D, **Oschatz S**, Illner S and Grabow N. Study of poly(l-lactide) using Fast Scanning Calorimetry, Curr. Dir. Biomed. Eng., 6, 2020, 422-425. https://doi.org/10.1515/cdbme-2020-3109

[20] **Oschatz S**, Reske T, Schmitz K-P, Illner S, Markhoff J, Eickner T and Grabow N. Degradable dual co-electrospun polyester based nonwovens for guided tissue regeneration, Curr. Dir. Biomed. Eng., 6, 2020, 168-171. https://doi.org/10.1515/cdbme-2020-3043

[21] Illner S, Ortelt J, Arbeiter D, Khaimov V, Wulf Katharina, **Oschatz S**, Reske T, Senz V, Schmitz K-P and Grabow N. Adaptable Superfibers as Implant Material, Curr. Dir. Biomed. Eng., 6, 2020, 465-468. https://doi.org/10.1515/cdbme-2020-3120

[22] **Oschatz S**, Arbeiter D, Eickner T, Grabow N and Illner S. Post-processed chemical treatment of polyimide electrospun nonwovens with ethylenediamine for biomedical applications, Curr. Dir. Biomed. Eng., 5, 2019, 327-329. https://doi.org/10.1515/cdbme-2019-0082

[23] Illner S, Arbeiter D, Teske M, Khaimov V, **Oschatz S**, Senz V, Grabow N, Kohse S and Schmitz K-P. Tissue biomimicry using cross-linked electrospun nonwoven fibre composites, Curr. Dir. Biomed. Eng., 5, 2019, 119-122. https://doi.org/10.1515/cdbme-2019-0031

[24] Eickner T, Kohse S, Illner S, **Oschatz S**, Teske M, Rekowska N, Senz V, Schmitz, K-P and Grabow N. Formation and characterisation of hydrogel diffusion channels for directed drug delivery, Curr. Dir. Biomed. Eng., 5, 2019, 323-325. https://doi.org/10.1515/cdbme-2019-0081

[25] **Oschatz S**, Kohse S, Senz V, Eickner T, Schmitz K-P and Grabow N. Accelerated in vitro-calcification of potential urethane based heart valve replacement materials, Curr. Dir. Biomed. Eng., 4, 2018, 221-224. https://doi.org/10.1515/cdbme-2018-0054

[26] Eickner T, Kopp F, Brietzke A, Kischkel S, **Oschatz S**, Schmitz K-P, Guthoff R and Grabow N. Quantification method for timolol from in vivo samples for the development of a new glaucoma drug depot, Curr. Dir. Biomed. Eng., 4, 2018, 225-227. https://doi.org/10.1515/cdbme-2018-0055

Abstracts

[1] **Oschatz S**, Bülow V, Fiedler N, Grabow N, Markhoff J. Modified 2D Flow System for Early-Stage In Vitro Testing of Stent Micro-Structures, 34th Conference of the European Society of Biomaterials (ESB 2025), Torino, Italien, accepted

[2] **Oschatz S**, Teske M, Koper D and Grabow N. Surface modification of porcine pericardium using plasma enhanced chemical vapour deposition, Abstract Booklet, P4-343, World Biomaterials Congress WBC, 26.-31.05.2024, Daegu, Südkorea

[3] Senz V, Teske M, Illner S, **Oschatz S**, Grabow N and Eickner T. Surface Characterization for Combination Products using X-Ray Photoelectron Spectroscopy, Abstract Booklet, P2-328, World Biomaterials Congress WBC, 26.-31.05.2024, Daegu, Südkorea

[4] Markhoff J, Teske M, Burmeister U, Illner S, Lang H, Senz V, Grabow N and **Oschatz S**. Fetuin A functionalization of biodegradable nonwovens for improved osteoblastic growth

behaviour, 7th International School and Conference on Biological Materials Science - BioInspired Materials, Abstract Booklet #29, 18.-20.03.2024, Löwenstein, Deutschland

[5] **Oschatz S**, Teske M, Markhoff J, Burmeister U, Illner S, Lang H, Grabow N. Fetuin A functionalization of biodegradable nonwovens towards biomimetic guided bone regeneration, Main Abstract Book, 32st Conference of the European Society of Biomaterials (ESB 2022), p. 174, 04.-08.09.2022, Bordeaux, Frankreich

[6] Markhoff J, **Oschatz S**, Teske M, Burmeister U, Illner S, Lang H, Grabow N. Improved osteoblastic growth behavior on Fetuin A functionalized biodegradable nonwovens, Book of Abstracts - Posters, p. 497, 32st Conference of the European Society of Biomaterials (ESB 2022), 04.-08.09.2022, Bordeaux, Frankreich

[7] Gatzke M, **Oschatz S**, Grabow N, Markhoff J. Modification of a flow chamber system to study biomaterials under flow conditions, Abstract Booklet, 32st Conference of the European Society of Biomaterials (ESB 2022), 04.-08.09.2022, Bordeaux, Frankreich

[8] Senz V, Teske M, Lange H, Illner S, **Oschatz S**, Wulf K, Grabow N and Eickner T. Surface Characterization for Combination Products using X-Ray Photoelectron Spectroscopy, Biomed. Eng.-Biomed. Tech., 2022, 67(s1). https://doi.org/10.1515/bmt-2022-2001

[1] **Oschatz S**, Arbeiter D, Schultz S, Fiedler N and Grabow N. Thermal annealing of injection molded VHMW PLLA, Biomed. Eng.-Biomed. Tech., 2022, 67(s1). https://doi.org/10.1515/bmt-2022-2001

[9] Teske M, Lange H, Wulf K, Senz V, Grabow N, Eickner T and **Oschatz S**. Chemical characterization of plasma polymerized allylamine coatings with addition of ammonia and oxygen by XPS, Biomed. Eng.-Biomed. Tech., 2022, 67(s1). https://doi.org/10.1515/bmt-2022-2001

[10] Markhoff J, **Oschatz S**, Grabow N. Modification of thermoplastic polyurethane with zwitterionic oligomers for tailored cell behavior. 55th Annual Conference of the German Society for Biomaterials (DGBM), 2022, https://dgbm-kongress.de/fileadmin/media/dgbm/2024/docs/2022/DGBM2022_Programme.pdf.

[11] Markhoff J, **Oschatz S**, Teske M, Grabow N. Plasma surface modification for controlled cell behavior, Abstract Booklet, PS1-15-461, 31st Conference of the European Society of Biomaterials (ESB 2021), Porto, 5 – 9 September

[12] Teske M, Illner S, Markhoff J, Grabow N and **Oschatz S**. Ultrathin fibre coatings on nanofibrous nonwovens by plasma enhanced chemical vapor deposition, Biomed. Eng.-Biomed. Tech. 2021; 66(s1). https://doi.org/10.1515/bmt-2021-6065

[2] Fiedler N, Arbeiter D, **Oschatz S**, Grabow N and Lebahn K. Definition of test parameters for dynamic mechanical testing of polymeric implant materials, Biomed. Eng.-Biomed. Tech. 2021; 66(s1). https://doi.org/10.1515/bmt-2021-6018

[13] Arbeiter D, **Oschatz S**, Lebahn K, Illner S and Grabow N. Dry vs. wet testing: quasi-static tensile experiment setup for polymer based biomaterials, Biomed. Eng.-Biomed. Tech. 2021; 66(s1). https://doi.org/10.1515/bmt-2021-6016

[14] Tautorat C, Lebahn K, **Oschatz S**, Arbeiter D, Schmitz K-P, Grabow N and Schmidt W. Thermal welding of polymeric biomaterials: Development of a novel device for temperature controlled local application, Biomed. Eng.-Biomed. Tech. 2021; 66(s1). https://doi.org/10.1515/bmt-2021-6004

[15] **Oschatz S**, Illner S, Reske T, Schmitz K-P, Woitschach F, Sombetzki M, Reisinger E C and Grabow N. Antibiotic-loaded nonwovens as protection against implant-associated infection, Biomed. Eng.-Biomed. Tech. 2021; 66(s1). https://doi.org/10.1515/bmt-2021-6027

[16] Lebahn K, Stöffler K, **Oschatz S**, Arbeiter D, Reske T, Schmitz K-P, Paasche G, Lenarz T and Grabow N. Polymer selection for Eustachian tube stent application based on mechanical, thermal and degradation behavior, Biomed. Eng.-Biomed. Tech. 2021; 66(s1). https://doi.org/10.1515/bmt-2021-6029

[17] Finck J, Oldenburg J, Kuske T, Grabow N, Schmitz K-P, Siewert S, **Oschatz S**, Stiehm M and Kaule S. TAVI-Mimic for testing of heart valve leaflet materials in physiological loading situations, Biomed. Eng.-Biomed. Tech. 2021; 66(s1). https://doi.org/10.1515/bmt-2021-6013

[18] Ratna Tuladhar S, Teske M, **Oschatz S**, Illner S, Schilling T, Schmidt W, Grabow N, Haverich A and Schmitz K-P. Cell colonization potential of thermoplastic silicone-based polyurethane nonwovens for novel heart valve prosthesis, Biomed. Eng.-Biomed. Tech. 2021; 66(s1). https://doi.org/10.1515/bmt-2021-6008

[19] Arbeiter D, **Oschatz S**, Illner S and Grabow N. Study of poly(L-lactide) using Fast Scanning Calorimetry, Biomed. Eng.-Biomed. Tech. 2020; 65(s1). https://doi.org/10.1515/bmt-2020-6040

[20] **Oschatz S**, Reske T, Schmitz K-P, Illner S, Markhoff J, Eickner T and Grabow N. Degradable dual co-electrospun polyester based nonwovens for guided tissue regeneration, Biomed. Eng.-Biomed. Tech. 2020; 65(s1). https://doi.org/10.1515/bmt-2020-6017

[21] Illner S, Ortelt J, Arbeiter D, Khaimov V, Wulf Katharina, **Oschatz S**, Reske T, Senz V, Schmitz K-P and Grabow N. Adaptable Superfibers as Implant Material, Biomed. Eng.-Biomed. Tech. 2020; 65(s1). https://doi.org/10.1515/bmt-2020-6040

[22] **Oschatz S**, Arbeiter D, Eickner T, Grabow N and Illner S. Post-processed chemical treatment of polyimide electrospun nonwovens with ethylenediamine for biomedical applications, Biomed. Eng.-Biomed. Tech. 2019; 64(s2). https://doi.org/10.1515/bmt-2019-6023

[23] Arbeiter D, Grabow N, Illner S and **Oschatz S**. The effect of diamine treatment on the physico-chemical properties of polyimide electrospun nonwovens, Biomed. Eng.-Biomed. Tech. 2019; 64(s2). https://doi.org/10.1515/bmt-2019-6023

[24] Illner S, Arbeiter D, Teske M, Khaimov V, **Oschatz S**, Senz V, Grabow N, Kohse S and Schmitz K-P. Tissue biomimicry using cross-linked electrospun nonwoven fibre composites, Biomed. Eng.-Biomed. Tech. 2019; 64(s2). https://doi.org/10.1515/bmt-2019-6013

[25] Eickner T, Kohse S, Illner S, **Oschatz S**, Teske M, Rekowska N, Senz V, Schmitz, K-P and Grabow N. Formation and characterisation of hydrogel diffusion channels for directed drug delivery, Biomed. Eng.-Biomed. Tech. 2019; 64(s2). https://doi.org/10.1515/bmt-2019-6023

[26] **Oschatz S**, Kohse S, Senz V, Eickner T, Schmitz K-P and Grabow N. Accelerated in vitro-calcification of potential urethane based heart valve replacement materials, Biomed. Eng.-Biomed. Tech. 2018; 63(s1). https://doi.org/10.1515/bmt-2018-6032

[27] Eickner T, Kopp F, Brietzke A, Kischkel S, **Oschatz S**, Schmitz K-P, Guthoff R and Grabow N. Quantification method for timolol from in vivo samples for the development of a new glaucoma drug depot, Biomed. Eng.-Biomed. Tech. 2018; 63(s1). https://doi.org/10.1515/bmt-2018-6033

6. Patente

erteilte Patente

Patentfamilie 1

[1] **Oschatz ST**, Siewert S, Bellé P, Behnke R, Burmeister U, Schmitz KP, Lang H, Grabow N. Three-chamber-capsule application system for medical applications, EP4210624B1, 2024

Patentfamilie 2

[2] **Oschatz ST**, Claus J, Eickner T, Brietzke A, Grabow N, Kragl U. Wirkstoffdepotsystem sowie Kit zur in situ Polymerisation des Wirkstoffdepotsystems, DE102019126672B4, 2021

angemeldete Patente

zu Patentfamilie 1

[3] **Oschatz ST**, Siewert S, Bellé P, Behnke R, Burmeister U, Schmitz KP, Lang H, Grabow N. Three-chamber-capsule application system for medical applications, WO2022053594A1, 2021

[4] **Oschatz ST**, Siewert S, Bellé P, Behnke R, Burmeister U, Schmitz KP, Lang H, Grabow N. Dreikammer-Kapsel-Applikationssysteme für medizinische Anwendungen, DE102020123589A1, 2021

Patentfamilie 3

[5] Huling J, Eickner T, **Oschatz ST**, Grabow N, Sterencak K, Stahnke T, Stachs O, Füllen G, Jünemann A. Antifibrotische Formulierung zur ophthalmologischen Behandlung, WO2024083956A1, 2024.

[6] Huling J, Eickner T, **Oschatz ST**, Grabow N, Sterencak K, Stahnke T, Stachs O, Füllen G, Jünemann A. Antifibrotische Formulierung zur ophthalmologischen Behandlung, EP4356929A1, 2024.

Patentfamilie 4

[7] **Oschatz ST**, Teske M, Markhoff J, Illner S, Burmeister U, Lang H, Grabow N. Faservliesstoff und Verfahren zur Herstellung eines Faservliesstoffes, DE102022119473A1, 2022

[8] **Oschatz ST**, Teske M, Markhoff J, Illner S, Burmeister U, Lang H, Grabow N. Nonwoven fabric and method for producing a nonwoven fabric, WO2024028241A1, 2023

Patentfamilie 5

[9] **Oschatz ST**, Illner S, Khaimov V, Grabow N, Reisinger E C, Schmitz KP. Umhüllung zur Aufnahme eines Implantats sowie Verfahren zu dessen Herstellen, DE102021101064A1, 2022

[10] **Oschatz ST**, Illner S, Khaimov V, Grabow N, Reisinger E C, Schmitz KP. Enclosure for receiving an implant, and method for the production thereof, WO002022157160A1, 2022

[11] **Oschatz ST**, Illner S, Khaimov V, Grabow N, Reisinger E C, Schmitz KP. Enclosure for receiving an implant, and method for the production thereof, EP4281177A1, 2022

davon Patente mit industrieller Verwertung

Patentfamilie 6

[12] Dohr D, Bajer D, **Oschatz ST**, Teske M, Grabow N, Illner S, Müller H. Scaffold-Multi-Coating, WO2024240434A1, 2024.

Patentfamilie 7

[13] **Oschatz ST**, Teske M, Koper D, Rzany A, Grabow N. Process for applying a polymer coating to a protein-containing biological material, EP4536303A1, 2022

[14] **Oschatz ST**, Teske M, Koper D, Rzany A, Grabow N. Process for applying a polymer coating to a protein-containing biological material, WO2023237406A1, 2023

[15] **Oschatz ST**, Teske M, Koper D, Rzany A, Grabow N. Process for applying a polymer coating to a protein-containing biological material, CN119255827A, 2023

[16] **Oschatz ST**, Teske M, Koper D, Rzany A, Grabow N. Process for applying a polymer coating to a protein-containing biological material, US2025205388A1, 2024

Patentfamilie 8

[17] **Oschatz ST**, Illner S, Ortelt J, Arbeiter D, Teske M, Müller H, Grabow N, Momma C, Schmitz KP. Adaptive chemical post-processing of nonwovens for cardiovascular applications, WO2021110559A1, 2019

[18] **Oschatz ST**, Illner S, Ortelt J, Arbeiter D, Teske M, Müller H, Grabow N, Momma C, Schmitz KP. Adaptive chemische Nachbehandlung von Vliesstoffen für kardiovaskuläre Anwendungen, EP000004069901A1, 2019

[19] **Oschatz ST**, Illner S, Ortelt J, Arbeiter D, Teske M, Müller H, Grabow N, Momma C, Schmitz KP. Adaptive chemical post-processing of nonwovens for cardiovascular applications, US020230001056A1, 2019

[20] **Oschatz ST**, Illner S, Ortelt J, Arbeiter D, Teske M, Müller H, Grabow N, Momma C, Schmitz KP. Adaptive chemical post-processing of nonwovens for cardiovascular applications, CN114729484A, 2019

7. Vorträge und Posterpräsentationen

[1] **Oschatz S**. Schultz S, Fiedler N and Grabow N. Temperature dependency of shape retention and shape recovery of HMW and UHMW poly-(l-lactide). 58. Jahrestagung der Deutschen Gesellschaft für Biomedizinische Technik (DGBMT) im VDE, 18.-20.09.2024, Stuttgart (Vortrag).

[2] **Oschatz S**, Teske M, Koper D, Senz V, Grabow N. Surface modification of porcine pericardium using plasma enhanced chemical vapour deposition. 12th World Biomaterials Congress, 26. - 31. Mai 2024, Daegu, Südkorea (Poster).

[3] **Oschatz S**, Arbeiter D, Schultz S, Fiedler N and Grabow N. Thermal annealing of injection molded VHMW PLLA. Gemeinsame Jahrestagung der Deutschen (DGBMT), Österreichischen (ÖGBMT) und Schweizer (SSBE) Gesellschaften für Biomedizinische Technik, 28.-30. September 2022, Innsbruck, Österreich (Poster).

[4] **Oschatz S**, Teske M, Markhoff J, Burmeister U, Illner S, Lang H and Grabow N. Fetuin A functionalization of biodegradable nonwovens towards biomimetic guided bone regeneration. 32nd Annual Conference of the European Society of Biomaterials 04.-08. September 2022 Bordeaux, Frankreich (Vortrag).

[5] **Oschatz S**, Illner S, Khaimov V, Schmitz K-P and Grabow N. ReaLusion - Anti-infective implant envelope for cardiac pacemaker application. 55. Jahrestagung der Deutschen Gesellschaft für Biomedizinische Technik (DGBMT) im VDE, 05.-07. Oktober 2021, Hannover (Vortrag).

[6] Lebahn K, Stöffler K, **Oschatz S**, Arbeiter D, Reske T, Schmitz K-P, Paasche G, Lenarz T and Grabow N. Polymer selection for Eustachian tube stent application based on mechanical, thermal and degradation behavior. 55. Jahrestagung der Deutschen Gesellschaft für Biomedizinische Technik (DGBMT) im VDE, 05.-07. Oktober 2021, Hannover (Vortrag).

[7] **Oschatz S**, Illner S, Reske T, Schmitz K-P, Woitschach F, Sombetzki M, Reisinger E C and Grabow N. Antibiotic-loaded nonwovens as protection against implant-associated infection. 55. Jahrestagung der Deutschen Gesellschaft für Biomedizinische Technik (DGBMT) im VDE, 05.-07. Oktober 2021, Hannover (Poster).

[8] **Oschatz S**. Degradable composite nonwovens with tuneable porosity for covered cardiovascular stent applications, Workshop im Forschungsschwerpunkt "Biomedizintechnik/Biomaterialien", 05. November 2020, Online-Veranstaltung (Vortrag).

[9] **Oschatz S**, Reske T, Schmitz K-P, Illner S, Markhoff J, Eickner T and Grabow N. Degradable dual co-electrospun polyester based nonwovens for guided tissue regeneration. 54. Jahrestagung der Deutschen Gesellschaft für Biomedizinische Technik (DGBMT) im VDE, 29. September - 01. Oktober 2020, Leipzig (Vortrag).

[10] **Oschatz S**, Arbeiter D, Eickner T, Grabow N and Illner S. Post-processed chemical treatment of polyimide electrospun nonwovens with ethylenediamine for biomedical

applications. 53. Jahrestagung der Deutschen Gesellschaft für Biomedizinische Technik (DGBMT) im VDE, 25.-26. September 2019, Frankfurt am Main (Poster).

[11] **Oschatz S**, Kohse S, Senz V, Eickner T, Schmitz K-P and Grabow N. Accelerated in vitro-calcification of potential urethane based heart valve replacement materials. 52. Jahrestagung der Deutschen Gesellschaft für Biomedizinische Technik (DGBMT) im VDE, 26.-28. September 2018, Aachen (Vortrag).

Sitzungsvorsitz (Session Chair)

[1] Seidl K., **Oschatz S**., 23b. Biomaterials and Implants 2, 58. Jahrestagung der Deutschen Gesellschaft für Biomedizinische Technik (DGBMT) im VDE, 19.09.2024, Stuttgart.

8. Danksagung

An dieser Stelle danke ich allen, die mich bei der Entstehung dieser Arbeit unterstützt haben.

Mein besonderer Dank gilt Prof. Dr.-Ing. Niels Grabow, der mich in meiner wissenschaftlichen Weiterentwicklung stets allumfassend unterstützt und gefördert hat und mir die Möglichkeit gegeben hat, diese Arbeit am Institut für Biomedizinische Technik durchzuführen.

Ebenso danke ich all meinen Kolleginnen und Kollegen am Institut für Biomedizinische Technik für die immer angenehme und produktive Zusammenarbeit, die maßgeblich zum Gelingen dieser Arbeit beigetragen hat. Mein Dank gilt den Leiterinnen und Leitern der Arbeitsgruppen am IBMT für die exzellente Zusammenarbeit in diesem multidisziplinären Fachgebiet, insbesondere Dr. Sabine Illner, Dr.-Ing. Kerstin Lebahn, Dr. Jana Markhoff, Dr. Thomas Eickner, Dr.-Ing. Wolfram Schmidt und Dr. Volkmar Senz.

Meinen Kolleginnen und Kollegen aus der AG Chemie danke ich, vor allem Dr. Katharina Wulf und Dr. Michael Teske, sowie den weiteren Wissenschaftlerinnen und Wissenschaftlern am IBMT, vor allem Dr. Sabine Kischkel, Dr.-Ing. Andreas Götz und Dr.-Ing. Carsten Tautorat, M.Sc. Selina Schultz und M.Sc. Nicklas Fiedler, für die langjährige angenehme Zusammenarbeit. Ich bedanke mich bei all den wissenschaftlichen Hilfskräften über die Jahre, insbesondere bei M.Sc. Charlotte Nelz, B.Sc. Lucia Schulz und B.Sc. Jonas Flügge, für die tatkräftige Unterstützung im Labor. Für die hervorragende technische Unterstützung bedanke ich mich sehr bei Caroline Dudda, Katja Hahn und Babette Hummel, Gabriele Karsten und Martina Nerger, Dalibor Bajer, Jens Großmann und Manfred Strotmeier. Für die administrative Unterstützung danke ich Manuela Fischer, Silke Hagedorn, Astrid Queißer und Ute Vehlow.

Ein besonderer Dank geht Prof. Dr.-Ing. Klaus-Peter Schmitz als Direktor des Instituts für ImplantatTechnologie und Biomaterialien IIB e.V. und Dipl.-Soz. Verw. Andrea Bock als Geschäftsführerin des IIB e.V., sowie den Mitarbeiterinnen und Mitarbeitern, vor allem Dr.-Ing. Daniela Koper, Dr. Thomas Reske, Dipl.-Ing. Christoph Brandt-Wunderlich und Andrea Rohde, für die wertvolle fachliche und technische Unterstützung.

Mein Dank gilt auch allen Kooperationspartnern an der Universitätsmedizin Rostock, vor allem Prof. Dr. med. habil. Hermann Lang und Dr. med. dent. Ulrike Burmeister aus der der Poliklinik für Zahnerhaltung und Parodontologie, sowie PD Dr. rer. nat. habil. Martina Sombetzki aus der Abteilung für Tropenmedizin und Infektionskrankheiten. Ich danke dem Lehrstuhl für Technische Chemie der Universität Rostock, insbesondere Prof. Dr. Udo Kragl, Dr. Johanna Meyer und M.Sc. Johanna Romischke.

Nicht zuletzt danke ich von ganzem Herzen meiner Familie und meinen Freunden, die mir während der letzten Jahre unermüdlich den Rücken freigehalten haben.

Danke für alles!

9. Eidesstattliche Erklärung

Hiermit erkläre ich, dass die vorliegende Habilitationsschrift selbstständig und ohne unerlaubte fremde Hilfe von mir verfasst wurde. Es wurden keine anderen als die im Literaturverzeichnis angeführte Quellen genutzt und sämtliche Textstellen, die wörtlich oder sinngemäß aus veröffentlichten oder unveröffentlichten Schriften entnommen wurden, wurden als solche kenntlich gemacht. Ich versichere weiterhin, dass diese Arbeit weder vorher noch zeitgleich bei einer anderen Einrichtung als an der Universitätsmedizin Rostock zur Eröffnung eines Habilitationsverfahrens eingereicht worden ist.

Rostock,

Stefan Oschatz

10. Publikationen der Habilitationsschrift

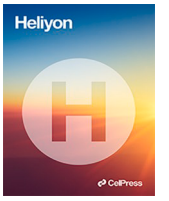
Heliyon 10 (2024) e26268



Contents lists available at ScienceDirect

Heliyon

journal homepage: www.cell.com/heliyon



Research article



Melt blending of poly(lactic acid) with biomedically relevant polyurethanes to improve mechanical performance

Stefan Oschatz [a,*], Selina Schultz [a], Nicklas Fiedler [a], Volkmar Senz [a], Klaus-Peter Schmitz [a,c], Niels Grabow [a,b], Daniela Koper [a,c]

[a] Institute for Biomedical Engineering, Rostock University Medical Center, Friedrich-Barnewitz-Straße 4, 18119, Rostock, Germany
[b] Department Life, Light & Matter (LLM), University of Rostock, 18051, Rostock, Germany
[c] Institute for ImplantTechnology and Biomaterials e.V., Friedrich-Barnewitz-Straße 4, 18119, Rostock, Warnemünde, Germany

ARTICLE INFO

Keywords:
PLLA
PLLA polyurethane blends
Shape memory polymers
Polymer stent

ABSTRACT

Minimally invasive surgery procedures are of utmost relevance in clinical practice. However, the associated mechanical stress on the material poses a challenge for new implant developments. In particular PLLA, one of the most widely used polymeric biomaterials, is limited in its application due to its high brittleness and low elasticity. In this context, blending is a conventional method of improving the performance of polymer materials. However, in implant applications and development, material selection is usually limited to the use of medical grade polymers. The focus of this work was to investigate the extent to which blending poly-L-lactide (PLLA) with low contents of a selection of five commercially available medical grade polyurethanes leads to enhanced material properties. The materials obtained by melt blending were characterized in terms of their morphology and thermal properties, and the mechanical performance of the blends was evaluated taking into account physiological conditions. From these data, we found that mixing PLLA with Pellethane 80A is a promising approach to improve the material's performance, particularly for stent applications. It was found that PLLA/Pellethane blend with 10% polyurethane exhibits considerable plastic deformation before fracture, while pure PLLA fractures with almost no deformation. Furthermore, the addition of Pellethane only leads to a moderate reduction in elongation at yield and yield stress. In addition, dynamic mechanical analysis for three different PLLA/Pellethane ratios was performed to investigate thermally induced shape retention and shape recovery of the blends.

1. Introduction

Polymer based bioresorbable stents are regaining interest after the Abbott Absorb shock [1,2], and several new approaches are currently under investigation and in pre- and clinical studies, e.g. Abbott Falcon, Boston Renuvia or MicroPort Firesorb [3]. In this regard, poly(L-lactide) (PLLA) is an established and common used bio- and implant material with a wide range of applications. Due to the minimally invasive implantation strategy, there is a high need for contrary mechanical material specifications in the field of vascular stents. The radial deformability, independent from specific implant design, should ensure both small interventional diameters and deformation reserve for dilating to an appropriate target diameter. Given the primary functional objective of reopening an

* Corresponding author.
E-mail address: stefan.oschatz@uni-rostock.de (S. Oschatz).

https://doi.org/10.1016/j.heliyon.2024.e26268
Received 2 February 2024; Received in revised form 8 February 2024; Accepted 9 February 2024
Available online 23 February 2024
2405-8440/© 2024 The Author(s). Published by Elsevier Ltd. This is an open access article under the CC BY license (http://creativecommons.org/licenses/by/4.0/).

obstructed vessel, a high radial deformation resistance is required for dilated vascular stents. Material properties such as sufficient plastic deformation capacity (crimping, dilatation), high Young's modulus and yield stress (high radial strength) and structural, as well as mechanical, resistance to cyclic alternating load cases are essential for a functional biomedical device. In particular, mechanical stress during the balloon-assisted dilatation process may lead to fatal implant failure due to fractures, if the material is inadequately ductile. In addition, radial resilience of dilated stents in particular results from plastic deformation behavior.

Yet, its brittleness and low elasticity leave untreated PLLA seemingly less suited for a number of sophisticated biomedical uses where mechanic load occurs, e.g. as material in stent applications. Thus, further processing steps such as an elaborated post processing protocol is required for the manufacture of functional implants, in particular blow molding (Abbott), die drawing (Arterius) or thermal annealing (Elixir) to adjust chain orientation and crystallinity [4,5]. Moreover, to ensure the required mechanical performance, a common approach to adjust polymer mechanical properties is blending with small molecules (as hardener or plasticizer) or with another polymer [6]. In this context, beside using PLLA/PU copolymers [7,8], several PLLA blends and corresponding investigations regarding their thermo-mechanical behavior have been reported in the literature. In particular, it was shown that blending with thermoplastic polyurethanes (TPU) increases elongation at break from ~5% up to ~20% and beyond when compared to pure PLLA, paired with distinct plastic deformation, while maintaining material yield strength [9]. The mechanical behavior of PLLA/PU blends, however, depends strongly on the choice of PU, whereas even several 100% elongation at break were observed [10–12]. Yet, phase interaction when blending PLLA with PU is complex, as such blends are also prone to phase separation, with better compatibility when soft segments of TPU, e.g. ether blocks, can interact with PLLA chains [13].

In a biomedical context, however, the use of a material for implant purposes must comply with strict regulatory requirements in terms of biocompatibility and (longterm-) safety, and the materials have to be specifically manufactured for medical purposes. Consequently, polymers designated for implant applications must be assessed regarding the USP classification of plastics, whereas class IV and VI are designated for materials intended for the use in implants and medical devices. In particular, the tests to be conducted according to USP are intravenous and intraperitoneal injection of sample extracts and intramuscular implantation of sample strips [14]. Moreover, tests regarding acute systemic toxicity, intracutaneous reactivity and tissue reaction after implantation have to be performed following DIN-ISO 10993 [15]. These tests should furthermore be in accordance to the Principles of Good Laboratory Practice (GLP). Thus, the choice of blending partners is limited when avoiding or reducing expensive and time-consuming extensive studies for approval, as blending partners should also be of medical grade. In addition, physiological conditions should also be considered during mechanical testing and for evaluating material suitability, as body fluids and corresponding salts can diffuse into the material, interact with the polymer chains, and further affect mechanical performance.

The present work focuses on melt blending medical grade very high molecular weight (VHMW) PLLA, Resomer L210, with small amount of established medical grade polyurethane based polymers. Very and ultra high M_w PLLA is of particular interest for biomedical engineering due to its beneficial properties regarding tissue response and reduced inflammatory potential compared to lower M_w PLLA [16]. The obtained materials were characterized in terms of mechanical and thermal properties, as well as morphology. The following biomedical grade polymers were used as blend partners: Pellethane 2363 80A, and Tecothane TT 1055D, both being aromatic polyether-based thermoplastic polyurethanes, Chronothane P75D, an aromatic polyether-based polyurethane elastomer, Adiamat, a polycarbonate urethane, and ElastEon, a siloxane segmented polyurethane. These polyurethanes have in common that they are proven in biomedical engineering and of major interest in prototyping and manufacturing of biomedical devices and implants, in particular for the manufacture of artificial heart valves [17–19], blood vessel replacement [20] and as insulating material for cardiac pacemaker electrodes [21]. The selected polyurethanes, however, differ in their structural composition and shore hardness. Thus, the influence on mechanical performance and morphology when using these polymers as blending partner with PLLA cannot easily be predicted.

Aim of this study is to obtain a material with a similar tensile strength compared to PLLA paired with enhanced plastic deformation and increased elongation at break. For further evaluating the suitability of the selected PLLA/PU blends as base material for biomedical devices, in particular regarding stent applications, mechanical testing was conducted after incubation in physiological saline solution. Moreover, PLLA/Pellethane blends were selected for further studying their shape memory behavior.

Notably, blending PLLA with polyurethanes seemingly eradicates one of its most beneficial properties regarding biomedical applications – namely biodegradability. Yet, since the polyurethane proportion is low compared to PLLA, what remains is no bulk polymer but only small fragments. Whether these fragments show negative long-term effects on the surrounding tissue must be investigated in further studies, preferably *in vivo*, to assess the advantages of blending with PU over partial loss of degradability.

2. Materials and methods

2.1. Polymers

All polymers used were of medical grade. PLLA L210 was purchased from Evonik Industries (Essen, Germany), Pellethan 2363 80A was purchased from Lubrizol Advanced Materials (Cleveland, OH, USA), Tecothane TT 1055D was purchased from Velox (Hamburg, Germany), Chronothane P75D was purchased from AdvanSource (Wilmington, MA, USA), Adiamat was purchased from adiam life science AG (Erkelenz, Germany) and ElastEon was provided by RUA life Science (Glasgow, Scotland).

2.2. Sample preparation

Blends of PLLA and 10 percentage by weight (wt%) of different PUs were fabricated by melt extrusion using a HAAKE MiniLab II co-rotating twin-screw extruder (Thermo Fisher Scientific, Karlsruhe, Germany) with different screw speeds and nozzle temperatures,

listed in Table 2. The extruded filaments were subsequently pelleted. Following this, samples for further testing were fabricated by injection molding using a Haake MiniJet II (Thermo Fisher Scientific, Karlsruhe, Germany) equipped with a 60 × 10 × 1 mm^3 stainless steel mold. Pure PLLA samples without the addition of PU were fabricated solely by injection molding without previous extrusion process. Extrusion and injection molding parameters are given in Table 2.

Annealing temperature to diminish cold crystallization has been identified using DSC analysis. Thermal annealing following to the injection molding process was performed using a standard lab heating plate at 85 °C (PLLA) and 75 °C (PLLA/PU blends). Specimens were placed on a common lab heating plate and covered with a previously thermal equilibrated aluminum block equipped with a drilled hole for the heating plate temperature sensor. After thermal annealing for the selected time (see Table 2), samples were cooled under ambient conditions.

2.3. Morphology

Macrophotographical imaging was performed using a Canon EOS 80D equipped with a Sigma 18–250 mm macro objective (both Canon Inc., Japan). SEM imaging of cryo-fractured surface morphology was performed with a SEM QUANTA FEG 250 (FEI Deutschland GmbH, Germany) operating in low vacuum with an accelerating voltage of 5 kV, using a secondary electron detector (LVD). Samples were flash-frozen with liquid nitrogen and manually fractured using pincers. To enhance visibility of morphological characteristics, one half of each fractured sample was chemically etched using 1 M NaOH for 72 h, rinsed with distilled water and dried under ambient conditions, whereas the other side of the fracture edge acted as direct reference sample. The specimens were fixed onto aluminum trays with conductive carbon adhesive pads and the aluminum trays were mounted on custom 90° angle brackets to orient fracture edges toward the electron beam source.

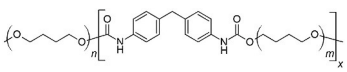
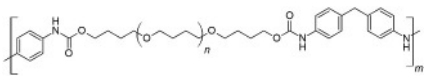
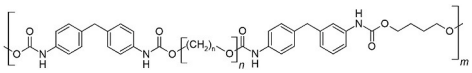
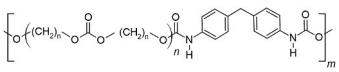
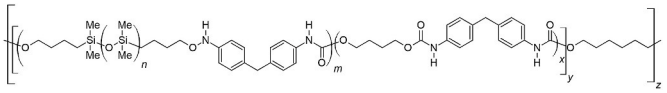
2.4. Thermal analysis

Thermal properties of the PLLA/PU blends were investigated using a DSC 1 star^e system (Mettler Toledo, Zurich, Switzerland). Conventional calibration methods with highly pure standards were used. Test specimens were sliced from injection molded tensile bars and were heated up from $T = -60$ °C at a rate of 10 K/min operating under nitrogen at atmospheric pressure. End temperature was $T =$ 240 °C. Sample weights were in the range of $m = 3$–7 mg. Thermograms were analyzed with respect to glass transition (T_g), crystallization temperature (T_c), melting temperature (T_m), and degree of crystallinity (χ). Heats of fusion and degree of crystallinity were quantitatively evaluated by determining the endothermic peak areas, which were compared with the melting peak area of totally crystalline PLLA ($\chi_{100} = 93.7$ J/g) [27]. Degree of crystallinity χ for PLLA was quantitatively evaluated by means of Equation (1)

$$\chi = 100\% \bullet \left[\frac{\Delta H_m}{\Delta H_{m0}}\right] \bullet \frac{1}{W} \tag{1}$$

where ΔH_{m0} is the enthalpy value of a pure crystalline material, ΔH_m is the enthalpy corresponding to the fusion process and W the amount of PLLA component in the PLLA/TPU blend system. All results were averaged over n = 5 samples.

Table 1
Overview on the polymer structures for PLLA and the PUs used for blend fabrication.

Polymer	Structure	Polymer class	Lit.
PLLA		polyester	
Pellethane		aromatic polyether-based thermoplastic polyurethane	[22]
Tecothane			[23]
Chronothane		aromatic polyether-based polyurethane elastomer[a]	[24]
Adiamat		polycarbonate urethane[b]	[18, 25]
ElastEon		siloxane segmented polyurethane	[26]

[a] General PU elastomer structure. Detailed structural information is not readily available for Chronothane.
[b] General PCU structure. Detailed structural information is not readily available for Adiamat.

Table 2
Extrusion and injection molding parameters for PLLA reference and PLLA/PU blend samples.

Sample name	extrusion		injection molding			
	T_{Nozzle} (°C)	RPM (1/s)	$T_{cylinder}$ (°C)	T_{mold} (°C)	$p_{injection}$ (bar)	p_{hold} (bar)
PLLA	/	/	220	67	680 for 5 s	300 for 10 s
PLLA/Pellethane	190	10	205	60	820 for 5 s	300 for 10 s
PLLA/Tecothane	195	10	215	55	600 for 5 s	300 for 10 s
PLLA/Chronothane	185	5	205	55	600 for 5 s	300 for 10 s
PLLA/Adiamat	195	20	225	66	970 for 5 s	300 for 10 s
PLLA/ElastEon	190	20	210	58	750 for 5 s	300 for 10 s

2.5. Mechanical analysis

Tensile tests were carried out using a uniaxial tensile test instrument zwickiLine Z 1.0 (Zwick/Roell, Ulm, Germany) equipped with a Canon EOS 80D for simultaneous video recording of sample strain behavior. Samples were cut into 5B dogbone shape specimens according to DIN EN ISO 527-2 [28] using a Speedy 300 CO_2 laser system (TROTEC Laser GmbH, Marchtrenk, Austria). Measurements were carried out at room temperature under ambient conditions, and in physiological saline solution at an ambient temperature of $T =$ 37 °C. For wet measurements, samples were stored for 7 days at 37 °C in physiological saline solution. Tests were conducted with a 1 kN load cell and a crosshead speed of 5 mm/min. Tensile force as a function of elongation was measured. Based on these data, Young's modulus (E) was calculated in the linear elastic region. Yield strain (ε_y) and yield stress (σ_y) were determined using 0.2% offset method, and intersections of the straight lines for $E_{0.2\%offset}$ with stress-strain curves of the blends were determined using Origin curve intersection minitool (OriginPro 2018b, OriginLab, Northampton, USA). All results were averaged over n = 5 samples.

2.6. Shape memory experiments

Shape memory behavior of PLLA and PLLA/Pellethane blends was investigated in line with the method reported by Shirole et al. [29], using a DMA 850 test bench (TA Instruments Inc., USA). Experiments were carried out in single cantilever mode, with a sample size of 17.5 mm × 10 mm x 1 mm. In a first step, the test chamber was heated to strain temperature $T_s = 70$ °C and the sample was equilibrated for 30 min before a force of 8.0 N was applied at a rate of 0.8 N/min in a second step. The samples were held at 8.0 N for 30 min before temperature was lowered to the fixing temperature $T_f = 15$ °C at 5 K/min. Samples were kept at T_f for 30 min. Afterwards, the force was released and held at 0 N (force control) for 5 min at 15 °C before the temperature was increased to 70 °C at 5 K/min with F set to 0 N. Lastly, samples were kept at 70 °C at $F = 0$ N for 90 min. Starting with the second step, the cycle was repeated twice. From displacement, force and temperature as function of time plots, displacement at strain values D_s were extracted at highest deformation at strain temperature T_s, recoil displacement values D_r were extracted as first value after the force was released at fixing temperature T_f, and recovery displacement values D_R were extracted as last value at the end of the cycle.

2.7. ATR-FTIR spectroscopy

ATR-FTIR-measurements were performed using a Bruker Vertex 70 IR-Spectrometer (Bruker, Leipzig, Germany) equipped with a DLaTGS-detector. Data were collected in the range of $\tilde{\nu} = 600$ cm^{-1} to 4000 cm^{-1} with a resolution of $\tilde{\nu} = 4$ cm^{-1} averaged over 32 scans in reflection mode using a Graseby Golden Gate Diamond ATR-unit. All spectra were subsequently baseline corrected and atmospheric compensation has been performed using Bruker OPUS software.

3. Results and discussion

For the development of a matching thermal annealing protocol, preliminary tests for each blend were carried out in a DSC device. In an initial step, micro samples were heated to 80 °C (above T_g) for selected annealing times (15, 30, 45, 50 and 90 min, respectively). The minimum annealing time, where no more cold crystallization of the material could be observed, was selected and further tests

Table 3
DSC results (glass transition (T_g), crystallization temperature (T_c) and melting temperature (T_m)) for PLLA and PLLA/PU blends after injection molding compared to values obtained after injection molding and thermal annealing at given temperature/time.

sample name	as obtained from injection molding				after thermal annealing			
	$T_{g,PLLA}$ (°C)	$T_{c,PLLA}$ (°C)	$T_{m,PLLA}$ (°C)	χ_{PLLA} (%)	annealing parameters	$T_{g,PLLA}$ (°C)	$T_{m,PLLA}$ (°C)	χ_{PLLA} (%)
PLLA	60.2 ± 0.4	110.1 ± 1.4	179.9 ± 0.4	6.7 ± 1.5	85 °C for 90 min	67.4 ± 0.7	179.9 ± 1.5	48.2 ± 2.6
PLLA/Pellethane	62.0 ± 0.4	83.0 ± 0.4	180.6 ± 0.5	27.2 ± 0.5	all @ 75 °C for 30 min	64.7 ± 0.9	181.0 ± 1.8	64.7 ± 0.9
PLLA/Tecothane	61.0 ± 0.2	88.9 ± 2.8	180.6 ± 1.0	26.0 ± 2.5		63.6 ± 0.8	179.1 ± 1.0	58.4 ± 1.5
PLLA/Chronothane	60.0. ± 0.6	83.6 ± 0.5	180.7 ± 0.9	15.1 ± 1.0		63.9 ± 0.5	177.9 ± 0.5	62.5 ± 0.5
PLLA/Adiamat	62.3 ± 0.4	84.5 ± 0.9	180.1 ± 0.5	8.61 ± 4.4		65.0 ± 0.3	179.3 ± 0.3	51.4 ± 1.2
PLLA/ElastEon	62.5 ± 0.3	83.6 ± 0.5	180.7 ± 0.9	28.6 ± 1.9		63.8 ± 0.8	180.5 ± 0.7	54.5 ± 2.6

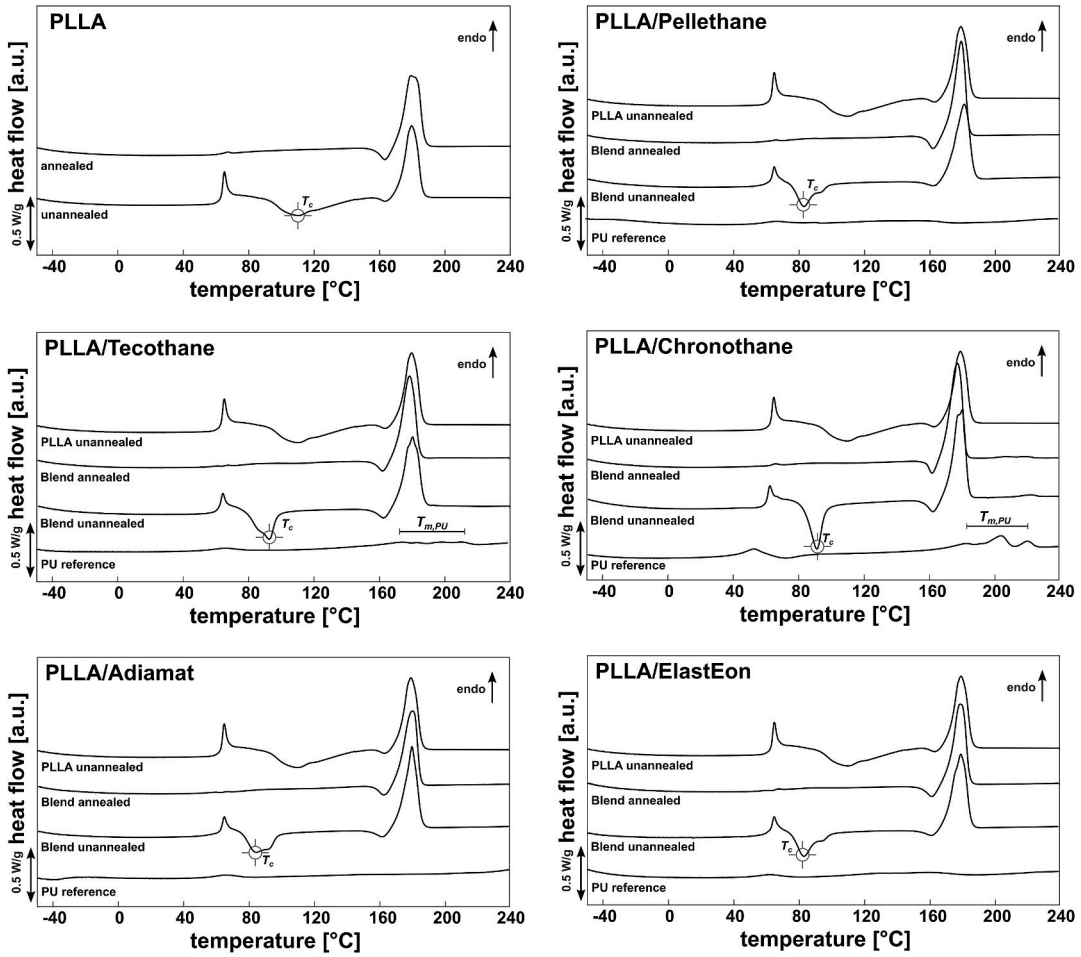


Fig. 1. DSC thermograms of PLLA and PLLA/PU-blends as obtained by injection molding and after thermal annealing.

regarding annealing temperature (55, 65 and 75 °C) were conducted for identification of minimal annealing time-temperature pairing, resulting in 85 °C/90 min annealing for pure PLLA, and 75 °C/30 min for all tested PLLA/PU blends. Following this, large-scale samples were thermally annealed using common heating plate and subsequently analyzed by DSC measurements. Thermal annealing parameters for PLLA/PU blends and values for characteristic thermal parameters are given in Table 3.

Thermograms of PLLA and PLLA/PU blend samples obtained by injection molding before and after thermal annealing are shown in Fig. 1. For reference, corresponding thermograms of pure PU are also given.

From DSC thermograms, it can be concluded that for pure PLLA and PLLA/PU blends, after injection molding without thermal annealing, the material shows clear cold crystallization signals as well as distinct enthalpy relaxation, indicating that the material is not in equilibrium state due to quenching after sample preparation. Cold crystallization peaks for all PLLA/PU blends were less broad and shifted to lower values compared to pure PLLA. After thermal annealing, no cold crystallization was detected. Blending PLLA with the selected PUs did not show to affect T_m, whereas T_g was shifted to lower values after blending.

All Blends showed crystal distortion as indicated by the endothermal peak in front of the melting signal. This is usually an indication of an α'→α transition of PLLA upon heating, but whether the PLLA phase in the blends exhibits such crystals cannot be answered by means of DSC analysis alone. As for pure Tecothane and pure Chronothane, they exhibit a melting range of $T_{m,Chronothane}$ = 187–221 °C and $T_{m,Tecothane}$ = 175–219 °C, showing multiple melting peaks, indicating complex crystal structures. When blended with PLLA, only for PLLA/Chronothane a PU melting signal was detected, indicating a separated crystalline PU phase. Pure Adiamat shows a melting temperature peak $T_{m,Adiamat}$ = 65.8 ± 0.6 °C, overlapping with $T_{g,PLLA}$, thus, although PU crystallites were found in SEM imaging, no PU melting signal could be detected in the blend. For the other blends, no signs of PU melting were found in DSC thermograms. In general, after thermal annealing, PLLA/PU blends appear to be in a thermal stable condition, which is crucial regarding further processing to biomedical devices and shelf life.

Assuming homogeneous distribution of PUs in the blend in the DSC samples, crystallinity χ of PLLA was calculated (Table 3). As obtained by injection molding, pure PLLA is amorphous. After thermal annealing, crystallinity increases to χ_{PLLA} = 48.2 ± 2.6%. Blending with Pellethane, Tecothane, Chronothane and ElastEon lead to a higher initial crystallinity after injection molding even

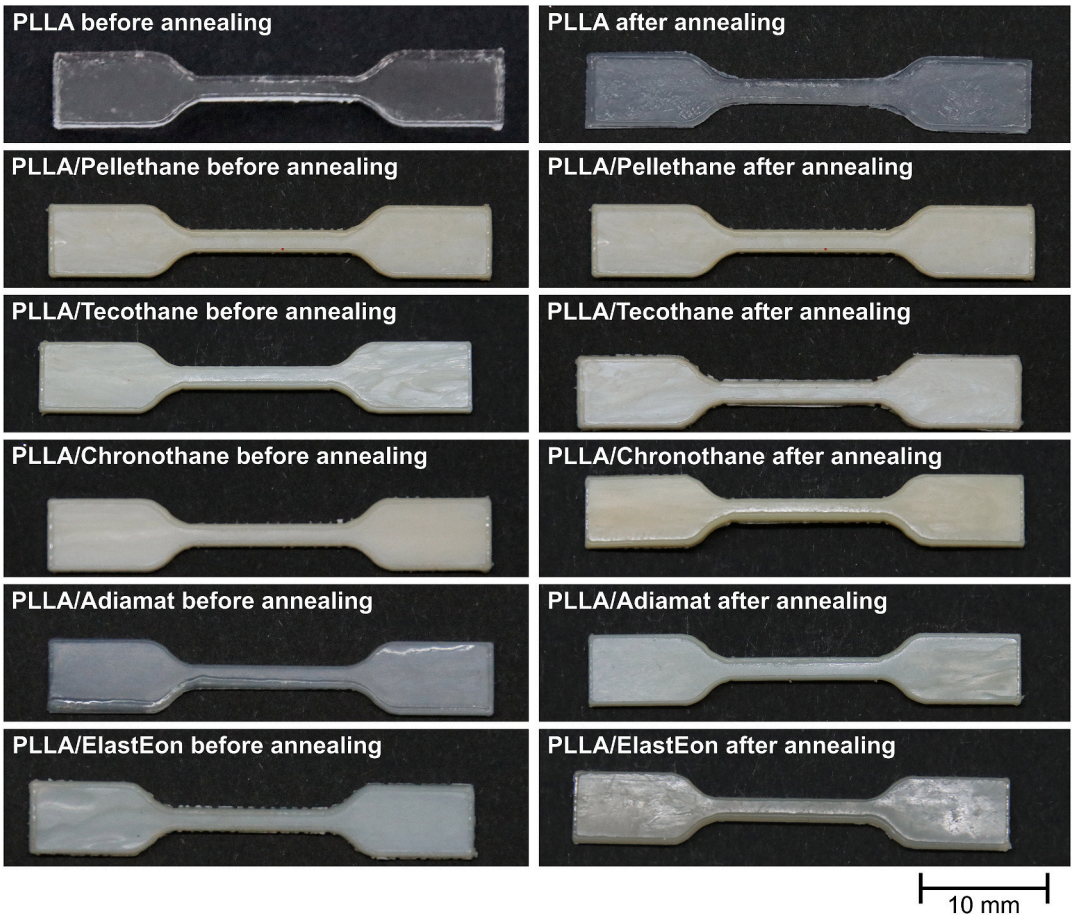


Fig. 2. Macrophotographical images of PLLA and PLLA/PU-blend dog bone specimens for mechanical testing as obtained by Laser cutting and after thermal annealing.

without thermal annealing, up to $\chi_{PLLA/\text{ElastEon}} = 28.6 \pm 1.9\%$ and $\chi_{PLLA/Pellethane} = 27.2 \pm 0.5\%$, which is considerably different from values reported in the literature where no such increase in χ was observed for PLLA/PU blends [30]. Also, after thermal annealing, blends with Pellethane, Tecothane, and Chronothane exhibited a higher PLLA-crystallinity of up to $\chi_{PLLA/Pellethane} = 64.7 \pm 0.9\%$, although annealing of PLLA/PU blends was performed at a lower annealing temperature, which also corresponds to the lower crystallization temperatures of the PLLA/PU blends. It can be assumed that the higher crystallinity of PLLA in the blends is due to the induced crystallization of PLLA at the PLLA-PU phase boundary [31].

In terms of morphological changes after thermal annealing, macrophotographical images are shown in Fig. 2. Pure PLLA was transparent after injection molding, and turned highly opaque paired with a more rough surface after thermal annealing, indicating recrystallization, also in accordance to DSC thermograms. Except PLLA/Adiamat, all polymer blends were highly opaque after sample preparation without thermal annealing. After thermal annealing, PLLA/Tecothane and PLLA/Chronothane also showed roughening of the surface, and PLLA/Adiamat showed an increase in opacity. Beyond that, no changes in morphology were detected, leading to the assumption that the annealing protocol was both sufficient and low-impact in terms of decomposition.

To evaluate phase separation and inner morphology, the prepared polymer blends were etched with NaOH (Fig. 3). The basic solution hydrolyzes the amorphous PLLA phase faster than crystalline domains. It is reasonable the selected non-biodegradable PUs to only be slightly affected by hydroxide ions [32]. This effect being due to the butane diol soft segments (Table 1) inhibiting oxidative degradation [33], and the overall hydrophobic nature of PUs furthermore delaying hydrolysis of the urethane groups [34]. Still, a certain degree of depolymerization of PU must be considered. To reduce strain stress on the specimens while cutting, samples were deep frozen using liquid nitrogen and cryo-fractured. One side was not treated with NaOH and served as reference, allowing direct comparison.

Regarding SEM images of the cry-fractured specimens, spherulites of high crystalline domains for pure PLLA became visible after etching (i). For PLLA/Pellethane, a distinguishable PU domain (ii, enlarged at iii and iv) could be observed. As for PLLA/Choronothane (vii), PLLA/Tecothane (v, enlarged at vi) and PLLA/ElastEon (ix, enlarged at x and xi), hollow spaces became visible after etching. These hollows can be attributed to low crystalline PLLA locally surrounded by PU. For PLLA/Adiamat and PLLA/ElastEon (viii), PU crystallites were observed after etching. For the Chronothane blend, however, DSC resulted in multiple melting signals for the

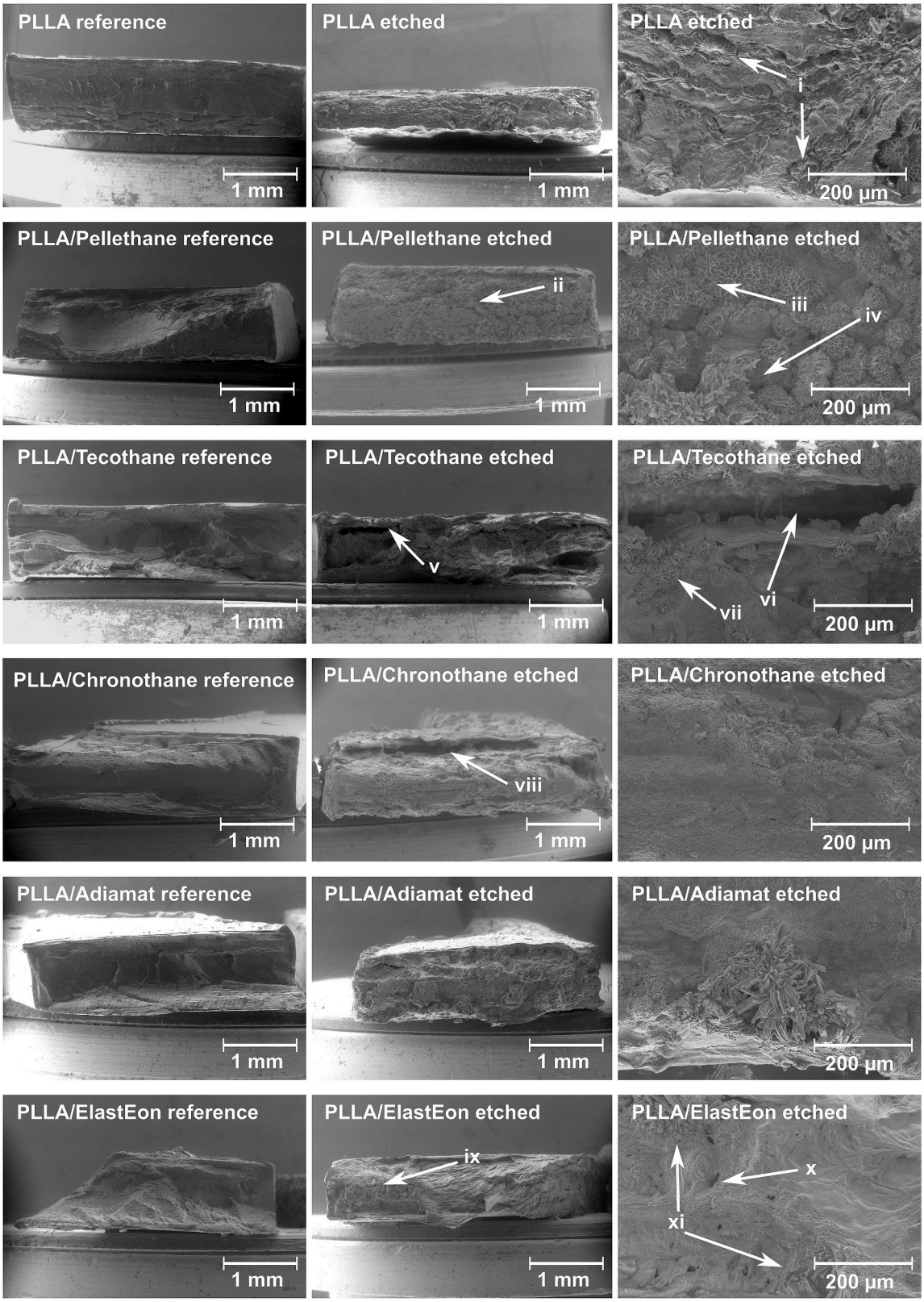


Fig. 3. Cross-sectional SEM images of cryo-fractured PLLA/PU blends after etching for 72 h with 1 M NaOH.

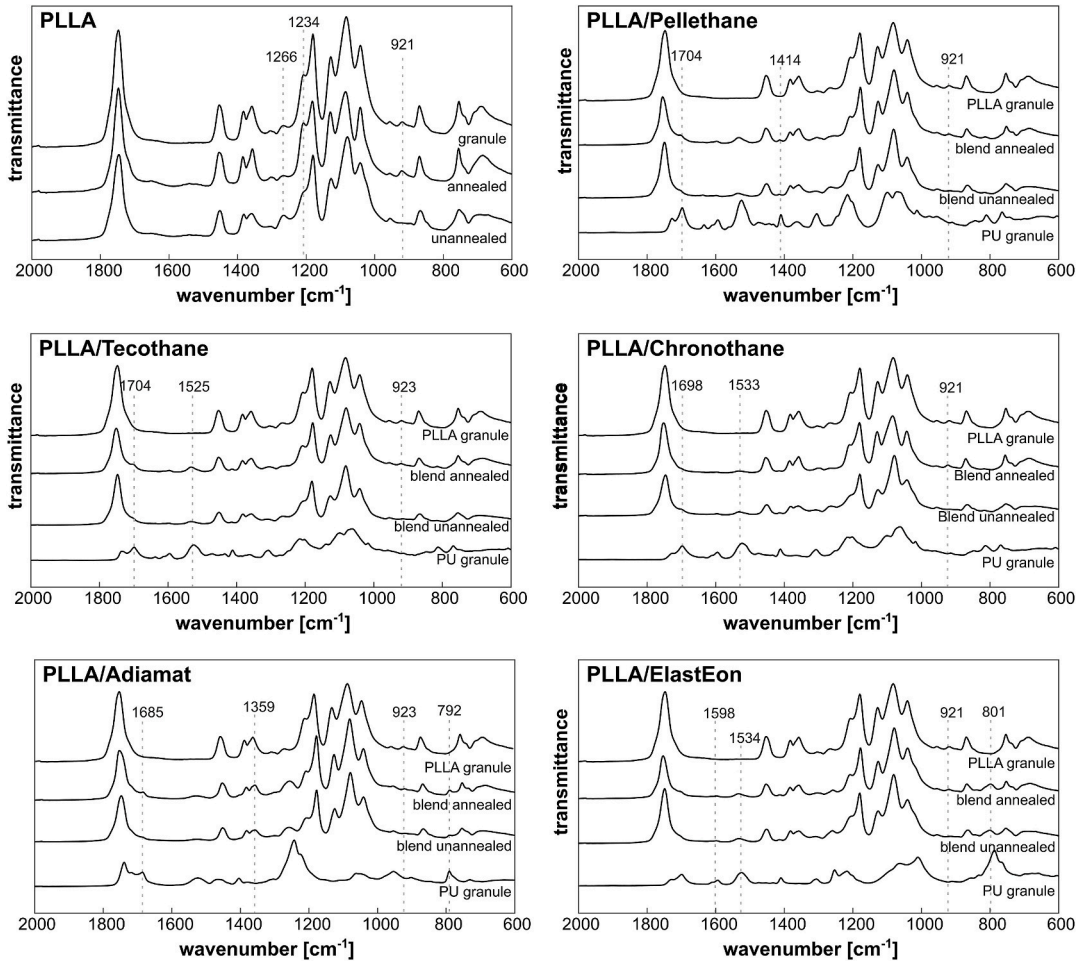


Fig. 4. ATR-FTIR spectra of PLLA and PLLA/PU blends before and after thermal annealing. As reference, spectra of pure polymer granules were added. Characteristic bands of PLLA and PU are indicated with dotted lines. To enhance visibility, the spectra were stretched in y-axis.

polyurethane in the blend at $T_m = 187–221$ °C. As no large crystallites were found and the T_m signal intensity was very low, we assume Chronothane microcrystallites embedded in the PLLA matrix. For PLLA/Adiamat, no PU melting signal was found, as the melting signal taken from the reference thermogram was overlapping with T_g of PLLA.

In the ATR-FTIR spectrum (Fig. 4), PLLA shows characteristic changes in crystallinity sensitive bands after thermal annealing, in particular at $\tilde{\nu} = 921\ \mathrm{cm}^{-1}$, but also at $\tilde{\nu} = 1234\ \mathrm{cm}^{-1}$ and $\tilde{\nu} = 1266\ \mathrm{cm}^{-1}$, indicating an increase in crystallinity [35,36]. The changes at $\tilde{\nu} = 921\ \mathrm{cm}^{-1}$ band are also visible for all PLLA/PU blends, except PLLA/Adiamat, where this band is overlaid with PU bands. In addition, the respective PU characteristic bands were observable after blending. As no distinct changes in bands for the blends attributed to PLLA were detectable, it can be concluded that there is no interaction between the respective polymers on a molecular level when being blended.

To evaluate the extent to which blending with 10 wt% biomedical grade PU leads to an improvement in elasticity and plastic deformability, uniaxial tensile tests have been performed of the dry blends (Fig. 5). Pure PLLA obtained by injection molding showed a strain at break of $\varepsilon_B = 3.6 \pm 0.2\%$, which is comparable to results reported in the literature [37]. Blending with 10 wt% Pellethane lead to an increase in ε_B, paired with distinct plastic deformation before break. Tecothane as blending partner showed the tendency for only a slight increase in ε_B. Blending with Chronothane and Adiamat did not lead to such an increase in ε_B and the blends did not show distinct plastic deformation, which can be attributed to the PU crystals, which were found in cross-sectional SEM images. Blending with ElastEon lead to comparable results as with Pellethane. However, blending with Pellethane, Tecothane and ElastEon lead to an increase in statistical variance.

For the suitability of a polymer for biomedical devices, mechanical performance is a crucial aspect. PLLA in particular, although exhibiting high tensile strength, is limited in its uses due to its brittleness and low plasticity. The increase in ε_B can be attributed to the PU phase, providing sufficient ductility. Where PLLA due to its rigid nature and brittleness easily breaks, embedding PUs may allow for a considerably higher strain, increasing ε_B by 660% in the case of Pellethane ($\bar{\varepsilon}_{B,PLLA/Pellethane} = 28 \pm 7\%$ vs. $\bar{\varepsilon}_{B,PLLA} = 3.6 \pm 0.3\%$, measured in dry state, Fig. 5) as blending partner.

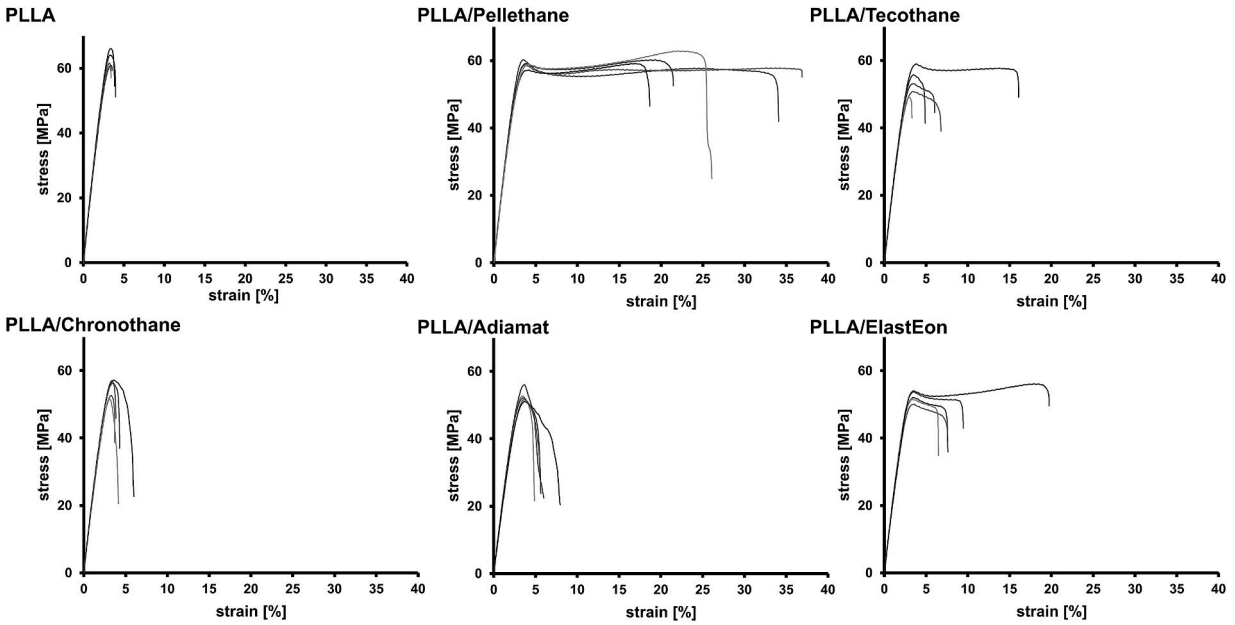


Fig. 5. Stress strain curves of PLLA and PLLA/PU blends after injection molding and thermal annealing measured in dry state.

Table 4
Young's modulus values, yield strain (ε_y) and yield stress (σ_y) for PLLA/PU blends with 10 wt% PU after injection molding and thermal annealing measured in dry state and after incubation in physiological saline solution for 7 days, extracted from stress-strain curves.

	PLLA	PLLA/Pellethane	PLLA/Tecothane	PLLA/Chronothane	PLLA/Adiamat	PLLA/ElastEon
E dry (MPa)	2370 ± 50	2227 ± 50	2145 ± 83	2070 ± 60	1930 ± 260	2101 ± 23
E medium (MPa)	2280 ± 40	1920 ± 70	1915 ± 79	2090 ± 40	1800 ± 100	1942 ± 78
ε_y dry (%)	2.56 ± 0.11	2.27 ± 0.04	2.26 ± 0.12	2.55 ± 0.19	2.58 ± 0.06	2.25 ± 0.14
ε_y medium (%)	2.62 ± 0.13	2.44 ± 0.18	2.47 ± 0.12	2.50 ± 0.18	2.56 ± 0.15	2.47 ± 0.14
σ_y dry (MPa)	55.7 ± 2.3	46.0 ± 1.5	44.0 ± 1.1	49 ± 4	46.0 ± 1.6	43 ± 3
σ_y medium (MPa)	55 ± 4	43 ± 5	43.5 ± 2.0	48 ± 5	43 ± 4	44.1 ± 1.4

Notably, both, Pellethane and Tecothane are aromatic polyether-based thermoplastic polyurethanes with a comparable chemical composition. However, stress strain-curves revealed a highly different influence on strain at break when blended with PLLA ($\overline{\varepsilon}_{B,PLLA/Pellethane} = 28 \pm 7\%$ versus $\overline{\varepsilon}_{B,PLLA/Tecothane} = 7 \pm 5\%$). We conclude that this is due to the different content of soft segment in the PU, which is directly indicated by the difference in shore hardness of 80A (Pellethane) versus 55D (Tecothane). The soft segment can in turn interact with PLLA phase, thus, the higher the soft segment, the softer the materials (Pellethane) and the higher the influence on ε_B. However, it was shown that the molecular differences of all PUs (soft segment content, siloxane content and carbonate content) as blending partners did not show to have a different influence on Young's modulus and yield point (Table 4).

To further investigate on how the PLLA/PU blends perform under relevant conditions in terms of implant application, polymer specimens were incubated for 7 days in physiological saline solution and stress strain curves were measured from wet samples (Fig. 6). Investigating mechanical performance in medium contact must be considered for biomedical applications, as water and ions from the medium diffuse into the polymer and may affect mechanical properties.

After storing in medium, for pure PLLA, PLLA/Tecothane, PLLA/Chronothane and PLLA/ElastEon, no pronounced changes in mechanical behavior were observed compared to dry state. For PLLA/Pellethane and PLLA/Adiamat, a decrease in ε_B was found. Notably, for PLLA/Pellethane stress strain curves showed less variance for the wet tested specimens compared to the dry ones. In the case of PLLA/Adiamat blend, after incubation, the material showed an increase in ε_B paired with plastic deformation, which could not be observed for the dry tested samples. Plastic deformation, as observed for PLLA/Pellethane, PLLA/Tecothane, PLLA/ElastEon and, when wet, for PLLA/Adiamat, is a crucial parameter for biomedical uses, in particular regarding application as stent material, as crimping and dilation require the material must withstand these processes without failure.

From stress strain curves of dry and wet tested blends, the material parameters yield strain (ε_y) and yield stress (σ_y) were extracted to evaluate the plastic resilience of the materials (Table 4 and Fig. 7). Incubation in physiological saline has no effect on the *E* value of PLLA, but decreased *E* in the case of blending with Pellethane, Tecothane and ElastEon.

Overall, blending did lead to a decrease of ε_y and σ_y compared to pure PLLA. Still, all materials showed to endure a strain of minimum 2.2% without plastic deformation, as can be seen from overview of yield stress versus yield strain in Table 4 and Fig. 7. The values remained comparable for each blend either in dry or wet state. As for the yield stress, the value decreased for all the blends with

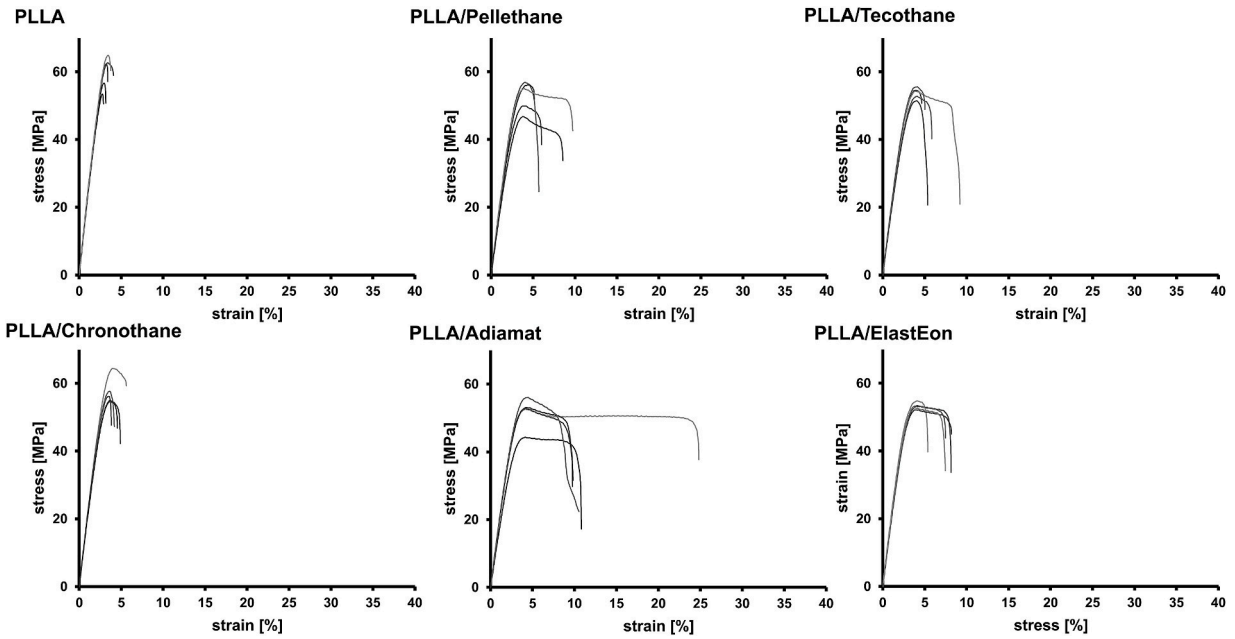


Fig. 6. Stress strain curves (averaged over 5 measurements) of PLLA and PLLA/PU blends after injection molding and thermal annealing measured after incubation in physiological saline solution for 7 d.

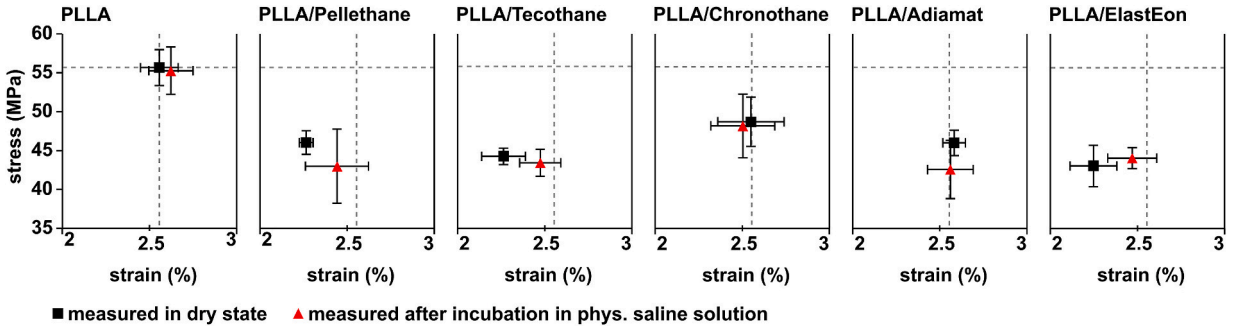


Fig. 7. Yield stress versus yield strain of PLLA/PU blends with 10 wt% PU after injection molding and thermal annealing measured in dry state and after incubation in physiological saline solution for 7 days, calculated from stress-strain curves by 0.2% offset method. Dashed line indicate PLLA values, measured in dry state as reference.

10 wt% Polyurethane, with the lowest value dropping from $\sigma_y = 55.67 \pm 2.3$ MPa for pure PLLA to $\sigma_y = 43.0 \pm 3$ MPa for PLLA/Adiamat. This in turn may affect the performance of the material, in particular for stent application, where radial fatigue is a critical parameter. However, how the differences in yield strength affect the resulting radial force, including the influence of other parameters such as implant design, needs to be evaluated for specific stent prototypes.

To further evaluate the effect of PU as blending partners on mechanical properties, PLLA/Pellethane blends with higher PU fractions, 20 and 30 wt% Pellethane in the blend, were investigated (Fig. 8).

First, blending 20 wt% of Pellethane lead to a further increase in ε_B, as well as reduction of scattering of the resulting values for PLLA/Pellethane 80:20, indicating a higher homogeneity of the blend. A higher amount of 30 wt% Pellethane did not show to further affect ε_B. However, blending with higher amounts of Pellethane lead to a further decrease of ε_y and σ_y, down to $\sigma_{y,70:30} = 20.88 \pm 3.05$ MPa and $\varepsilon_{y,70:30} = 1.79 \pm 0.16\%$ (Fig. 8 and Table 5).

PLLA/polyurethane blends have gained attention in implant development, as they have been reported to show thermally induced shape memory (SM) behavior [31,38]. In brief, the amorphous domain acts as reversible phase, enabling shape recovery when heated above T_g [39]. As for PLLA and PLLA/PU blends, SM results from the deformation of the polymer above T_g of PLLA, providing sufficient plasticity as the amorphous regions are in the viscous state. PLLA crystallites then serve as anchor points for highly flexible phase. According to the literature, in the case of PLLA/PU blends, the rubbery elastic PU phase in addition acts as load carrier, preventing PLLA from breaking and allowing higher elongation. On cooling under load, the energy is stored in the material. When polymer is then reheated above $T_{g,PLLA}$, the material regains molecular mobility, causing recovery to the initial shape [31]. SM polymers are of high

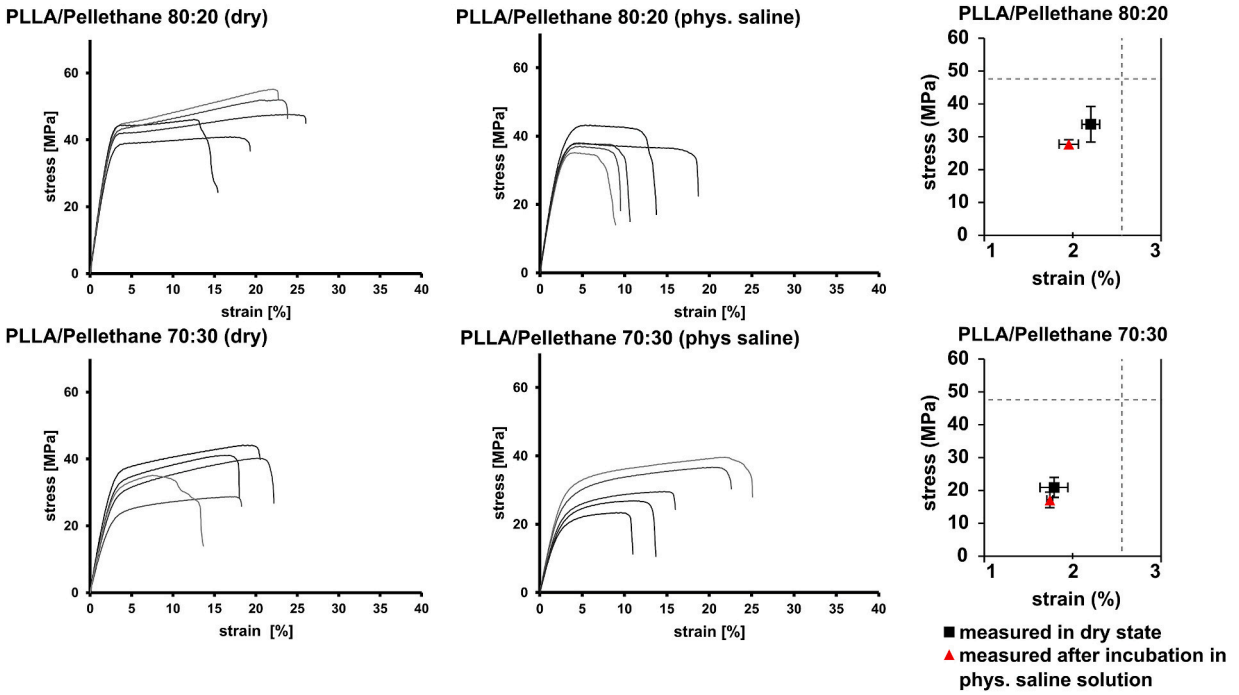


Fig. 8. Stress strain curves of PLLA/Pellethane blends with a ratio of 80:20 and 70:30 after injection molding and thermal annealing measured in dry state, and yield stress versus yield strain of PLLA/Pellethane 80:20 and 70:30 measured in dry state and after incubation in physiological saline solution for 7 days, calculated from stress-strain curves by 0.2% offset method. Dashed line indicate PLLA values measured in dry state as reference.

Table 5
Young's modulus values, yield strain (ε_y) and yield stress (σ_y) for PLLA/Pellethane 80:20 and 70:30 measured in dry state and after incubation in physiological saline solution for 7 days, extracted from stress-strain curves.

	PLLA/Pellethane 80:20	PLLA/Pellethane 70:30
E dry (MPa)	1674 ± 206	1336 ± 112
E medium (MPa)	1591 ± 79	1110 ± 131
ε_y dry (%)	2.21 ± 0.10	1.79 ± 0.16
σ_y dry (MPa)	34 ± 6	21 ± 3
ε_y medium (%)	1.95 ± 0.11	1.74 ± 0.03
σ_y medium (MPa)	27.8 ± 1.4	17.2 ± 2.3

interest in applications such as 4D printing [40], but also as material in biomedical engineering. Based on the mechanical data for all blends, SM behavior of PLLA/Pellethane was selected to be further investigated for 90:10, 80:20 and 70:30 blends using DMA (Figs. 9 and 10, Fig. 10 and Table 6).

In DMA experiments (Fig. 9 I), PLLA and PLLA/Pellethane blends showed a recoil after fixation at 15 °C and releasing the force (D_s-D_r). When the heating above T_g, all of the selected polymers exhibited recovery towards the initial state (D_R). The recovered state can then be restored in cyclic experiments (Fig. 9 II). From the DMA experiments, it can be seen that blending with PU leads to higher displacement under load due to the increased flexibility of the material, also in accordance with uniaxial tensile tests. In addition, with increasing PU fraction, recovery decreases (Table 7).

For better visualization, shape recovery was additionally investigated on samples that were displaced in a controlled manner using the DMA device and thermal shape recovery was induced by immersion in water at 70 °C.

Videos of the thermally induced shape recovery by immersion in 70 °C water have been recorded and are provided below:

Supplementary video related to this article can be found at https://doi.org/10.1016/j.envres.2024.118137

Shape retention and thermally induced shape recovery of PLLA/Pellethane blends were determined using DMA. Our finding was that SM behavior is not as pronounced for the selected PLLA/Pellethane blends as for pure PLLA. However, when considered in conjunction with the mechanical performance, in particular the higher plasticity, the blends may be of benefit regarding the material performance for stent applications, manufacturing and processing. Notably, SM behavior of PLLA and PLLA/Pellethane is triggered when heated above $T_{g,PLLA} = \sim 68$ °C. As this is above body temperature, SM is not of particular relevance for direct exploitation when implanted. However, it may be highly beneficial for manufacturing of biomedical devices, in particular in the context of polymer stents, as the transition of a temporary to the initial shape may facilitate stent dilation in the body. Although SM is not as pronounced in

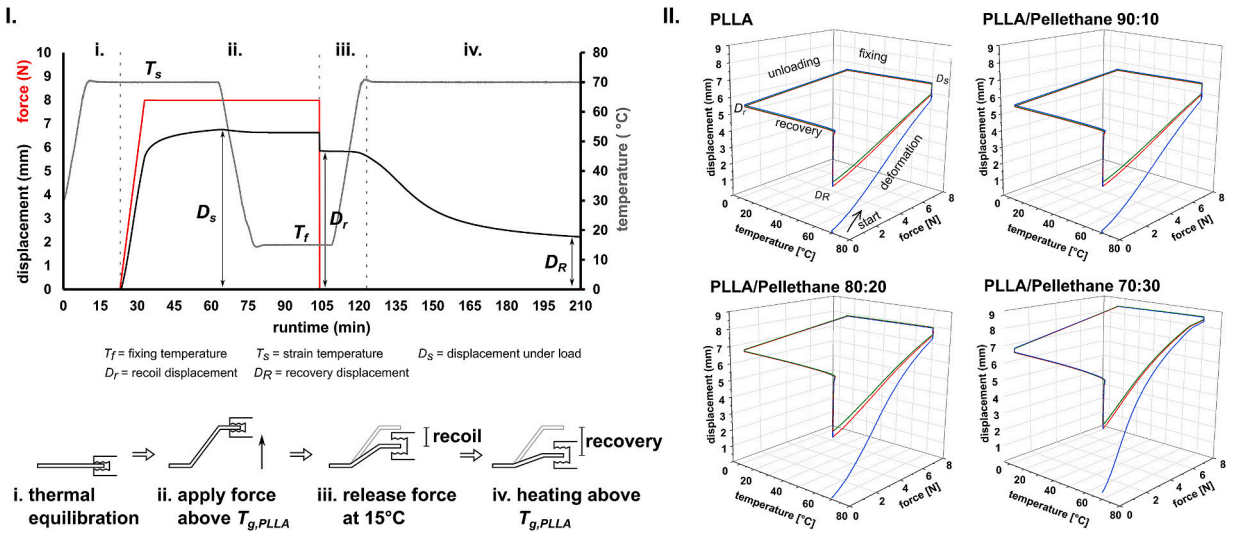


Fig. 9. I: Representative diagram of displacement, force and temperature as function of time for pure PLLA for the first complete DMA cycle for SM characterization and schematic of the mechanical load on the sample. Characteristic values D_s, D_r and D_R are indicated. 2nd and 3rd cycles were similar, except the initial thermal equilibration step (i) was skipped. DMA protocol was the same for all measured samples. II: Representative 3D plots of DMA measurements for PLLA and PLLA/Pellethane blends (90:10, 80:20 and 70:30) after three cycles. Colors are indicative for cycle 1 (blue), cycle 2 (red) and cycle 3 (green). Thermal equilibration step is not shown in 3D plots.

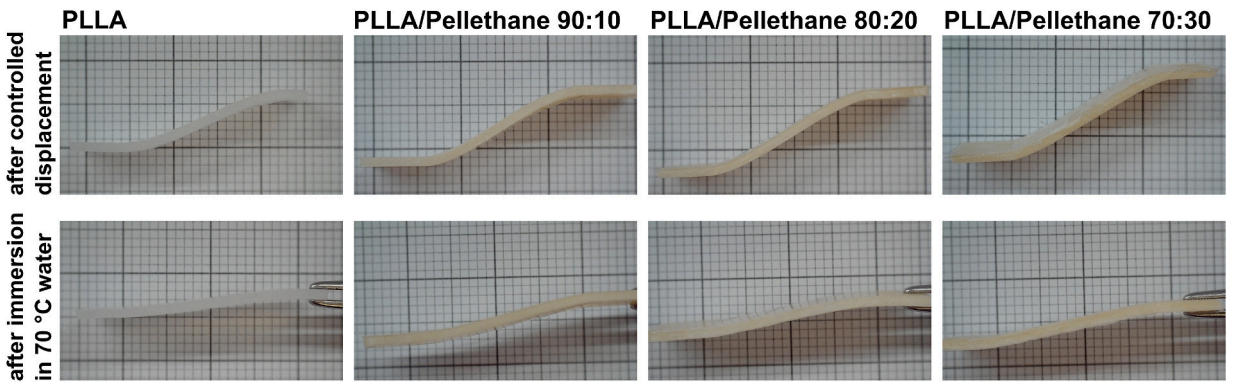


Fig. 10. Photographic images of PLLA and PLLA/Pellethane after controlled displacement using DMA device. The test chamber was heated to 70 °C and the sample was equilibrated for 30 min before a force of 8.0 N was applied at a rate of 0.8 N/min. The samples were held at 8.0 N for 30 min before temperature was lowered to 15 °C. Samples were kept at 15 °C for 30 min, and then the force was released. The bottom line shows photographic images of the same samples after 1 min immersion in deionized water heated to 70 °C.

Table 6
Shape memory parameters displacement under load (D_s), recoil displacement (D_r) and recovery displacement (D_R) for the first and the third cycle obtained by DMA experiments as shown in Fig. 9.

	first cycle (n = 3)			third cycle (n = 3)		
	D_s (mm)	D_r (mm)	D_R (mm)	D_s (mm)	D_r (mm)	D_R (mm)
PLLA	6.5 ± 0.3	5.7 ± 0.3	2.4 ± 0.2	6.6 ± 0.5	5.7 ± 0.4	2.8 ± 0.2
PLLA/Pellethane 90:10	8.1 ± 0.1	7.2 ± 0.1	3.3 ± 0.1	8.1 ± 0.1	7.2 ± 0.1	3.7 ± 0.1
PLLA/Pellethane 80:20	8.1 ± 0.3	7.2 ± 0.2	3.5 ± 0.1	8.1 ± 0.2	7.1 ± 0.2	3.9 ± 0.1
PLLA/Pellethane 70:30	8.5 ± 0.1	7.1 ± 0.1	3.9 ± 0.9	8.5 ± 0.1	7.1 ± 0.1	4.2 ± 0.1

Table 7
Shape retention rate = D_rx100/D_s and shape recovery rate = (D_r-D_R)x100/D_s calculated from SM parameters (Table 6) according to Lu et al. [41].

	Shape retention rate for the first cycle (n = 3)	Shape recovery rate for the first cycle (n = 3)	Shape retention rate for the third cycle (n = 3)	Shape recovery rate for the third cycle (n = 3)
PLLA	87.2 ± 0.2%	73.2 ± 3.2%	86.6 ± 0.5%	66.6 ± 3.2%
PLLA/Pellethane 90:10	88.4 ± 0.3%	66.9 ± 0.5%	88.3 ± 0.3%	61.6 ± 0.7%
PLLA/Pellethane 80:20	88.2 ± 0.7%	64.3 ± 2.3%	87.9 ± 0.7%	58.6 ± 2.9%
PLLA/Pellethane 70:30	83.6 ± 0.5%	65.5 ± 1.3%	83.1 ± 0.6%	61.5 ± 1.7%

PLLA blends compared to SM alloys such as nitinol, it may help overcome one of the main disadvantages of PLLA, its brittleness and low plasticity, and enable innovative device designs.

4. Conclusion

Blending PLLA with polyurethanes is a powerful tool to improve the material's mechanical performance for biomedical applications, particularly in the context of biodegradable polymer stent development. In this context, thermal and mechanical properties are of major importance to be able to develop functional and safe biomedical devices. However, the choice of blending partners is limited to medical grade materials to bypass time-consuming and expensive approval processes. The chemical structure of the polyurethane influences the interaction of the polymers when blended, leading to complex phase behavior. Our finding was, that from the selected polyurethanes, in particular blending PLLA with Pellethane lead to a major improvement of the mechanical characteristics paired with thermal stability and good shape recovery properties, which, in turn, has the potential to open for new aspects in stent manufacturing processes.

Data availability statement

The raw/processed data required to reproduce these findings cannot be shared at this time due to technical or time limitations.

CRediT authorship contribution statement

Stefan Oschatz: Writing – original draft, Visualization, Methodology, Data curation, Conceptualization. **Selina Schultz:** Writing – review & editing, Methodology, Data curation. **Nicklas Fiedler:** Writing – original draft, Methodology. **Volkmar Senz:** Writing – review & editing, Methodology. **Klaus-Peter Schmitz:** Writing – review & editing, Funding acquisition. **Niels Grabow:** Writing – review & editing, Funding acquisition. **Daniela Koper:** Writing – original draft, Methodology, Investigation, Conceptualization.

Declaration of competing interest

The authors declare that they have no known competing financial interests or personal relationships that could have appeared to influence the work reported in this paper.

Acknowledgments

The authors thank Katja Hahn for her expert technical assistance. Financial support by the Federal Ministry of Education and Research (BMBF) within RESPONSE "Partnership for Innovation in Implant Technology", grant numbers 03ZZ0922A and 03ZZ0922G, is gratefully acknowledged.

Appendix A. Supplementary data

Supplementary data to this article can be found online at https://doi.org/10.1016/j.heliyon.2024.e26268.

References

[1] D.J. Kereiakes, S.G. Ellis, C. Metzger, R.P. Caputo, D.G. Rizik, P.S. Teirstein, M.R. Litt, A. Kini, A. Kabour, S.O. Marx, J.J. Popma, R. McGreevy, Z. Zhang, C. Simonton, G.W. Stone, 3-Year clinical outcomes with everolimus-eluting bioresorbable coronary scaffolds: the ABSORB III trial, J. Am. Coll. Cardiol. 70 (2017) 2852–2862, https://doi.org/10.1016/j.jacc.2017.10.010.
[2] S.B. King, B.D. Gogas, Can the vanishing stent reappear?: fix the technique, or fix the device? J. Am. Coll. Cardiol. 70 (2017) 2875–2877, https://doi.org/10.1016/j.jacc.2017.10.009.

[3] C.E. Raphael, A. El-Sabbagh, M. Corban, S.E. Hajj, A. Prasad, Chapter 24 - emerging therapies in coronary balloon angioplasty, stenting, and bioabsorbable scaffolds, in: U. Nussinovitch (Ed.), Emerging Technologies for Heart Diseases: Volume 2: Treatments for Myocardial Ischemia and Arrhythmias, Elsevier Science & Technology, San Diego, 2020, pp. 527–557.

[4] Sean Mcmahon, N. Bertollo, Eoin D. O' Cearbhaill, J. Salber, Luca Pierucci, Patrick Duffy, T. Durig, Vivian Bi, Wenxin Wang, Bio-resorbable polymer stents: a review of material progress and prospects, Prog. Polym. Sci. 83 (2018) 79–96, https://doi.org/10.1016/j.progpolymsci.2018.05.002.

[5] N. Bink, V.B. Mohan, S. Fakirov, Recent advances in plastic stents: a comprehensive review, Int. J. Polym. Mater. 70 (2021) 54–74, https://doi.org/10.1080/00914037.2019.1685519.

[6] S. Farah, D.G. Anderson, R. Langer, Physical and mechanical properties of PLA, and their functions in widespread applications - a comprehensive review, Adv. Drug Deliv. Rev. 107 (2016) 367–392, https://doi.org/10.1016/j.addr.2016.06.012.

[7] X. Fan, B.H. Tan, Z. Li, X.J. Loh, Control of PLA stereoisomers-based polyurethane elastomers as highly efficient shape memory materials, ACS Sustain. Chem. Eng. 5 (2017) 1217–1227, https://doi.org/10.1021/acssuschemeng.6b02652.

[8] W. Wang, P. Ping, X. Chen, X. Jing, Polylactide-based polyurethane and its shape-memory behavior, Eur. Polym. J. 42 (2006) 1240–1249, https://doi.org/10.1016/j.eurpolymj.2005.11.029.

[9] C. Kaynak, S.D. Varsavas, Performance comparison of the 3D-printed and injection-molded PLA and its elastomer blend and fiber composites, J. Thermoplast. Compos. Mater. 32 (2019) 501–520, https://doi.org/10.1177/0892705718772867.

[10] J.-J. Han, H.-X. Huang, Preparation and characterization of biodegradable polylactide/thermoplastic polyurethane elastomer blends, J. Appl. Polym. Sci. 120 (2011) 3217–3223, https://doi.org/10.1002/app.33338.

[11] H. Xiu, X. Qi, H. Bai, Q. Zhang, Q. Fu, Simultaneously improving toughness and UV-resistance of polylactide/titanium dioxide nanocomposites by adding poly (ether)urethane, Polym. Degrad. Stabil. 143 (2017) 136–144, https://doi.org/10.1016/j.polymdegradstab.2017.07.002.

[12] A. Jayswal, J. Liu, G. Harris, S. Adanur, Thermo-mechanical properties of composite filaments for 3D printing of fabrics, J. Thermoplast. Compos. Mater. (2023) 089270572311634, https://doi.org/10.1177/08927057231163489.

[13] D.-Y. Zuo, L. Zhang, C.-H. Yi, H.-T. Zuo, Effects of compatibility of poly(l -lactic-acid) and thermoplastic polyurethane on mechanical property of blend fiber, Polym. Adv. Technol. 25 (2014) 1406–1411, https://doi.org/10.1002/pat.3382.

[14] USP 36-NF 31, United States Pharmacopeia: National Formulary, United States Pharmacopeial Convention, 2013. Rockville, Md.

[15] DIN EN ISO 10993-23:2021-10, Biologische Beurteilung von Medizinprodukten_- Teil_23: Prüfungen auf Irritation (ISO_10993-23:2021); Deutsche Fassung EN_ISO_10993-23:2021, Beuth Verlag GmbH, Berlin.

[16] A.M. Lincoff, J.G. Furst, S.G. Ellis, R.J. Tuch, E.J. Topol, Sustained local delivery of dexamethasone by a novel intravascular eluting stent to prevent restenosis in the porcine coronary injury model, J. Am. Coll. Cardiol. 29 (1997) 808–816, https://doi.org/10.1016/S0735-1097(96)00584-0.

[17] S.H. Daebritz, J.S. Sachweh, B. Hermanns, B. Fausten, A. Franke, J. Groetzner, B. Klosterhalfen, B.J. Messmer, Introduction of a flexible polymeric heart valve prosthesis with special design for mitral position, Circulation 108 (Suppl 1) (2003) II134–I139, https://doi.org/10.1161/01.cir.0000087655.41288.dc.

[18] R.L. Li, J. Russ, C. Paschalides, G. Ferrari, H. Waisman, J.W. Kysar, D. Kalfa, Mechanical considerations for polymeric heart valve development: biomechanics, materials, design and manufacturing, Biomaterials 225 (2019) 119493, https://doi.org/10.1016/j.biomaterials.2019.119493.

[19] A. Mahomed, D.W. Hukins, S.N. Kukureka, D.E. Shepherd, Effect of accelerated aging on the viscoelastic properties of Elast-Eon™: a polyurethane with soft poly (dimethylsiloxane) and poly(hexamethylene oxide) segments, Mater. Sci. Eng. C 30 (2010) 1298–1303, https://doi.org/10.1016/j.msec.2010.07.014.

[20] B. Zhang, Y. Xu, S. Ma, L. Wang, C. Liu, W. Xu, J. Shi, W. Qiao, H. Yang, Small-diameter polyurethane vascular graft with high strength and excellent compliance, J. Mech. Behav. Biomed. Mater. 121 (2021) 104614, https://doi.org/10.1016/j.jmbbm.2021.104614.

[21] S.D. Bruck, E.P. Mueller, Materials aspects of implantable cardiac pacemaker leads, Med. Prog. Technol. (1988) 149–160.

[22] L. Zhao, V. Semetey, Recycling polyurethanes through transcarbamoylation, ACS Omega 6 (2021) 4175–4183, https://doi.org/10.1021/acsomega.0c04855.

[23] A.E. Stepien, J. Zebrowski, Ł. Piszczyk, V.V. Boyko, S.V. Riabov, T. Dmitrieva, V.I. Bortnitskiy, M. Gonchar, R. Wojnarowska-Nowak, J. Ryszkowska, Assessment of the impact of bacteria Pseudomonas denitrificans, Pseudomonas fluorescens, Bacillus subtilis and yeast Yarrowia lipolytica on commercial poly(ether urethanes), Polym. Test. 63 (2017) 484–493, https://doi.org/10.1016/j.polymertesting.2017.08.038.

[24] P. Kasprzyk, E. Głowińska, J. Datta, Structure and properties comparison of poly(ether-urethane)s based on nonpetrochemical and petrochemical polyols obtained by solvent free two-step method, Eur. Polym. J. 157 (2021) 110673, https://doi.org/10.1016/j.eurpolymj.2021.110673.

[25] M. Crago, A. Lee, S. Farajikhah, F. Oveissi, D.F. Fletcher, F. Dehghani, D.S. Winlaw, S. Naficy, The evolution of polyurethane heart valve replacements: how chemistry translates to the clinic, Mater. Today Commun. 33 (2022) 104916, https://doi.org/10.1016/j.mtcomm.2022.104916.

[26] N.C. Kekec, M.B. Akolpoglu, U. Bozuyuk, S. Kizilel, N. Nugay, T. Nugay, J.P. Kennedy, Calcification resistance of polyisobutylene and polyisobutylene-based materials, Polym. Adv. Technol. 30 (2019) 1836–1846, https://doi.org/10.1002/pat.4616.

[27] E.W. Fischer, H.J. Sterzel, G. Wegner, Investigation of the structure of solution grown crystals of lactide copolymers by means of chemical reactions, Kolloid-Z.u. Z.Polymere 251 (1973) 980–990, https://doi.org/10.1007/BF01498927.

[28] Plastics Determination of Tensile Properties, BSI British Standards, London, 2019.

[29] A. Shirole, C.U. Perotto, S. Balog, C. Weder, Tailoring the shape memory properties of segmented poly(ester urethanes) via blending, ACS Appl. Mater. Interfaces 10 (2018) 24829–24839, https://doi.org/10.1021/acsami.8b07083.

[30] Y.-D. Shi, Y.-H. Cheng, Y.-F. Chen, K. Zhang, J.-B. Zeng, M. Wang, Morphology, rheological and crystallization behavior in thermoplastic polyurethane toughed poly(l-lactide) with stereocomplex crystallites, Polym. Test. 62 (2017) 1–12, https://doi.org/10.1016/j.polymertesting.2017.06.013.

[31] X. Jing, H.-Y. Mi, X.-F. Peng, L.-S. Turng, The morphology, properties, and shape memory behavior of polylactic acid/thermoplastic polyurethane blends, Polym. Eng. Sci. 55 (2015) 70–80, https://doi.org/10.1002/pen.23873.

[32] S. Yamane, R. Watanabe, S. Ata, J. Mizukado, H. Shinzawa, Solvent-induced degradation of polyurethane studied by two-dimensional (2D) infrared (IR) correlation spectroscopy, Vib. Spectrosc. 108 (2020) 103062, https://doi.org/10.1016/j.vibspec.2020.103062.

[33] L.H. Chan-Chan, R. Solis-Correa, R.F. Vargas-Coronado, J.M. Cervantes-Uc, J.V. Cauich-Rodríguez, P. Quintana, P. Bartolo-Pérez, Degradation studies on segmented polyurethanes prepared with HMDI, PCL and different chain extenders, Acta Biomater. 6 (2010) 2035–2044, https://doi.org/10.1016/j.actbio.2009.12.010.

[34] A. Takahara, R.W. Hergenrother, A.J. Coury, S.L. Cooper, Effect of soft segment chemistry on the biostability of segmented polyurethanes. II. In vitro hydrolytic degradation and lipid sorption, J. Biomed. Mater. Res. 26 (1992) 801–818, https://doi.org/10.1002/jbm.820260609.

[35] E. Meaurio, N. López-Rodríguez, J.R. Sarasua, Infrared spectrum of poly(l -lactide): application to crystallinity studies, Macromolecules (Washington, DC, U. S.) 39 (2006) 9291–9301, https://doi.org/10.1021/ma061890r.

[36] J. Zhang, Y. Duan, H. Sato, H. Tsuji, I. Noda, S. Yan, Y. Ozaki, Crystal modifications and thermal behavior of poly(l -lactic acid) revealed by infrared spectroscopy, Macromolecules (Washington, DC, U. S.) 38 (2005) 8012–8021, https://doi.org/10.1021/ma051232r.

[37] L. Meinig, R. Boldt, Y. Spoerer, I. Kuehnert, M. Stommel, Correlation between processing parameters, morphology, and properties of injection-molded polylactid acid (PLA) specimens at different length scales, Polymers 15 (2023), https://doi.org/10.3390/polym15030721.

[38] X. Ji, F. Gao, Z. Geng, D. Li, Fabrication of thermoplastic polyurethane/polylactide shape-memory blends with tunable optical and mechanical properties via a bilayer structure design, Polym. Test. 97 (2021) 107135, https://doi.org/10.1016/j.polymertesting.2021.107135.

[39] X. Lu, W. Cai, L.C. Zhao, Study on the shape memory behavior of poly (L-Lactide), Inside MS 475–479 (2005) 2399–2402, https://doi.org/10.4028/www.scientific.net/MSF.475-479.2399.

[40] Y. Li, F. Zhang, Y. Liu, J. Leng, 4D printed shape memory polymers and their structures for biomedical applications, Sci. China Technol. Sci. 63 (2020) 545–560, https://doi.org/10.1007/s11431-019-1494-0.

[41] X.L. Lu, W. Cai, Z. Gao, W.J. Tang, Shape memory effects of poly(L-lactide) and its copolymer with poly(ε-caprolactone), Polym. Bull. 58 (2007) 381–391, https://doi.org/10.1007/s00289-006-0680-6.

Materials & Design 256 (2025) 114255

Contents lists available at ScienceDirect

Materials & Design

journal homepage: www.elsevier.com/locate/matdes

PLLA/PEO blend as self-curing material for a biodegradable Eustachian tube stent

Stefan Oschatz [a,*], Selina Schultz [a], Nicklas Fiedler [a], Jana Markhoff [a], Michael Teske [a], Daniela Koper [b], Volkmar Senz [a], Christoph Brandt-Wunderlich [b], Klaus-Peter Schmitz [a,b], Niels Grabow [a,c], Kerstin Lebahn [a]

[a] Institute for Biomedical Engineering, University Medical Center Rostock, Friedrich-Barnewitz-Straße 4, 18119 Rostock, Germany
[b] Institute for ImplantTechnology and Biomaterials e.V., Friedrich-Barnewitz-Straße 4, 18119 Rostock-Warnemünde, Germany
[c] Department Life, Light & Matter (LLM), University of Rostock, Albert-Einstein Str. 25, 18051 Rostock, Germany

ARTICLE INFO

Keywords:
Poly-L-lactide
Polyethylene oxide
Polymer-based stent
Eustachian tube
PLLA/PEO blend

ABSTRACT

Within this work, blending of high molecular weight (HMW) PLLA with HMW polyethylene oxide (PEO) as self-curing biodegradable stent material for potential treatment of Eustachian tube dysfunction (ETD) is reported. Blending with PEO significantly enhances the material's mechanical properties, enabling the stent to conform to the non-circular, tapered cross-sectional shape of the Eustachian tube (ET). Elution of PEO leads to self-curing of the stent, enabling long-term support of the ET. The PLLA/PEO stents were able to withstand radial deformation of up to 33 % and up to 12 %. Radial strength of the stent prototypes (90/10: 203 ± 37 kPa and 80/20: 232 ± 52 kPa) was slightly lower compared to the benchmarked commercial Absorb, Elixir and RevaMedical stents (250/218/318 kPa), but exceeded the values of the former two after 7 d post-curing *in vitro* (90/10: 301 ± 59 kPa and 80/20: 324 ± 12 kPa). Radial stiffness (90/10: 7.63 ± 2.74 kPa and 80/20: 9.15 ± 3.03 kPa) was also comparable (Absorb/Elixir/RevaMedical stents: 6.08/5.31/6.99), but increased to 15.07 ± 2.57 kPa (90/10) and 15.89 ± 1.53 kPa (80/20) after PEO elution over 7d *in vitro*, substantially increasing scaffolding properties.

1. Introduction

Eustachian tube dysfunction (ETD) with insufficient ventilation of the middle ear affects about 1 % of the general adult population, and approximately 40 % of children develop at least transient ETD [1]. It is one of the major causes for chronic *otitis media* and can lead to massive impairment of quality of life and irreversible middle ear damage. With appropriate early treatment, ETD is often reversible, but can trigger severe, irreversible disorders if untreated and the progression is complicated. In this context, stenting the Eustachian tube (ET) is a promising concept to provide an effective and safe therapy. Besides balloon Eustachian tuboplasty [2], implanting a stent in the ET for treating these patients can minimize consequential damage, restoring ventilation of the middle ear for a certain period of time (biodegradable stent) or permanently (permanent stent) [3,4]. In particular, biodegradable polymer-based stents that restore impaired tube function and dissolve after they have fulfilled their supportive purpose are in the current focus of development [5]. Still, no device for stenting the ET is yet commercially available.

In this context, typical problems with polymer-based bioresorbable stents (BRS) from cardiovascular applications are only of minor importance, in particular negative effects on blood flow and the associated risk of thrombosis due to the generally more bulky design dictated by the mechanical properties of polymers and resulting in a larger surface area in blood contact [6]. Still, material properties such as sufficient plastic deformation capacity, a high modulus of elasticity and high yield stress as well as high resistance to cyclic loading are essential for a functioning device. Moreover, the tapered geometry of the ET [5] requires either a form-fitting or even patient individualized, design or a stent manufactured from a shape-adapting material.

Poly-L-lactic acid (PLLA) is one of the most widely used materials for bioresorbable implants. High molecular weight (HMW) PLLA is commonly used in biomedical applications as this material offers sufficient tensile strength. PLLA is FDA-approved and known to be of low toxicity compared to other synthetic polymers. It is frequently used in medical implants since it maintains integrity in *in vitro* and *in vivo*

* Corresponding author.
E-mail address: stefan.oschatz@uni-rostock.de (S. Oschatz).

https://doi.org/10.1016/j.matdes.2025.114255
Received 24 December 2024; Received in revised form 19 May 2025; Accepted 15 June 2025
Available online 16 June 2025
0264-1275/© 2025 The Author(s). Published by Elsevier Ltd. This is an open access article under the CC BY license (http://creativecommons.org/licenses/by/4.0/).

Table 1
Parameters for the fabrication of PLLA/PEO blends by melt compounding and fabrication of test specimens by injection molding.

m_{PLLA}/m_{PEO} [% w/w]	Melt blending			injection molding			annealing		
	$T_{extruder}$ [°C]	T_{nozzle} [°C]	n [min^{-1}]	T_{cyl} [°C]	T_{mold} [°C]	p_{inj} [bar]	p_{hold} [bar]	T_A [°C]	t_A [min]
100/0	–	–	–	220	65	750	300	85	90
90/10	185	185	15	195	60	880		70	15
85/15	185	185		190	55	830		80	15
80/20	185	185		190	50	830		80	15
75/25	185	185		185	45	830		80	15
70/30	180	170		185	45	850		80	30
0/100	–	–	–	185	50	900		–	–

$T_{extruder}$: Temperature in the mixing chamber; T_{nozzle}: Temperature at extruding nozzle; n: twin-screw rotation speed; T_{cyl}: Temperature of IM system cylinder; T_{form}: Temperature of IM mold; p_{inj}: Injection pressure, p_{hold}: Holding pressure; T_A: Annealing temperature; t_A: Annealing time.

applications with regard to mechanical and structural aspects [7]. Nevertheless, its moderate hydrophilic surface properties might inhibit the biocompatibility by affecting protein absorption and resulting cell adhesion [8]. However, PLLA-based implant degradation times are comparatively long with up to several years, at least in cardiovascular application [9,10]. Another major drawback of PLLA is the high brittleness induced by thermal processing, resulting in only low deformation before fracture, usually below $\varepsilon_B = 10$ % [11]. Regardless of the implant design, radial deformability must allow for a small deployment diameter while still allowing for dilatation to the target size. For example, stents used to open occluded organs require high radial resistance, robust plastic deformation capacity, high modulus and yield strength, and strong resistance to cyclic loading. Sophisticated processing protocols, such as blow molding, thermal annealing, or die drawing, are therefore required to adjust the orientation of the polymer chains and the overall crystallinity and thus the mechanical performance of the implant material [12–15]. Switching to solvent-based processes could overcome this problem, as protocols such as dip coating for the production of semi-finished tubular products influence the mechanical properties but only allow a low throughput in production and require careful removal of solvent residues to avoid potential harmful effects.

A suitable large animal model for ETD-treatment using a PLLA-based stent has already been successfully established in sheep, with substantial contributions from our research group [16]. In that preclinical study, the stent concept based on pure PLLA was successfully evaluated *in vivo* in terms of implantation feasibility, tissue compatibility, and basic functional performance. Building on these findings, the present study focuses on systematic material optimization for Eustachian tube stent application through the incorporation of high molecular weight polyethylene oxide (PEO).

Besides the use of copolymers, one approach is the utilization of PLLA-blends to increase plastic deformability while maintaining yield strength. Polyethylene glycol (PEG) and polyethylene oxide (PEO), both being aliphatic polyesters with the formula $H_3CO(C_2H_4O)_nCH_3$ but different in molecular chain length ($M_{n,PEG} < 20\,000$ g/mol $< M_{n,PEO}$), are very suitable plasticizing blend partners for PLLA [17,18]. Both are miscible in the amorphous state and it is known that PEO can enhance the mechanical performance of PLLA [19]. In particular, elongation at break is increased, but tensile strength is reduced. In addition, the hydrophilicity of the mixture is enhanced compared to pure PLLA, which increases the degradation rate of the material, allowing adjustment of degradation time suitable for the application site [20]. PLLA/PEO blends have been reported for use in biomedical applications, in particular for drug delivery and the production of fiber mats by electrospinning [21,22]. However, to the best of the authors' knowledge, there is no report in the literature on the use of PLLA/PEO blends as bulk material for the production of self-curing stents.

Our hypothesis was that a blend of HMW PLLA with HMW PEO as plasticizer would result in improved mechanical performance of the material, enabling sufficient plastic deformability for successful stent expansion without structural damage, conforming to the non-circular cross-section and tapered shape of the ET, while maintaining a high elastic modulus and yield strength, ensuring sufficient initial radial strength of the device. As PEO is a water-soluble polymer, elution of PEO and removal of this plasticizer would restore the basic mechanical properties of PLLA, resulting in post-curing or self-curing of the material after stent deployment, ensuring patency of the Eustachian tube until PLLA scaffold degradation. HMW PEO was chosen as it has a very low elution rate compared to short-chain derivatives, allowing sufficient time for the device to be expanded and to adapt to the shape of the ET.

In this study, the influence on the thermal and mechanical properties of melt-blending PLLA with 10, 15, 20, 25 and 30 % w/w PEO was investigated. Based on these data, selected combinations were subjected to further testing in order to assess their elution behavior, biocompatibility and suitability for fabrication into stents using laser-cutting techniques. Subsequently, the stent prototypes were evaluated for elastic recoil, radial strength and radial stiffness. Our results indicate that blending of HMW PLLA with HMW PEO enhanced the material properties, particularly plastic deformability. Also, post-curing by PEO elution led to the expected increase in radial strength and radial stiffness, increasing stent patency after implantation. With this, we aim to to establish a solid foundation for subsequent in vivo studies and further translational development.

2. Materials and methods

PLLA L210 (Resomer L210, $M_n = 320\,000$ g/mol, Evonik Industries, Essen, Germany) and PEO ($M_n = 400\,000$ g/mol, Scientific Polymer Products, Inc., Ontario, NY, USA) were dried prior to thermal processing at 40 °C and reduced pressure in a vacuum drying oven overnight.

2.1. Sample preparation

Blends of PLLA and PEO with 90/10, 85/15, 80/20, 75/25 and 70/30 % w/w (m_{PLLA}/m_{PEO}) were fabricated by melt compounding using a HAAKE MiniLab II co-rotating twin-screw extruder (Thermo Fisher Scientific, Karlsruhe, Germany). Blending parameters are given in Table 1. The extruded filaments were subsequently pelleted and samples for further testing were fabricated by injection molding (IM) using a Haake MiniJet II (Thermo Fisher Scientific, Karlsruhe, Germany). Pure PLLA samples without the addition of PEO were fabricated solely by injection molding without previous extrusion process. Thermal annealing following the injection molding process was performed using a standard lab heating plate equipped with a previously thermally equilibrated aluminum block with a drilled hole for the heating plate temperature sensor. After thermal annealing for the selected time, samples were cooled under ambient conditions.

Elution of PEO from PLLA/PEO blends was carried out in phosphate buffered saline (PBS) at pH = 7.4 and 37 °C for up to 4 weeks. At the defined sampling times, specimens were briefly rinsed with water and dried at 30 °C and 60 mbar in a drying chamber.

2.2. Morphology

Macrophotographical imaging was performed using a BRESSER Analyth LCD Microscope with a Sony IMX335 CMOS camera sensor (Bresser GmbH, Rhede, Germany). SEM imaging of surface morphology and cross-sectional samples was performed with a SEM QUANTA FEG 250 (FEI Deutschland GmbH, Dreieich, Germany) operating in low vacuum with an accelerating voltage of 5 kV, using a secondary electron detector (LVD). For cross-sectional imaging using SEM, samples were cryo-fractured. For this, samples were flash-frozen with liquid nitrogen and manually fractured to avoid shear effects. The specimens were fixed onto aluminum trays with conductive carbon adhesive pads and the aluminum trays were mounted on custom 90° angle brackets to orient fracture edges toward the electron beam source.

2.3. Thermal analysis

Thermal properties of the PLLA/PEO blends were investigated using a DSC 1 star^e system (Mettler Toledo, Zurich, Switzerland) as reported by our group before [10]. Thermograms were analyzed with respect to glass transition ($T_{g,PLLA}$), crystallization temperature ($T_{c,PLLA}$), melting temperature ($T_{m,PLLA}$), and degree of crystallinity (χ_{PLLA}) of the PLLA component [23]. All results were averaged over $n = 5$ samples.

2.4. Mechanical analysis

Tensile tests were carried out using a uniaxial tensile test instrument zwickiLine Z 1.0 (Zwick/Roell, Ulm, Germany) equipped with a Canon EOS 80D for simultaneous video recording of deformation behavior. Therefore, 5B dog-bone shape specimens according to DIN EN ISO 527-2 [24] and were fabricated using custom-made injection molds. Measurements were carried out at room temperature under ambient conditions. For measurements of wet samples, specimens were stored for 7 days at 37 °C in phosphate buffered physiological saline solution (PBS) and taken out directly before the measurement. Tests were conducted with a 1 kN load cell and a crosshead speed of 5 mm/min. Tensile force as a function of elongation was measured. Based on these data, Young's modulus (E) was calculated in the linear elastic region (0.05–0.25 % strain) using the tangential method. Yield strain ($\varepsilon_{0.2\%}$) and yield stress ($\sigma_{0.2\%}$) were determined using the 0.2 % offset method, and intersections of the straight lines for $E_{0.2\%offset}$ with stress–strain curves of the blends were determined using Origin curve intersection minitool (OriginPro 2018b, OriginLab, Northampton, MA, USA). All results were averaged over $n = 5$ samples.

2.5. DMA experiments

Dynamic mechanical analysis and investigation of shape recovery behavior of PLLA and PLLA/PEO blends was performed using a DMA 850 test bench (TA Instruments Inc., New Castle, DE, USA). Determination of the parameters storage modulus E', loss modulus E'' and damping factor $tan\delta_{max}$ were carried out using a dual cantilever clamp. Glass transition T_{gO} was determined using the onset point from storage modulus curves. Examined temperature range was 0–120 °C with $q = 2$ K/min heating rate and an equilibration time of 10 min. Oscillation amplitude was 10 μm with $f = 1$ Hz and preconditioning was set to 0.1 N. Force-Track Function of TRIOS Software (TA Instruments Inc., New Castle, DE, USA) was activated to optimize static force depending on dynamic force and prevent form overstraining.

Shape retention and shape recovery experiments were carried out in single cantilever mode, with a sample size of 17.5 mm x 10 mm x 1 mm over $n = 3$ samples [25]. In a first step, the test chamber was heated to strain temperature $T_s = 70$ °C and the sample was equilibrated for 30 min before a force of 8.0 N was applied at a rate of 0.8 Nmin^{-1} in a second step. The samples were held at 8.0 N for 30 min before temperature was lowered to the fixing temperature $T_f = 15$ °C at 5 Kmin^{-1}. Samples were kept at T_f for 30 min. Afterwards, the force was released and held at 0 N (force control) for 5 min at 15 °C before the temperature was increased to 70 °C at 5 Kmin^{-1} with F set to 0 N. Lastly, samples were kept at 70 °C at $F = 0$ N for 90 min. Starting with the second step, the cycle was repeated twice. From displacement, force and temperature as function of time plots, displacement at strain values D_s were extracted at highest deformation at strain temperature T_s, recoil displacement values D_r were extracted as first value after the force was released at fixing temperature T_f, and recovery displacement values D_R were extracted as last value at the end of the cycle.

2.6. ATR-FTIR spectroscopy

ATR-FTIR measurements were performed using a Bruker Vertex 70 IR-Spectrometer (Bruker, Leipzig, Germany) equipped with a DLaTGS-detector. Data were collected in the range of $\tilde{\nu} = 600$ cm^{-1} to 4000 cm^{-1} with a resolution of $\tilde{\nu} = 4$ cm^{-1} averaged over 32 scans in reflection mode using a Graseby Golden Gate Diamond ATR-unit. All spectra were subsequently baseline corrected and atmospheric compensation was performed using Bruker OPUS software. Chemical mapping of the samples was carried out using a Bruker Hyperion II FTIR microscope (Bruker, Leipzig, Germany) with 14x8 measuring spots with 200 μm distance in x-x and y-y direction, giving 1.6 x 2.8 mm^2 area for each sample. The ratio of characteristic band area for PLLA ($\tilde{\nu}_{max} = 1753$ cm^{-1}, $\int\tilde{\nu} = 1920$–1620 cm^{-1}) and PEO ($\tilde{\nu}_{max} = 2877$ cm^{-1}, $\int\tilde{\nu} = 3030$–2730 cm^{-1}) was used for imaging.

2.7. Cell biological testing

For initial *in vitro* tests, the commercially available cell lines EA.hy926 (human-endothelial-derived cell line) and HT-1080 (human fibrosarcoma cell line) were used. Cell cultivation was carried out in an incubator Memmert ICO240med (Memmert GmbH, Schwabach, Germany) under simulated *in vivo* conditions at 5 % CO_2, 21 % O_2, and 37 °C. Tissue culture polystyrene (TCPS) served as a common surface for growth control (negative control NC). A positive control group (PC) was treated with a cytotoxic concentration of 10^{-4} M disulfiram/tetraethylthiuramdisulfide (TETD).

Cells were cultured in Modified Eagle's Medium (MEM) (with 2 mM L-glutamine and 1.5 g/L $NaHCO_3$) with 10 % fetal calf serum (FCS) and 1 % penicillin/streptomycin (all: PAN Biotech GmbH, Aidenbach, Germany) and harvested from the culture flask using trypsin. Pure PLLA (100/0) and PLLA/PEO 90/10 and 80/20 blend specimens as received after thermal annealing (0 d) and after PEO elution for 1 d, 7 d and 14 days were tested. Test samples (Ø 6 mm) were fabricated using injection molding using a 6 mm diameter mold and were disinfected using 70 % EtOH for 3 min. Samples were weighed down in the microwell plate using PTFE rings and directly seeded with cells at a density of 10 000 cells per 96 well (~29 500 cells/cm^2) in 200 μL of culture medium in five parallel wells for every material configuration, respectively. Three independent experiments have been conducted. Cultivation was carried out over 48 h without any medium changes. The metabolic activity of cells was determined via CellQuanti Blue Assay (BioAssay Systems, Biotrend Chemicals GmbH, Cologne, Germany) after 48 h (five wells per test in duplicates, $n = 3$) as described earlier [26]. For statistical analysis, Kruskal-Wallis test was conducted. Cell morphology was analyzed by fluorescence staining of cells using phalloidin (AlexaFluor™ 488) for actin filaments, as well as DAPI (NucBlue™ Fixed Cell ReadyProbes™) for cell nuclei (both: Invitrogen/Thermo Fisher, Dreieich, Germany) using one drop per one milliliter phosphate buffered saline (PBS), followed by 30 min incubation in the dark at room temperature. For imaging, an Olympus BX53M microscope (Olympus, Hamburg, Germany) was used.

Table 2
Parameters for fabrication of semi-finished tube products by melt extrusion.

m_{PLLA}/m_{PEO} [% w/w]	d_{nozzle} [mm]	$d_{mandrel}$ [mm]	$T_{extruder}$ [°C]	T_{nozzle} [°C]	N [min^{-1}]	v [cm/s]
100/0	2.2	1.77	190	165	2–5	0.145–0.5
90/10			185	170–175	2–7	0.15–1.0
80/20			185	170	4–8	2.0–3.0

d_{nozzle}: Diameter of the extrusion nozzle; $d_{mandrel}$: Diameter of the extrusion piercing mandrel; $T_{extruder}$: Temperature in the mixing chamber; T_{nozzle}: Temperature of the extruding nozzle; n: twin-screw rotation speed; v: Pull-off speed.

2.8. Contact angle measurements

Contact angle measurements of sessile drops were carried out using a DSA 25 – Drop Shape Analyzer (KRÜSS GmbH, Hamburg, Germany). Measurements were performed with 2 µL drop volume and 1.5 s equilibration time under constant conditions. Deionized water and diiodomethane (MeI_2) served as test liquids with different polarities to calculate the surface free energy according to the manufacturer's specifications, following Owens, Wendt, Rabel and Kaelble. Contact angles were determined for each sample ($n = 5$) by averaging the values of both drop sides. Surface free energy (SFE) as well as polar and dispersive components were calculated using Krüss' Advance software (V.1.13).

2.9. Stent prototyping

Polymer tube semi-finished products for stent prototyping were obtained by melt extrusion on a HAAKE MiniLab II co-rotating twin-screw extruder (Thermo Fisher Scientific, Karlsruhe, Germany) using the following parameters (Table 2):

For further processing, the polymer pipes were segmented and only partial sections with a suitable outer diameter and wall thickness were selected. The outer diameter d of the tube segments was determined using a ODAC 32XY Laser system (ZUMBACH Elektronik AG, Orpund, Schweiz) on manually cut ~30 mm tubes tightly mounted on a 1.4 mm mandrel at $n = 3$ measuring spots each and wall thickness t was calculated using the mandrel diameter. Geometric dimensions for the selected polymer tubes were $d_{100/0} = 1.76 \pm 0.06$ mm, $d_{90/10} = 1.81 \pm 0.06$ mm and $d_{80/20} = 1.80 \pm 0.10$ mm, and $d_{100/0} = 178.4 \pm 30.9$ µm, $t_{90/10} = 203.9 \pm 31.7$ µm and $t_{80/20} = 202.2 \pm 52.1$ µm. After removing the mandrel, the obtained polymer tubes were thermally annealed by placing the semi-finished products in a thermally equilibrated aluminum block with fitting cavities (PLLA: $T_A = 85$ °C; PLLA/PEO 90/10 and 80/20: $T_A = 80$ °C) for $t_A = 90$ min in the case of pure PLLA and $t_A = 15$ min in the case of PLLA/PEO 90/10 and 80/20. Subsequently, the tubes were mounted on Al_2O_3 mandrels ($d = 1.4$ mm) and stents were cut using an LP 1007 CO_2 laser system (Wild Emco Lasertec, Hallein, Austria) using a cut pattern as reported by our group before [27,28].

2.10. Stent testing

Stent prototypes were tested according to DIN EN ISO 25539-2 [29] regarding their expansion behavior (including elastic recoil) as well as their radial strength and radial stiffness. Stent prototypes were mounted on commercially available balloon catheters (Pantera 3.0 x 20 mm, BIOTRONIK AG, Bülach, Switzerland) and automatically expanded in a water bath (37 °C) using an automated laser scanning test setup [30]. Expansion was conducted stepwise with a pressure interval of $\Delta p = 1$ atm and a holding time of $t_{hold} = 15$ s up to a nominal pressure of $NP = 7$ atm to obtain a stent inner diameter of $d = 3$ mm. Outer stent diameter was measured after each expansion step over a length of $l = 10$ mm in steps of $\Delta l = 0.5$ mm. After 30 s at NP, the balloon was deflated and the outer stent diameter was measured again. Measurements were performed for $n = 12$ stent prototypes. The acute elastic recoil was determined from the diameter d at NP (p_{max}) and the diameter after balloon deflation (p_0) using Equation (1):

$$recoil\ [\%] = \frac{d(p_{max}) - d(p_0)}{d(p_{max})} \times 100 \quad (1)$$

For calculation of stent foreshortening (Δl) the stent length before (l_0) and after expansion to NP (l_1) were used according to Equation (2):

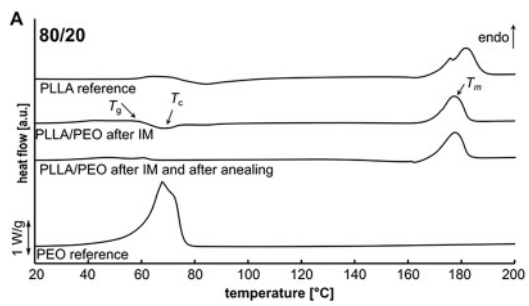
$$\Delta l\ [\%] = \frac{l_0 - l_1}{l_0} \times 100 \quad (2)$$

For investigation of radial strength and radial stiffness, a radial force test bench (J-Crimp, Blockwise Engineering LLL, Tempe, AZ, USA) equipped with a 100 lbf load cell and a segmented test head with $d_{max} = 16$ mm was used. Radial force measurements were performed at $T = 37$ °C and were started at test head diameter $d = 3.8$ mm. Test head diameter was decreased to $d = 2$ mm at 0.1 mm/s and subsequently increased to $d = 3.8$ mm at 0.1 mm/s. To compensate friction of the machine, a friction force curve of the test head without test specimen was recorded and subtracted from the measuring curves. The determination of radial strength and radial stiffness was performed according to ASTM F3067 [31] and Brandt-Wunderlich *et al.* [32]. Radial pressure is calculated as the radial force F_R divided by the instantaneous stent cylindrical area using Equation (3):

$$radial\,pressure\ \left[N/mm^2\right] = \frac{F_R}{\pi d l} \quad (3)$$

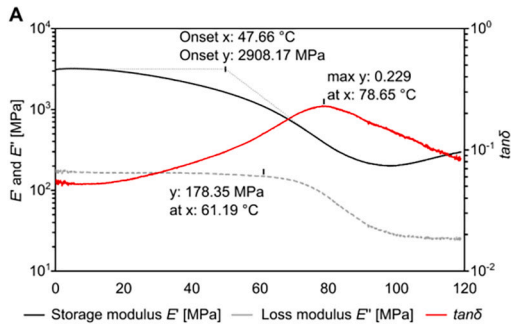
where d is the instantaneous stent diameter and l the initial stent length. Radial strength was determined by parallel shifting the unloading line, defined as steepest slope of the unloading curve, to the diameter representing 10 % of plastic deformation. The intercept with the radial pressure-diameter curve is the radial strength with respect to the predefined plastic deformation. However, if the peak load occurs prior the intercept, radial strength is the peak load itself. Radial stiffness is the slope of the loading line, which is defined as the steepest slope of the

Table 3
Exemplary DSC heating curves for PLLA/PEO 80:20 specimen after IM and thermal annealing and PLLA and PEO reference (A) and characteristic thermal parameters of PLLA (mean ± SD), glass transition T_g, melting temperature T_m and crystallinity χ in the blends after thermal annealing ($n = 5$ each).



m_{PLLA}/m_{PEO} [% w/w]	$T_{g,PLLA}$ [°C]	$T_{m,PLLA}$ [°C]	χ_{PLLA} [%]
100/0	65.2 ± 0.4	179.9 ± 0.2	51.9 ± 0.9
90/10	52.2 ± 0.9	178.1 ± 0.4	43.2 ± 1.4
85/15	55.0 ± 1.2	177.9 ± 0.6	40.4 ± 3.8
80/20	52.4 ± 1.1	178.8 ± 0.6	31.4 ± 3.8
75/25	53.3 ± 2.2	178.2 ± 0.4	27.5 ± 1.2
70/30	52.4 ± 0.8	178.2 ± 0.2	21.9 ± 2.7

Table 4
Representative DMA curves for PLLA/PEO (80:20) blend as obtained after IM and thermal annealing (A). Overview of thermo-mechanical parameters storage modulus E', loss modulus E'', damping factor $tan\delta_{max}$ and T_{gO} values of PLLA reference and PLLA/PEO blends ($n = 3$ each).



m_{PLLA}/m_{PEO} [% w/w]	E' [MPa]	E'' [MPa]	$tan\delta_{max}$	$T_{gO,PLLA}$ [°C]
100/0	6000 ± 900	680 ± 93	0.274 ± 0.005	70.1 ± 0.6
90/10	4000 ± 530	250 ± 15	0.249 ± 0.008	53.6 ± 2.3
85/15	3000 ± 280	180 ± 13	0.228 ± 0.003	50.5 ± 1.9
80/20	3700 ± 780	220 ± 34	0.232 ± 0.022	46.5 ± 0.9
75/25	2800 ± 350	180 ± 13	0.198 ± 0.035	39.6 ± 3.3
70/30	2900 ± 43	200 ± 10	0.214 ± 0.059	39.5 ± 5.5

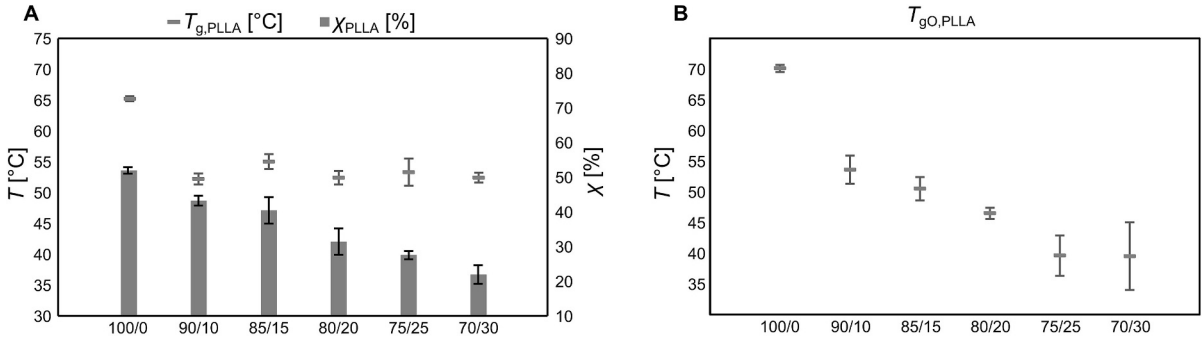


Fig. 1. Visualization of $T_{g,PLLA}$ and χ_{PLLA} of PLLA/PEO blends after IM and thermal annealing as obtained by DSC measurements (A) and $T_{gO,PLLA}$ values of PLLA/PEO blends after IM and thermal annealing as obtained by DMA (B, mean ± SD).

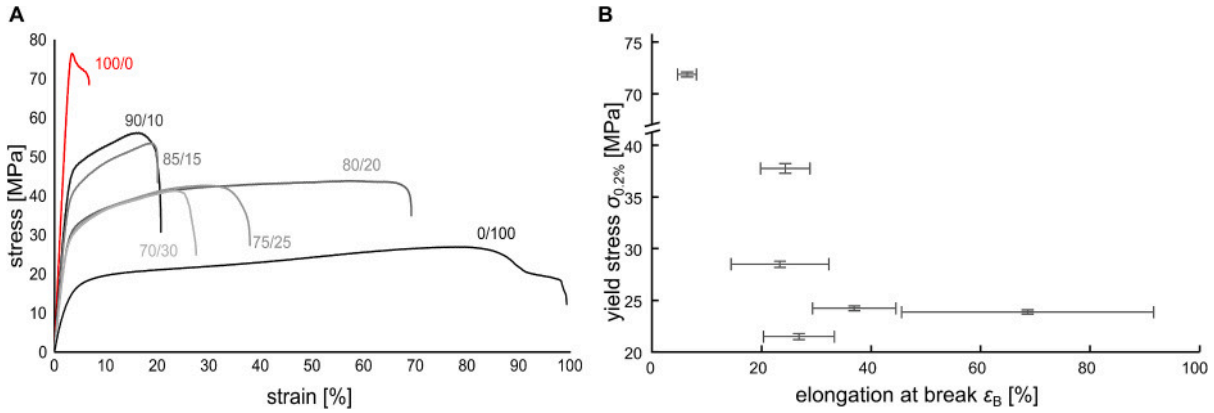


Fig. 2. Representative stress–strain curves for PLLA/PEO blends as obtained by uniaxial tensile testing measured in dry state under ambient conditions (A) and visualization of elongation at break (ε_B) versus yield stress ($\sigma_{0.2\%}$), calculated from stress-strain curves by 0.2 % offset method (B, $n = 5$ each).

initial linear part of the radial pressure-diameter curve. For determination of radial strength and radial stiffness, a custom made user software was used. Measurements were performed with $n = 5$ for each sampling group.

3. Results and discussion

3.1. General PLLA/PEO blend characterization

In summary, injection molding (IM) after melt blending resulted for all selected combinations in homogeneous appearing polymer specimens. After melt blending, DSC analysis was performed to investigate the influence of PEO as plasticizer on the thermal properties of the blends and to develop a thermal annealing (TA) protocol to eliminate the cold crystallization T_c of PLLA (Table 3) that occurred after the IM process. As reported in the literature, blending PLLA with PEO leads to a drastic decrease in $T_{g,PLLA}$, which is evident for the plasticizing effect of PEO [33,34]. Blending with already 10 % w/w PEO, led to a notable decrease in $T_{g,PLLA}$ down to ~ 52 °C, and increasing the PEO content had no further considerable effect (Table 3, Fig. 2). In addition, the crystallinity of PLLA was also strongly affected by blending, showing a decrease from $\chi_{PLLA} = 51.9$ % (100/0) down to $\chi_{PLLA} = 21.9$ % (70/30) after TA, indicating the interaction of PLLA and PEO at the molecular level. $T_{m,PLLA}$ was only slightly affected.

However, as $T_{g,PLLA}$ (between 52–65 °C, see Table 3) and $T_{m,PEO}$ (67.8 ± 0.5 °C) were overlapping, DSC data is only of limited

Table 5
Values for Young's modulus (E), yield stress ($\sigma_{0.2\%}$), yield strain ($\varepsilon_{0.2\%}$), tensile strength R_m and elongation at break ε_B for PLLA/PEO blends (mean ± SD, $n = 5$ each).

PLLA/PEO [% w/w]	E [MPa]	$\sigma_{0.2\%}$ [MPa]	$\varepsilon_{0.2\%}$ [%]	R_m [MPa]	ε_B [%]
100/0	2770 ± 75	72.96 ± 4.74	2.89 ± 0.24	77.6 ± 1.9	6.7 ± 1.8
90/10	1970 ± 44	38.48 ± 4.94	2.37 ± 0.48	54.9 ± 0.9	25.3 ± 4.7
85/15	1760 ± 74	28.83 ± 4.05	1.88 ± 0.31	53.2 ± 2.5	24.3 ± 9.3
80/20	1350, ± 42	24.00 ± 1.87	2.16 ± 0.21	42.6 ± 1.8	71.3 ± 23.9
75/25	1350 ± 28	24.39 ± 1.92	2.25 ± 0.25	41.7 ± 1.2	38.4 ± 7.9
70/30	1450 ± 37	21.54 ± 2.63	1.75 ± 0.30	43.1 ± 2.0	27.9 ± 6.7
0/100	690 ± 81	9.10 ± 1.99	1.81 ± 0.34	21.7 ± 4.8	200 ± 150

informative value regarding glass transition. For this reason, DMA was additionally carried out to determine onset glass transition values T_{gO} (Table 4).

A reduction in the PLLA content leads to a decrease in T_{gO}, favoring the properties of PEO with a T_{gO} far below $T_{g,PLLA}$ (Fig. 1). The homogeneity of the samples also decreases as the standard deviations of the measurements for T_{gO} increase with the reduction in PLLA content. A quantitative evaluation of the thermo-mechanical parameters is only feasible to a limited extent, as the variability in the samples investigated precludes the formulation of precise assertions. Notably, while the total values of E' and E'' are discernible, there is minimal variation observed for $tan\delta_{max}$ (Table 4). Therefore DMA experiments show a reduction in T_{gO} with higher PEO content and slightly reduced damping behavior due to the differences in the E''/E' relation. In particular, the differentiation in T_{gO} progression cannot be observed for PLLA contents under 85 % in DSC thermograms.

Following this, mechanical testing was performed for annealed specimens. For an initial material characterization, uniaxial tensile tests were carried out in ambient air, well knowing that aqueous media or body fluids have a considerable influence on the material's mechanical performance. The strain rate was chosen to be in the relevant range for stent expansion, which represents the most critical mechanical load situation, approximated to be 5 mm/min. Stress–strain curves for PLLA/PEO blends and visualization of values for yield stress ($\sigma_{0.2\%}$) extracted from stress-strain curves using 0.2 % offset method and strain at break (ε_B) are shown in Fig. 2. Pure PLLA showed low plastic deformation capability. As reported in the literature, PEO acts as plasticizer, leading

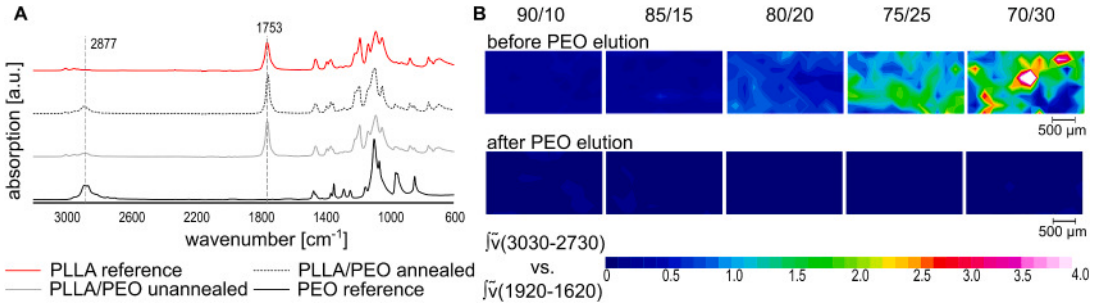
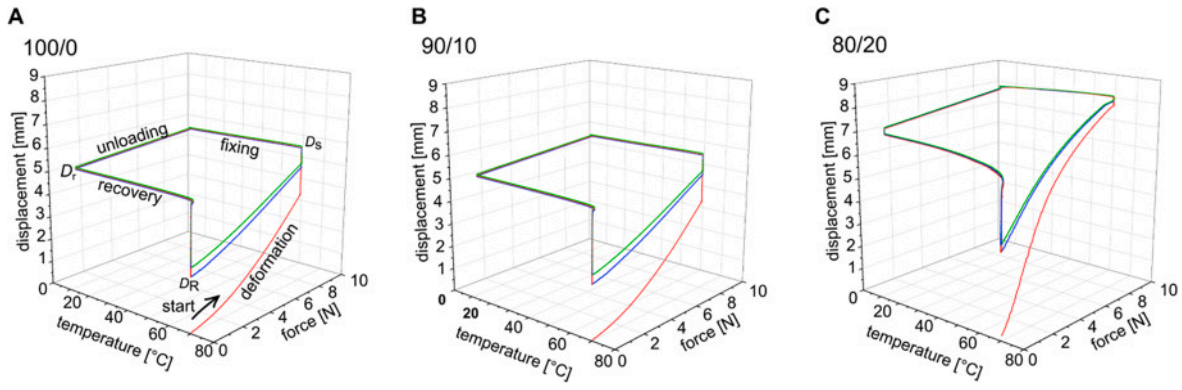


Fig. 3. Exemplary FTIR spectra of PLLA/PEO 80/20 blend before and after thermal annealing compared to pure PLLA and pure PEO (A). Characteristic bands for PLLA ($\tilde{\nu} = 1753\ cm^{-1}$) and PEO ($\tilde{\nu} = 2877\ cm^{-1}$) are indicated. Chemical mapping of PLLA and PEO phases in the blends as obtained by IM after thermal annealing acquired by ATR-FTIR-microscopy at 118 measuring points (B). False-color mapping shows ratio of band areas of $\tilde{\nu} = 3030–2730\ cm^{-1}$ versus $\tilde{\nu} = 1920–1620\ cm^{-1}$. In addition, chemical mapping of PLLA/PEO blends after elution of PEO is shown.

Table 6
Representative 3D plots of shape retention and shape recovery experiments obtained by DMA for PLLA (A: 100/0) and PLLA/PEO blends (B: 90/10 and C: 80/20) for three cycles. Colors are indicative for cycle 1 (red), cycle 2 (blue) and cycle 3 (green), and related characteristic values (mean ± SD) displacement under load D_s, recoil displacement D_r, recovery displacement D_R, shape retention rate $R_f = D_r \times 100/Ds$, shape recovery rate $R_r = (D_r\text{-}D_R) \times 100/D_s$ and recovery distance $\Delta D = D_r – D_R$ with $n = 3$ each.



PLLA/PEO [% w/w]	D_S [mm]	D_r [mm]	D_R [mm]	$R_{f,1.cycle}$ [%]	$R_{r,1.cycle}$ [%]	ΔD [mm]
100/0	6.23 ± 0.29	5.53 ± 0.18	2.39 ± 0.17	88.85 ± 2.09	50.59 ± 2.15	3.15 ± 0.01
90/10	7.90 ± 0.05	7.12 ± 0.07	2.88 ± 0.09	90.03 ± 0.56	53.66 ± 0.49	4.24 ± 0.04
80/20	8.35 ± 0.09	7.32 ± 0.08	3.61 ± 0.06	87.76 ± 0.12	44.52 ± 0.48	3.72 ± 0.06

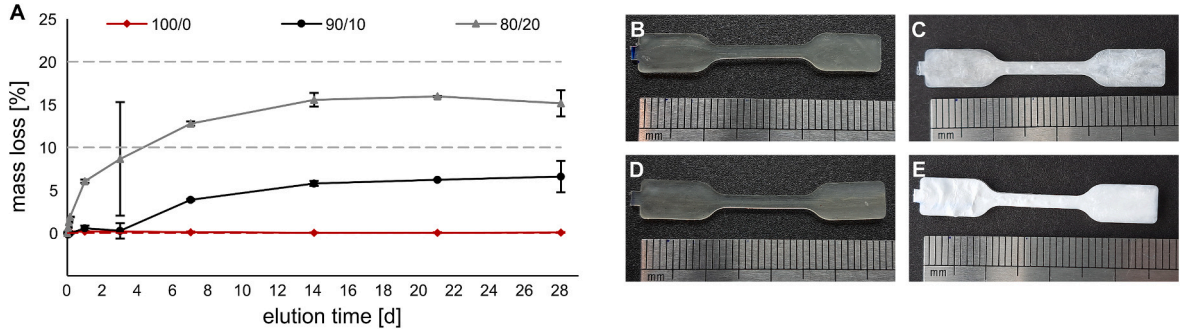


Fig. 4. Mass loss progression of PLLA/PEO (90/10 and 80/20) blend specimens compared to pure PLLA after immersion in PBS for up to 4 weeks (A, mean ± SD) and macrographs of PLLA/PEO 90/10 (B, C) and 80/20 (D, E) dog-bone specimens before (B, D) and after (C, E) elution of PEO for 4 weeks.

to a drastic increase in plastic deformability of the material [19]. Strain at break increased to a maximum of 70 % for PLLA/PEO 80/20, however, the addition of higher PEO content lead to a decrease in ε_B, indicating phase separation.

For all blends, a decrease in yield point was observed from $\sigma_{0.2\%}$ = 73.0 ± 4.7 MPa (100/0) down to 21.5 ± 2.6 MPa (70/30), see Table 5. Elongation at break (ε_B) increased with increasing PEO content up to 80/20 % w/w, and drastically decreased upon the addition of higher amounts of PEO, leading to the conclusion that saturation and thus phase separation occurred, weakening the material.

For a deeper insight of polymer distribution in the blends, chemical mapping using FTIR microscopy was performed (Fig. 3A). The value of the quotient of the areas of the wavelength ranges of characteristic PEO ($\tilde{\nu}$ = 3030–2730 cm^{-1}) and PLLA ($\tilde{\nu}$ = 1920–1620 cm^{-1}) bands was calculated (Fig. 3 B). For 90/10 and 85/15, PEO appeared to be homogeneously distributed in the PLLA matrix ($\frac{\int_{3030-2730}}{\int_{1920-1620}} < 1$, blue areas). With increasing PEO content in the blend, the occurrence of PEO rich regions increases, indicating clear phase separation (red to white areas) for 70/30 ($\frac{\int_{3030-2730}}{\int_{1920-1620}} > 4$). After incubation for 7 days in PBS (see also section 3.2), no residual PEO could be observed on the surface for all samples ($\frac{\int_{3030-2730}}{\int_{1920-1620}} < 0.5$).

Based on the chemical mapping and the mechanical data, PLLA/PEO 90/10 and 80/20 were selected for further testing, as for 75/25 and 70/30 pronounced phase separation was observed in FTIR, and 90/10 showed the lowest decrease in $\sigma_{0.2\%}$ and 80/20 resulted in the highest elongation at break of the blend combinations tested.

PLLA and its blends, including PEO as a blend partner, are known to exhibit shape memory (SM) behavior [33,35–37]. This may be beneficial for stent applications, as catheter size could be reduced by exploiting (particularly) self-deployment of the stent [38]. However, in the case of PLLA/PEO blends, shape recovery behavior requires heating above a transition temperature, in this case T_g. As glass transition of the blend is above body temperature, the shape recovery behavior cannot be exploited directly during the implantation process. If T_g of the polymer is below body temperature, the material would remain in a rubbery state and may undergo creep, potentially leading to critical device failure. However, the shape recovery effect can be leveraged in that a stent, pre-programmed with its expanded (permanent) shape, will be crimped into a smaller temporary shape above T_g for catheter-based delivery. This would lower the forces required during crimping, facilitating implantation and deployment, reducing strut failure risk and enable shape adaptation to the tapered shape of the ET [38].

DMA single cantilever experiments [25] revealed that PLLA as well as the two blends 90/10 and 80/20 showed good shape retention R_f (Table 6) in the range from 87.76 ± 0.12 % (80/20) to 90.03 ± 0.56 % (90/10). Shape recovery R_r for the two blends was also in a comparable range to that of pure PLLA (R_r = 44.52 ± 0.48 % for 80/20 up to R_r = 53.66 ± 0.49 % for 90/10). Due to the overall higher plasticity, the blends exhibited overall higher displacement under load D_S, and the recovery distance ΔD was also considerably higher for both blends compared to pure PLLA ($\Delta D_{100/0}$ = 3.15 ± 0.01 mm versus $\Delta D_{90/10}$ = 4.24 ± 0.04 mm and $\Delta D_{80/20}$ = 3.72 ± 0.06 mm).

3.2. Elution of PEO component

In the following, the effect of PEO elution on the material properties was investigated (Fig. 4, A). Specimens of PLLA/PEO 90/10 % w/w and 80/20 % w/w were incubated in PBS for up to 28 days and the mass loss was determined. Pure PLLA (100/0) served as reference. In general, PEO dissolves very well in water, but the rate of dissolution is strongly dependent on the molecular weight, with high molecular weight PEO dissolving considerably slower [39,40]. After 14 days of incubation and PEO elution, the samples turned highly opaque. A plateau in mass loss

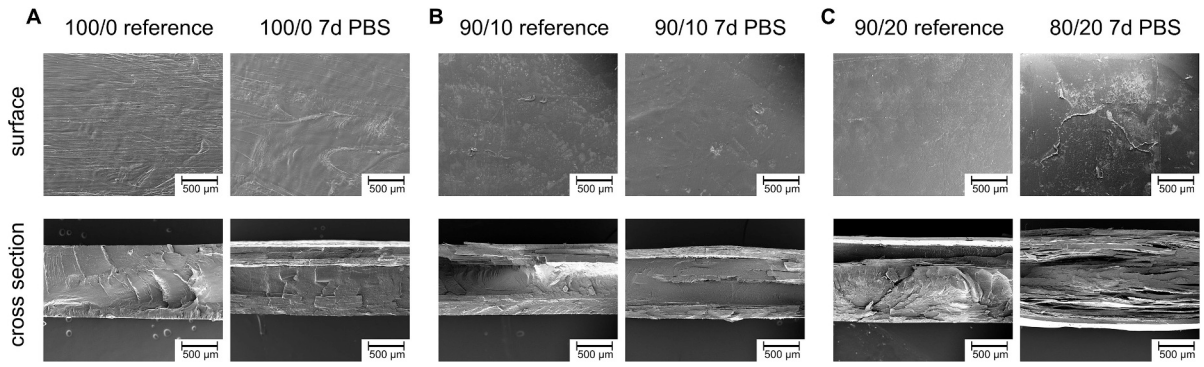


Fig. 5. Cross-section SEM images of PLLA (A: 100/0) and PLLA/PEO (B: 90/10 and C: 80/20) specimens as obtained by IM and after thermal annealing and after elution of PEO for 7 days.

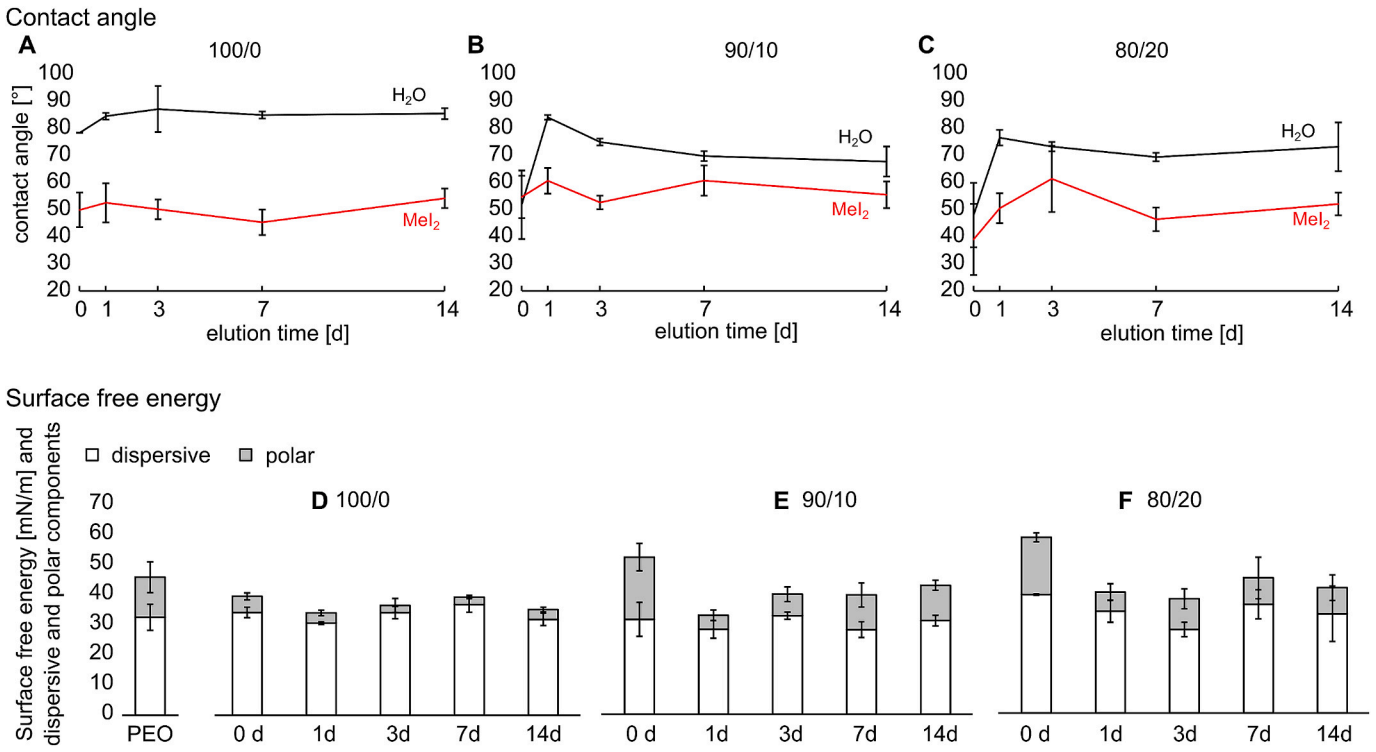


Fig. 6. Visualization of water contact angle and MeI_2 contact angle of PLLA (A: 100/0) and PLLA/PEO (B: 90/10 and C: 80/20) blends as obtained by IM after thermal annealing and after PEO elution for up to 14 days and surface free energy (SFE) values and visualization of polar and dispersive components of SFE (D – F, mean ± SD).

was reached for both combinations, which in both cases was below the theoretical amount of PEO in the blend. This is most likely due to the integration of PEO into the PLLA matrix, preventing the residual PEO from elution out of the bulk. Still, the integrity of the samples was maintained. As the major part of the PEO had already dissolved from the samples after 7 days, this time was chosen as the end point of PEO elution for further tests.

SEM imaging was performed for assessing blend morphology (Fig. 5). For the selected blend combinations (90/10 and 80/20), SEM revealed a uniform and homogeneous surface morphology after IM as well as thermal annealing. In addition, cross-sectional SEM imaging was performed. To minimize shear stress of the samples, which may affect sample morphology at the edge, cryo-fracturing was carried out rather than cutting. Again, a uniform morphology was observed. After PEO elution, however, a laminar structure accompanied by the formation of cavities became visible for both blends, but more pronounced for 80/20, whereas no notable changes in pure PLLA were observable.

To assess the extent to which the addition and elution of 10 and 20 % w/w PEO lead to changes in surface polarity, contact angle measurements were performed (Fig. 6). In line with the literature [20], the addition of PEO led to an enhanced wettability of the surface, as observable by the reduced water contact angles. Contact angles of MeI_2, however, were unaffected by blending with PEO.

After PEO elution, an increase in water contact angle was observed, which remained below the values for pure PLLA reference. This may be due to minimal changes in surface morphology, leading to increased wettability. The surface free energy showed a strong increase of the polar component before elution with respect to pure PLLA, comparable to the SFE components of pure PEO. After PEO elution, the polar component decreased, but was still higher as for PLLA. Dispersive component of the blends were unaffected.

Regarding the mechanical properties of both of the blends after PEO

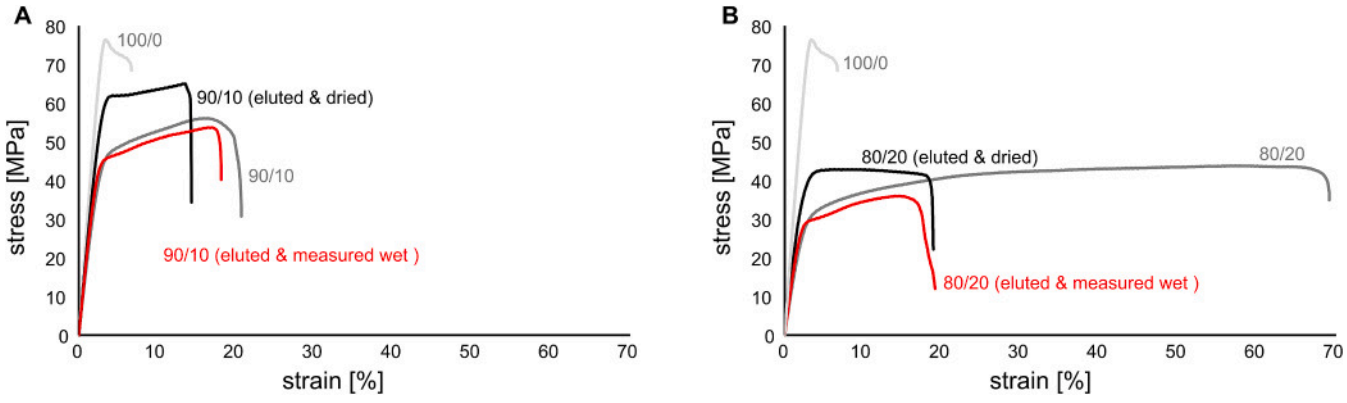


Fig. 7. Exemplary stress–strain curves of PLLA (100/0) and PLLA/PEO (A: 90/10 and B: 80/20) after PEO elution measured in dry state under ambient conditions and directly after incubation in phys. saline solution for 7 days without drying compared to the material as obtained by IM after thermal annealing and pure PLLA.

Table 7
Characteristic thermal parameters of PLLA (mean ± SD), glass transition Tg, melting temperature Tm and crystallinity χ in the selected blends after thermal annealing and PEO elution in PBS for 7 days (n = 5 each).

	$T_{g,PLLA}$ [°C]	$T_{m,PLLA}$ [°C]	χ_{PLLA} [%]
100/0	68.2 ± 2.5	181.4 ± 0.2	50.7 ± 0.7
90/10	61.7 ± 0.3	179.3 ± 0.9	50.9 ± 6.4
80/20	49.1 ± 4.5	179.9 ± 1.4	52.3 ± 1.7

Table 8
Mechanical properties (Young's modulus E, yield stress $\sigma_{0.2\%}$, elongation at break ε_B, and tensile strength R_m, mean ± SD) of PLLA (100/0) and PLLA/PEO (90/10 and 80/20) after IM and thermal annealing and after elution of PEO as obtained by uniaxial tensile testing measured in dry state under ambient conditions (eluted & dry) and directly after incubation in physiological saline solution for 7 days (eluted & wet).

		E [MPa]	$\sigma_{0.2\%}$ [MPa]	ε_B [%]	R_m [MPa]
100/0	dry	2770 ± 75	72.9 ± 4.7	6.7 ± 1.8	77.6 ± 1.9
	eluted & dry	2732 ± 137	68.9 ± 2.6	5.9 ± 1.7	78.9 ± 2.8
	eluted & wet	2719 ± 81	62.1 ± 5.7	9.8 ± 1.3	70.4 ± 3.5
90/10	dry	1968 ± 44	38.5 ± 4.9	25.3 ± 4.8	55.0 ± 1.0
	eluted & dry	2286 ± 46	52.1 ± 1.9	15.3 ± 3.1	62.7 ± 2.2
	eluted & wet	2020 ± 39	40.9 ± 1.0	17.9 ± 5.8	50.2 ± 3.7
80/20	dry	1352 ± 42	24.0 ± 1.9	71.3 ± 24.0	42.6 ± 1.8
	eluted & dry	1803 ± 105	32.8 ± 3.6	17.7 ± 1.6	42.9 ± 4.5
	eluted & wet	1544 ± 54	27.6 ± 1.0	22.9 ± 7.4	37.0 ± 2.1

elution, an increase in E and $\sigma_{0.2\%}$ was observed when measured in dry state (Fig. 1, Fig. 7). For 90/10 and 80/20, ε_B remained higher compared to pure PLLA after PEO elution.

For 80/20, a strong decrease in ε_B was observed after PEO elution, approximating the values for 90/10. Notably, even after PEO elution, a pronounced plastic deformability was found for both blends in contrast to pure PLLA (Table 8).

To reproduce the *in vivo* conditions, the samples were further tested in wet state directly after being removed from the medium in order to consider the effect of water in the polymer bulk. When measured wet, compared to the experiments with dry specimens stored in physiological saline for 7 days, both blends as well pure PLLA showed a drop in $\sigma_{0.2\%}$. Elongation at break for pure PLLA measured in wet state was 9.8 ± 1.3 %, which was considerably higher as for the dry samples. Both blends exhibited a generally higher elongation at break compared to PLLA 100/0, being $\varepsilon_{B,90/10}$ = 17.9 ± 5.8 % and $\varepsilon_{B,80/20}$ = 22.9 ± 7.4 %. These results are in line with gravimetric PEO elution experiments (Fig. 4), indicating residual PEO in the PLLA matrix acting as plasticizer. The tensile strength of the blends was reduced and for 80/20 was only about 50 % of the values of pure PLLA, which in turn can lead to a lower load-bearing capacity of this material when used for implants.

PEO elution led to an increase in crystallinity (data before/after PEO elution: $\chi_{90/10}$ = 43.2 ± 1.4/50.9 ± 6.4 % and $\chi_{80/20}$ = 31.4 ± 3.8/52.3 ± 1.7 %, see also Table 7), approaching the values for pure PLLA (χ_{PLLA} = 51.9 ± 0.09 % before incubation in PBS, see also Table 3). Incubation of pure PLLA in PBS as reference did not lead to pronounced changes in thermal properties. This also supports the increase in tensile strength, and the reduction in yield strength and elongation at break, which results in the material approaching the properties of pure PLLA again.

3.3. In vitro biocompatibility

Biocompatibility of pure PLLA (100/0) as well as PLLA/PEO 90/10 and 80/20 blend specimens as received after thermal annealing and after PEO elution for up to 14 days was analyzed according DIN EN ISO 10993-5 [41]. If the viability is reduced to <70 % of the control group (here NC), the test item has a cytotoxic potential. Established fibroblast (HT-1080) and endothelial (EA.hy926) cell lines were used for a first assessment of cytotoxicity as recommended in the ISO standard [41], knowing that functional evaluation of the Eustachian tube stent will need to be continued in future studies using primary epithelial cells. Statistical analysis was carried out specifically for selected groups. In particular pure PLLA (100/0) was compared to the negative control (TCPS) and further to all samples eluted for 7 d in PBS, which were also compared with each other, respectively (Fig. 9), as biocompatibility was restored at this time point. Overall, no significant differences were verified, indicating no cytotoxicity after PEO elution.

PLLA is generally considered biocompatible, nevertheless its cytotoxicity is influenced by various factors, including synthesis methods, concentration and surface modifications [42]. Yet, PLLA is known for its moderate hydrophilicity that might result in limited cell adhesion and low hydraulic permeability [43]. In accordance to the literature, PLLA values for water contact angle (78.4 ± 0.11°, Fig. 6) are in a medium range, if 90° is taken as the limit between hydrophilic and hydrophobic [44]. However, modifying the surface to be hydrophilic does not necessarily increase biocompatibility. In fact, Szustakiewicz *et al.* showed that reducing the water contact angle to 35° by UV irradiation resulted in a significant reduction in cell viability and morphological changes in the seeded fibroblasts [44].

Biocompatibility tests were carried out to determine how the processing of the material, the PLLA/PEO ratio and the PEO elution over different time periods would affect the viability of the cells. In our study, changes in contact angle and SFE showed only slight variations over time and does not appear to be the decisive factor for the decrease in cell viability especially for the pure PLLA. Contact angles of the blend specimens were overall slightly lower than on pure PLLA, and PEO incorporation led to a higher polar component of SFE. As reported by Bauer *et al.*, a concentration-, time- and molar mass-dependent effect on cell viability was observed for fibroblasts on PEG and PEO samples, with values for PEG decreasing with PEG M_n and longer cultivation time [45]. Within the study of Goonoo *et al.*, fibroblast morphology on PLLA/PEG blends showed appropriate adherence, growth and migration *in vitro* [46]. In addition, cell confluence was distinctly decreased with small molar mass of PEO with simultaneously altered cell morphology. HMW PEO (200 000 g/mol) has been shown to maintain cytocompatibility, especially when incorporated into formulations, e.g. hyaluronic acid nanofibers [47]. Pure PEO (200 000 g/mol) showed only low cytotoxic effects compared to PEO/starch blends in varying ratios [48]. Lower molecular weight PEO (e.g. 100 000 g/mol and below) may exhibit different cytotoxic effects. Research suggests that lower molecular weights could lead to increased cytotoxicity under certain conditions, particularly when subjected to thermal treatment [49]. However, the lack of established guidelines complicates the characterization of PEO's safety across different molecular weights and formulations [50]. No comparable biocompatibility results were found in the literature for the HMW PEO (400 000 g/mol) used in this study. Notably, within our study, a high viscosity of cell culture medium was noticed for PLLA/PEO blend specimens when given into cell culture medium for all samples until 7 d of PEO elution (Fig. 8), which is expected to be responsible for influencing cell behavior.

The impact of high viscosity environments on cell viability, in turn, is a complex interplay influenced by various factors, including mechanical properties, cellular responses, and the specific type of cells involved. The viscosity of the medium can influence various cellular processes, including proliferation and viability. In some cases, high viscosity has been associated with reduced cell lengths and mobility, potentially

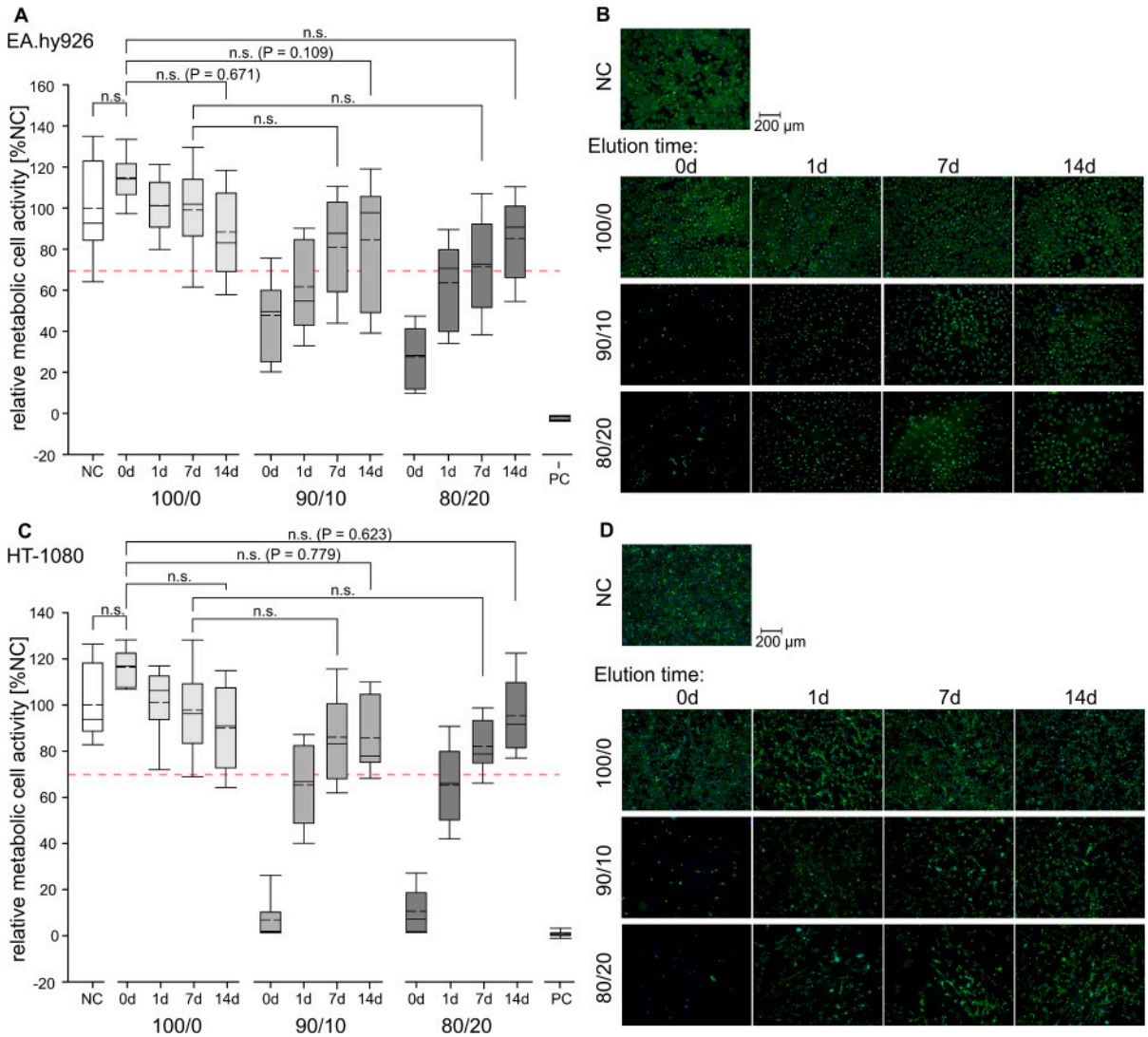


Fig. 8. Relative metabolic cell activity of endothelial cells (A, EA.hy926) and fibroblasts (C, HT-1080) seeded on pure PLLA (100/0) and PLLA/PEO 90/10 and 80/20 blend specimens as received after thermal annealing and after PEO elution for up to 14 days. Shown is the cell colonization after 48 h in direct contact on pure PLLA (100/0) and PLLA/PEO 90/10 and 80/20, after 0d, 1d, 7d, and 14d elution of PEO in PBS, respectively. Boxes denote interquartile ranges, horizontal continuous lines within the boxes denote medians, dotted lines denote mean values, and whiskers denote minimum and maximum values. Data are related to negative control (NC) as 100 %. Red dashed line indicates 70 % biocompatibility threshold according to DIN EN ISO 10993–5. The tests were conducted with $n = 3$ replicates, each with five parallel wells. For statistical analysis, Kruskal-Wallis test was conducted. Fluorescence microscopy images of endothelial cells (B, EA.hy926) and fibroblasts (D,: HT-1080) seeded on pure PLLA (100/0) and PLLA/PEO 90/10 and 80/20 blend specimens as received after thermal annealing and after PEO elution for up to 14 days stained with phalloidin and DAPI (green = actin filaments, blue = cell nuclei), magnification: 10x, scale bar: 200 µm.

leading to decreased overall viability if the mechanical environment becomes too restrictive [51]. While certain high-viscosity environments may promote migration and adaptation, they can also induce stress responses, affecting cell viability negatively. For example, increased mechanical loading can lead to cellular stress responses that might compromise long-term viability if not balanced by supportive environmental factors [52]. However, *in vivo* data of blends of PLLA and HMW PEO implanted in rat tibia for up to 16 weeks, showed a comparable biocompatibility to that of PLLA [18]. In our *in vitro* experiments, we observed an increase in metabolic cell viability over time due to PEO elution by PBS, showing a comparable biocompatibility of pure PLLA after 7 d of PEO elution. Exemplary fluorescence images of endothelial cells (EA.hy926) and fibroblasts (HT-1080) on the test samples confirmed cell viability results, showing a time-dependent restoration of a nearly confluent cell layer and typical cell morphology on the PLLA/PEO blend specimens, which was stable on the pure PLLA specimens. Thereby, no distinct differences were obvious between the 90/10 and 80/20 blend specimens.

However, it should be noted that while HT-1080 is commonly used in ISO 10993–5 standardized cytotoxicity testing, it is a fibrosarcoma-derived cell line and known for its high resilience to stress. This may limit its sensitivity in detecting subtle cytotoxic effects. In addition, although the ISO threshold is set to 70 % relative cell viability, values below 80 % indicate the need for further evaluation, particularly using more sensitive primary cell models.

3.4. Stent prototyping and testing

Stents were fabricated using a slotted-tube design. Apart from the formation of distinct heat-affected zones due to CO_2 laser cutting (Fig. 9), no macroscopic changes or differences were observed in the manufactured stent prototypes for pure PLLA (100/0) and the two blends. However, the 100/0 stents could not be expanded. Due to the low plastic deformability and brittleness of pure PLLA after thermal

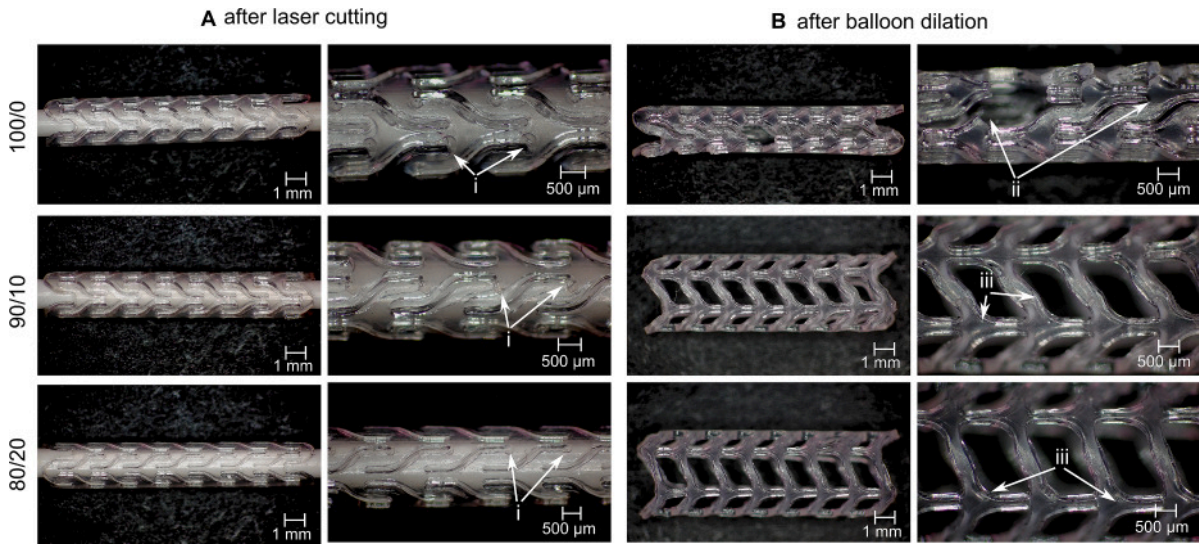


Fig. 9. Macrographs of PLLA (100/0) and PLLA/PEO (90/10 and 80/20) stent prototypes after CO_2 laser cutting mounted on Al_2O_3 mandrels (A). The heat-affected zone is indicated (i). Macrographs of PLLA (100/0) and PLLA/PEO (90/10 and 80/20) stent prototypes after thermal annealing and balloon dilation (B). For pure PLLA (100/0), the stent could not be expanded and strut fractures were observed (ii). For PLLA/PEO (90/10 and 80/20), crazing was observed (iii), but expansion was successful without strut fracturing.

annealing, strut fracturing was observed below nominal pressure (Fig. 10). This is in contrast to earlier results for this stent design made of pure PLLA [27,53].

Partially, this may be due to the differences in the manufacturing process. While thermally extruded semi-finished products served as the basis in this study, the tubes in the earlier study were produced using a solvent-based dip-coating process. The different manufacturing processes affect the molecular weight and the orientation of the molecular chains and thus influence the mechanical properties of the material and the ability of stents to be expanded without fracture. Expansion speed can also influence strut fracturing. In the aforementioned earlier studies, stents from PLLA and PLLA/P(4HB) were expanded at 1 bar/min and 3 bar/min, respectively. In the current study, all stents were expanded with 3 bar/min. In contrast to pure PLLA, stents fabricated from the two blend combinations could be fully expanded at the set expansion rate without strut fracturing. The stents made of both blend materials began to open at 1 atm balloon pressure, and the target diameter was almost reached at 5 atm balloon pressure. At higher balloon pressure, only a slight increase in diameter was observed.

The acute recoil after dilation was 4.0 ± 0.6 % (90/10) and 4.2 ± 0.8 % (80/20) and is thus comparable to, or even slightly lower than that measured for commercially available coronary biodegradable stents [54]. Low elastic recoil is considered beneficial, as it allows safe fixation of the stent and optimal luminal patency. The change in length due to expansion was −5.6 ± 1.5 % (90/10) and −5.4 ± 1.6 % (80/20), respectively. Small length change is usually beneficial as it enables safe delivery and precise placement of the stent. Stents fabricated from PLLA/PEO 90/10 and 80/20 were subsequently tested regarding their radial strength and radial stiffness. To assess the effect of PEO elution, the experiments were performed with specimens which were eluted after balloon dilation in order to remove the PEO component from the stent material, as well as with stents without elution. Based on ASTM F3067, a minimum diameter of 2 mm was chosen for stent testing [31].

After elution of the PEO component from the stent following dilation (Fig. 11 A), the stents turned highly opaque, comparable to the injection molded samples (Fig. 4). Also, in the SEM images (Fig. 11 B), non-continuous cracks can be seen for the stents tested before PEO elution, but the struts remaining intact and still maintaining load-bearing capacity after applying radial force. Furthermore, the SEM images revealed a spatially limited thermal laser influence zone due to the CO_2 laser cutting process.

After expansion and PEO elution, the surface of the expanded stents shows superficial fissures which are likely to derive from the PEO component, but remained otherwise intact. Material embrittlement, and probably also the observed formation of a laminar structure and cavities after PEO elution (Fig. 11) led to strut fractures after initial load bearing capacity at a plastic deformation of approx. 15–20 % during radial force testing. The strut failure revealed in the macrographs is also evident in the radial force testing diagrams (Fig. 12A, B).

Stenting the Eustachian tube in a large animal model was successfully performed using cobalt-chromium alloy stents, as well as polymer stents [4,16]. However, as no data on the mechanical properties of Eustachian tube stents are currently published and no polymer-based biodegradable stent dedicated to the treatment of Eustachian tube dysfunction is commercially available, numerical data for radial strength and stiffness of clinically relevant polymer stents for coronary application are taken from Qiu *et al.* [55] as a reference in order to assess the suitability of PLLA/PEO blends in combination with the selected slotted-tube stent design for application in ETD treatment (Table 9). Radial strength, which describes the ability of the stent to withstand external radial forces, was determined by parallel shifting the unloading line to the diameter representing 10 % of plastic deformation to obtain values comparable to those in the literature for established BRS designs [55]. Regarding radial strength, data for the PLLA/PEO stent prototypes before PEO elution were slightly lower compared to the Absorb, Elixir and RevaMedical stents. However, the initially more ductile state of PLLA/PEO may allow for safe implantation and high conformation with the non-circular cross-section and tapered geometry of the ET, whereas the self-curing may improve scaffolding properties and prevent stent malapposition or migration. Elution of PEO led to post-curing of the stent material, evident in an increase in radial strength for both blends by a factor of 1.5 (90/10) and 1.4 (80/20), leading to higher values than those for the Absorb and the Elixir stents. The radial stiffness of both PLLA/PEO blends before PEO elution was in a comparable range to the reference data (Table 9). Elution of PEO, however, did lead to a pronounced increase in radial stiffness. This indicates that the stent undergoes structural stiffening, enabling increased scaffolding capability to keep the ET open after PEO elution by the surrounding medium.

It is worth mentioning that there is no specific threshold value for radial stent deformation in the literature or in standards. Normally, a stent should be able to withstand the physiological loads exerted by the vessel or hollow organ. For ETD treatment, a stent would be typically

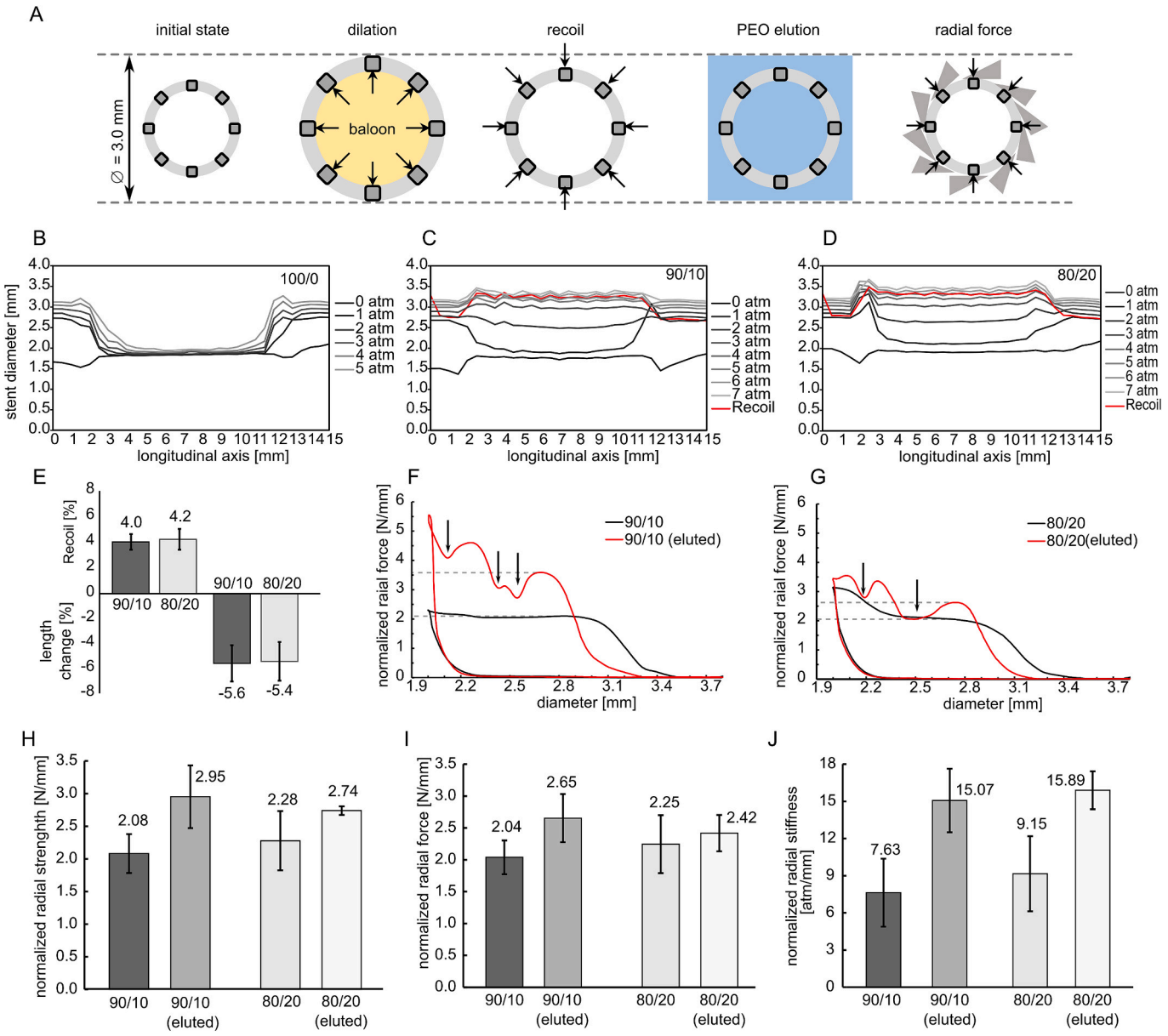


Fig. 10. Schematic of the general stent testing procedure (A). Determined elastic recoil and length change due to expansion (B, mean ± SD) of 90/10 and 80/20 stents. Representative stent diameter per balloon pressure curves for the expansion of PLLA (C), PLLA/PEO 90/10 (D) and 80/20 (E) stent prototypes.

positioned in the cartilaginous part of the ET at some distance from the pharyngeal opening, allowing ventilation but avoiding permanent opening while preserving the valve mechanism for natural opening of the tube during swallowing and yawning [5,16]. Thus, a certain degree of rigidity of the stent is therefore desirable in order to ensure patency of the ET. The external loading of the stent results from the passive closure of the tube, which is caused by an adjacent vascular plexus, the Ostmann fat pad and the cartilage of the tube, which closes the ET in a spring-like mechanism. The PLLA/PEO stents presented were able to withstand complete radial deformation of up to 1 mm (33 %) before PEO elution without stent failure. To evaluate the stents after PEO elution, the diameters for radial deformation at stent failure were measured at the site of the first force drop (Fig. 12) and averaged for 5 stents. Self-curing of the stent material was accompanied by strut fracture during radial force testing, however, after PEO elution the stents were able to withstand a radial deformation of up to 12.1 ± 0.6 % (0.37 ± 0.02 mm, 90/10) and 11.6 ± 1.4 % (0.34 ± 0.04 mm, 80/20) without strut failure. The data are comparable, even between the two groups, as exhibited by the small standard deviation. Yet, even after strut failure, the stents maintained load-bearing capacity. These results present an initial evaluation of the self- or post-curing material concept and form the basis for further investigations, in particular on creep behavior as well as long-term recoil after implantation in the cartilage area of the ET.

Future studies will also need to assess stent behavior in preclinical setups, accounting for the natural repeated or cyclic diameter changes and asymmetric loading conditions in the ET over the entire stent life cycle. The degradation behavior of BRS in ET differs from that of cardiovascular stents, as the mucus in ET has a different composition compared to blood (e.g. reported value for pH = 7.24 [56], different viscosity ranging from viscous to serous [57]. These characteristics can, however, vary considerably depending on the pathology). The exact mechanisms of stent degradation, transport of degradation products and fragments are not yet fully understood, especially for polymer-based BRS. Since the ET is directly connected to the pharynx, we assume that most of the degradation products are easily transported by mucus drainage and probably swallowed by the patient. Since PLLA and PEO

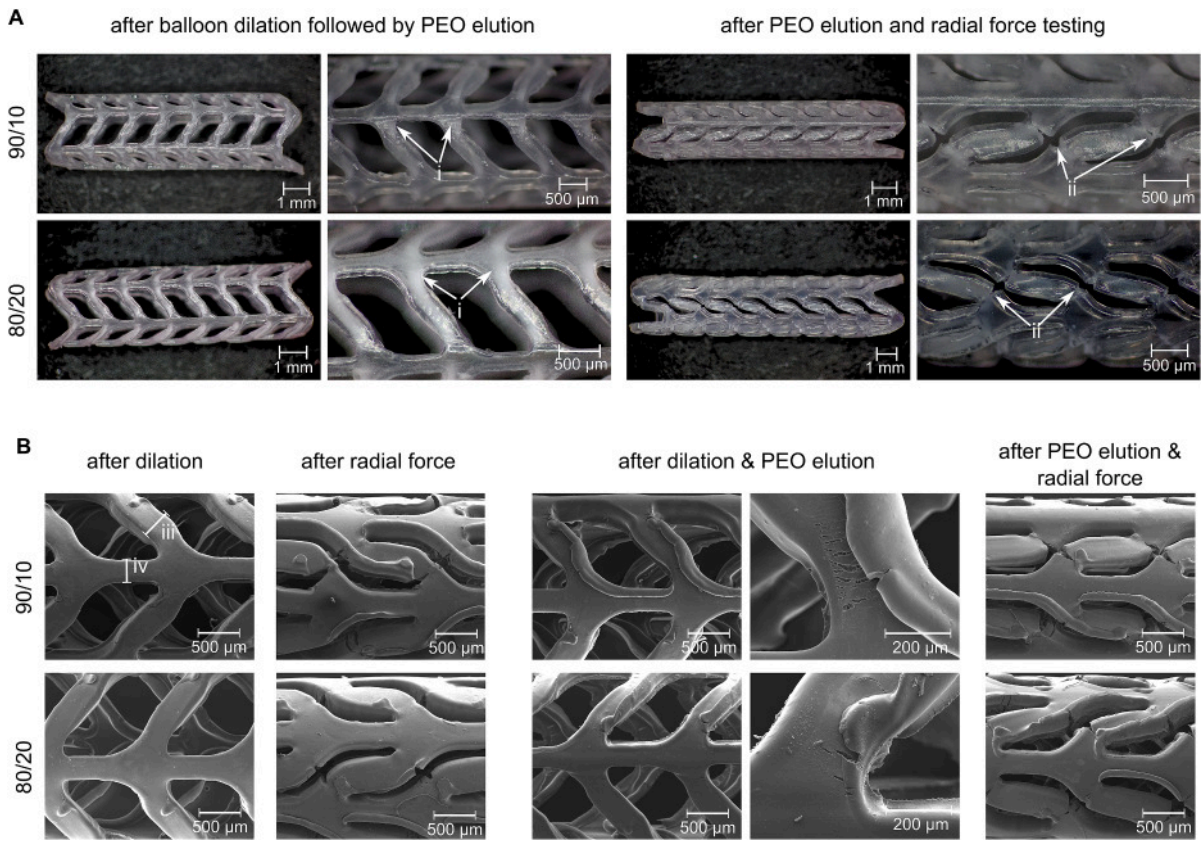


Fig. 11. Representative macrographs of PLLA/PEO 90/10 and 80/20 stents after balloon dilation followed by PEO elution of the dilated stents (A). Stent dimensions were: circumferential strut width (as indicated by iii): 298 ± 22 µm and longitudinal strut width (as indicated by iv): 234 ± 34 µm (as determined by SEM), strut thickness as given by tube wall thickness 100/0 = 178.4 µm ± 30.9 µm, 90/10 = 203.9 µm ± 31.7 µm and 80/20 = 202.2 µm ± 52.1 µm, and 8 longitudinal strut repetitions and 6 circumferential repetitions. Crazing was observed for both materials (i). After radial force testing, strut failure and crack formation were visible (ii). SEM images of stents made of PLLA/PEO 90/10 and 80/20 after dilation and radial force testing with and without PEO elution (B). For both blends without PEO elution, non-continuous cracks were visible in the material after the radial force test. After PEO elution of the expanded stent, superficial fissures became visible. After radial force testing, strut fracturing due to material embrittlement caused by the released plasticizer (PEO) was visible.

are considered safe for food applications, no serious side effects are expected.

4. Conclusions

In conclusion, blends of HMW PLLA with HMW PEO are a promising material for the fabrication of stents for treatment of ETD. Blending up to 20 % w/w PEO as plasticizer does not negatively affect the material, e. g. by phase separation. PEO blending ensures the material exhibits sufficient flexibility and plasticity, thereby enabling the stent to be expanded without damage or strut failure. As PEO is a water-soluble polymer, it is eluted and the properties of the base material PLLA are restored after 7 days of PEO elution in PBS. Initial cytocompatibility testing using established cell lines showed no significant cytotoxic effects after PEO elution, indicating a promising biological profile of the PLLA/PEO blends. However, further studies using primary cells, particularly fibroblasts and epithelial cells, as well as more detailed biological assays, are necessary to assess long-term tissue compatibility, inflammatory reactions, and functional integration in the Eustachian tube environment.

Although the addition of PEO results in a significant increase in plastic deformation capacity and a corresponding decrease in yield point, the stent's properties are similar to those of commercially available pure PLLA stents. The slow elution of the PEO enables conformation to the irregular shape of the ET. The stent material undergoes self-curing by PEO elution, during which tensile strength and Young's modulus of the material are increased, enabling stent patency in the ET or other hollow organs, as demonstrated by the increased radial stiffness of the stent after curing. Our results show the potential of PLLA/PEO as self-curing biomaterial for stent applications, although further studies on the long-term behavior under loading conditions in a preclinical set-up are required in order to advance clinical translation.

CRediT authorship contribution statement

Stefan Oschatz: Writing – review & editing, Writing – original draft, Visualization, Methodology, Investigation, Data curation, Conceptualization. **Selina Schultz:** Writing – review & editing, Visualization, Methodology, Data curation, Conceptualization. **Nicklas Fiedler:** Writing – review & editing, Methodology, Data curation. **Jana Markhoff:** Writing – review & editing, Methodology, Data curation. **Michael Teske:** Writing – review & editing, Methodology. **Daniela Koper:** Writing – review & editing, Methodology. **Volkmar Senz:** Writing – review & editing, Methodology. **Christoph Brandt-Wunderlich:** Writing – review & editing, Methodology. **Klaus-Peter Schmitz:** Writing – review & editing, Supervision, Funding acquisition. **Niels Grabow:** Writing – review & editing, Supervision, Resources, Funding acquisition. **Kerstin Lebahn:** Writing – review & editing, Writing – original draft, Project administration, Methodology, Data curation.

Declaration of competing interest

The authors declare that they have no known competing financial

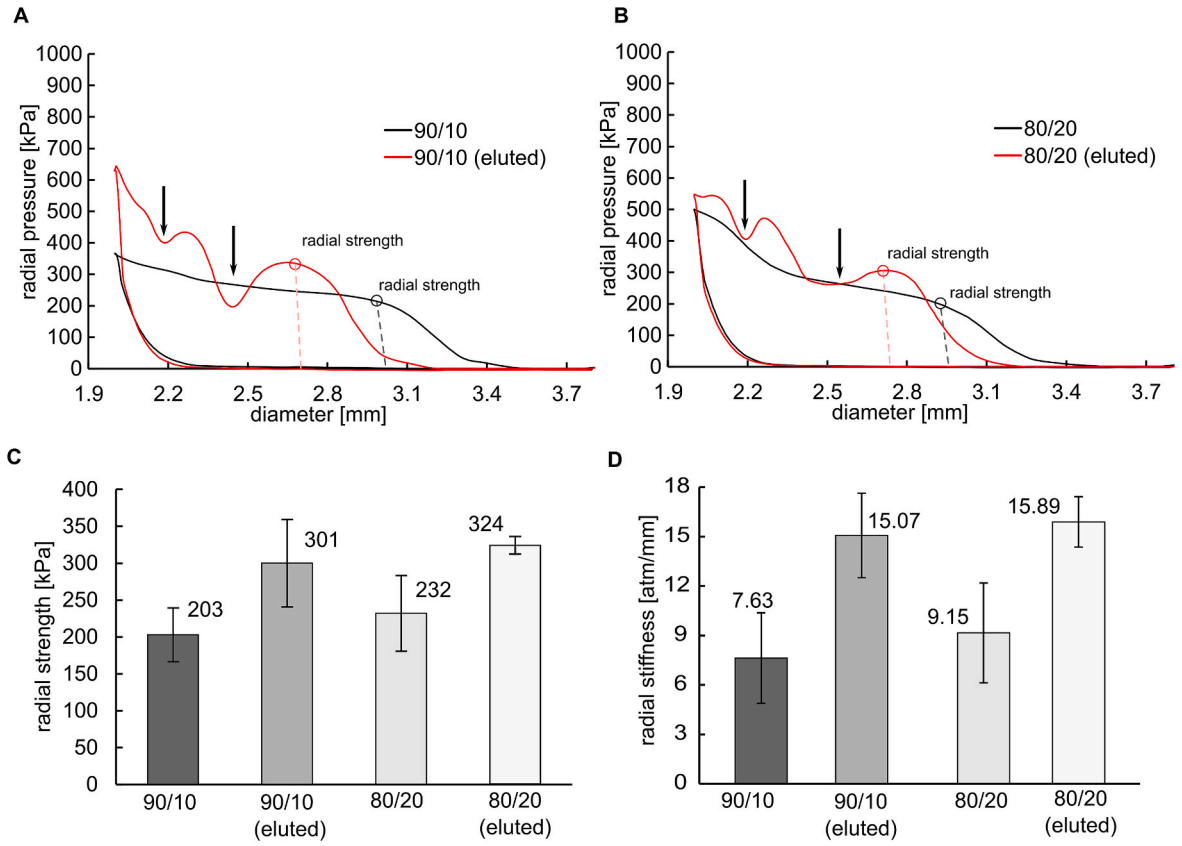


Fig. 12. Representative curves of radial force behavior of the stents before and after PEO elution (A, B). Arrows indicate points of stent failure and dashed lines show the slopes for the loading and the unloading lines, the latter shifted by 10 % of the initial diameter. Bar graphs (mean ± SD) of radial strength (C) and radial stiffness (D) of PLLA/PEO 90/10 and PLLA/PEO 80/20 stent prototypes before and after PEO elution for 7 days ($n = 5$).

Table 9
Radial strength and radial stiffness (mean ± SD) for the PLLA/PEO 90/10 and 80/20 stents (n = 5), taken from radial force measurements and literature data (FEA) for three clinically relevant PLLA stents [55].

	90/10		80/20		Absorb[a]	Elixir[b]	RevaMedical[c]
	Before PEO elution	After PEO elution	Before PEO elution	After PEO elution			
Radial strength [kPa]	203 ± 37	301 ± 59	232 ± 52	324 ± 12	250	218	318
Radial stiffness [atm/mm]	7.63 ± 2.74	15.07 ± 2.57	9.15 ± 3.03	15.89 ± 1.53	6.08	5.31	6.99

[a] final diameter: 3.25 mm, recoil: 6.8 %;
[b] final diameter: 2.88 mm, recoil: 8.82 %;
[c] final diameter: 3.12 mm, recoil: 8.34 % (values taken from [55]).

interests or personal relationships that could have appeared to influence the work reported in this paper.

Acknowledgements

Partially financial support from ESF and ERDF (Grant numbers: GHS-20-0005, GHS-18-0018 and GHS-16-0018) is gratefully acknowledged. The work and technical assistance of Katja Hahn, Gabriele Karsten, Martina Nerger, Caroline Dudda and Babette Hummel are gratefully acknowledged.

Data availability

Data for this article are available at Zenodo at https://doi.org/10.5281/zenodo.15056467.

References

[1] S. Schröder, U. Reineke, M. Lehmann, J. Ebmeyer, H. Sudhoff, Chronic obstructive eustachian tube dysfunction in adults. Long-term results of balloon eustachian tuboplasty, HNO 61 (2013) 142–151, https://doi.org/10.1007/s00106-012-2573-3.
[2] S.-W. Choi, S.-J. Oh, Y. Kim, M.Y. Kwak, M.-W. Suh, M.K. Park, C.K. Lee, H.J. Park, S.-K. Kong, A multicenter, randomized, active-controlled, clinical trial study to evaluate the efficacy and safety of navigation guided balloon Eustachian tuboplasty, Sci. Rep. 11 (2021) 23296, https://doi.org/10.1038/s41598-021-02848-1.
[3] J.M. Kang, S.H. Kim, D.S. Ryu, Y. Park, D.-S. Won, J.W. Kim, C.H. Zeng, W.S. Kang, J.-H. Park, H.J. Park, Tapered self-expandable metallic stent optimized for Eustachian tube morphology in a porcine ET model, Sci. Rep. 12 (2022) 20290, https://doi.org/10.1038/s41598-022-24615-6.
[4] F. Pohl, R.A. Schuon, F. Miller, A. Kampmann, E. Bültmann, C. Hartmann, T. Lenarz, G. Paasche, Stenting the Eustachian tube to treat chronic otitis media - a feasibility study in sheep, Head Face Med. 14 (2018) 8, https://doi.org/10.1186/s13005-018-0165-5.
[5] L. Rosenbusch, R. Schuon, T. Wilfling, P. Krüger, K. Lebahn, S. John, O. Sahmel, N. Grabow, M. Schulze, A. Wree, K.-P. Schmitz, T. Stein, T. Lenarz, G. Paasche, Investigation of stent prototypes for the eustachian tube in human donor bodies, Bioengineering (Basel) 10 (2023), https://doi.org/10.3390/bioengineering10060743.

[6] Ł.A. Mazurkiewicz, J. Bukała, J. Małachowski, M. Tomaszewski, P.P. Buszman, BVS stent optimisation based on a parametric model with a multistage validation process, Mater. Des. 198 (2021) 109363, https://doi.org/10.1016/j.matdes.2020.109363.

[7] G. Li, M. Zhao, F. Xu, B. Yang, X. Li, X. Meng, L. Teng, F. Sun, Y. Li, Synthesis and biological application of polylactic acid, Molecules 25 (2020) 5023, https://doi.org/10.3390/molecules25215023.

[8] J. Ju, X. Peng, K. Huang, L. Li, X. Liu, C. Chitrakar, L. Chang, Z. Gu, T. Kuang, High-performance porous PLLA-based scaffolds for bone tissue engineering: preparation, characterization, and in vitro and in vivo evaluation, Polymer 180 (2019) 121707, https://doi.org/10.1016/j.polymer.2019.121707.

[9] R. Harting, K. Johnston, S. Petersen, Correlating in vitro degradation and drug release kinetics of biopolymer-based drug delivery systems, Int. J. Biobased Plast. 1 (2019) 8–21, https://doi.org/10.1080/24759651.2018.1563358.

[10] D. Arbeiter, K. Lebahn, T. Reske, V. Senz, T. Eickner, K.-P. Schmitz, N. Grabow, S. Oschatz, Comparison of accelerated and enzyme-associated real-time degradation of HMW PLLA and HMW P3HB films, Polym. Test. 107 (2022) 107471, https://doi.org/10.1016/j.polymertesting.2021.107471.

[11] G. Perego, G.D. Cella, C. Bastioli, Effect of molecular weight and crystallinity on poly(lactic acid) mechanical properties, J. Appl. Polym. Sci. 59 (1996) 37–43, https://doi.org/10.1002/(SICI)1097-4628(19960103)59:1<37:AID-APP6>3.0.CO;2-N.

[12] A. Kirillova, T.R. Yeazel, D. Asheghali, S.R. Petersen, S. Dort, K. Gall, M.L. Becker, Fabrication of Biomedical Scaffolds using Biodegradable Polymers, Chem. Rev. 121 (2021) 11238–11304, https://doi.org/10.1021/acs.chemrev.0c01200.

[13] C. Zengwen, Z. Lu, H. Pan, J. Bian, L. Han, H. Zhang, L. Dong, Y. Yang, Structuring poly (lactic acid) film with excellent tensile toughness through extrusion blow molding, Polymer 187 (2020) 122091, https://doi.org/10.1016/j.polymer.2019.122091.

[14] G. Li, B. Yang, W. Han, H. Li, Z. Kang, J. Lin, Tailoring the thermal and mechanical properties of injection-molded poly (lactic acid) parts through annealing, J. Appl. Polym. Sci. 138 (2021) 49648, https://doi.org/10.1002/app.49648.

[15] L.-T. Lim, R. Auras, M. Rubino, Processing technologies for poly(lactic acid), Prog. Polym. Sci. 33 (2008) 820–852, https://doi.org/10.1016/j.progpolymsci.2008.05.004.

[16] S. Winkelmann, K. Lebahn, M. Ezzat, K. Schmitt, A. Napp, N. Oppel, F. Pohl, A. Kampmann, N. Grabow, T. Lenarz, G. Paasche, First in vivo test of a biodegradable polymeric stent for the Eustachian tube in sheep, Front. Audiol. Otol. 2 (2024), https://doi.org/10.3389/fauot.2024.1414831.

[17] J.-Z. Li, J.M. Schultz, C.-M. Chan, The relationship between morphology and impact toughness of poly(l-lactic acid)/poly(ethylene oxide) blends, Polymer 63 (2015) 179–188, https://doi.org/10.1016/j.polymer.2015.02.049.

[18] R.A. Zoppi, E. Duek, D.C. Coraça, P.P. Barros, Preparation and characterization of poly (L-lactic acid) and poly(ethylene oxide) blends, Mat. Res. 4 (2001) 117–125, https://doi.org/10.1590/S1516-14392001000200014.

[19] Y. Eom, B. Choi, S. Park, A study on mechanical and thermal properties of PLA/PEO blends, J. Polym. Environ. 27 (2019) 256–262, https://doi.org/10.1007/s10924-018-1344-y.

[20] A.J. Nijenhuis, E. Colstee, D.W. Grijpma, A.J. Pennings, High molecular weight poly(l-lactide) and poly(ethylene oxide) blends: thermal characterization and physical properties, Polymer 37 (1996) 5849–5857, https://doi.org/10.1016/S0032-3861(96)00455-7.

[21] E.A. Ozturk, Z.R. Ege, S. Murat, G. Erdemir, S. Kuruca, Z.E. Erkmen, O. Duygulu, O. Gunduz, T. Caykara, M.S. Eroglu, Poly(L-lactic acid)/poly(ethylene oxide) based composite electrospun fibers loaded with magnesium-aluminum layered double hydroxide nanoparticles, Int. J. Biol. Macromol. 217 (2022) 562–571, https://doi.org/10.1016/j.ijbiomac.2022.07.055.

[22] S. Honarbakhsh, B. Pourdeyhimi, Scaffolds for drug delivery, part I: electrospun porous poly(lactic acid) and poly(lactic acid)/poly(ethylene oxide) hybrid scaffolds, J. Mater. Sci. 46 (2011) 2874–2881, https://doi.org/10.1007/s10853-010-5161-5.

[23] E.W. Fischer, H.J. Sterzel, G. Wegner, Investigation of the structure of solution grown crystals of lactide copolymers by means of chemical reactions, Kolloid-Z.u.Z. Polymere 251 (1973) 980–990, https://doi.org/10.1007/BF01498927.

[24] DIN EN ISO 527-2:2012-06, Kunststoffe_- Bestimmung der Zugeigenschaften_- Teil_2: Prüfbedingungen für Form- und Extrusionsmassen (ISO_527-2:2012); Deutsche Fassung EN_ISO_527-2:2012, DIN Media GmbH, Berlin.

[25] S. Oschatz, S. Schultz, N. Fiedler, V. Senz, K.-P. Schmitz, N. Grabow, D. Koper, Melt blending of poly(lactic acid) with biomedically relevant polyurethanes to improve mechanical performance, Heliyon (2024) e26268, https://doi.org/10.1016/j.heliyon.2024.e26268.

[26] S. Oschatz, M. Teske, U. Burmeister, S. Illner, V. Senz, H. Lang, N. Grabow, J. Markhoff, Fetuin a functionalisation of biodegradable PLLA-co-PEG nonwovens towards enhanced biomineralisation and osteoblastic growth behaviour, Biomater. Sci. 11 (2023) 5240–5250, https://doi.org/10.1039/D3BM00141E.

[27] N. Grabow, C.M. Bünger, K. Sternberg, S. Mews, K. Schmohl, K.-P. Schmitz, Mechanical Properties of a biodegradable balloon-expandable stent from poly(L-lactide) for peripheral vascular applications, J. Med. Devices 1 (2007) 84–88, https://doi.org/10.1115/1.2355683.

[28] N. Grabow, M. Schlun, K. Sternberg, N. Hakansson, S. Kramer, K.-P. Schmitz, Mechanical properties of laser cut poly(L-lactide) micro-specimens: implications for stent design, manufacture, and sterilization, J. Biomech. Eng. 127 (2005) 25–31, https://doi.org/10.1115/1.1835349#.

[29] DIN EN ISO 25539-2:2021-01, Kardiovaskuläre Implantate_- Endovaskuläre Implantate_- Teil_2: Gefäßstents (ISO_25539-2:2020); Deutsche Fassung EN_ISO_25539-2:2020, Beuth Verlag GmbH, Berlin.

[30] W. Schmidt, P. Lanzer, Instrumentation, in: P. Lanzer (Ed.), Catheter-Based Cardiovascular Interventions, Springer Berlin Heidelberg, Berlin, Heidelberg, 2013, pp. 445–472.

[31] ASTM F3067-14 (reapproved 2021): Guide for Radial Loading of Balloon Expandable andSelf Expanding Vascular Stents. ASTM International 2019, www.astm.org., https://doi.org/10.1520/F3067-14R21.

[32] C. Brandt-Wunderlich, W. Schmidt, A. Thiesen, F. Reinhardt, M. Stiehm, K.-P. Schmitz, S. Siewert, Test methods for evaluation of balloon expandable vascular stents – measurement of radial strength and stiffness, Curr. Dir. Biomed. Eng. 9 (2023) 415–418, https://doi.org/10.1515/cdbme-2023-1104.

[33] W. Nonkrathok, T. Trongsatitkul, N. Suppakarn, Role of maleic anhydride-grafted poly(lactic acid) in improving shape memory properties of thermoresponsive poly (ethylene glycol) and poly(lactic acid) blends, Polymers (Basel) 14 (2022) 3923, https://doi.org/10.3390/polym14183923.

[34] Y. Wang, L. Liu, C. Qin, Y. Wang, C. Liu, C. Shen, Effect of a small amount of poly (ethylene oxide) on crystal polymorphism of poly(l-lactic acid), Polym. Bull. 78 (2021) 6837–6846, https://doi.org/10.1007/s00289-020-03464-1.

[35] Y. Ding, H. Ma, X. Liu, S. Qin, J. Liu, G. Qu, Y. Bai, L. Zhao, Improvement of the mechanical and shape memory properties in polylactide/polyethylene glycol blends by reactive graphene oxide, Int. J. Biol. Macromol. 253 (2023) 127346, https://doi.org/10.1016/j.ijbiomac.2023.127346.

[36] M.E. Pekdemir, E. Özen Öner, M. Kök, A. Cherkezova, Thermo-responsive shape memory polymer blends based on polylactic acid and polyethylene glycol, Macromol. Res. (2024) 1–6, https://doi.org/10.1007/s13233-024-00287-1.

[37] S. Boyacioglu, M. Kodal, G. Ozkoc, A comprehensive study on shape memory behavior of PEG plasticized PLA/TPU bio-blends, Eur. Polym. J. 122 (2020) 109372, https://doi.org/10.1016/j.eurpolymj.2019.109372.

[38] T.R. Yeazel, M.L. Becker, Advancing toward 3D printing of bioresorbable shape memory polymer stents, Biomacromolecules 21 (2020) 3957–3965, https://doi.org/10.1021/acs.biomac.0c01082.

[39] L. Maggi, L. Segale, M.L. Torre, M.E. Ochoa, U. Conte, Dissolution behaviour of hydrophilic matrix tablets containing two different polyethylene oxides (PEOs) for the controlled release of a water-soluble drug. Dimensionality study, Biomaterials 23 (2002) 1113–1119, https://doi.org/10.1016/S0142-9612(01)00223-X.

[40] A. Körner, A. Larsson, L. Piculell, B. Wittgren, Molecular information on the dissolution of polydisperse polymers: mixtures of long and short poly(ethylene oxide), J. Phys. Chem. B 109 (2005) 11530–11537, https://doi.org/10.1021/jp044332s.

[41] DIN EN ISO 10993-5:2009-10, Biologische Beurteilung von Medizinprodukten_-Teil_5: Prüfungen auf In-vitro-Zytotoxizität (ISO_10993-5:2009); Deutsche Fassung EN_ISO_10993-5:2009, DIN Media GmbH, Berlin.

[42] E. Capuana, F. Lopresti, M. Ceraulo, V. La Carrubba, Poly-l-lactic acid (PLLA)-based biomaterials for regenerative medicine: a review on processing and applications, Polymers (Basel) 14 (2022), https://doi.org/10.3390/polym14061153.

[43] T. Elakkiya, R. Sheeja, K. Ramadhar, T.S. Natarajan, Biocompatibility studies of electrospun nanofibrous membrane of PLLA-PVA blend, J. Appl. Polym. Sci. 128 (2013) 2840–2846, https://doi.org/10.1002/APP.38464.

[44] K. Szustakiewicz, B. Kryszak, P. Dzienny, B. Poźniak, M. Tikhomirov, V. Hoppe, P. Szymczyk-Ziółkowska, W. Tylus, M. Grzymajło, A. Gadomska-Gajadhur, A. J. Antończak, Cytotoxicity study of UV-laser-irradiated PLLA surfaces subjected to bio-ceramisation: a new way towards implant surface modification, Int. J. Mol. Sci. 22 (2021) 8436, https://doi.org/10.3390/ijms22168436.

[45] M. Bauer, C. Lautenschlaeger, K. Kempe, L. Tauhardt, U.S. Schubert, D. Fischer, Poly(2-ethyl-2-oxazoline) as alternative for the stealth polymer poly(ethylene glycol): comparison of in vitro cytotoxicity and hemocompatibility, Macromol. Biosci. 12 (2012) 986–998, https://doi.org/10.1002/mabi.201200017.

[46] N. Goonoo, A. Bhaw-Luximon, D. Jhurry, Biodegradable polymer blends: miscibility, physicochemical properties and biological response of scaffolds, Polym. Int. 64 (2015) 1289–1302, https://doi.org/10.1002/pi.4937.

[47] O.M. Ionescu, A. Mignon, A.T. Iacob, N. Simionescu, L.G. Confederat, C. Tuchilus, L. Profire, New hyaluronic acid/polyethylene oxide-based electrospun nanofibers: design, characterization and in vitro biological evaluation, Polymers (Basel) 13 (2021) 1291, https://doi.org/10.3390/polym13081291.

[48] A. Pereira, A.T. Paulino, C.V. Nakamura, E.A. Britta, A.F. Rubira, E.C. Muniz, Effect of starch type on miscibility in poly(ethylene oxide) (PEO)/starch blends and cytotoxicity assays, Mater. Sci. Eng. C 31 (2011) 443–451, https://doi.org/10.1016/j.msec.2010.11.004.

[49] N. Babanejad, U. Kandalam, R. Ahmad, Y. Omidi, H. Omidian, Abuse-deterrent properties and cytotoxicity of poly(ethylene oxide) after thermal tampering, Int. J. Pharm. 600 (2021) 120481, https://doi.org/10.1016/j.ijpharm.2021.120481.

[50] D. Kim, R. Natu, R. Malinauskas, J.H. Baek, P.W. Buehler, X. Feng, H. Qu, J. Pinto, X. Xu, L. Herbertson, In vitro test methods for evaluating high molecular weight polyethylene oxide polymer induced hemolytic and thrombotic potential, Toxicol. In Vitro 97 (2024) 105793, https://doi.org/10.1016/j.tiv.2024.105793.

[51] X. Peng, Ž. Janićijević, S. Lemm, S. Hauser, M. Knobel, J. Pietzsch, M. Bachmann, L. Baraban, Impact of viscosity on human hepatoma spheroids in soft core-shell microcapsules, Adv. Healthc. Mater. 13 (2024) e2302609, https://doi.org/10.1002/adhm.202302609.

[52] B. Meesaragandla, Y. Komaragiri, R. Schlüter, O. Otto, M. Delcea, The impact of cell culture media on the interaction of biopolymer-functionalized gold nanoparticles with cells: mechanical and toxicological properties, Sci. Rep. 12 (2022) 16643, https://doi.org/10.1038/s41598-022-20691-w.

[53] C.M. Bünger, N. Grabow, K. Sternberg, L. Ketner, C. Kröger, B. Lorenzen, K. Hauenstein, K.-P. Schmitz, H.J. Kreutzer, D. Lootz, H. Ince, C.A. Nienaber, E. Klar, W. Schareck, Iliac anastomotic stenting with a biodegradable poly-L-lactide

stent: a preliminary study after 1 and 6 weeks, J. Endovasc. Ther. 13 (2006) 539–548, https://doi.org/10.1583/05-1726MR.1.
[54] W. Schmidt, P. Behrens, C. Brandt-Wunderlich, S. Siewert, N. Grabow, K.-P. Schmitz, In vitro performance investigation of bioresorbable scaffolds - Standard tests for vascular stents and beyond, Cardiovasc. Revasc. Med. 17 (2016) 375–383, https://doi.org/10.1016/j.carrev.2016.05.001.
[55] T.Y. Qiu, M. Song, L.G. Zhao, A computational study of crimping and expansion of bioresorbable polymeric stents, Mech. Time Depend. Mater. 22 (2018) 273–290, https://doi.org/10.1007/s11043-017-9371-y.
[56] S. Ingelstedt, B. Jonson, H. Rundcrantz, Gas tension and pH in middle ear effusion, Ann. Otol. Rhinol. Laryngol. 84 (1975) 198–202, https://doi.org/10.1177/000348947508400210.
[57] O.F. Boztepe, M. Demir, T. Gün, N. Bilal, N.A. Ensari, H. Doğru, A novel predictive marker for the viscosity of otitis media with effusion, Int. J. Pediatr. Otorhinolaryngol. 79 (2015) 2355–2358, https://doi.org/10.1016/j.ijporl.2015.10.043.

Polymer Testing 107 (2022) 107471

Contents lists available at ScienceDirect

Polymer Testing

journal homepage: www.elsevier.com/locate/polytest

Comparison of accelerated and enzyme-associated real-time degradation of HMW PLLA and HMW P3HB films

Daniela Arbeiter [a,*], Kerstin Lebahn [a], Thomas Reske [b], Volkmar Senz [a], Thomas Eickner [a], Klaus-Peter Schmitz [a,b], Niels Grabow [a], Stefan Oschatz [a]

[a] Institute for Biomedical Engineering, Rostock University Medical Center, Friedrich-Barnewitz-Straße 4, 18119, Rostock-Warnemünde, Germany
[b] Institute for Implant Technology and Biomaterials e.V, Friedrich-Barnewitz-Straße 4, 18119, Rostock-Warnemünde, Germany

ARTICLE INFO

Keywords:
Poly-L-lactide
Poly-3-hydroxybutyrate
Enzyme-associated degradation
Accelerated degradation
Molecular weight
Crystallinity

ABSTRACT

Designing laboratory-scale degradation experiments for polymer-based biomaterials is crucial for the development of safe and functional implants, in particular regarding high molecular weight polyesters. Within this work, we compared accelerated degradation of solvent cast HMW-PLLA and HMW-P3HB films at 55 °C (16 weeks) with enzyme-associated (proteinase K and lipases) real-time degradation at 37 °C (108 weeks). During real-time degradation, PLLA showed mass loss up to 83%, in contrast to accelerated conditions, where no changes occurred. Moreover, we observed wave-shape development of crystallinity for PLLA and PHB for both degradation conditions applied, whereby PLLA χ value nearly doubled to up to 75%. These results were used to develop a correlation model based on molecular weight decrease and were furthermore discussed in light of a detailed literature review. In summary, real-time *in vitro* studies could be adapted to accelerated protocols providing the same limiting conditions such as molecular weight and initial crystallinity are given.

1. Introduction

Accelerated *in vitro* degradation protocols for polymeric materials allow to reproduce long-term behavior in a relatively short experiment [1]. In general, the hydrolytic degradation rate of biodegradable polymers is raised by increasing temperature or altering pH. Ideally, finding a correlation between real-time and accelerated conditions, according to the relevant standards e.g. ISO 10993 [2], would allow process-related analytics and the development of a validation protocol of absorbable polymers which can substantially accelerate future degradation studies, saving resources and research funds. However, as various factors, such as the involvement of enzymes, play a role in *in vivo* degradation, the realistic situation can only be represented to a limited extent by *in vitro* experiments, especially under accelerated conditions.

In the field of biodegradable polyesters, poly-L-lactide (PLLA) and poly-3-hydroxybutyrate (P3HB) exhibit a still increasing importance [3–6]. PLLA can be applied as implant coating [7], drug carrying matrix [8], surgical sutures [9] or solid implant material [10,11]. As for the latter, currently several ultrathin strut PLLA-based biodegradable stents are under clinical and preclinical investigation [12–16]. P3HB in turn is used, among other applications, as porous patches for pericardial replacement in fields of cardiology for example [17] or as bone graft material [18].

Due to their inherent properties, PLLA and P3HB can be processed by several methods, such as extrusion [7] or melt electrospinning [19], as well as solvent-based manufacturing methods. In general, solvent-based manufacturing protocols are in particular relevant, as most industrial coating techniques rely on the use of polymer solutions. Dissolving a polymer in an adequate solvent enables a variety of different processes such as electrospinning and -spraying, air-brush [20], spin coating [21] and ultrasonic spraying to generate homogeneous and reproducible coatings on complex structures, such as stents, TAVR or cardiac pacemakers. Dipcoating [22,23] is another noteworthy method to access films or cylindrical semi-finished products, whereas the latter can furthermore be processed into implants, e.g. stents by laser cutting [7]. This process is especially suitable for lab scale prototyping. Moreover, compared to thermal processing, solvent-based protocols allow for the incorporation of active compounds, e.g. drugs, growth factors, or particles for various reasons [24–26].

Notably, processing methods have a considerable influence on the properties of the resulting material, e.g. surface morphology, crystallinity, polymer chain alignment and distribution of crystalline and

* Corresponding author.
E-mail address: daniela.arbeiter@uni-rostock.de (D. Arbeiter).

https://doi.org/10.1016/j.polymertesting.2021.107471
Received 24 August 2021; Received in revised form 15 November 2021; Accepted 30 December 2021
Available online 6 January 2022
0142-9418/© 2022 The Authors. Published by Elsevier Ltd. This is an open access article under the CC BY-NC-ND license (http://creativecommons.org/licenses/by-nc-nd/4.0/).

amorphous domains [27,28]. Compared to thermal processing, solvent cast techniques require additional post-treatment of the materials, which can be either washing or annealing or a combination of both, to remove solvent residues as those may alter material properties or even show toxic effects [25,29]. In addition, molecular weight of the polymer material influences material properties.

Despite similar chemical composition with P3HB exhibiting just one additional CH_2-group compared to PLLA, PLLA and P3HB differ considerably regarding their degradation behavior. Whereas PLLA undergoes plain hydrolytic degradation within about 3 years, it is reported in the literature that scission of P3HB chains at physical conditions requires support by enzymatic catalysis and takes place over a period of about 4 years [30,31]. Moreover, effects such as autocatalysis [32,33] or mid-chain ester hydrolysis versus end-group scission have to be taken into account [34]. For more detailed predictions on auto and non-catalytic hydrolysis, Gleadall et al. [35] developed reaction kinetic models accounting the nature of the chain scissions (random or end). As reported by Scaffaro et al., PLLA degradation proceeds in 3 stages. Stage 1 describes surface degradation, while stage 2 explains the degradation penetration. They suggested that in the case of complete autocatalytic degradation or remarkable bulk depletion during long-term immersion, a third stage could be observed, often associated with pronounced erosional phenomena [36]. Real-time degradation studies for investigation of such behavior, however, remain challenging as degradation takes place over up to several years.

Literature overview on degradation experiments for PLLA

Due to complexity of the topic and the sheer amount of factors to be considered, a remarkable amount of experiments have been conducted to understand the degradation of PLLA. Yet, those studies vary in used molecular mass, specimen manufacturing protocol as well as choice of degradation medium and conditions. A brief overview on selected degradation studies on PLLA is given in Table 1.

Early studies on the degradation of PLLA mainly focused on morphology of the material and its influence on degradation behavior. In 1990, Li et al. prepared PLLA samples via compression molding followed by subsequent quenching or annealing to yield amorphous and semi crystalline specimens, respectively [37]. They pointed out that the early stage of degradation is independent of the initial morphology and rather depends on the thermal history and crystallinity of the material. However, remaining polymer residues appeared to be very resistant at the end of the degradation. Extensive investigations were focused on the crystallization behavior during the degradation process [37,48].

Tsuji et al. studied the hydrolysis of solution cast PLLA films showing different degrees of crystallinity, which was adjusted by previous annealing processes [28]. One of their results was that PLLA hydrolysis took place dominantly in the amorphous region in between the

Table 1
Overview on selected degradation studies performed on PLLA as reported in the literature.

	molecular weight M_W (Da)	manufacturing process	crystallinity χ (%)	degradation conditions		
				media	temperature	time[a]
Li et al. (1990) [37]	1.3×10^5	injection molding & quenched	0	saline & PBS, pH = 7.4	not specified	2 years
		injection molding & annealed at 130 °C for 2 h	73	PBS, pH = 7.4		
Pistner et al. (1993) [38]	4.5×10^5	injection molding	36	*in vivo* (rats)		2 years
	9.5×10^5	as-polymerized PLLA block	73			
Gogolewski et al. (1993) [39]	2.75×10^5	injection molding	52	*in vivo* (mouse)		6 months
Cam et al. (1995) [40]	3×10^5	CH_2Cl_2 without further process	30	0.01 M NaOH	37 °C	175 days
	4.5×10^5		15			
	6.5×10^5		5			
	3×10^6		3			
Bergsma et al. (1995) [1]	8.8×10^5	granulate	64	PBS; pH = 7.4	90 °C	6 weeks
Tsuji et al. (2000) [28]	1.3×10^6	CH_2Cl_2 washed in Methanol and 1 week in vacuum oven, melted at 200 °C & quenched at 0 °C	0	PBS; pH = 7.4	37 °C	2 years
		annealed for 15 min	2			
		annealed for 30 min	30			
		annealed for 45 min	45			
		annealed for 60 min	54			
Iannace et al. (2001) [41]	6×10^5	solvent cast in $CHCl_3$, evaporated & isothermal crystallization at 90 °C	46	PBS; pH = 7.02	37 °C	40 weeks
		as above at 130 °C	44			
Weir et al. (2004) [42]	4.24×10^5	compression molding, annealed at 120 °C for 4 h	40	PBS; pH = 7.4	37 °C	57 weeks
Weir et al. (2004) [43]	4.24×10^5	compression molding, annealed at 120 °C for 4 h	47	PBS; pH = 7.4	50 °C	115 days
			57.5	PBS; pH = 7.4	70 °C	23 days
Salguero et al. (2012) [44]	n.a.	commercial available polymer	36	PBS; pH = 7.02	37 °C	40 days
Deplaine et al. (2014) [45]	1.65×10^5	freeze extraction and porogen-leaching methods	13	PBS; pH = 7.02	37 °C	12 months
Felfel et al. (2015) [46]	1.2×10^5	compression molding, melted at 210 °C for 10 min	9.2	PBS; pH = 7.4	21 °C 37 °C 50 °C 65 °C 75 °C 85 °C	56 days
Wang et al. (2016) [47]	5.0×10^4	compression molding at 190 °C and 15 MPa, annealed at 115 °C for 1 h	19.5 ± 5.3	*in vivo* (rabbits)		1 year
Porfyris et al. (2018) [48]	1.79×10^5	compression molding at 190 °C for semi-crystalline	50	80% RH	70 °C	140 h
	1.49×10^5	160 °C for amorphous	0			
Fuoco et al. (2021) [49]	2.65×10^5	solvent cast in $CHCl_3$	76	PBS; pH = 7.4	60 °C	15–20 days

[a] Degradation times are extracted from the original literature and thus cannot be easily harmonized.

crystalline regions and hydrolysis rate was higher in that specific domain in comparison to free amorphous region. In general, they presumed that higher crystallinity and hence higher crystal thickness lead to more defects in the amorphous domain, promoting hydrolysis by enhanced water diffusion.

Cam et al. analyzed PLLA samples with a broad range of molecular weights in terms of their degradation behavior [40]. They showed that an increase in molecular weight leads to a decrease of initial crystallinities, yet the degradation rate increased. This may be contradictory compared to the aforementioned influence of crystallinity, but the authors stated that residual solvent could have influenced degradation behavior. They concluded that it is necessary to remove the solvent completely from the polymer.

Weir et al. analyzed the degradation of compression molded PLLA samples in an accelerated time period and compared the data with real time degradation [42,43]. Thus, at higher temperature, degradation proceeds by a very similar mechanism to that observed at 37 °C, *in vitro* as well as *in vivo*.

Still, concerns remained about the validity of testing above glass transition temperature T_g of PLLA when predicting results at degradation temperatures below T_g and the significance of autocatalysis as temperature is increased [43]. Thus, Weir et al. contradicted Bergsma's statement [1] that, although degradation temperature is well above glass transition temperature and not comparable to physiological temperatures, there seems to be good correlation between *in vitro* degraded and physiologically degraded material.

Moreover, conditions for performing *in vitro* degradation of PLLA have been standardized by ISO 13781:2017, specifying the use of Sørensen buffer (0.012 M KH_2PO_4, 0.055 M Na_2HPO_4 in water) with pH adjusted to 7.4 ± 0.2 at 37 °C ± 1 °C. The minimum solution volume has to be 10 ml and is recommended to be more than 30:1 to the test sample mass [50].

Literature overview on degradation experiments for P3HB

Regarding the *in vitro* degradation of P3HB, a summary on relevant degradation studies is given in Table 2.

Compared to PLLA, similar studies have been performed with P3HB. Doi et al. investigated the effects of polymer composition on the degradation rates of different PHB variations at different temperatures [51]. They concluded that hydrolytic degradation of PHB occurs in two steps: first random hydrolytic chain scission of the ester groups, followed by weight loss just at low M_w. Kurcok et al. concluded that the degree of crystallinity of P3HB due to chain orientation influences the rate of its hydrolytic degradation, with atactic P3HB showed faster degradation compared to semicrystalline polymer [52].

Regarding the need for enzymatic support in the P3HB degradation, Freier et al. [30] observed a slower pure hydrolytic degradation of P3HB in comparison to PLLA but a threefold accelerated loss in M_w when using porcine pancreatin, a mixture of lipases, amylases α-chymotrypsin, trypsin and proteases. Still, it remained uncertain if P3HB degradation behavior observed in their study was based on enzymatic catalysis.

In a very recent study, Zhuikov et al. [54] observed a wave-shape change of crystallinity during degradation of P3HB due to the fact that amorphous regions degrade faster than crystalline domains, leading to an increase of crystallinity. By hydrolysis of crystalline regions, amorphous components are formed, leading to an up-and-down in χ during degradation experiments. Overall, P3HB has not as extensively been investigated regarding accelerated degradation behavior as PLLA.

Objective of this study

Biodegradable polyesters with high molecular weight (HMW) are of particular interest in biomedical engineering, as mechanical and physico-chemical properties can be enhanced by increasing M_w [55,56].

Yet, in the case of HMW PLLA, with $M_w > 300$ kDa, and HMW P3HB with $M_w > 700$ kDa, no studies for solvent cast materials concerning the comparison of accelerated and enzyme-associated real-time degradation have been reported in the literature. Depicting the *in vivo* degradation allows for analyzing biomaterials in terms of changes in deflection, fatigue and tensile strength, changes in surface roughness and thus fluid mechanics, or fragmentation and particle formation.

Aim of our work is to contribute to the understanding of the degradation behavior of solvent cast HMW PLLA and HMW P3HB film materials. We investigated polymer film degradation in a real-time study with the use of lipases and proteinase K degradation in comparison to accelerated conditions at 55 °C. In addition to gravimetric measurements, morphological as well as thermal analyses and gel-permeation chromatography (GPC) were performed in order to be able to compare the results with literature data and to evaluate the accelerated degradation protocol. Two key findings of this work are that our choice of lipases did not catalyze the degradation of HMW P3HB but affected HMW PLLA. Moreover, we were able to observe that accelerated PLLA degradation induces more drastic changes in crystallinity compared to enzyme-associated real-time conditions. Overall, our results hold implications regarding the setup of test parameters and thus for the conclusions drawn from *in vitro* data.

2. Materials and methods

Materials: Poly-L-lactide (PLLA L210, M_w = 320.000 g/mol and PLLA L214, M_w = 700.000 g/mol) was purchased from Boehringer Ingelheim Pharma (Ingelheim, Germany). Poly-3-hydroxybutyrate (P3HB, M_w = 750.000 g/mol) was supplied by

Table 2
Overview on selected degradation studies performed on P3HB as reported in the literature.

	molecular weight M_W (Da)	manufacturing process	crystallinity χ (%)	degradation conditions		
				media	temperature	time[a]
Doi et al. (1989) [51]	n.a.	solvent cast in $CHCl_3$	59	PBS, pH = 7.4	37 °C 70 °C	200 days
Gogolewski et al. (1993) [39]	1.29×10^5	injection molding	60.7	*in vivo* (mouse)		6 months
Kurcok et al. (1995) [52]	2.34×10^4	granulate	n.a.	PBS; pH = 7.4	70 °C	80 days
Canetti et al. (1999) [53]	1.66×10^5	solvent cast in CH_2Cl_2, melted at 185 °C for 2 min & crystallization at 50 °C	51	Potassium phosphate buffer; pH = 7.0	37 °C	300 h
Freier et al. (2002) [30]	6.4×10^5	solvent cast in $CHCl_3$, 1 week in vacuum oven	69	PBS; pH = 7.4; porcine pancreatin	37 °C 70 °C	1 year
Salguero et al. (2012) [44]	6.0×10^5	solvent cast in $CHCl_3$ at 62 °C	53	PBS; pH = 7.02	37 °C	40 days
Zhuikov et al. (2020) [54]	1.1×10^6	solvent cast in $CHCl_3$, 72 h in vacuum oven	63	PBS; pH = 7.4; porcine pancreatic lipase	37 °C	6 months

[a] Degradation times are extracted from the original literature and thus cannot be easily harmonized.

Umweltforschungszentrum Leipzig-Halle GmbH (Leipzig-Halle, Germany).

Sample preparation: Degradation studies were performed using films cast from chloroform (Merck, Darmstadt, Germany) solutions (1 g polymer in 25 ml chloroform) employing petri dishes (Ø = 9 cm). After evaporation of the solvent, films were washed for two days in methanol (Merck, Darmstadt, Germany) and two days in deionized water at 25 °C, and dried for 7 days in a vacuum oven, model Scientific 45001 (Bioblock Fisher Scientific, Schwerte, Germany), at 40 °C. Polymer samples were punched in form of round slices of Ø = 5 mm. For real-time degradation study the following initial thickness was obtained (mean ± sample standard deviation of n = 3 samples with 3 measurements each): d = 133 ± 6 μm (PLLA L210), d = 118 ± 2.6 μm (PLLA L214) and d = 155 ± 5 μm (P3HB). For the accelerated study, sample thickness was: d = 101 ± 15 μm (PLLA L210), d = 104 ± 7 μm (PLLA L214) and d = 124 ± 12 μm (P3HB).

Degradation conditions: The degradation conditions were chosen according to the standards ISO 13781 [57] and ISO 15814 [50,58]. 37 °C were chosen as established temperature to simulate *in vivo* conditions and to ensure maximum enzyme activity. Furthermore, following Van't Hoff rule, a temperature of 55 °C was chosen to generate accelerated degradation conditions that allow us to degrade polymers within a very short time, for which several years would normally have to be invested. In addition, the studies had to be performed below the glass transition temperature of PLLA to avoid structural changes caused by degradation above T_g and to ensure comparability of the two chosen degradation conditions. Degradation assays for enzyme-associated real-time studies were conducted using Sørensen buffer at pH = 7.4 (MORPHISTO, Frankfurt am Main, Germany) containing 5.0 mg/l proteinase K (a ≥30 U/mg; Sigma-Aldrich, Darmstadt, Germany), 5.0 mg/l pseudomonas lipase (a ≥30 U/mg; Sigma-Aldrich, Darmstadt, Germany), and 7.7 mg/l aspergillus lipase (a = 181 U/mg; Sigma-Aldrich, Darmstadt, Germany). Each sample was incubated individually in 2 ml buffer at 37 °C and shaken with 100 rpm. Every two weeks, Sørensen buffer was changed in each vial. Specimens were taken out for investigations after 2, 4, 12, 24, 36, 48, 60, 72, 84, 96 and 108 weeks. Each polymer specimen wwas washed three times with distilled water and then dried for one week at 40 °C under reduced pressure.

For accelerated studies, each sample was incubated individually in 2 ml Sørensen buffer without enzymes at pH = 7.4 (MORPHISTO, Frankfurt am Main, Germany). Samples were shaken with 100 rpm at 55 °C. Every week, Sørensen buffer was changed in each vial. For investigations, specimens were taken out after 0.2, 1, 2, 3, 4, 6, 8, 10, 12, 14 and 16 weeks. The buffer solution was changed every week. After removal, specimens were treated precisely as in real-time study.

Microscopy: The polymer films were analyzed by means of light microscopic photography using an Olympus SC50 digital camera mounted on an Olympus SZX10 stereo microscope and cellSens Standard imaging software (Olympus, Tokyo, Japan). Scanning electron microscopy (SEM) was carried out using a SEM Quanta FEG 250 (FEI Company, Frankfurt, Germany). For SEM imaging, the samples were fixed onto aluminum trays with conductive carbon pads. The SEM investigations were performed using high vacuum and 10 kV with a working distance of approx. 10 mm. The images were taken at 800× magnification.

Mass change: Prior to degradation study, the polymer film sample mass was determined using an electronic microbalance XP6U (Mettler Toledo, Zurich, Switzerland). On removal, the same specimens were being weighed after washing three times with distilled water and drying for one week at 40 °C under reduced pressure. The overall percentage mass change was calculated from the mass before degradation.

GPC measurements: The molecular weight (M_w) and number average molecular weights (M_n) of polymer samples at different degradation time points were obtained at 30 °C using a PSS SECcurity SEC system (Polymer Standard Services, Mainz, Germany) including a RI detector combined with a WGE Dr. Bures g 2010 viscosity detector (WGE Dr. Bures, Dallgow, Germany). Separation was carried out with three PSS SDV columns (103, 105 and 106 Å, respectively). Chloroform stabilized with ethanol was the eluent with a flow rate of 1 ml/min. The samples were prepared with a concentration of 1.5 mg/ml in chloroform with hexylbenzene as internal standard and the injection volume was 0.1 ml. The molecular weights were calculated by the universal calibration method using twelve polystyrene calibration standards in a range between 376 and 2570.000 g/mol.

Thermal analysis: Thermal properties were investigated in a DSC FP84HT (Mettler Toledo, Zurich, Switzerland) for real-time degradation and DSC 1 (Mettler Toledo, Zurich, Switzerland) for accelerated degradation. Conventional calibration methods with highly pure standards were used. Real-time degradation samples were heated from +40 °C up to 225 °C with a heating rate of q = 10 K/min (FP84HT without active cooling system) operating at ambient atmospheric pressure. Accelerated degradation samples were heated from −40 °C up to 225 °C with a heating rate of q = 10 K/min (DSC 1 with intracooling system) operating under nitrogen at ambient atmospheric pressure. Sample weights were in the range of 3–6 mg. We analyzed the samples with respect to glass transition (T_g), melting temperature (T_m), and degree of crystallinity (χ). The heats of fusion and crystallization were quantitatively evaluated by determining the endothermic peak areas, which were compared with the melting peak area of totally crystalline PLLA (χ_{100} = 93.7 J/g) [59] and P3HB (χ_{100} = 146 J/g) [60].

FTIR-ATR-measurements: FTIR-ATR-measurements were performed using a Bruker Vertex 70 IR-Spectrometer (Bruker, Leipzig, Germany) equipped with a DLaTGS-detector. Data were collected in the range of $\tilde{\nu}$ = 500 cm^{-1} to 4000 cm^{-1} with a resolution of $\tilde{\nu}$ = 4 cm^{-1} averaged over 100 scans in reflection mode using a Graseby Golden Gate Diamond ATR-unit. Atmospheric compensation has been performed. All spectra were subsequently baseline corrected and finally normalized with OPUS vector-normalization-function for better visualization.

3. Results and discussion

General properties of the investigated polymers prior to degradation as taken from DSC and GPC experiments are summarized in Table 3.

To address the *in vivo* situation, our approach was the use of lipases for PLLA and proteinase K for P3HB as this protocol has been described before [30,61]. The role of enzymes in *in vivo* degradation of polymer biomaterials is being broadly discussed in the literature [31,53,62–65]. Some authors reported about enzyme contribution during the late stages of polymer degradation, with a high grade of material fragmentation and already drastically decreased molecular weight (<20.000 g/mol) [42,66]. Cam et al. stated that enzyme catalysis is nearly negligible regarding the biodegradation of PLLA [40]. Moreover, they illustrated that enzymes, being macromolecules themselves, are inhibited to penetrate into the polymer bulk due to their molecular size, thus bulk degradation by chain scissoring takes place just by hydrolysis. Still, surface degradation may be influenced by enzymes [67]. This, without bulk hydrolysis, would lead to the observation that M_w remains constant during degradation, whereas sample mass decreases as surface degradation products are easily washed out. In contrast, bulk hydrolysis without enzyme contribution on surface degradation would lead to M_w

Table 3
Material properties of polymers addressed in this study.

	PLLA		P3HB
	L210	L214	
molecular weight M_w	320.000 g/mol	700.000 g/mol	750.000 g/mol
glass transition temperature T_g	62 °C	65 °C	0 °C
melting temperature T_m	175 °C	178 °C	180 °C
crystallinity χ	37%	24%	68%

decrease at constant sample mass as hydrolysis products remain entrapped in the polymer. This assumption is taken into concern for the following analyses, as PLLA initial mass loss observed during our study must derive from enzymatic surface degradation, as molecular weight decrease proceeds considerable slower.

Surface morphology during degradation

First, changes in morphology during enzyme-associated *in vitro* degradation process at 37 °C and accelerated degradation at 55 °C were investigated by means of macrophotography and SEM. Within both degradation studies, PLLA L210 showed considerable visual changes (Fig. 1). The samples turned opaque and showed clear cracks after 16 weeks (accelerated) and 108 weeks (real-time), respectively. PLLA L214 became only opaque after 2 weeks in the real-time study but no further macroscopic changes were observed. In contrast to this, L214 samples did not show any optical changes during accelerated degradation. P3HB showed no optical changes during both degradation studies. Macro photography documentation of the degradation process of PLLA can be found in supporting information (Figs. S1–S6).

For a more detailed view, SEM imaging has been used to investigate the microscopic appearance of the degraded polymer samples. At 800× magnification, no such thing as microcrystals or other inhomogeneities as well as changes in surface morphology could be observed for PLLA L214 and P3HB, each for both degradation conditions. These samples appeared smooth and comparable to the initial state before degradation (images can be found in supporting information (Figs. S7–S12). PLLA L210 appeared to have one uniform rough surface, which did not change during real-time degradation. However, during accelerated degradation, growth of small spherulite crystals could be observed. After 16 weeks of degradation at 55 °C, continuous cracks at spherulite phase-phase-interfaces could be detected (Fig. 2f), presumably indicating propagation of hydrolytic degradation processes [36]. Fig. 2d) and e) each show the side which was attached to the surface of the Petri dish, thus resulting in a generally smoother surface.

Changes in mass during degradation

During enzyme-associated real-time degradation, PLLA L210 and L214 showed an almost linear mass loss from 10 weeks on to a residual of 71% and 27% of the starting mass after 108 weeks, respectively (Fig. 3). Accelerated degradation at 55 °C exhibited almost no mass loss with residual mass of 98% for L210 and 99% for L214 after 16 weeks. In the case of P3HB, there was no mass loss observable during both studies, real-time and accelerated degradation.

For enzyme-associated real-time degradation at 37 °C, L214 showed fast decrease in residual sample mass whereas M_w showed only low decrease until 24 weeks. Overall, we observed linear mass loss for film materials of PLLA L210 of about 30% and for L214 up to 73%, respectively. However, the increasing standard deviations can be explained by the advancing degradation due to the disintegration of the samples and the removal of free floating fragments during the media changes.

Regarding P3HB, enzyme-associated real-time at 37 °C, as well as accelerated degradation at 55 °C, did not result in a considerable mass loss of the samples.

Molecular mass loss during degradation

The molecular mass of PLLA L210 remained stable for the first 4 weeks. For PLLA L214, decrease in molecular mass could just be observed after 12 weeks of real-time degradation. In the following, both polymers exhibited an almost linear degradation behavior during the remaining time. After 108 weeks, both PLLA species retained 11–12% of their initial molecular mass. The real-time degradation of PLLA L210 and PLLA L214 was almost congruent in the end stage of degradation.

The initial molecular weight of P3HB showed fast decrease already during the first weeks of real-time degradation compared to PLLA (Fig. 4), reaching 80% of the initial value after 12 weeks. The molecular mass of P3HB decreased in an almost linear fashion until the end of the study. The mean values of the relative loss after 108 weeks were 53% for P3HB.

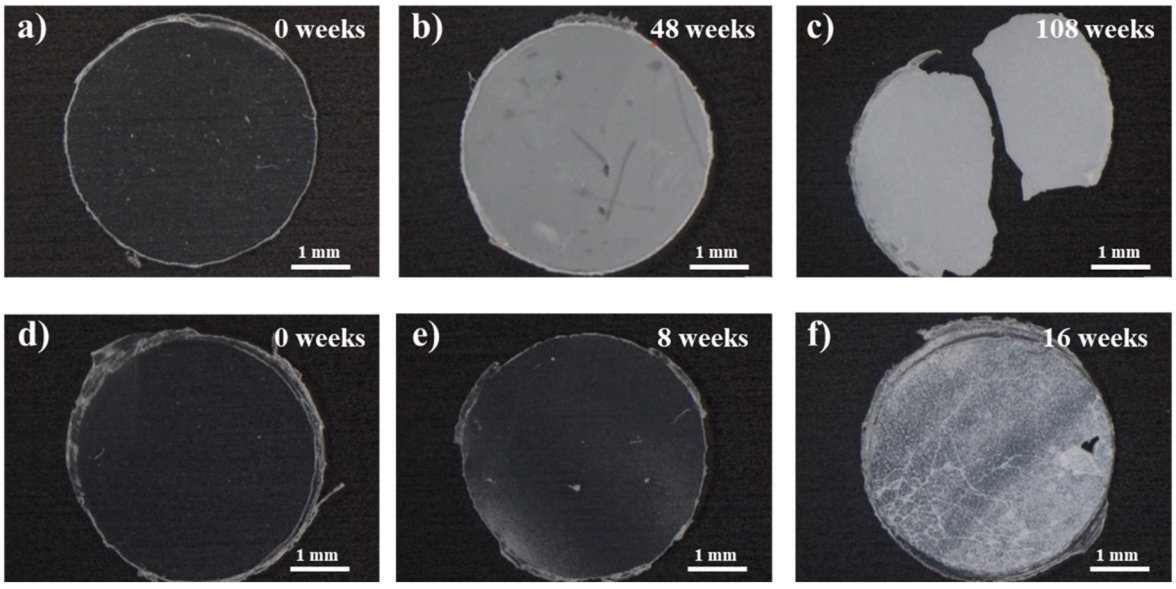


Fig. 1. Macroscopic documentation of real-time (a–c) and accelerated (d–f) degradation-induced changes of PLLA L210 morphology: (a,d) initial state, (b) after 48 weeks, (c) after 108 weeks, (e) after 8 weeks and (f) after 16 weeks.

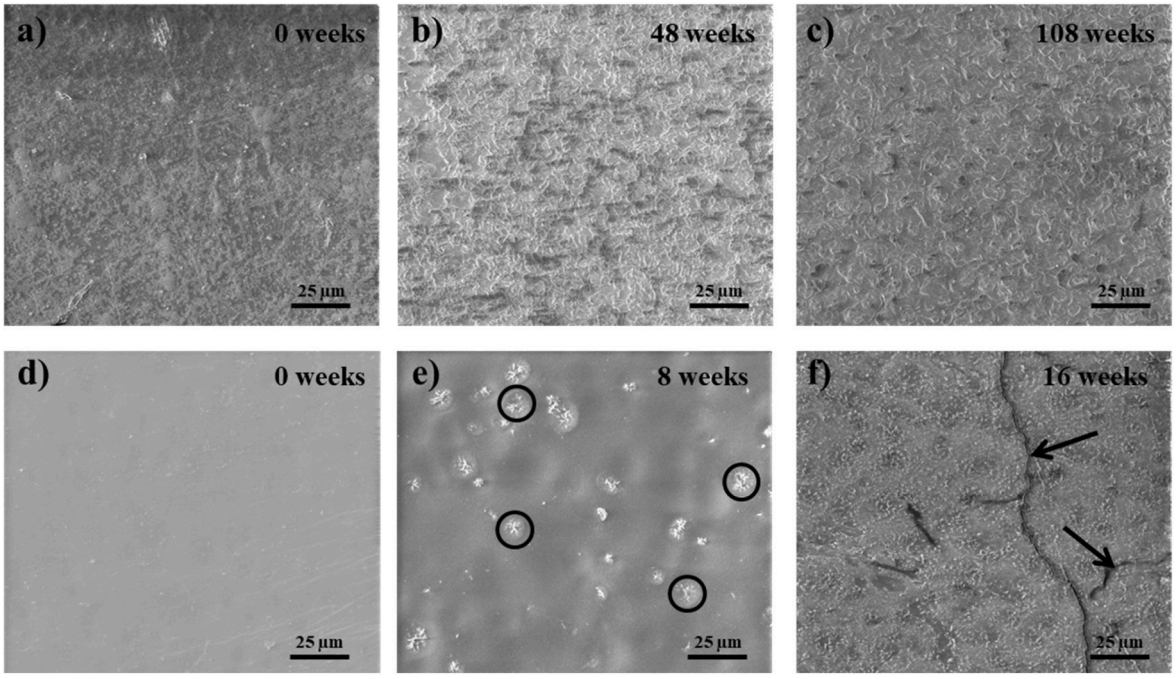


Fig. 2. SEM documentation of real-time (a–c) and accelerated (d–f) degradation-induced changes of PLLA L210 morphology: (a,d) initial state, (b) after 48 weeks, (c) after 108 weeks, (e) after 8 weeks and (f) after 16 weeks (800× magnification). The encircled structures in e) and arrows in f) show changes induced by accelerated degradation study.

After 12 weeks of degradation at 55 °C, molecular weight of PLLA L210 was reduced to less than 20% of its initial value. The linear degradation curve also appears to flatten out towards the end due to fragmentation of the material. Similar behavior was observed for PLLA L214, resulting in linear decrease in M_w, although not quite as fast when compared to PLLA L210. Comparable to L210, L214 M_w plots showed an increased standard deviation at the last time points and flattening of the curve. Accelerated degradation of P3HB at 55 °C resulted in 31% residual M_w after 16 weeks. Loss in M_w showed exponential decrease during degradation. Molecular weight (g/mol), polydispersity PI and mass loss (%) for all time points for both, real-time and accelerated degradation, (Tables S1–S3), as well as exemplary chromatograms of the GPC measurements from beginning, middle of end of degradation can be found in the supporting information (Figs. S13–S18).

When combining data for mass loss and M_w decrease, literature data for PLLA real-time degradation without enzymes, conducted by Weir et al. (compression molding sample preparation) [42] and Tsuji et al. (solvent cast sample preparation) [28], did not show mass loss during early stages of degradation, albeit decrease in M_w. The collateral decrease of M_w indicated furthermore additional bulk degradation by hydrolysis. PLLA L214 with higher M_w showed to be more affected by enzymes when compared to PLLA L210. Our results are consistent with those of Cam et al. [40] showing that due to the higher mass loss in L214, enzymes favor surface degradation with consistently decreasing M_w.

Regarding P3HB, our results indicated a decrease in M_w up to 70% but no considerable mass loss. Therefore, we assumed that the lipases we used did not catalyze P3HB chain scissoring, but simple bulk hydrolysis occurred.

Changes in thermal properties during degradation

The DSC curves of all polymers are shown in Fig. 5. The degree of crystallinity versus time is presented in Fig. 6. The χ values, glass transitions (T_g) and melting temperature (T_m) for all time points for both, real-time and accelerated degradation, can be found in the supplement data (Tables S4–S6).

PLLA L210 and PLLA L214 showed comparable thermal behavior during real-time degradation study. The DSC heating curves of PLLA cast films for both molecular weights exhibited a glass transition temperature of approximately T_g = 65 °C before degradation. No exothermic peak, but an endothermic melting peak at T_m = 179 °C was observed for L210 and L214, which was comparable to reported T_m data for HMW PLLA [4], see Table 3.

Decrease in T_m by hydrolysis for more than 12 months in both PLLAs (values in Tables S4–S5) was consistent with the literature [28,32,68]. Still noteworthy is that we measured T_g from dried samples and therefore is not reflective of T_g in the medium. Faster increase in crystallization values may be attributed to the fact that medium temperature is in the range of T_g. The amorphous portions were thus more mobile, allowing water to diffuse more rapidly through it, causing faster degradation. Regarding T_m, P3HB remained unaffected, due to the fact that degradation has not occurred yet in the crystallites, but only chain scission started in the amorphous regions.

Regarding crystallinity development, both HMW PLLA species, L210 and L214, exhibited a wave-shaped behavior during real-time degradation, whereas χ showed only little changes during the first 36 weeks. After 108 weeks, χ of both polymers nearly doubled, from χ_{L210} (36 weeks) = 31 ± 4% to χ_{L210} (108 weeks) = 57 ± 4%, and χ_{L214} (36 weeks) = 26 ± 4% to χ_{L214} (108 weeks) = 48 ± 5%. A similar trend was observed for the accelerated degradation study for both PLLA species.

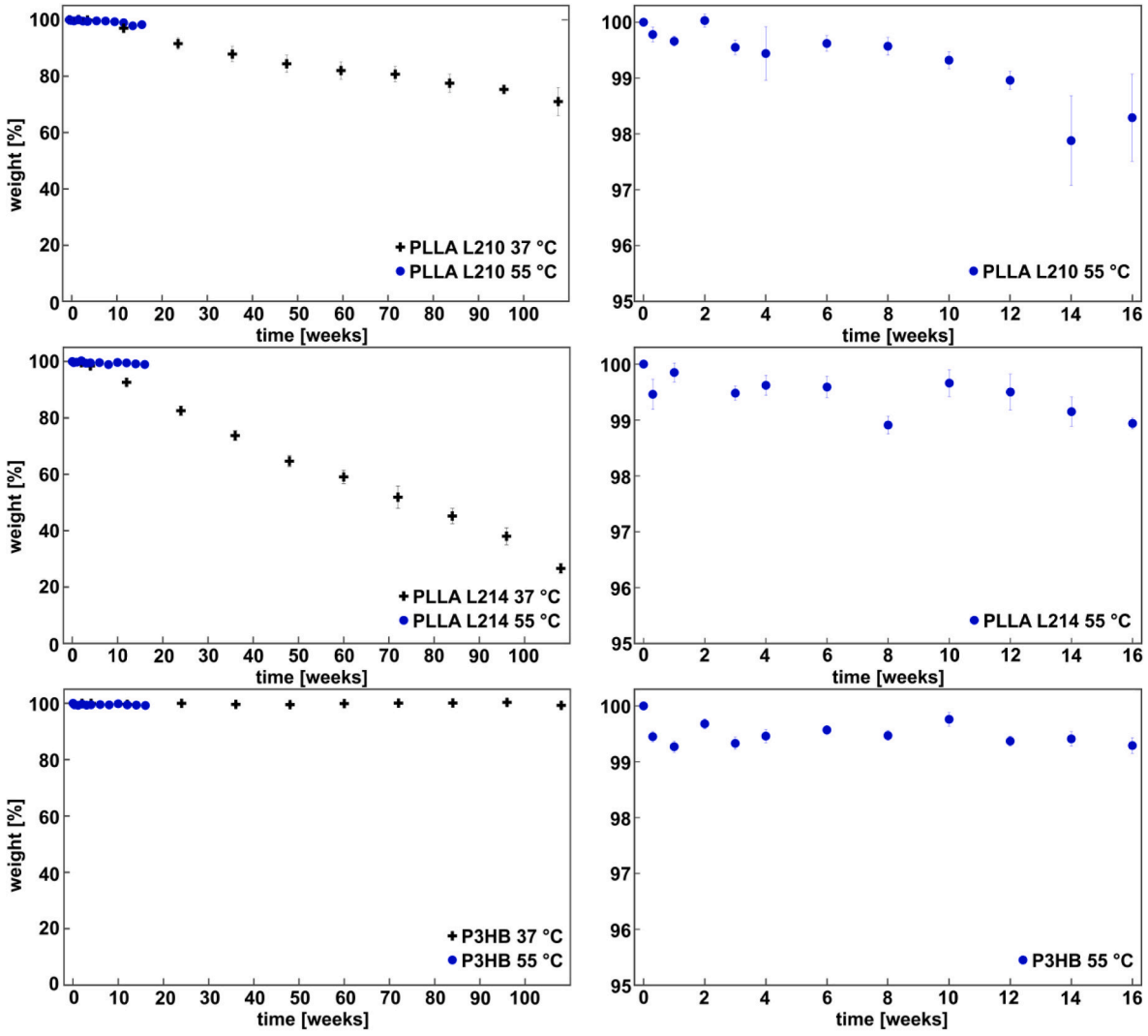


Fig. 3. Changes in mass of PLLA L210 (top), PLLA L214 (middle) and P3HB (bottom) during real-time degradation at 37 °C (black points) and accelerated degradation at 55 °C (blue points). All data points are means of n = 8 measurements except n = 7 at 10 weeks, L210 and 12 weeks, L210. For a better view, mass loss during accelerated degradation has been magnified on the right. (For interpretation of the references to colour in this figure legend, the reader is referred to the Web version of this article.)

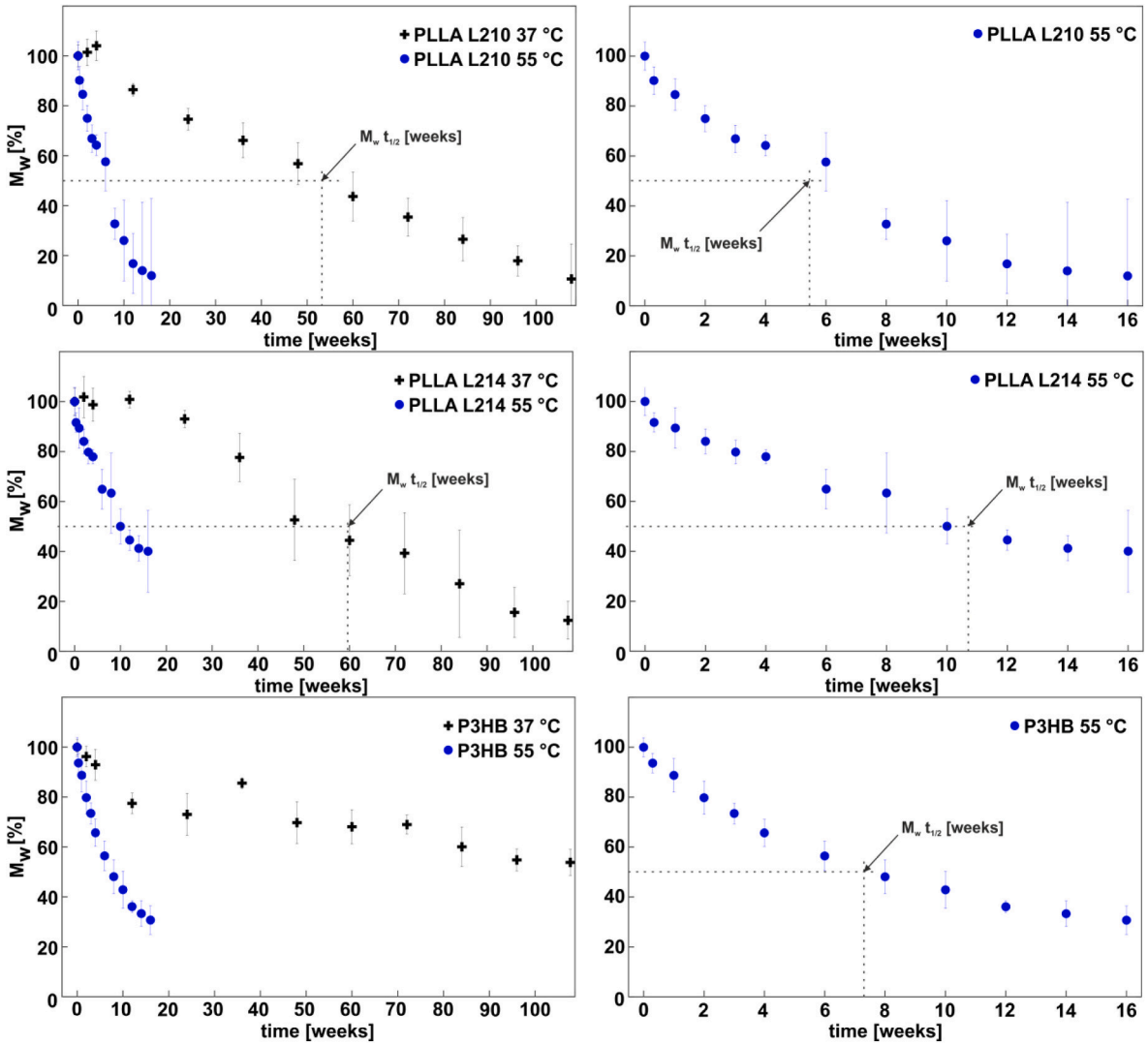


Fig. 4. Decrease in molecular weight of PLLA L210 (top), PLLA L214 (middle) and P3HB (bottom) during real-time degradation at 37 °C (black points) and accelerated degradation at 55 °C (blue points). Intersection of dotted lines represents molecular weight half-life (M_w $t_{1/2}$) with Mw $t_{1/2}$ (L210) = 53 weeks (37 °C) and Mw $t_{1/2}$ (L210) = 5.5 weeks (55 °C), and Mw $t_{1/2}$ (L214) = 59 weeks (37 °C) and Mw $t_{1/2}$ (L214) = 10.5 weeks (55 °C). M_w $t_{1/2}$ of P3HB during real-time degradation at 37 °C has not been reached after 108 weeks and Mw $t_{1/2}$ (P3HB) = 7.5 weeks (55 °C). All data points are mean values of 3 (accelerated degradation) and 5 measurements (real-time degradation), respectively. (For interpretation of the references to colour in this figure legend, the reader is referred to the Web version of this article.)

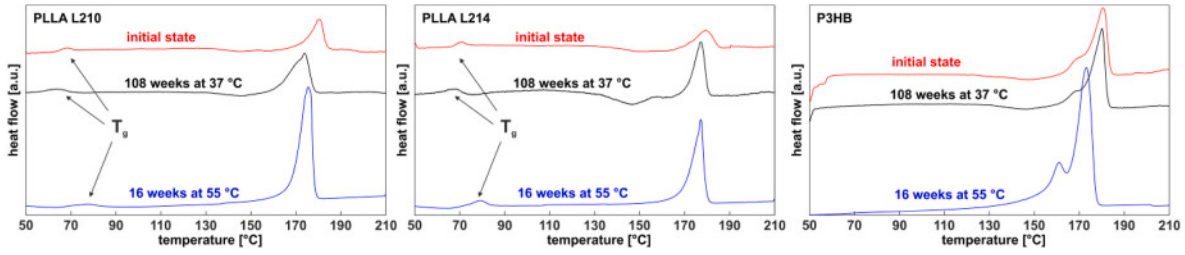


Fig. 5. DSC thermograms of PLLA L210 (left), PLLA L214 (middle) and P3HB (right) during real-time degradation at 37 °C (black line) and accelerated degradation at 55 °C (blue line). The red curve corresponds to the initial state before degradation. (For interpretation of the references to colour in this figure legend, the reader is referred to the Web version of this article.)

Until 8 weeks of degradation at $T = 55$ °C, χ_{L210} remained almost constant at approximately 40%, followed by an increase in χ up to 75 ± 7%, This behavior was also apparent with L214, although not as pronounced as for L210. Until 6 weeks, χ_{L214} is about 35%, followed by an increase until 16 weeks to $\chi_{L214} = 44 \pm 8\%$.

P3HB showed an initial crystallinity of $\chi_{P3HB} = 68 \pm 5\%$. During real-time and accelerated degradation study, also wave-shaped changes in thermal properties, T_g, T_m, and χ_{P3HB}, could be observed. This alternation can be attributed to degradation initially affecting predominantly amorphous regions, which exhibited a degradation rate of up to 20-fold

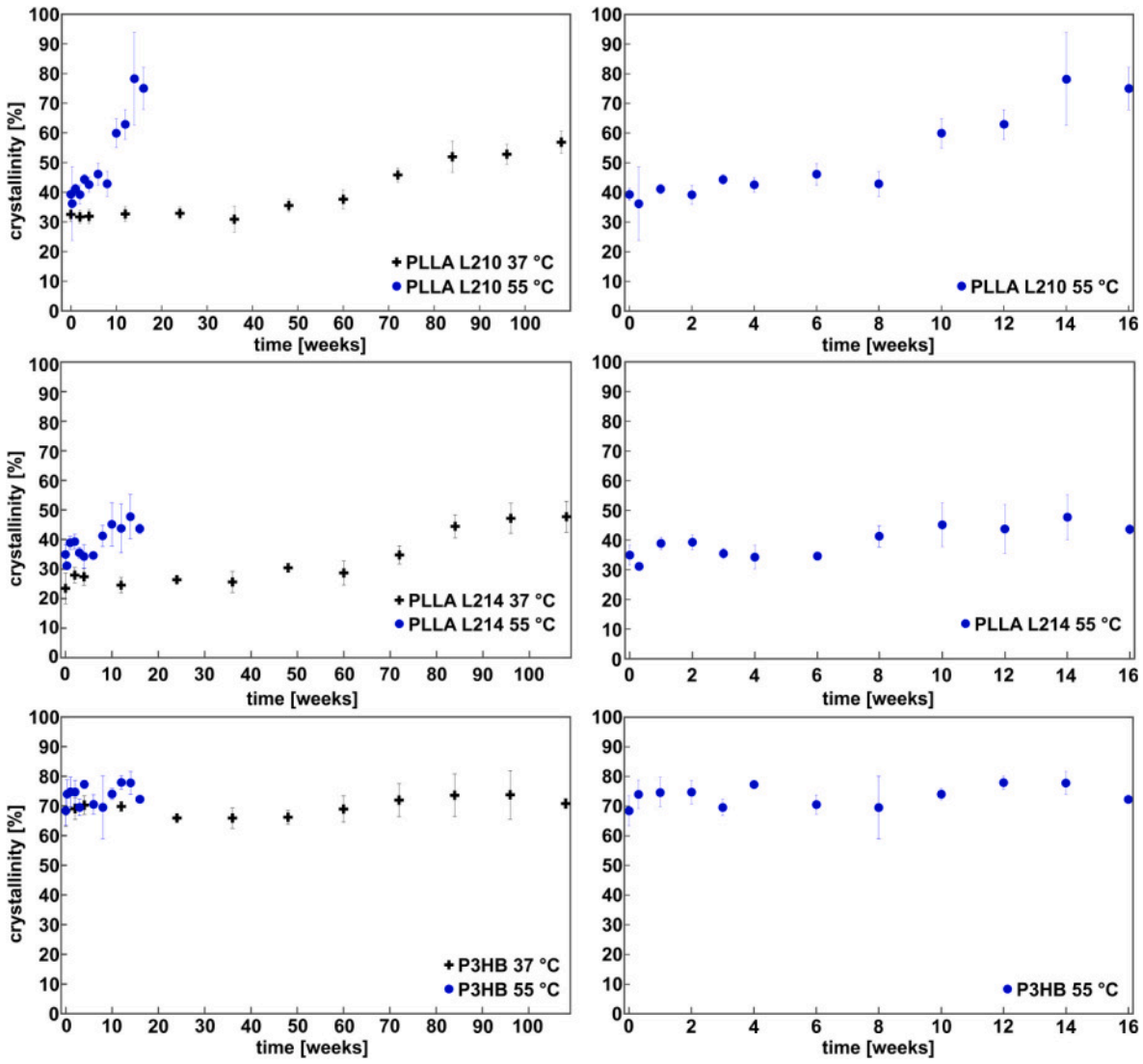


Fig. 6. Changes in χ of PLLA L210 (top), PLLA L214 (middle) and P3HB (bottom) during real-time degradation at 37 °C (black points) and accelerated degradation at 55 °C (blue points). All data points are means of 5 measurements. (For interpretation of the references to colour in this figure legend, the reader is referred to the Web version of this article.)

compared to the crystalline ones [1,69]. Polymer chain fragments in such regions are washed out more quickly due to the fact that water could easily migrate into amorphous domains, resulting in a decrease in amorphous fractions [38]. Fischer et al. quantified the decrease of average distance of crystalline regions during hydrolysis and showed that the loss of amorphous fractions leads to an increase in enthalpy of fusion and melting temperature decrease (see, Table S4) [59]. In accordance to this, our data show the same development in T_m and in ΔH, thus, we conclude the same mechanistic background. However, as hydrolysis is undirected, also crystalline domains were affected. This again led to a subsequent decrease in crystalline domains and reformation of amorphous regions due to short chain polymer fragments and secondary crystallites.

Comparison of real-time experiments with accelerated conditions

Qualitative FTIR-ATR spectroscopy has been performed to compare enzyme-associated real-time degradation with accelerated degradation at selected sampling points (t = 0/60/112 w (37 °C) and t = 0/6/16 w (55 °C)). All spectra can be found in the supplements (Figs. S19–24). According to literature findings [70], changes in bands at $\tilde{\nu} = 1210\ cm^{-1}$ and $\tilde{\nu} = 1230\ cm^{-1}$, which are associated to asymmetric C–O–C stretching and asymmetric CH_3 rocking vibrations, respectively, were examined for PLLA L210 and L214 to follow the degradation progress at 37 °C and 55 °C. As for P3HB, FTIR spectra for both degradation conditions showed a comparable decrease in the amorphous C–O–C band at $\tilde{\nu} = 1183\ cm^{-1}$ [71]. The data show a similar progression of spectra changes for both degradation conditions for all polymers, thus real-time and accelerated degradation yield a comparable outcome.

For the comparison of enzyme-associated real-time degradation with accelerated degradation at 55 °C based on molecular weight and crystallinity, degradation times have been normalized to the point of first mass loss, respectively. However, one boundary condition was set that the initial crystallinity is similar in both studies and exhibits comparable behavior over time.

For comparison, molecular weight loss is plotted in Fig. 7 (left) with

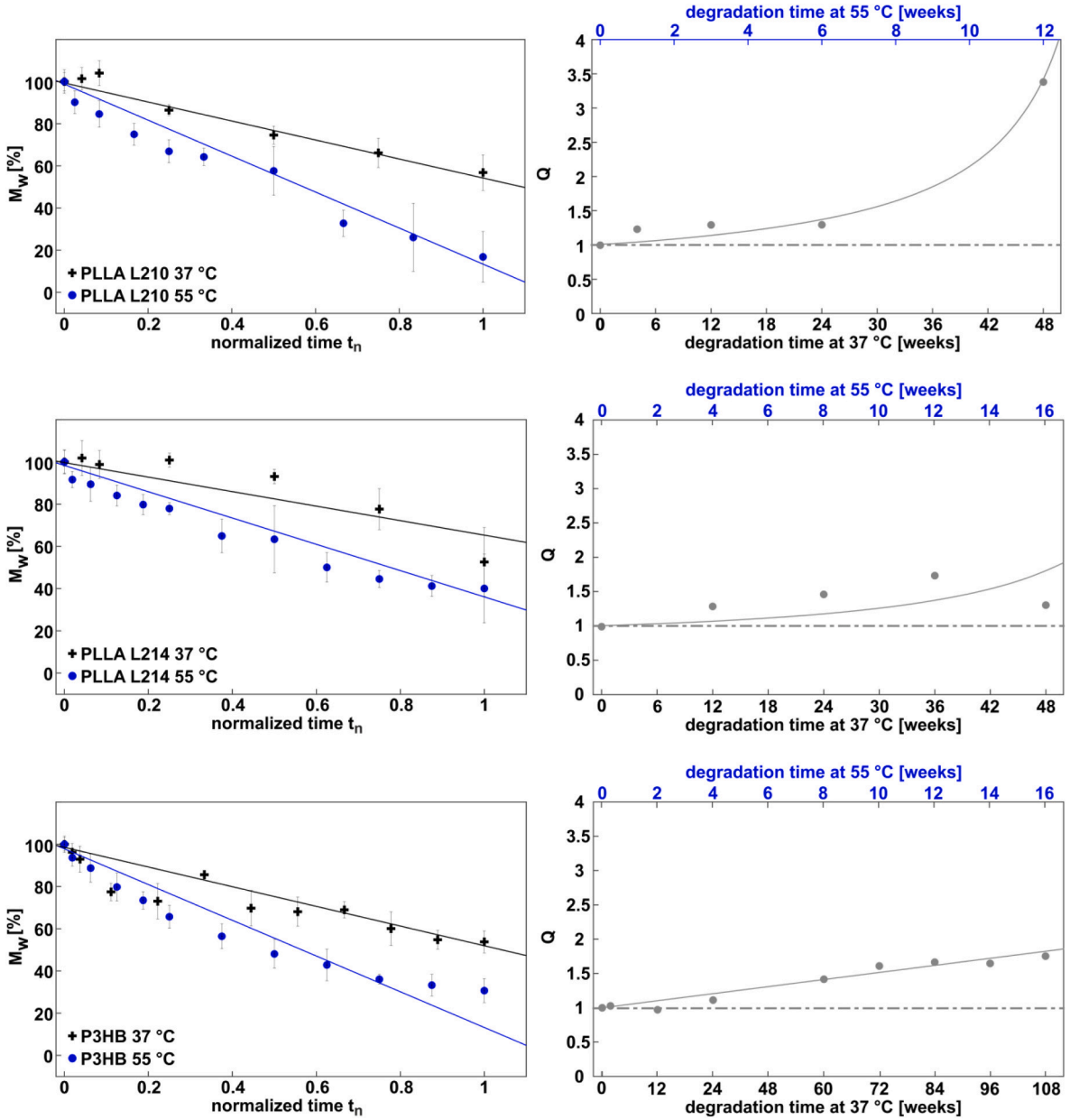


Fig. 7. M_W-correlation model of real-time and accelerated degradation of PLLA L210 (top), PLLA L214 (middle) and P3HB (bottom). Left: Plots of molecular weight loss of the real-time and accelerated degradation studies over normalized time points (t_n). For better illustration, linear trend lines have been added. Right: Plots of calculated quotient of the molecular weights of the accelerated experiments to those of the real-time study. The solid line presents the correlation trend line for *Q* over degradation time, while the dashed line represents idealized correlation.

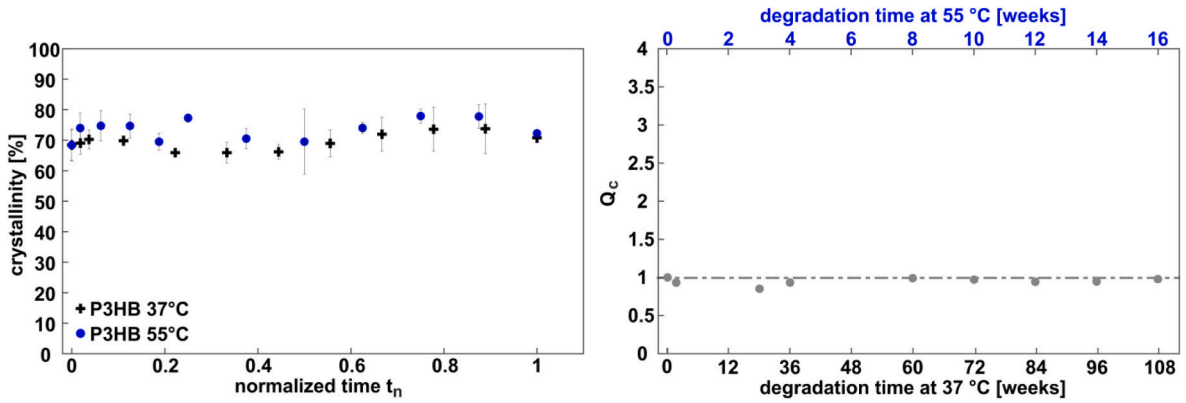


Fig. 8. χ-correlation model of real-time and accelerated degradation of P3HB. Left: Plots of crystallinity of the real-time and accelerated degradation studies over normalized time points (t_n). Right: Plots of calculated quotient of the crystallinity of accelerated experiments to those of real-time study. The dashed line represents idealized correlation.

added with linear trend lines for better illustration. The resulting overlapping normalized time points for the polymers based on the normalized curves were subsequently taken into account for further calculations.

Using the resulting data, quotients of the molecular weights of the accelerated experiments to those of the real-time study were determined by calculating

$$Q = \frac{M_w\ (37\ °C;\ t_n)}{M_w\ (55\ °C;\ t_n)} \quad (1)$$

And plotted in Fig. 7 (right).

A correlation trend line for Q over degradation time was generated. In the case of PLLA L210, it was indicated that a real-time study of half a year can be reproduced by an accelerated study of 6 weeks, yielding 1.5 fold decrease in M_w for accelerated conditions compared to real-time degradation. As for PLLA L214, 16 weeks degradation at 55 °C reproduce 48 weeks of real-time degradation, resulting in a 1.3 fold loss in M_w. However, the progression of PLLA crystallinity over time at 37 °C vs. 55 °C, showing a non-linear but wave-shaped progression, must be considered as limitation for the model (Fig. 6).

Real-time studies over 2 years on P3HB were reproduced by 16 weeks degradation under accelerated conditions, giving a 1.3 fold decrease in M_w.

Regarding crystallinity, P3HB showed, in contrast to PLLA, a well matching development when degradation times are normalized (108 versus 16 weeks). When forming the quotient

$$Q_c = \frac{\chi\ (37\ °C;\ t_n}{\chi\ (55\ °C;\ t_n)} \quad (2)$$

Acorrelation with respect to thermal properties with a correlation factor of 1 over the entire degradation time was found (Fig. 8).

For P3HB, 16 weeks of accelerated degradation were suitable to reproduce 108 weeks of real-time degradation, in particular with respect to development of crystallinity over time. However, further investigations are necessary for validation of these findings. As for M_w decrease, it must be noted that with the correlation of 108 to 16 weeks, the M_w change increased 1.3 fold during accelerated degradation.

Autocatalytic versus non-catalytic bulk degradation

Regarding reaction kinetics of polymer chain scission with respect to autocatalysis, plotting $1/M_n$ and ln M_n versus time has been reported to be used for modeling the non-catalyzed and autocatalyzed degradation mechanisms [42,72]. In summary, a linear relationship between $1/M_n$ vs. t should exist for non-catalytic ester hydrolysis and a linear relationship between ln M_n vs. t should exist for the autocatalytic model. The applied model is based on the boundary condition that degradation has not progressed too far. Thus, only data until first mass loss can be considered and erosion phenomena cannot be taken into account. The corresponding plots of PLLA and P3HB are shown in Fig. 9 including linear regression lines and R^2 correlation coefficients displayed.

Autocatalysis plays an important role for the degradation of polyesters. The model by Anderson et al. [72] may be used to consider the contribution of autocatalyzed or non-catalyzed ester hydrolysis. With the assumption that bulk degradation occurs just by hydrolysis, we determined the fitting (R^2) to either lnM_n (autocatalysis) or $1/M_n$ (non-catalytic) during degradation until first mass loss (Fig. 9).

As both PLLA species already exhibited mass loss from the beginning of the study due to enzyme-associated degradation, time points for first mass loss (48 weeks) were taken from Weir et al. and Tsuji et al. [42,68] to calculate R^2. Under accelerated conditions, PLLA L210 mass loss started after 12 weeks and PLLA L214 after 16 weeks. Regarding P3HB, normalization was performed until the end of the study, as there was no mass loss observed over the entire test period.

Concerning PLLA L210, R^2 fitting of $1/M_n$ and ln M_n showed no distinct tendency. R^2 values for 37 °C gave $1/M_n = 0{,}921$ and ln $M_n = 0{,}898$. As for 55 °C, R^2 values were $1/M_n = 0{,}838$ and ln $M_n = 0{,}972$. Weir et al. [42] observed similar values for PLLA degradation and reported R^2 values of 0.85 (tensile samples) and 0.95 (extruded rod samples) for the autocatalyzed model and 0.63 (tensile samples) and 0.90 (extruded rod samples) for the non-catalyzed model. They concluded that both non-catalytic and autocatalytic ester hydrolysis are present.

For PLLA L214, however, we assume a more non-catalytic ester hydrolysis at 37 °C ($R^2 = 0.767$ vs. 0.533). As R^2 fittings show no clear difference at 55 °C ($R^2 = 0.951$ vs. 0.941), both hydrolysis mechanisms appear to be present. However, the low R^2 values for L214 (M_w = 700.000 g/mol) real-time study suggest that, in contrast to L210 (M_w =

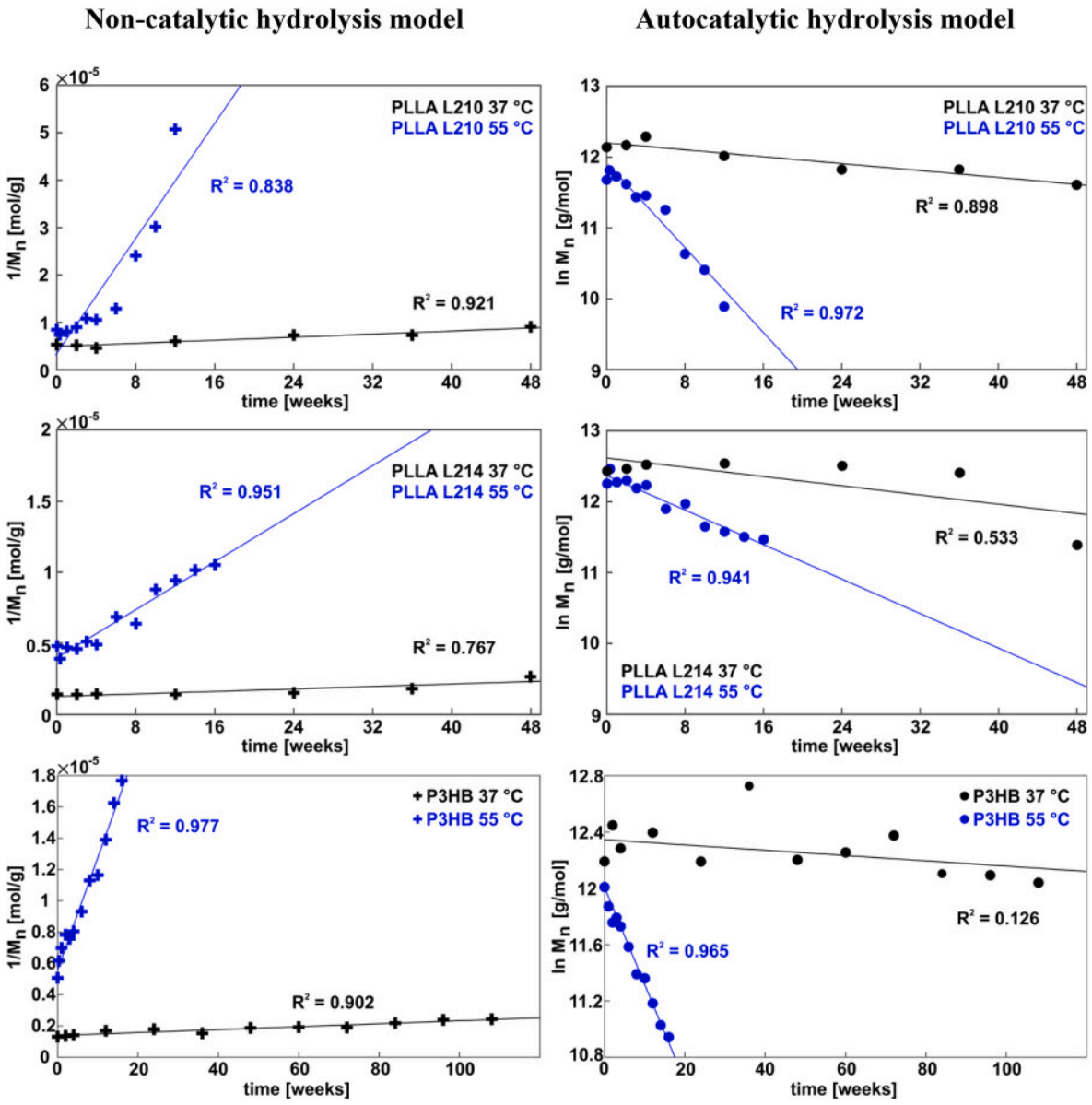


Fig. 9. Comparison of non-catalyzed and autocatalyzed models of PLLA L210 (top), PLLA L214 (middle) and P3HB (bottom) at enzyme-associated real-time degradation (black) and accelerated degradation (blue) following Weir et al. [42]. (For interpretation of the references to colour in this figure legend, the reader is referred to the Web version of this article.)

320.000 g/mol), the theory developed by Anderson et al. [72] may not be applicable. In consequence, although chemically similar, degradation behavior concerning autocatalysis cannot be easily predicted for equivalent polymers with different molecular weights.

For P3HB, the results showed distinct differences in R^2 fitting at 37 °C. P3HB is expected to undergo non-catalytic ester hydrolysis at 37 °C ($R^2 = 0.902$ vs. 0.126). In contrast, R2 fitting shows no differences at 55 °C, therefore both mechanisms appear to be apparent.

Influence of processing protocol on degradation of PLLA

In comparison to our work, Weir et al. [42] used compression molded samples in their real-time degradation studies with nearly the same initial M_w (4.24×10^5 g/mol) and χ (40.7%). Their reported results are comparable in means of M_w decrease (83%) and mass loss (constant until 57 weeks) during 65 weeks of degradation at 37 °C. Tsuji et al., however, used solvent cast PLLA from $CHCl_3$ with considerably higher molecular weight ($M_w = 1.3 \times 10^6$ g/mol) [68]. Regarding M_w and χ development during degradation, their results showed a comparable outcome as our data. However, they did not observe any mass loss during the first 24 months of degradation at 37 °C, which, with respect to our data, implies that enzymes are critical factors for surface degradation. As our results for PLLA L210 and L214 indicate, initial molecular weight has a pronounced influence on the rate of surface erosion with enzyme participation. This is particularly relevant considering the comparability of the outcome of accelerated experiments with *in vivo* studies. Enzyme-associated effects cannot be reproduced at higher temperatures due to enzyme denaturation. Thus, no surface erosion takes part and chain fragments from bulk degradation remain entrapped in the body, leading to no observable mass loss at early experimental stages.

In terms of accelerated degradation at increased temperature, a study by Felfel et al. showed no mass loss on compression molded PLLA with lower molecular weight ($M_w = 1.2 \times 10^5$ g/mol) after 8 weeks of accelerated degradation at 50 °C [46]. However, it should be noted, that these data are only comparable to a certain extent, as no M_w development was specified. According to this, our studies on solvent cast PLLA

showed that sample mass remained nearly constant (≥99%) until 12 weeks (L210) and 16 weeks (L214). These findings were also consistent with the results of Weir et al. for degradation at 50 °C using compression molded HMW PLLA [43]. They also showed a decrease in M_w of 95% over 16 weeks, which was in a comparable range as our findings at 55 °C for 16 weeks (decrease in M_w of 90%). In contrast to this, accelerated studies performed by Fuoco et al. on solvent cast PLLA ($M_w = 1.18 \times 10^4$ g/mol) showed early sample mass loss of 10% after only 20 days even without the use of enzymes [49]. Although their processing protocol was similar to ours, however, specimens with substantially higher initial crystallinity ($\chi = 76\%$) were obtained. This indicates that crystallinity affects the degradation rate, although it must be taken into account that their degradation temperature has been very close to T_g.

Based on these data, independent of sample preparation, comparability of *in vitro* degradation data can be achieved using either solvent based or compression mold methods, provided comparable initial crystallinity. Noteworthy, molecular mass plays a crucial role when it comes to enzyme-associated surface degradation processes and related mass loss and should be taken into account for *in vitro* study design.

4. Conclusion

The aim of this study was to compare real-time enzyme-associated degradation with accelerated degradation at increased temperatures in order to contribute an understanding of the degradation processes of PLLA and P3HB. Analyzing the degradation of HMW PLLA (L210 and L214) and HMW P3HB films we found that our choice of enzymes, comprising proteinase K, pseudomonas lipase and aspergillus lipase, did not show to affect degradation of P3HB but did have an effect on PLLA degradation. In summary, according to our results and in comparison with the literature, we conclude that in contrast to the initial polymer crystallinity, the manufacturing processes show only a minor impact on the degradation behavior. Regarding molecular weight decrease of both degradation studies, it was found that a real-time study can be reproduced by an accelerated study, such that for PLLA L210 6 weeks at 55 °C reproduces a 26 weeks real-time degradation and for PLLA L214 16 weeks at 55 °C reproduces a 48 weeks real-time degradation. In the case of P3HB, 16 weeks of accelerated degradation can reproduce 108 weeks of real-time degradation. However, it must be considered that wave-like progression of χ limits this developed model. Consequently, accelerated experiments require boundary conditions in terms of identical molecular weight, initial crystallinity, and degradation parameters in order to reproduce degradation processes more realistically.

Author statement

Conceptualization: D.A. and S·O.; methodology: D.A., T.E., K.L. and S·O.; SEM imaging: V·S.; gravimetric analysis, K.L.; GPC measurements: T.R.; DSC analysis: D.A.; writing—original draft preparation: D.A. and S·O.; writing—review and editing: all; project administration: K.-P.S. and N.G.; funding acquisition: K.-P.S. and N.G. All authors have read and agreed to the published version of the manuscript.

Declaration of competing interest

The authors declare that they have no known competing financial interests or personal relationships that could have appeared to influence the work reported in this paper.

Acknowledgements

The authors thank Andrea Rohde, Katja Hahn and Caroline Dudda for their expert technical assistance. Furthermore, financial support by the Federal Ministry of Education and Research (BMBF) within RESPONSE “Partnership for Innovation in Implant Technology” (03ZZ0921A, 03ZZ0922G, 03ZZ0926A) is gratefully acknowledged.

Appendix A. Supplementary data

Supplementary data to this article can be found online at https://doi.org/10.1016/j.polymertesting.2021.107471.

References

[1] J.E. Bergsma, F.R. Rozema, R.R.M. Bos, G. Boering, In vitro predegradation at elevated temperatures of poly(lactide), J. Mater. Sci. Mater. Med. (1995) 642–646, https://doi.org/10.1007/BF00123445.
[2] International Standard Organisation, 10993-13:2019: Biological Evaluation of Medical Devices - Part 13: Identification and Quantification of Degradation Products from Polymeric Medical Devices, 2019.
[3] T. Barrows, Degradable implant materials: a review of synthetic absorbable polymers and their applications, Clin. Mater. 1 (1986) 233–257, https://doi.org/10.1016/S0267-6605(86)80015-4.
[4] C. Migliaresi, A. de Lollis, L. Fambri, D. Cohn, The effect of thermal history on the crystallinity of different molecular weight PLLA biodegradable polymers, Clin. Mater. 8 (1991) 111–118, https://doi.org/10.1016/0267-6605(91)90018-B.
[5] M. Prakasam, J. Locs, K. Salma-Ancane, D. Loca, A. Largeteau, L. Berzina-Cimdina, Biodegradable materials and metallic implants-A review, J. Funct. Biomater. 8 (2017), https://doi.org/10.3390/jfb8040044.
[6] M. Vert, Degradable and bioresorbable polymers in surgery and in pharmacology: beliefs and facts, J. Mater. Sci. Mater. Med. 20 (2009) 437–446, https://doi.org/10.1007/s10856-008-3581-4.
[7] N. Grabow, D.P. Martin, K.-P. Schmitz, K. Sternberg, Absorbable polymer stent technologies for vascular regeneration, J. Chem. Technol. Biotechnol. 85 (2010) 744–751, https://doi.org/10.1002/jctb.2282.
[8] K. Wulf, M. Teske, C. Matschegewski, D. Arbeiter, D. Bajer, T. Eickner, K.-P. Schmitz, N. Grabow, Novel approach for a PTX/VEGF dual drug delivery system in cardiovascular applications-an innovative bulk and surface drug immobilization, Drug Deliv. and Transl. Res. 8 (2018) 719–728, https://doi.org/10.1007/s13346-018-0507-7.
[9] C. Bigalke, F. Luderer, K. Wulf, T. Storm, M. Löbler, D. Arbeiter, B.M. Rau, H. Nizze, B. Vollmar, K.-P. Schmitz, E. Klar, K. Sternberg, VEGF-releasing suture material for enhancement of vascularization: development, in vitro and in vivo study, Acta Biomater. 10 (2014) 5081–5089, https://doi.org/10.1016/j.actbio.2014.09.002.
[10] L.-D. Hou, Z. Li, Y. Pan, M. Sabir, Y.-F. Zheng, L. Li, A review on biodegradable materials for cardiovascular stent application, Front. Mater. Sci. 10 (2016) 238–259, https://doi.org/10.1007/s11706-016-0344-x.
[11] C. Mc Conville, I. Major, D.R. Friend, M.R. Clark, A.D. Woolfson, R.K. Malcolm, Development of polylactide and polyethylene vinyl acetate blends for the manufacture of vaginal rings, J. Biomed. Mater. Res. B Appl. Biomater. 100 (2012) 891–895, https://doi.org/10.1002/jbm.b.31919.
[12] L. Song, Z. Sun, C. Guan, H. Yan, M. Yu, J. Cui, C. Mu, H. Qiu, Y. Tang, Y. Zhao, S. Qiao, H. Suryapranata, R. Gao, B. Xu, First-in-man study of a thinner-strut sirolimus-eluting bioresorbable scaffold (FUTURE-I): three-year clinical and imaging outcomes, Catheter, Cardiovasc. Interv. 95 (1) (2020) 648–657, https://doi.org/10.1002/ccd.28722.
[13] C.J. Li, B. Xu, L. Song, M.Y. Yu, H.B. Yan, H. Qiu, C.W. Mu, J.G. Cui, C.D. Guan, Z. W. Sun, S.B. Qiao, R.L. Gao, The safety and efficacy of Firesorb bioresorbable scaffold in first-in-man study for coronary artery disease: the four-year outcomes, Zhonghua Xinxueguanbing Zazhi 49 (2021) 128–135, https://doi.org/10.3760/cma.j.cn112148-20201110-00897.
[14] A. Chieffo, S.A. Khawaja, A. Latib, B. Vesga, M. Moncada, J.A. Delgado, J. Fonseca, L. Testa, G. Esposito, M. Ferrone, B. Cortese, A. Maehara, J.F. Granada, A. Colombo, First-in-human evaluation of a novel sirolimus-eluting ultra-high molecular weight APTITUDE bioresorbable scaffold: 9- and 24-month imaging and clinical results of the RENASCENT II trial, EuroIntervention 16 (2020) e133–e140, https://doi.org/10.4244/EIJ-D-19-00600.
[15] P. Gasior, Y. Cheng, J. Xia, G.B. Conditt, J.C. McGregor, R. Virmani, J.F. Granada, G.L. Kaluza, Two-year longitudinal evaluation of a second-generation thin-strut sirolimus-eluting bioresorbable coronary scaffold with hybrid cell design in porcine coronary arteries, Cardiol. J. 27 (2020) 115–125, https://doi.org/10.5603/CJ.a2018.0095.
[16] X. Peng, W. Qu, Y. Jia, Y. Wang, B. Yu, J. Tian, Bioresorbable scaffolds: contemporary status and future directions, Front. Cardiovasc. Med. 7 (2020), https://doi.org/10.3389/fcvm.2020.589571.
[17] T. Malm, S. Bowald, A. Bylock, T. Saldeen, C. Busch, Regeneration of pericardial tissue on absorbable polymer patches implanted into the pericardial sac. An immunohistochemical, ultrastructural and biochemical study in the sheep, Scand. J. Thorac. Cardiovasc. Surg. 26 (1992) 15–21, https://doi.org/10.3109/14017439209099048.
[18] P.A. Holmes, Applications of PHB-a microbially produced biodegradable thermoplastic, Phys. Technol. (1985), https://doi.org/10.1088/0305-4624/16/1/305.
[19] H. Zhou, T.B. Green, Y.L. Joo, The thermal effects on electrospinning of polylactic acid melts, Polymer 47 (2006) 7497–7505, https://doi.org/10.1016/j.polymer.2006.08.042.
[20] D. Arbeiter, T. Reske, M. Teske, D. Bajer, V. Senz, K.-P. Schmitz, N. Grabow, S. Oschatz, Influence of drug incorporation on the physico-chemical properties of poly(l-lactide) implant coating matrices-A systematic study, Polymers 13 (2021), https://doi.org/10.3390/polym13020292.

[21] K. Wulf, U. Tschierschky, T. Eickner, N. Grabow, R.G. Mundkowski, Studies on the interaction of polylactid-based planar and nanoparticular biomaterials with serum albumin and fibrinogen, Colloids Surf. B Biointerfaces 159 (2017) 1–6, https://doi.org/10.1016/j.colsurfb.2017.07.002.

[22] M. Grau, J. Matena, M. Teske, S. Petersen, P. Aliuos, L. Roland, N. Grabow, H. Murua Escobar, N.-C. Gellrich, H. Haferkamp, I. Nolte, In vitro evaluation of PCL and P(3HB) as coating materials for selective laser melted porous titanium implants, Materials 10 (2017), https://doi.org/10.3390/ma10121344.

[23] H. Gollwitzer, P. Thomas, P. Diehl, E. Steinhauser, B. Summer, S. Barnstorf, L. Gerdesmeyer, W. Mittelmeier, A. Stemberger, Biomechanical and allergological characteristics of a biodegradable poly(D,L-lactic acid) coating for orthopaedic implants, J. Orthop. Res. (2005) 802–809, https://doi.org/10.1016/j.orthres.2005.02.003.

[24] T.M. Bedair, W. Park, B.-J. Park, M.-W. Moon, K.-R. Lee, Y.K. Joung, D.K. Han, Dual-layer coated drug-eluting stents with improved degradation morphology and controlled drug release, Macromol. Res. 26 (2018) 641–649, https://doi.org/10.1007/s13233-018-6110-4.

[25] A. Rudolph, M. Teske, S. Illner, V. Kiefel, K. Sternberg, N. Grabow, A. Wree, M. Hovakimyan, Surface modification of biodegradable polymers towards better biocompatibility and lower thrombogenicity, PLoS One 10 (2015), e0142075, https://doi.org/10.1371/journal.pone.0142075.

[26] R.T. Liggins, H.M. Burt, Paclitaxel-loaded poly(L-lactic acid) microspheres 3: blending low and high molecular weight polymers to control morphology and drug release, Int. J. Pharm. 282 (2004) 61–71, https://doi.org/10.1016/j.ijpharm.2004.05.026.

[27] D. Arbeiter, T. Eickner, S. Oschatz, T. Reske, O. Specht, M. Teske, V. Senz, K.-P. Schmitz, N. Grabow, Physico chemical and phase separation characterization of high molecular PLLA blended with low molecular PCL obtained from solvent cast processes, Mater. Res. Express 7 (2020) 95302, https://doi.org/10.1088/2053-1591/abb2c9.

[28] H. Tsuji, Y. Ikada, Properties and morphology of poly(l-lactide) 4. Effects of structural parameters on long-term hydrolysis of poly(l-lactide) in phosphate-buffered solution, Polym. Degrad. Stabil. 67 (2000) 179–189, https://doi.org/10.1016/S0141-3910(99)00111-1.

[29] A.C. Renouf-Glauser, J. Rose, D.F. Farrar, R.E. Cameron, The effect of crystallinity on the deformation mechanism and bulk mechanical properties of PLLA, Biomaterials 26 (2005) 5771–5782, https://doi.org/10.1016/j.biomaterials.2005.03.002.

[30] T. Freier, C. Kunze, C. Nischan, S. Kramer, K. Sternberg, M. Saß, U.T. Hopt, K.-P. Schmitz, In vitro and in vivo degradation studies for development of a biodegradable patchbased on poly(3-hydroxybutyrate), Biomaterials (2002) 2649–2657.

[31] M.R. Roohi, M. Kuddus Zaheer, PHB (poly-β-hydroxybutyrate) and its enzymatic degradation, Polym. Adv. Technol. 29 (2018) 30–40, https://doi.org/10.1002/pat.4126.

[32] H. Tsuji, Autocatalytic hydrolysis of amorphous-made polylactides: effects of l-lactide content, tacticity, and enantiomeric polymer blending, Polymer 43 (2002) 1789–1796, https://doi.org/10.1016/S0032-3861(01)00752-2.

[33] G.L. Siparsky, K.J. Voorhees, F. Miao, Hydrolysis of polylactic acid (PLA) and polycaprolactone (PCL) in aqueous acetonitrile solutions: autocatalysis, J. Environ. Polym. Degrad. 6 (1998) 31–41, https://doi.org/10.1023/A:1022826528673.

[34] C. Shih, Chain-end scission in acid catalyzed hydrolysis of poly (d,l-lactide) in solution, J. Contr. Release 34 (1995) 9–15, https://doi.org/10.1016/0168-3659(94)00100-9.

[35] A. Gleadall, J. Pan, M.-A. Kruft, M. Kellomaki, Degradation mechanisms of bioresorbable polyesters. Part 2. Effects of initial molecular weight and residual monomer, Acta Biomater. 10 (2014) 2233–2240, https://doi.org/10.1016/j.actbio.2014.01.017.

[36] R. Scaffaro, A. Maio, E.F. Gulino, Hydrolytic degradation of PLA/Posidonia Oceanica green composites: a simple model based on starting morpho-chemical properties, Compos. Sci. Technol. 213 (2021) 108930, https://doi.org/10.1016/j.compscitech.2021.108930.

[37] S. Li, H. Garreau, M. Vert, Structure-property relationships in the case of the degradation of massive poly(α-hydroxy acids) in aqueous media, J. Mater. Sci. Mater. Med. 1 (1990) 198–206, https://doi.org/10.1007/BF00701077.

[38] H. Pistner, D.R. Bendix, J. Mühling, J.F. Reuther, Poly(L-lactide): a long-term degradation study in vivo, Biomaterials 14 (1993) 291–298, https://doi.org/10.1016/0142-9612(93)90121-H.

[39] S. Gogolewski, M. Jovanovic, S.M. Perren, J.G. Dillon, M.K. Hughes, Tissue response and in vivo degradation of selected polyhydroxyacids: polylactides (PLA), poly(3-hydroxybutyrate) (PHB), and poly(3-hydroxybutyrate-co-3-hydroxyvalerate) (PHB/VA), J. Biomed. Mater. Res. 27 (1993) 1135–1148, https://doi.org/10.1002/jbm.820270904.

[40] D. Cam, S. Hyon, Y. Ikada, Degradation of high molecular weight poly(l-lactide) in alkaline medium, Biomaterials 16 (1995) 833–843, https://doi.org/10.1016/0142-9612(95)94144-A.

[41] S. Iannace, A. Maffezzoli, G. Leo, L. Nicolais, Influence of crystal and amorphous phase morphology on hydrolytic degradation of PLLA subjected to different processing conditions, Polymer 42 (2001) 3799–3807, https://doi.org/10.1016/S0032-3861(00)00744-8.

[42] N.A. Weir, F.J. Buchanan, J.F. Orr, G.R. Dickson, Degradation of poly-L-lactide. Part 1: in vitro and in vivo physiological temperature degradation, Proc. Inst. Mech. Eng. H 218 (2004) 307–319, https://doi.org/10.1243/0954411041932782.

[43] N.A. Weir, F.J. Buchanan, J.F. Orr, D.F. Farrar, G.R. Dickson, Degradation of poly-L-lactide. Part 2: increased temperature accelerated degradation, Proc. Inst. Mech. Eng. H 218 (2004) 321–330, https://doi.org/10.1243/0954411041932809.

[44] N.G. Salguero, M.F. del Grosso, H. Durán, P.J. Peruzzo, J.I. Amalvy, C. R. Arbeitman, G. García Bermúdez, Characterization of biodegradable polymers irradiated with swift heavy ions, Nucl. Instrum. Methods Phys. Res. B 273 (2012) 47–50, https://doi.org/10.1016/j.nimb.2011.07.035.

[45] H. Deplaine, V.A. Acosta-Santamaría, A. Vidaurre, J.L. Gómez Ribelles, M. Doblaré, I. Ochoa, G. Gallego Ferrer, Evolution of the properties of a poly(l -lactic acid) scaffold with double porosity during in vitro degradation in a phosphate-buffered saline solution, J. Appl. Polym. Sci. 131 (2014), https://doi.org/10.1002/app.40956 n/a-n/a.

[46] R.M. Felfel, K.M.Z. Hossain, A.J. Parsons, C.D. Rudd, I. Ahmed, Accelerated in vitro degradation properties of polylactic acid/phosphate glass fibre composites, J. Mater. Sci. 50 (2015) 3942–3955, https://doi.org/10.1007/s10853-015-8946-8.

[47] Z. Wang, Y. Wang, Y. Ito, P. Zhang, X. Chen, A comparative study on the in vivo degradation of poly(L-lactide) based composite implants for bone fracture fixation, Sci. Rep. 6 (2016) 20770, https://doi.org/10.1038/srep20770.

[48] A. Porfyris, S. Vasilakos, C. Zotiadis, C. Papaspyrides, K. Moser, L. van der Schueren, G. Buyle, S. Pavlidou, S. Vouyiouka, Accelerated ageing and hydrolytic stabilization of poly(lactic acid) (PLA) under humidity and temperature conditioning, Polym. Test. 68 (2018) 315–332, https://doi.org/10.1016/j.polymertesting.2018.04.018.

[49] T. Fuoco, M. Cuartero, M. Parrilla, J.J. García-Guzmán, G.A. Crespo, A. Finne-Wistrand, Capturing the real-time hydrolytic degradation of a library of biomedical polymers by combining traditional assessment and electrochemical sensors, Biomacromolecules 22 (2021) 949–960, https://doi.org/10.1021/acs.biomac.0c01621.

[50] International Standard Organisation, 13781:2017(E): Implants for Surgery - Homopolymers, Copolymers and Blends on Poly(lactide) - in Vitro Degradation Testing, 2017. Switzerland.

[51] Y. Doi, Y. Kanesawa, Y. Kawaguchi, M. Kunioka, Hydrolytic degradation of microbial poly(hydroxyalkanoates), Makromol. Chem. Rapid Commun. (1989) 227–230, https://doi.org/10.1002/marc.1989.030100506.

[52] P. Kurcok, M. Kowalczuk, G. Adamus, Z. Jedliński, R.W. Lenz, Degradability of poly(β-hydroxybutyrate)s. Correlation with chemical microstructure, J. Macromol. Sci. Phys. 32 (1995) 875–880, https://doi.org/10.1080/10601329508010300.

[53] M. Canetti, M. Urso, P. Sadocco, Influence of the morphology and of the supermolecular structure on the enzymatic degradation of bacterial poly(3-hydroxybutyrate), Polymer (1999) 2587–2594, https://doi.org/10.1016/S0032-3861(98)00503-5.

[54] V.A. Zhuikov, Y.V. Zhuikova, T.K. Makhina, V.L. Myshkina, A. Rusakov, A. Useinov, V.V. Voinova, G.A. Bonartseva, A.A. Berlin, A.P. Bonartsev, A. L. Iordanskii, Comparative structure-property characterization of poly(3-hydroxybutyrate-Co-3-Hydroxyvalerate)s films under hydrolytic and enzymatic degradation: finding a transition point in 3-hydroxyvalerate content, Polymers 12 (2020), https://doi.org/10.3390/polym12030728.

[55] F. Li, S. Rastogi, D. Romano, Synthesis of ultrahigh molecular weight PLAs using a phenoxy-imine Al(III) complex, ACS Omega 5 (2020) 24230–24238, https://doi.org/10.1021/acsomega.0c01952.

[56] T. Casalini, F. Rossi, A. Castrovinci, G. Perale, A perspective on polylactic acid-based polymers use for nanoparticles synthesis and applications, Front. Bioeng. Biotechnol. 7 (2019) 259, https://doi.org/10.3389/fbioe.2019.00259.

[57] International Standard Organisation, 13781:1997(E): Poly(L-Lactide) Resins and Fabricated Forms for Surgicals Implants - in Vitro Degradation Testing, 1997. Switzerland.

[58] International Standard Organisation, 15814:1999(E): Implants for Surgery - Copolymers and Blends Based on Poly(lactide) - in Vitro Degradation Testing, 1999. Switzerland.

[59] E.W. Fischer, H.J. Sterzel, G. Wegner, Investigation of the structure of solution grown crystals of lactide copolymers by means of chemical reactions, Kolloid-Z.u.Z. Polymere (1973) 980–990, https://doi.org/10.1007/BF01498927.

[60] P.J. Barham, A. Keller, E.L. Otun, P.A. Holmes, Crystallization and morphology of a bacterial thermoplastic: poly-3-hydroxybutyrate, J. Mater. Sci. 19 (1984) 2781–2794, https://doi.org/10.1007/BF01026954.

[61] K. Herzog, R.-J. Müller, W.-D. Deckwer, Mechanism and kinetics of the enzymatic hydrolysis of polyester nanoparticles by lipases, Polym. Degrad. Stabil. 91 (2006) 2486–2498, https://doi.org/10.1016/j.polymdegradstab.2006.03.005.

[62] M. Żenkiewicz, A. Richert, R. Malinowski, K. Moraczewski, A comparative analysis of mass losses of some aliphatic polyesters upon enzymatic degradation, Polym. Test. 32 (2013) 209–214, https://doi.org/10.1016/j.polymertesting.2012.10.011.

[63] A. Banerjee, K. Chatterjee, G. Madras, Enzymatic degradation of polymers: a brief review, Mater. Sci. Technol. 30 (2014) 567–573, https://doi.org/10.1179/1743284713Y.0000000503.

[64] G. Tomasi, M. Scandola, B.H. Briese, D. Jendrossek, Enzymatic degradation of bacterial poly(3-hydroxybutyrate) by a depolymerase from Pseudomonas lemoignei, Macromolecules 29 (1996) 507–513, https://doi.org/10.1021/ma951067n.

[65] K. Mukai, Y. Doi, Y. Sema, K. Tomita, Substrate specificities in hydrolysis of polyhydroxyalkanoates by microbial esterases, Biotechnol. Lett. 15 (1993) 601–604, https://doi.org/10.1007/BF00138548.

[66] S.C. Woodward, P.S. Brewer, F. Moatamed, A. Schindler, C.G. Pitt, The intracellular degradation of poly(epsilon-caprolactone), J. Biomed. Mater. Res. 19 (1985) 437–444, https://doi.org/10.1002/jbm.820190408.

[67] S. Li, M. Vert, Biodegradable Polymers, Principles & Applications: Biodegradation of Aliphatic Polyesters, Chapman & Hall, London, 1995, ISBN 0-412-59010-7.

[68] H. Tsuji, A. Mizuno, Y. Ikada, Properties and morphology of poly(L-lactide). III. Effects of initial crystallinity on long-termin vitro hydrolysis of high molecular weight poly(L-lactide) film in phosphate-buffered solution, J. Appl. Polym. Sci. 77

(2000) 1452–1464. https://doi.org/10.1002/1097-4628(20000815)77:7<1452:AID-APP7>3.0.CO;2-S.
[69] K. Sudesh, H. Abe, Y. Doi, Synthesis, structure and properties of polyhydroxyalkanoates: biological polyesters, Prog. Polym. Sci. (2000) 1503–1555, https://doi.org/10.1016/S0079-6700(00)00035-6.
[70] A. Leroy, S. Ribeiro, C. Grossiord, A. Alves, R.H. Vestberg, V. Salles, C. Brunon, K. Gritsch, B. Grosgogeat, Y. Bayon, FTIR microscopy contribution for comprehension of degradation mechanisms in PLA-based implantable medical devices, J. Mater. Sci. Mater. Med. 28 (2017) 87, https://doi.org/10.1007/s10856-017-5894-7.
[71] A. Tapadiya, N. Vasanthan, Crystallization and alkaline hydrolysis of poly(3-hydroxybutyrate) films probed by thermal analysis and infrared spectroscopy, Int. J. Biol. Macromol. 102 (2017) 1130–1137, https://doi.org/10.1016/j.ijbiomac.2017.04.095.
[72] J.M. Anderson, Perspectives on the in Vivo Responses of Biodegradable Polymers, CRC Press, Boca Raton, FL, USA, 1995, ISBN 084934896X.

ACS Biomaterials SCIENCE & ENGINEERING

pubs.acs.org/journal/abseba

Article

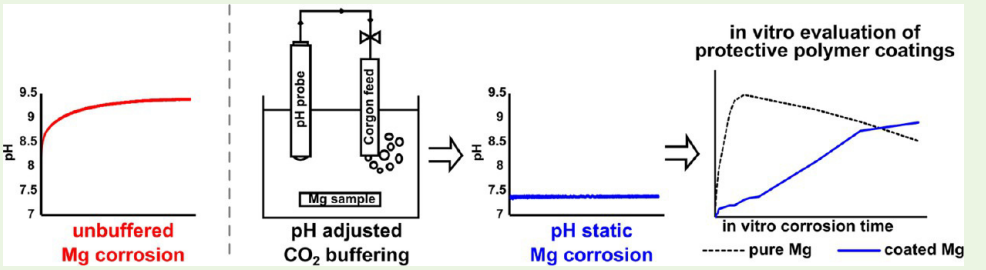
In Vitro Corrosion of Polyester-Coated Magnesium Alloy under pH-Static Conditions

Nicklas Fiedler,* Michael Teske, Sophie-Charlotte Nelz, Jonas Willem Flügge, Volkmar Senz, Dalibor Bajer, Niels Grabow, and Stefan Oschatz

Cite This: *ACS Biomater. Sci. Eng.* 2024, 10, 5844−5855

Read Online

ACCESS | Metrics & More | Article Recommendations



ABSTRACT: The resorption rate of bioresorbable implants requires tuning to match the desired field of application. The use of Mg as implant material is highly advantageous, as it provides sufficient mechanical strength combined with its biodegradability. Consequently, the implant vanishes after it has served its intended purpose, allowing the complete restoration of natural tissue and organ function. However, a biodegradable Mg implant requires a biodegradable coating to slow the rate of Mg corrosion, as a permanent coating would negate the benefits of using Mg as an implant material. Therefore, degradable polymers are the materials of choice, especially polyester-based coatings, such as PLLA, as they have been proven in clinical practice over the long term. Within this work, the degradation retarding effect of a physical barrier in form of four clinically relevant polyester-based coatings, poly-L-lactide (PLLA), poly-L-lactide-*co*-glycolide (PLGA), poly(L-lactide-*co*-PEG) triblock copolymer (PLLA-*co*-PEG), and polydioxanone (PDO), is investigated *in vitro* under pH-static conditions using CO_2 gas to compensate pH changes due to Mg corrosion. Coating thicknesses of 7.5 to 8.3 μm were comparable to commercially available stent systems. Quantitative analysis of magnesium concentration in buffered test medium by a photometric assay allows real-time monitoring. Shielding effect of different polyesters through polymer coating and formation of a protective passivation layer beneath the polymer coating was observed and characterized using SEM and EDX techniques. Our finding was that even imperfect polymer layers provide a considerable protective effect, and the used *in vitro* setup matches reported *in vivo* observations regarding elemental composition of corrosion products.

KEYWORDS: *magnesium alloy, implant material, biodegradable polymer coating, in vitro corrosion*

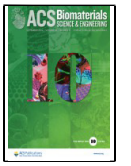
Downloaded via UNIV ROSTOCK on June 5, 2025 at 12:43:08 (UTC).
See https://pubs.acs.org/sharingguidelines for options on how to legitimately share published articles.

INTRODUCTION

In biomaterial sciences, the development and refinement of temporary implant materials are a major issue. Besides the benefits of degradable materials in general, primarily autonomous dissolution upon functional fulfillment or prevention of reoperations, metals offer application-specific advantages. In this context, both magnesium (Mg) and its alloys are potent substrates for load-bearing structures, e.g., in stent applications, osteosynthesis systems, or as bone screws.[1−4] Mg and its alloys provide beneficial properties in mechanical performance, degradability, as well as tissue-implant-interaction; they are bioactive and most importantly biocompatible.[2,5,6]

In vivo, the degradation of magnesium proceeds via corrosion processes. Pure magnesium shows very rapid dissolution in physiological media accompanied by strong H_2 evolution.[7−9] This leads to limited mechanical integrity of the implanted material combined with local negative or cell-toxic effects, due to the formation of an alkalized environment in the surrounding area of the implant surface.[5,10] Figure 1 presents a simplified schematic illustration of magnesium dissolution. The main reactions, along with detectable reaction products, are described. Moreover, the illustration on the right is extended by a polymer coating on the magnesium surface, influencing the reaction processes. Other studies indicate that diffusion-induced reactions of the magnesium substrate do occur, especially for coated substrates. The collection of evaporating hydrogen leads

Received: May 6, 2024
Revised: August 15, 2024
Accepted: August 16, 2024
Published: August 23, 2024



ACS Publications

© 2024 The Authors. Published by American Chemical Society

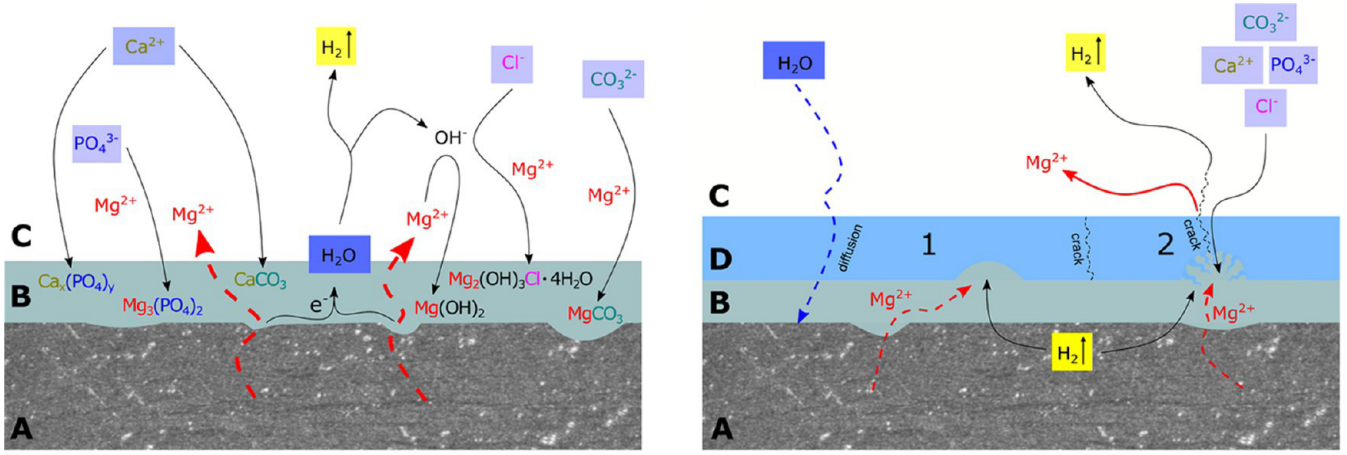


Figure 1. Schematic illustration of corrosion process for uncoated (left) and polymer-coated (right) magnesium specimens in physiological medium; (A) magnesium substrate, (B) layer of reaction products on magnesium surface, (C) surrounding medium, and (D) polymer coating. Blue shaded ions and molecules originate from the medium, yellow shaded hydrogen evaporates. Numbers 1 and 2 indicate the progress of damage to the layer integrity by generated H_2 (modified according to refs 11,12).

to a partial limitation of the coating's integrity and promotes cracks through the coating.[11]

Mg alloys containing aluminum and zinc (Mg−Al−Zn, e.g., AZ91 or AZ31) or rare earth elements (Mg-REE, e.g., WE43) showed to be less prone for rapid dissolution in water and are well described in the literature.[1,5,13−15] Besides improvements in corrosion kinetics, the alloying elements may also affect the microstructure and enhance the mechanical properties, biocompatibility and cytotoxicity.[15] In particular, Mg−Al alloys are used mainly as model materials in research, e.g., for coating evaluations.[16−18] Although Al must be considered toxic, in particular for the nervous system, the low content did not show to negatively influence cell viability *in vitro* and *in vivo*[13] A common approach to further control and delay Mg dissolution is to physically separate the surface from the surrounding medium, e.g., by applying a coating. These can comprise a variety of materials, in particular polymers, metals, ceramics, and composites thereof, and are accessible by a wide range of coating techniques such as spraying, dipping, or vapor deposition. To preserve one of the strongest benefits of Mg-based biomaterials, being their biodegradability, a common way is the use of degradable polymer coatings as these also vanish with the implant upon completion of their function.[9,14,19−21] Applying such polymer coatings leads to an initially completely shielded magnesium substrate, ensuring the integrity and the effectiveness of the implant during the critical post implantation time, before regenerative healing occurs. The protective effect of the coating is progressively weakened as the polymer degrades over time and thus gradually promotes corrosion of the magnesium substrate. Consequently, for the development of protective coatings or innovative Mg alloys, the rapid release of magnesium and possible alloying elements needs to be evaluated, as well as effects of local pH on surrounding cells and tissue.[22,23]

However, the development of process accompanying *in vitro* protocols for the evaluation of the protective effectiveness of coated Mg under physiological conditions is challenging due to the strong influence of the experimental conditions on Mg and the polymer degradation behavior. In this context, as most important parameters, medium composition, static or dynamic conditions, pH regulation, and temperature should be taken into account.[11] Furthermore, reaction-induced changes in environmental conditions, particularly increase in pH and total salt concentration of the medium, are critical to the test setup when investigating the corrosion of magnesium and its alloys.[24]

In the present study, we developed a test protocol for real-time evaluation of the protective potential of polymer coatings on Mg-based biomaterials. We used common polyesters, as this material class is frequently applied to biomaterials in clinical use.[25,26] Mg corrosion has a drastic impact on the pH of the surrounding medium. *In vivo*, this is compensated by the body fluids' high volume, permanent flow, and buffering effect. Yet, *in vivo* development studies are costly and time-consuming in preparation and implementation, and testing every developmental step on a living animal is comprehensibly unrealistic. Hence, there is a high demand for suitable *in vitro* models for the in-process testing of biomedical device innovations. Herein, studies on the *in vitro* Mg dissolution behavior of coated AZ31B substrates were carried out using the developed test bench, allowing for pH control for each test unit individually. As a versatile and simplistic approach in terms of lab equipment, we used a photometric assay known from clinical practice for the quantitative analysis of Mg dissolution.[27] Our approach enables data analysis and evaluation in real time, while the test specimen remains untouched. The stabilization of pH is achieved by the controlled addition of gaseous CO_2, which corresponds well with the impact of the carbonate buffer system in the human body. Buffering with organic systems such as TRIS (tris-(hydroxymethyl)aminomethane) or HEPES (4-(2-hydroxyethyl)-1-piperazineethanesulfonic acid) is not suitable in this approach due to the limited buffering capacity as well as the reduced formation of corrosion products with the resulting destabilization of the corrosion layer and the increase of the corrosion rate.[11,28] Despite the influence of flow conditions on the corrosion, this study targets a uniform circulation of the medium only.[23,29]

The experimental studies were performed and evaluated referring to ASTM G31-72 (2004) guideline for corrosion testing.[30] Aspects on the scope of the studies, test setup, preparation of the specimens, test conditions, and interpretation of the measurement results are chosen in accordance with ASTM G31-72. As we intended to simulate *in vivo* conditions, SBF (simulated body fluid) to reproduce physiologic ion concentrations was used. SBF in particular is susceptible to

https://doi.org/10.1021/acsbiomaterials.4c00835
ACS Biomater. Sci. Eng. 2024, 10, 5844−5855

changes in the ion concentration, especially due to the precipitation of Ca and Mg salts. One possible way to overcome this effect would be to change the medium regularly. However, this would disturb the solubility equilibria formed during the experiment and could therefore influence the Mg corrosion process.[23] In addition, media changes would be another potential source of error for real-time photometric Mg assay. *In vitro* Mg corrosion requires practical trade-offs, yet we approach the *in vivo* situation with our experimental setup by using CO_2 to buffer the pH change as it occurs in blood. However, we decided not to perform media changes in our study, especially given the relatively short duration of the experiment. Furthermore, as we wanted to measure the progression of Mg elution during the corrosion process, no Mg salts were added to the SBF used in this study. For long-term studies, however, the stability of the SBF must be taken into account.

However, using photometric determination to quantify the dissolved Mg instead of gravimetric determination (mass loss) differs from the ASTM recommendations as an alternative quantification approach. The selected sample geometry variation was necessary to avoid the machining processes with magnesium.

Comparable *in vitro* studies investigating coated magnesium substrates conclude that polymer coatings generally slow down corrosion.[9,31−35] In contrast to these studies, our research focus was on comparing bioresorbable polymer coatings and the protective effect against initial magnesium dissolution corrosion with real-time data.

Our data indicate that polyester coatings on AZ31B provide a protective barrier against excessive initial corrosion. Moreover, unlike other immersion corrosion studies, pH stabilization offers an insight into the elemental (e.g., Ca, P) composition of the corrosion layer, which corresponds well with reaction products described in the literature. As is known from the literature, higher pH values (pH 7.4 and above) promote the formation of hydroxyapatite-like material from the medium.[36] In the case of Mg corrosion, however, the pH rises drastically above the physiological range in a very short time. However, this change to very basic conditions has a considerable influence on Mg corrosion, as the passivation layer has a more protective effect with increasing pH.[23] However, the influence of CO_2 buffering on the formation of the passive layer must be taken into account. The presented experimental setup enables nondestructive real-time monitoring of the magnesium concentration in the corrosion medium and at the same time provides pH-stable corrosion conditions, mimicking *in vivo* pH regulation, suitable for an *in vitro* degradation study of Mg-based implants on a laboratory scale and for the evaluation of protective biomaterial coatings.

MATERIALS AND METHODS

Materials Preparation. Magnesium alloy specimens AZ31B with dimensions of 1 × 1 × 40 mm rods were obtained by shear cutting from sheet metal (MgAl3Zn1, Hans-Erich Gemmel & Co. GmbH, Berlin, Germany). Before further use, all Mg alloy specimens were rinsed using acetone and subsequently treated with Ar plasma for 30 min for superficial cleaning using a Diener Femto plasma chamber (Diener electronic GmbH & Co. KG, Ebhausen, Germany) at 13.56 MHz and 0.3 mbar chamber pressure and 80 W power output/capacity.

For spray coating, polymers used were poly(L-lactide (PLLA, RESOMER L 210 S, inherent viscosity ($CHCl_3$) η = 3.3−4.3 dL/g), poly(L-lactide-*co*-glycolide) (PLGA, RESOMER LG 857 S, inherent viscosity ($CHCl_3$) η = 5.0−7.0 dL/g), poly(L-lactide-*co*-PEG) triblock copolymer (PLLA-*co*-PEG, RESOMER LPt 46, inherent viscosity ($CHCl_3$) η = 1.8−2.6 dL/g), and poly(dioxanone) (PDO, RESOMER X 206 S, inherent viscosity ($CHCl_3$) η = 1.5−2.2 dL/g). All polymers were purchased from Evonik Industries AG, Essen, Germany, and used without further treatment. Chloroform was purchased from VWR International and was of technical grade.

SBF buffer was freshly prepared before each corrosion experiment by dissolving the respective salts in deionized water, yielding a final composition of $C(KCl)$ = 0.149 mg/mL, $C(NaCl)$ = 2.92 mg/mL, $C(NaHCO_3)$ = 1.13 mg/mL, $C(CaCl_2{\cdot}H_2O)$ = 0.184 mg/mL, and $C(KH_2PO_4)$ = 0.068 mg/mL. The corresponding ion concentrations are $C(Na^+)$ = 63.42 mM, $C(K^+)$ = 2.50 mM, $C(Ca^{2+})$ = 1.43 mM, $C(Cl^-)$ = 54.82 mM, $C(HCO_3^-)$ = 13.45 mM, and $C(H_2PO_4^-)$ = 0.50 mM.

For photometrical Mg^{2+} quantification, 100 μL of the medium was added to a solution of $C = 5.65 \times 10^{-2}$ mg/mL Xylidyl blue I buffered with ethanolamine (C = 0.06 mL/mL), to which EGTA (ethylene glycol-bis(β-aminoethyl ether)-N,N,N′,N′-tetraacetic acid, $C = 2.28 \times 10^{-2}$ mg/mL) was added as chelating agent for masking calcium ions. Measurements were performed in duplicates. Calibration of the assay has been conducted using $MgSO_4$ in SBF. Photometrical analysis was carried out at λ = 520 nm on a Thermo Scientific BioMate 3S UV-visible Spectrometer (Thermo Scientific, Darmstadt, Germany).

Spray Coating of Mg Rod Specimens. Polymer-coated Mg rod specimens were produced using airbrush spray coating process as reported by our group before.[26,37] In brief, the polymer was dissolved in $CHCl_3$, giving a final ratio of 0.27 mg/mL polymer/solvent. A total amount of m_{PLLA} = 1624 μg ± 67 μg, m_{PLGA} = 1798 μg ± 69 μg, $m_{PLLA\text{-}co\text{-}PEG}$ = 1667 μg ± 51 μg, and m_{PDO} = 1542 μg ± 28 μg polymer film was formed and checked via weighing. Residual solvent from the process was removed from the coated Mg rods by thermal annealing in a vacuum drying chamber under reduced pressure at 80 °C overnight.

Gravimetric Measurements. All gravimetrical measurements were performed using a MYA0.8/3.4Y precision balance (Radwag Waagen GmbH, Germany) at room temperature. For analysis of weight loss for corroded samples, measurements were repeated twice. The coating process with different polyesters was monitored by weighing before and after coating to determine coating mass. For determining the residual mass of (coated) magnesium rods after removal of corrosion layer, a chemical cleaning procedure following ASTM G1-03 (2017)[38] was applied. First, the polymer coating was removed by using $CHCl_3$. For comparability, this step was also performed for uncoated Mg specimens. Following, the samples were immersed for 5 min at room temperature in a chromic acid solution containing 4 g of chromium trioxide (CrO_3) and 0.2 g of silver nitrate ($AgNO_3$) in 20 mL of deionized water. Afterward, specimens were rinsed with acetone and dried in air.

Imaging. Mg alloy specimens were characterized by means of light microscopic photography using an Olympus SC50 digital camera mounted on an Olympus SZX10 stereomicroscope and cellSens Standard imaging software (Olympus, Tokyo, Japan). Scanning electron microscopy (SEM) was carried out using an SEM Quanta FEG 250 (FEI Company, Frankfurt, Germany). For SEM imaging, the samples were mounted onto aluminum trays with conductive carbon pads. For SEM imaging of cross sections of embedded samples, the samples were additionally contacted with copper adhesive tapes to reduce measurement artifacts due to the static charge of the sample. SEM investigations were performed using high vacuum and 10 kV with a working distance of approximately 10 mm using an Everhart-Thornley secondary electron detector (ETD). The images were taken at 800× magnification. Energy-dispersive X-ray spectroscopy (EDX) was performed by using an EDAX microanalysis system.

Embedding and Cross-Sectioning of Mg Samples. For cross-sectioning, Mg samples were embedded in epoxy resin (EpoxiCure and EpoxiCure 2, ratio 2:1, Buehler, Lake Bluff). After curing, transverse grinding was performed using a TegraPol 15 (Struers, Ballerup, Denmark) with water as medium, a grinding wheel to sample holder rotation ratio of 40:50, a contact force of 10 N, and grinding disks with a grid size of 1.000 to 2.400 for 1 min each. Final polishing was performed on an MD-Floc polishing cloth (Struers, Ballerup, Denmark) with

https://doi.org/10.1021/acsbiomaterials.4c00835
ACS Biomater. Sci. Eng. 2024, 10, 5844−5855

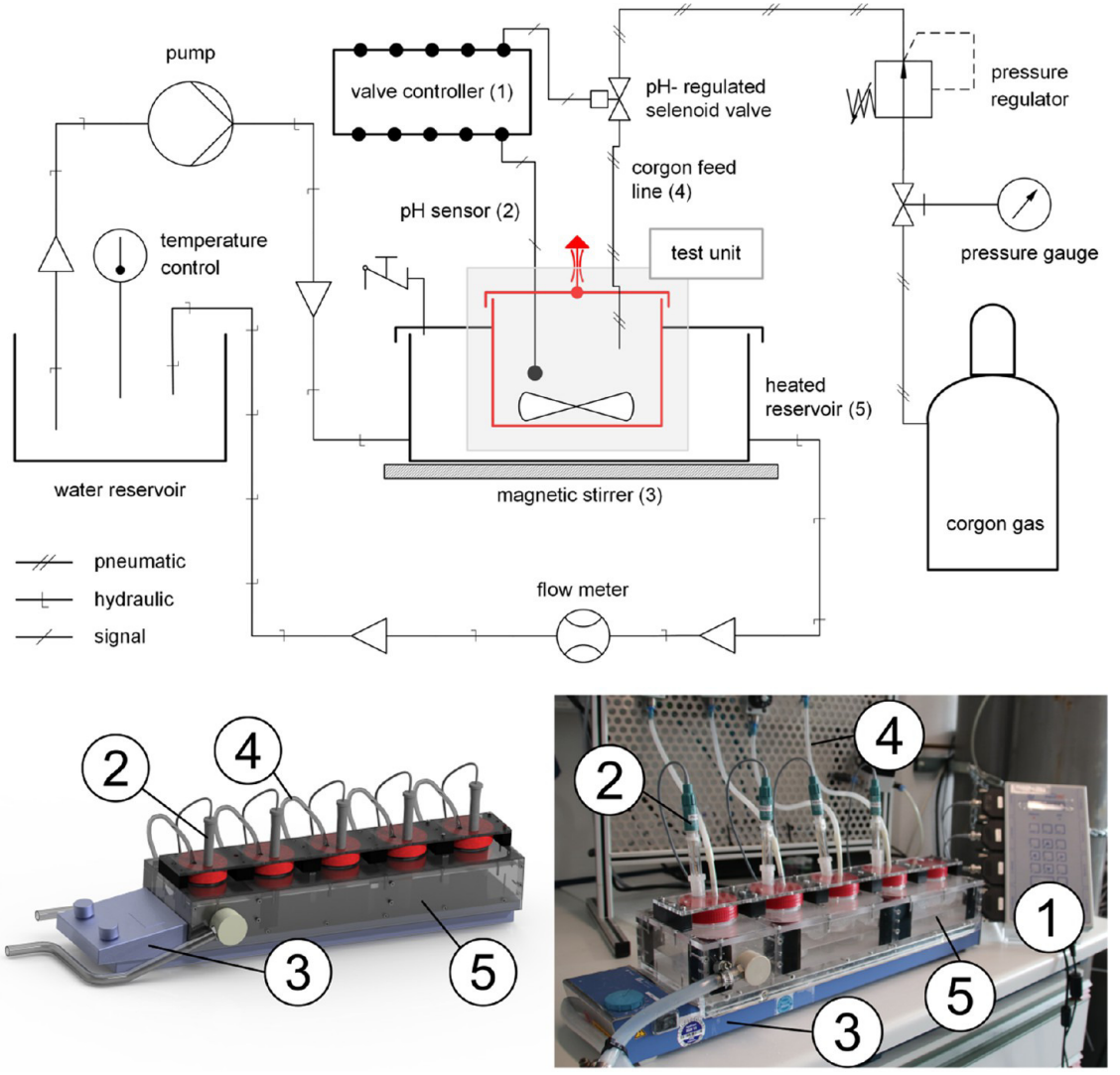


Figure 2. Block diagram illustrating the test bench function (top), rendered (bottom left), and photographical (bottom right) image of the manufactured test setup. (1) Valve controller, (2) pH sensor, (3) magnetic stirrer, (4) corgon feed line, (5) heated reservoir.

Al_2O_3 polishing suspension (MasterPrep, Buehler, Lake Bluff) at a ratio of 1:3 in water. After polishing, samples were briefly rinsed with EtOH and dried in air stream.

pH-Adjusted *In Vitro* Corrosion of Coated and Uncoated Mg Rod Specimens. For controlled *in vitro* corrosion experiments, a test environment was developed. A test chamber was indirectly temperature-controlled by a water circulation bath with constant recirculation speed and an integrated circulating thermostat. Test temperature was set to 37 °C. Samples were kept in separate reservoirs in SBF equipped with a magnetic stirrer, pH probe, and gas feed tube. The pH probe was connected to an iks aquastar (iks ComputerSysteme GmbH, Karlsbad, Germany) control unit, which was connected to electronically controlled valves. This test unit in 5-fold version was used corresponding to the study design. To ensure a constant and comparable flow around the test specimens, the medium was continuously circulated and specimens were placed on a 3D-printed perforated surface at fixed vertical level inside each test unit. pH was logged separately for each reservoir and thus for each sample (measuring interval = 10 min). Based on the comparison of target pH and measured pH, a solenoid valve was controlled for each sample reservoir. Corgon gas (Ar/CO_2 (90/10), Corgon 10, Linde GmbH, Pullach, Germany) was released into the medium to regulate pH ± 0.05 around the target value of pH, which was set to pH = 7.4. The block diagram in Figure 2 shows a schematic illustration of the test setup.

The individual reservoirs were left open to the atmosphere to compensate for the gas volume increase generated by gas injection. *In vitro* corrosion tests were performed over a period of 14 days. For quantification of eluted Mg ions, sampling of 100 μL of corrosion medium has been performed at determined intervals between 1 and 336 h (14 day) incubation.

RESULTS AND DISCUSSION

***In Vitro* Test Bench.** The corrosion reaction of AZ31B Mg alloy is complex (Figure 1), but can be summarized by the reactions shown in eqs 1−5[39,40]

Anodic reaction

$$Mg(s) \rightarrow Mg^{2+}(aq) + 2e^- \quad (1)$$

Cathodic reaction

$$2H_2O + 4e^- \rightarrow H_2(\uparrow) + 2OH^-(aq) \quad (2)$$

followed by

$$Mg^{2+}(aq) + OH^-(aq) \rightarrow Mg(OH)^+(aq) \quad (3)$$

and

$$Mg(OH)^+(aq) + OH^-(aq) \rightarrow Mg(OH)_2(s) \quad (4)$$

https://doi.org/10.1021/acsbiomaterials.4c00835
ACS Biomater. Sci. Eng. 2024, 10, 5844−5855

and with increasing pH followed by

$$Mg^{2+}(aq) + 3OH^{-}(aq) + Cl^{-}(aq) + 4H_2O \rightarrow Mg_2(OH)_3Cl{\cdot}4H_2O(s) \quad (5)$$

Figure 3 compares the pH evolution of unbuffered and CO_2-buffered SBF medium for corrosion of uncoated AZ31B specimens. In accordance with the literature, pH increases rapidly as magnesium dissolves due to the electrochemical formation of $Mg(OH)_2$ and other basic Mg salt species. The pH evolution progressively plateaus in a highly alkaline pH of about 9.5 after just about 40 h with increasing dissolution in unbuffered SBF (Figure 3).

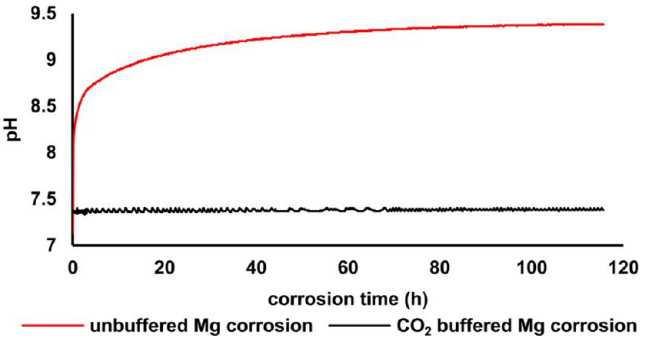
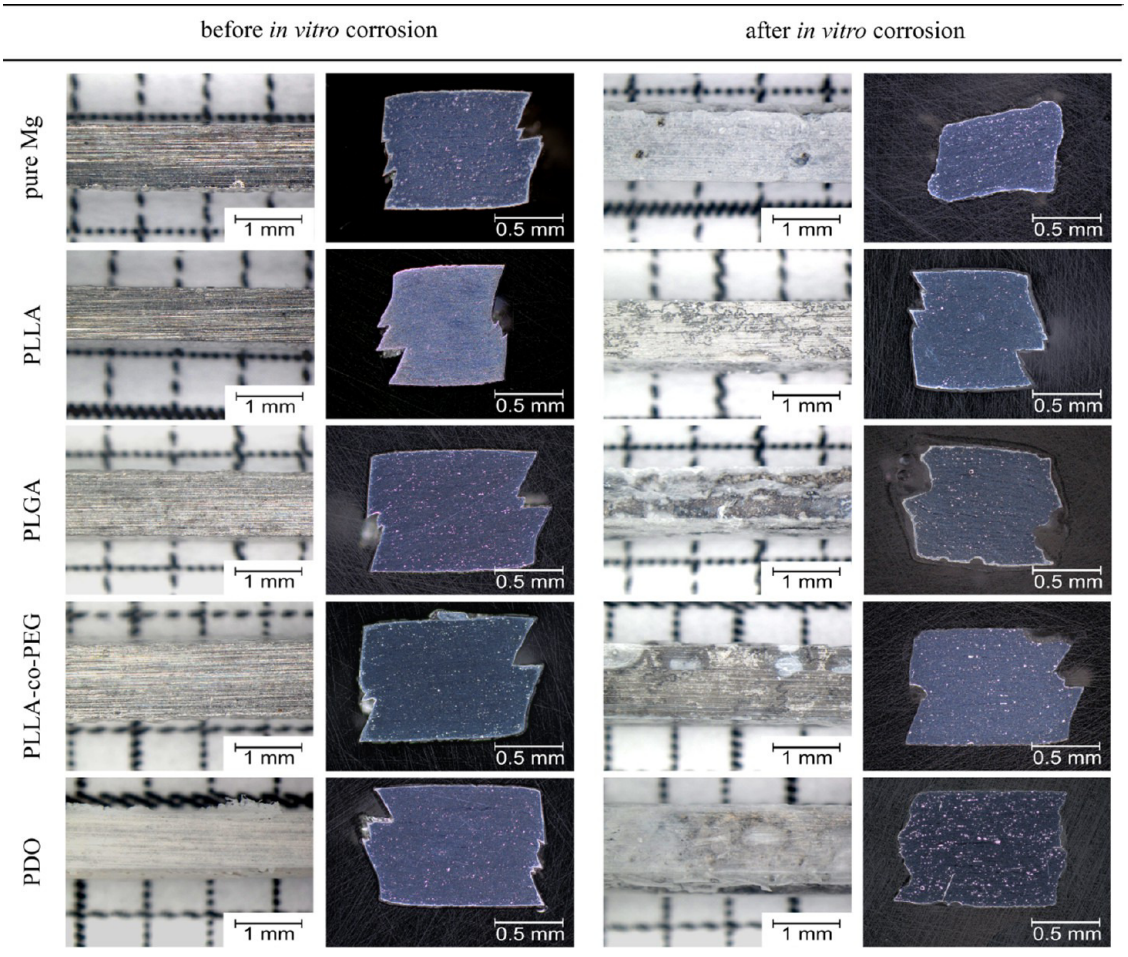


Figure 3. Unbuffered versus CO_2-buffered pH evolution of the SBF medium for corrosion of Mg specimens. After 120 h, for the unbuffered corrosion experiment, a plateau at pH ∼ 9.35 was formed. CO_2 buffering leads to the pH range of 7.33 to 7.40.

In contrast to this, CO_2 buffering ensured a stable pH = 7.33 to 7.40 until 120 h immersion time. Live monitoring of the pH for each vessel and pH-dependent release of CO_2 into the medium ensures pH stability, especially regarding acidity, and avoids overconcentration of carbonate. Opening and closing of the solenoid valves for Corgon depending on live monitoring of pH lead to apparent broadening but indeed wave-shaped behavior of the pH curve in Figure 3. An initial study of the SBF used showed that the medium was stable for up to 2 weeks at 37 °C on a laboratory shaker and that precipitates only formed after this period, which is also consistent with the literature.[41] However, a limitation of this setup is the low solubility of the hence formed $MgCO_3$ salts and subspecies. As Mg precipitates from the solution, the concentration equilibrium is shifted in such a way that Mg can in turn dissolve from the corrosion layer, influencing the formation of the passive layer, and also limiting quantitative analysis of the dissolved Mg in the medium due to

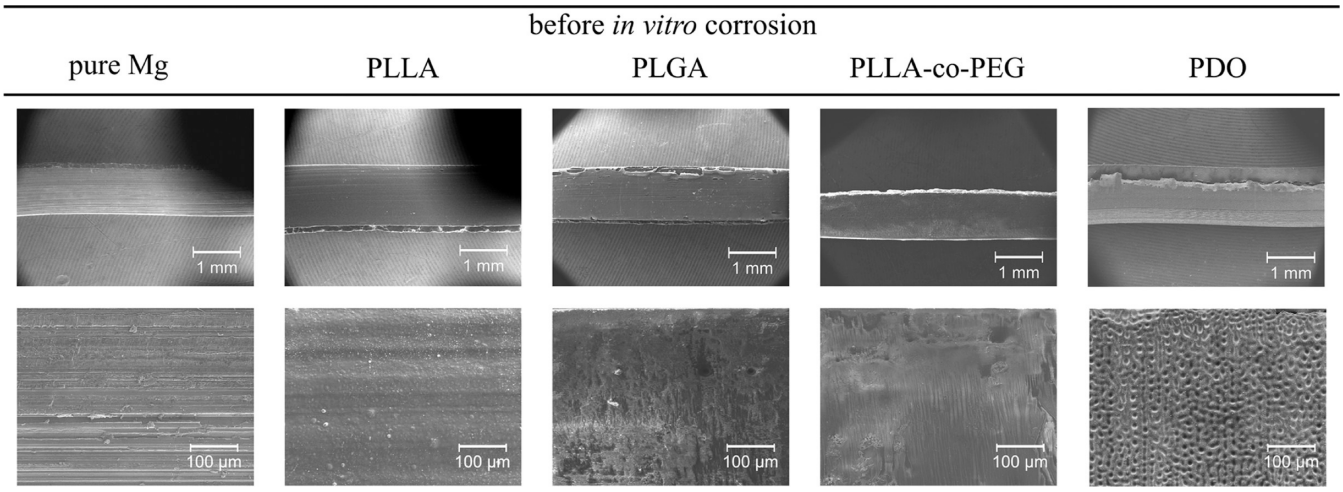
Table 1. Macrophotographical Characterization of Mg Specimen and Polyester-Coated Mg Specimen before and after 14 Days of *In Vitro* Corrosion[a]



[a]Dark-field microscopy was used to image cross sections of samples after embedding in epoxy resin.

https://doi.org/10.1021/acsbiomaterials.4c00835
ACS Biomater. Sci. Eng. 2024, 10, 5844−5855

Table 2. SEM Images of Mg Specimen and Mg Specimens Coated with PLLA, PLGA, PLLA-co-PEG, and PDO before *In Vitro* Corrosion[a]



[a]Top row: Overview images. Bottom row: Detailed micrographs of the specimen surface.

the low solubility.[42] A change in medium must still be considered for long-term tests.

Due to the constant gas input for buffering, the test unit is kept ventilated to avoid excess pressure. Thus, there is a loss of media volume due to evaporation and carryover of medium with the gas flow. When analyzing the magnesium concentration and interpreting the results accordingly, the volume loss of the test medium during the test period must therefore be taken into account. Thus, the volume loss of the medium was determined by a two-point calibration using linear fitting of the start and end points of the medium volume, and the Mg^{2+} concentration was volume-adjusted at each sampling point.

***In Vitro* Corrosion of Mg Alloy Specimens under pH-Static Conditions.** A biodegradable Mg implant requires a biodegradable coating to slow the rate of Mg corrosion, as a permanent coating would negate the benefits of using Mg as an implant material. Therefore, degradable polymers are the materials of choice, especially polyester-based coatings such as PLLA, as they have been proven in clinical practice over the long term. However, these polymers show an acidic degradation. Due to the low mass fraction of the polymer compared to magnesium and the much slower polymer degradation time compared to Mg corrosion, we estimate this influence to be negligible. Although this can lead to a change in the pH value in the microenvironment, we counteract this with a correspondingly large media volume and permanent stirring.

The polymer, more specifically polyester, coatings used in this study were selected for their relevance in research and clinical practice (e.g., orthopedic implants[35] or Mg-based stents[43]). The four selected coatings have in common the fact that their protective effect is of a passive nature, as the polymers mainly act as a physical diffusion barrier. For reasons of comparability, the spraying process was not optimized for each polymer, but a standard process was used, which resulted in different coating quality depending on the polymer.

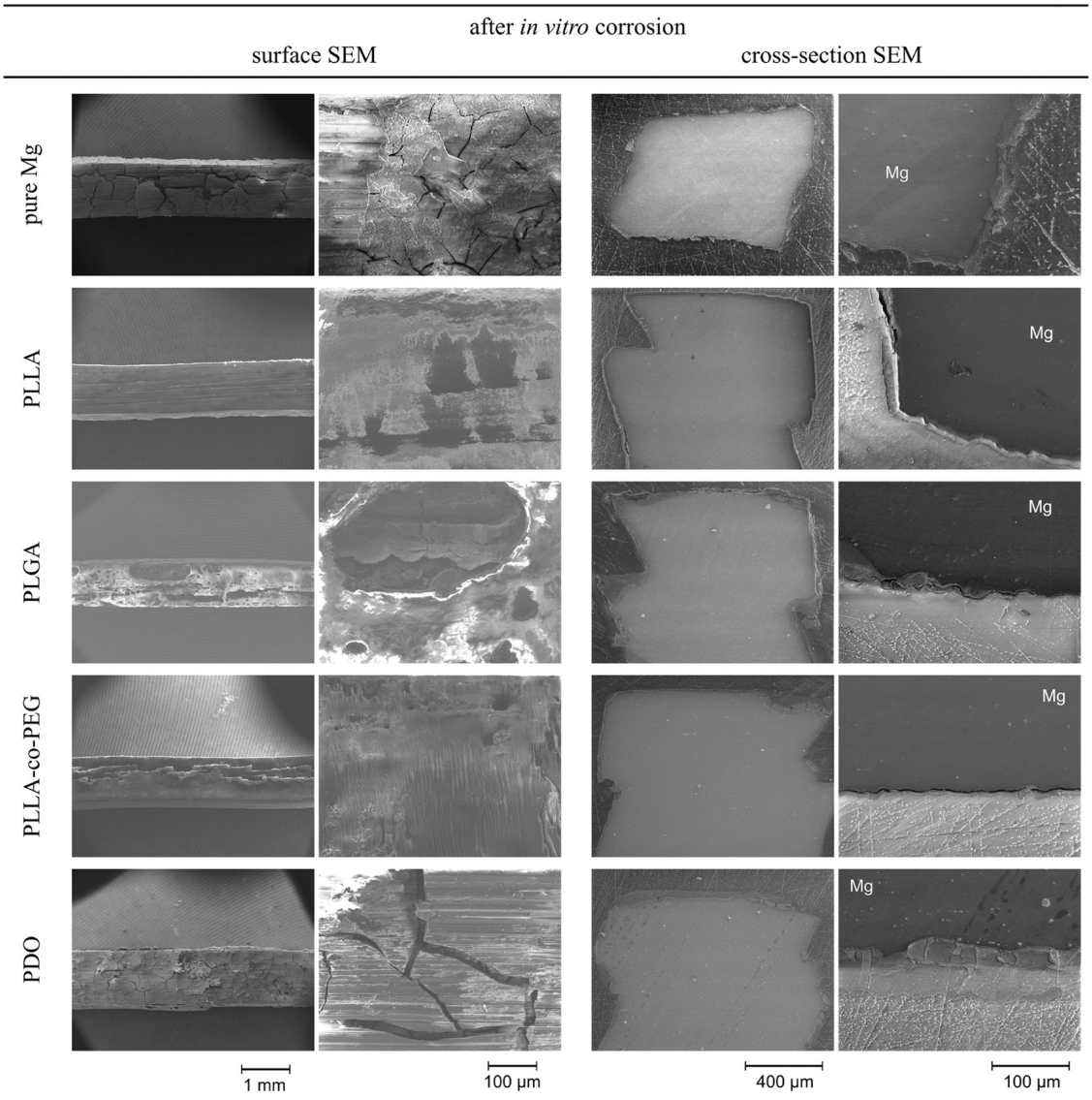
Film thickness was determined exemplarily for PLLA using SEM imaging for six spots and calculated for all polymers using film mass. Following this, thin films of a thickness of around $d_{PLLA} = 7.5\ \mu m$, $d_{PLGA} = 8.3\ \mu m$, $d_{PLLA\text{-}co\text{-}PEG} = 7.6\ \mu m$, and $d_{PDO} = 7.1\ \mu m$ were generated using a custom-made airbrush device and an adapted holder for the rod. For intercomparability, airbrush coating of Mg for all polymers has been performed with the same processing parameters regarding solvent, concentration, flow, and process time. These, however, lead to different outcomes of the coating morphology and integrity. Table 1 gives an overview of the morphology of coated Mg rods and coated Mg rods after *in vitro* corrosion. Due to destructive analysis (embedding and grinding to enable cross-sectioned imaging), different samples are shown. In the macrophotographical images of the cross sections, it can be seen that shear cutting of the specimen leads to an uneven surface on the cutting sides. However, the obtained shape resembles the complex structure of Mg-based implants such as screws or stents and is of particular interest regarding the coating integrity obtained from the spray coating process. From the cross-sectional images of the uncorroded specimens, it can be seen that polymer coating adapted to the complicated shape and the specimens were completely covered. Spray coating with different polyesters resulted in a polymer coating thickness of 7.1 μm (PDO) up to 8.3 μm (PLGA) which falls within the relevant range for commercially available stent systems for hemodynamic reasons.[26]

After CO_2 buffered corrosion, uncoated Mg showed the formation of white precipitates on the surface, which nearly completely covered the specimen surface. Cross-sectioning revealed strong material loss for uncoated and PDO-coated Mg, in particular, located at edges. This is primarily due to the larger surface area of the edges compared with a flat surface. In addition, sample preparation was carried out by shear cutting. However, this led to high residual tensile stresses at the interface, which changed the microstructure of the Mg alloy at the cut edges and made the material more susceptible to corrosion at these points.[44] In the case of PLLA, PLGA, and PLLA-*co*-PEG, the edges were less affected by corrosion and were clearly visible. From this, we conclude that these coatings are more protective than the PDO.

Regarding protective polyester coatings, formation of white Mg salt precipitates was observed in macrophotography for all selected coatings. Coating with PLLA slowed corrosion, in particular, regarding material loss and rounding of the samples. PLGA was revealed to be much less effective compared to PLLA, as the sample exhibited signs of increased dissolution. From macrophotography and cross-sectioning, PLLA-*co*-PEG was

https://doi.org/10.1021/acsbiomaterials.4c00835
ACS Biomater. Sci. Eng. 2024, 10, 5844−5855

Table 3. Surface SEM Images of Mg Specimen and Mg Specimens Coated with PLLA, PLGA, PLLA-co-PEG, and PDO before *In Vitro* Corrosion and Surface and Cross-Sectional SEM Images of Mg Specimens and Mg Specimen Coated with PLLA, PLGA, PLLA-co-PEG, and PDO after 14 days of *In Vitro* Corrosion under CO_2 Buffering



shown to be as effective as PLLA. PDO, on the other hand, appeared to be less effective, in particular, as high fragmentation of the polymer coating is visible.

For a more detailed view of coated surfaces, SEM imaging was performed (Table 2). Although the PLLA coating appeared to be very smooth, PLGA showed a cracked surface and PLLA-*co*-PEG and PDO coatings exhibited a porous morphology, which can be related to solvent evaporation. Overall, PLLA and PLLA-*co*-PEG gave an intact coating, whereas PLGA and PDO coating resulted in a fragmented and partially delaminated polymer layer. Still, the major parts of the specimen were covered for all four selected polymer coatings.

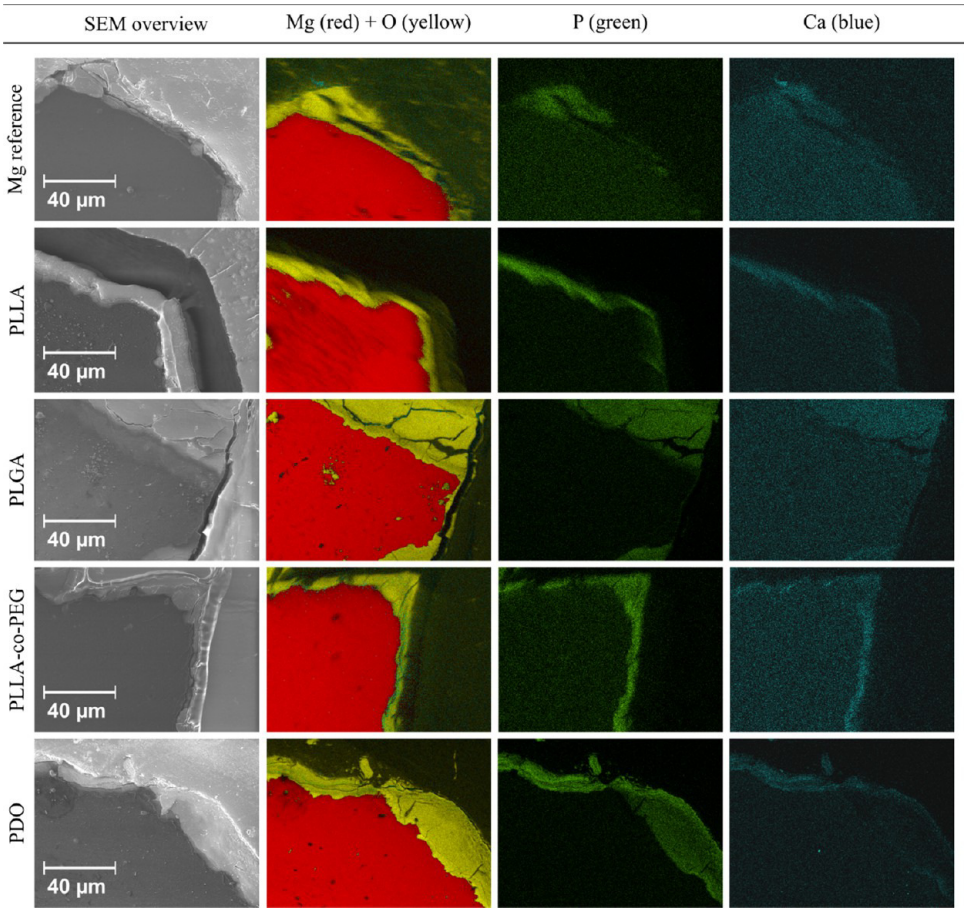
After embedding and cross-sectioning, the corrosion layer became clearly visible (Table 3). SEM imaging revealed the formation of plate-like[42] precipitates on the Mg species in the case of uncoated Mg and PDO-coated Mg specimen after *in vitro* corrosion. PLGA showed larger holes in the coating. In the cross-sectional SEM images, a thickness of the corrosion layer of up to 15 μm could be detected. This is, however, not quantitative due to the corrosion layer's uneven shape and strong variation in thickness.

Elemental analysis by EDX (Table 4) revealed the presence of not only Mg, C, and O species (related to $MgOH_2$, $MgCO_3$, MgO, and the coating polymer), but also P and Ca, being consistent with literature data.[39,42] These findings indicate that mineralization processes and the formation of mixed crystals from SBF occurred. This is relevant in terms of the *in vitro* reproducibility of *in vivo* processes, where complex ion exchange processes take place on the Mg surface. Salts with low solubility and foreign ions may interact with the corrosion layer, in particular phosphate, carbonate, chloride, and calcium.[45,46]

In vivo data as reported in the literature showed oxygen, carbon, nitrogen, magnesium, calcium, and phosphorus as the main elements of the reaction products formed on the magnesium surface, having a loose, gray-white appearance.[47] Different elemental compositions are formed in the reaction products at the substrate surface and the peripheral corrosion layers after a sufficient corrosion period. Oxygen-rich species are

https://doi.org/10.1021/acsbiomaterials.4c00835
ACS Biomater. Sci. Eng. 2024, 10, 5844−5855

Table 4. SEM Overview and EDX Mapping of Corrosion-Related Elements for Mg Specimen and Polyester-Coated Mg Specimens after 14 days of *In Vitro* Corrosion Shown as Stacked Images for Mg, O, and P and Ca. The cavity visible in the case of PLLA and PLGA is due to the shrinking of the epoxy resin during curing



particularly found on the magnesium surface and calcium phosphates tend to be found in the peripheral layers.[48,49] Some studies further indicate a promising Ca/P ratio for biocompatibility and osseointegration.[46] However, stoichiometric analysis of the corrosion layer is challenging, as magnesium tends to rapidly form an oxide layer, thus altering the elemental composition during the grinding and polishing process of the embedded samples. Still, with regard to coated Mg specimens, the formation of a corrosion layer beneath the protective layer was observed for all used polymers. Also for coated samples, EDX showed the presence of P and Ca beneath the coating. For better visualization of the formed corrosion layers, EDX mapping for different elements, Mg, O, P, and Ca, has been performed (Table 4). This showed that polyester-based polymers, albeit hydrophobic and unpolar, allow for the diffusion of different ions from the medium onto the Mg surface and vice versa for the diffusion of Mg ions from the sample surface into the medium. The formation of a passivating salt layer and the fact that the polymer coating shields this layer from detaching may further contribute to the corrosion-protective effect of polymer coatings. In particular phosphate ion species can form water-insoluble magnesium phosphate ($Mg_3(PO_4)_2$), increasing the protective effectiveness of the passivation layer.[39] In addition, EDX mapping for PLLA and PLLA-*co*-PEG revealed a thinner passivation layer, leading to the assumption that the polymer coating trapped the salts and further increased the protective effect; compared to PLGA and PDO, a much thicker salt layer is observed, showing a less pronounced protective effect.

The experimental setup presented here allows for real-time sampling of the medium and determination of Mg^{2+} concentration, thus evaluating the protective effect of the polymer coatings compared to uncoated Mg (Figure 4). Sampling of corrosion medium has been performed after 1, 2, 4, 8, 24, 36, 48, 61, 72, 96, and 336 h of corrosion, respectively.

Photometric analysis using Xylidyl blue-Mg^{2+}-complex showed a fast and high increase in the concentration of dissolved Mg for uncoated specimen. Mg concentration, however, reached a maximum at ∼0.06 mg/mL, which was constant for the residual corrosion time due to low solubility of the formed Mg^{2+} salts, in particular $MgCO_3$. Due to loss in medium volume by evaporation and carryover by the Corgon gas flow, correction of the resulting concentration values was performed by end point determination of the volume of the medium and approximation of linear volume loss. This, however, leads to a decrease in total, as the concentration of dissolved Mg remains constant due to precipitation processes in the vessel.

Regarding the protective effect of the polyester coatings, all four investigated polymers showed a pronounced reduction of initial Mg dissolution (Figure 4B–E) compared with uncoated Mg (Figure 4A). The protective effect was found to be strongest for PLLA and PLLA-*co*-PEG, but PLGA and PDO coatings provided a high degree of protection, albeit the coating was

https://doi.org/10.1021/acsbiomaterials.4c00835
ACS Biomater. Sci. Eng. 2024, 10, 5844−5855

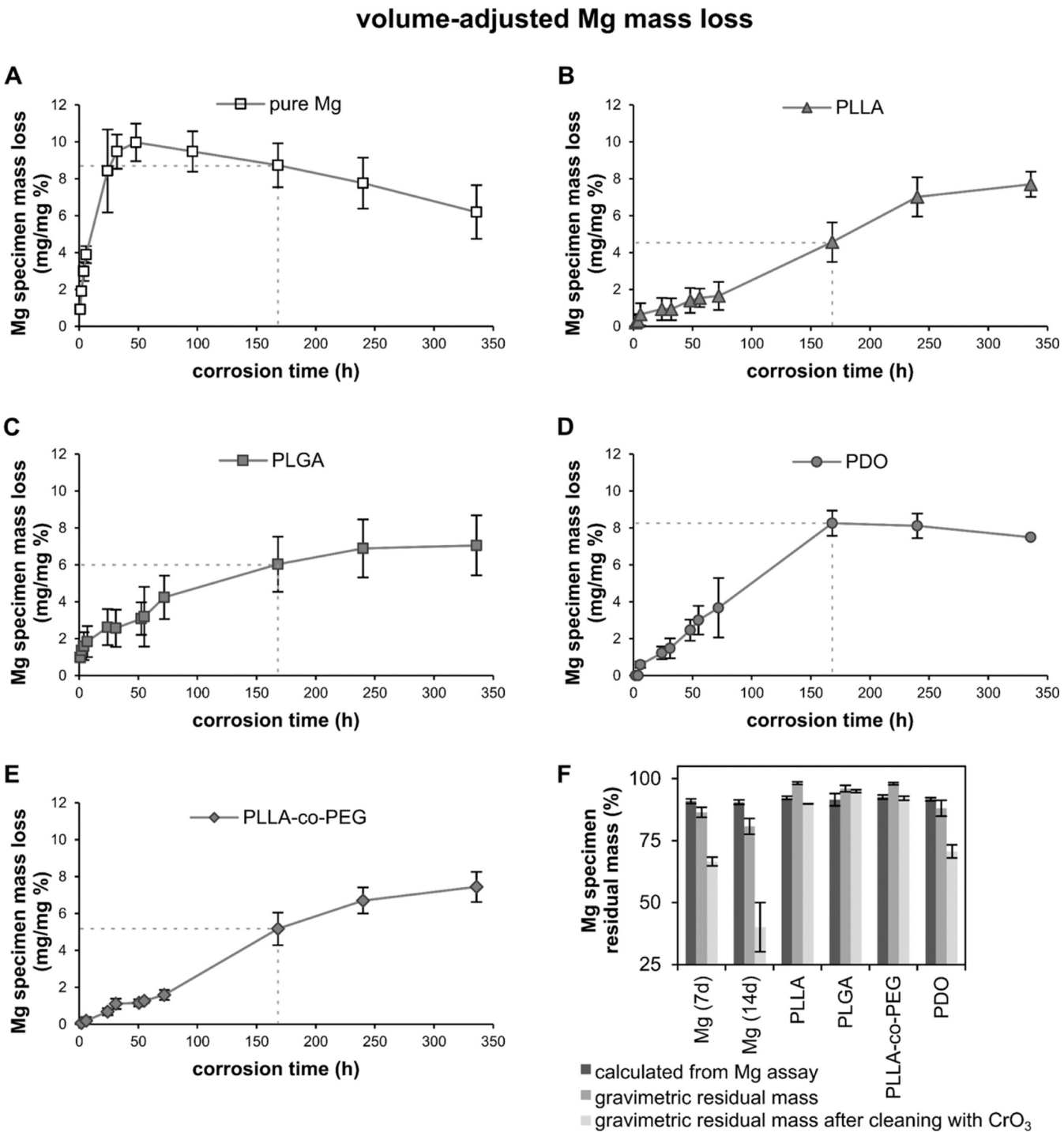


Figure 4. Medium-volume-adjusted Mg mass loss of polyester-coated rods with respect to initial specimen Mg mass in comparison to uncoated Mg as photometrically determined by Mg^{2+} concentration in the medium (A−E). Dashed lines indicate mass loss after 1 week (168 h) of *in vitro* corrosion. Mass loss of Mg and polyester-coated Mg specimens as determined by gravimetrical methods (without and after removal of corrosion layer using CrO_3) compared to calculated mass loss from photometrical Mg quantification after 14 d (F).

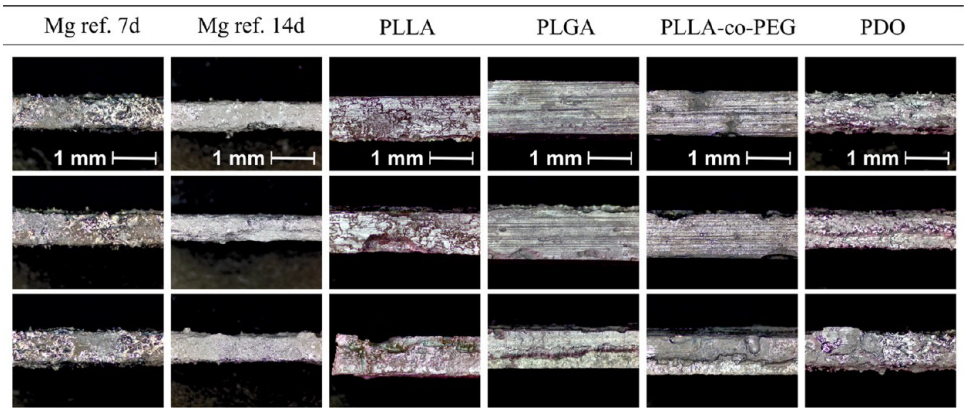
imperfect, fragmented, and delaminated, as was found in SEM imaging.

After 1 week of *in vitro* corrosion, PLLA and PLLA-*co*-PEG showed mass loss of just 4.5 and 5%, as indicated by dashed lines (Figure 4B,E), as calculated from photometrical quantification of dissolved Mg, compared to uncoated Mg rods with 7.5% mass loss, whereas PLGA and PDO show 7% and 8.5% loss, respectively. However, the formation of a Mg salt layer underneath the polymer coating in polymer-coated samples, in particular for $MgCO_3$ ($m_{carbonate}/m_{Mg}$ = 3.5) and $Mg_3(PO_4)_2$ ($m_{phosphate}/m_{Mg}$ = 10.9), leads to a shift to higher values in gravimetric analysis. This leaves the sole determination of mass loss inconclusive (Figure 4F).

Gravimetric analysis of degraded Mg samples without removal of the corrosion layer differed from photometric analysis of Mg dissolution and the calculated mass loss therefrom. Uncoated Mg rods and PDO-coated specimens showed higher gravimetric mass loss when compared to mass

https://doi.org/10.1021/acsbiomaterials.4c00835
ACS Biomater. Sci. Eng. 2024, 10, 5844−5855

Table 5. Macrophotographical Images of Mg Specimens and Polyester-Coated Mg Specimens after 14 Days of *In Vitro* Corrosion and Removal of the Protective Polyester Coating with $CHCl_3$ and Removal of the Corrosion Layer Using CrO_3/$AgNO_3$ Solution[a]



[a]For untreated Mg reference, also images after 7 days of *in vitro* corrosion are shown.

loss calculated from dissolved Mg, whereas PLLA, PLGA, and PLLA-*co*-PEG coating resulted in smaller gravimetric mass loss. For this, two effects must be considered: First, the low solubility of $MgCO_3$ leads to a limited reproduction of the correct amount of dissolved magnesium after just 48 h, as Mg salts precipitate at the vessel wall. Additionally, volume loss due to evaporation and the carryover by the Corgon gas also promote this. The low solubility of $MgCO_3^-$ and $MgPO_4^-$ species may be bypassed by adding chelating agents; this, however, may crucially influence the formation of passivation layer and thus the reproduction of *in vivo* processes. Medium evaporation, on the other hand, cannot easily be avoided in the presented setup. Moreover, it is shown in Figure 1. Mg dissolution is accompanied by the formation and conversion processes of several Mg salts, leading to a complex passivation layer, particularly in SBF, where Ca and P species are being integrated into the MgO_X matrix. This leads to a higher absolute sample mass, thus making these measurements invalid, in particular regarding early-stage corrosion.

In addition to the determination of gravimetric mass loss of specimens including the corrosion layer, specimens were weighed after the cleaning procedure with chromic acid (Figure 4F). These data show that for untreated Mg, after 14 days of *in vitro* corrosion, the corrosion layer accounts for a large proportion of the total mass of the sample. For PLLA, PLGA, and PLLA-*co*-PEG, the mass of the corrosion layer is substantially smaller compared to the untreated sample, leading to a good correlation between the calculated residual mass from eluted Mg. PDO showed the least effective corrosion protection, which can be explained by an imperfect coating.

Macrophotographical images in Table 5 illustrate selected sections of samples examined after cleaning with chromic acid. The starting point for all investigations was a cuboid rod sample for each column of Table 5, with three different representative sample spots. The images of the CrO_3-cleaned samples show differences in the sample surface morphology and depict the determined mass losses via a photometric assay. As a result, uncoated magnesium shows strong pitting on the surface, also progressively between 7 and 14 days of corrosion. This is in line with the results of Mg determination by the Xylidyl assay. The rough surface morphology is noticeably increased for corroded uncoated samples, which is due to the microstructural phases of the magnesium alloy composition.[50]

Mg rods coated with PLLA, PLGA, and PLLA-*co*-PEG showed comparable good preservation of the sample geometry after 14 days of *in vitro* corrosion. However, several cracks and local pitting spots were observed. In the case of PLGA coating, Mg shows a partially macroscopically intact surface while some areas of the sample showed sharply delimited pitting. This is due to the fact that the PLGA coating did not cover the whole sample and several holes could be observed in SEM imaging (Tables 2 and 3). Compared to the other coating materials, PDO showed a clearly progressed corrosion and noticeable sample rounding and an increase in surface roughness.

CONCLUSIONS

Protective polymer coatings are a versatile tool for adjusting the corrosion rate of Mg-based biomedical devices. Real-time characterization of *in vitro* corrosion of Mg alloy AZ31B provides further insight into future developments and is an applicable tool for the in-process development of functional Mg-based implants. As Mg corrosion leads to a drastic increase in pH, thus altering the corrosion conditions during the test, real-time pH adjustment is essential. In this study, we have established a suitable test setup to determine the protective effectiveness of polyester-based polymer thin-film coatings by maintaining a pH-stable environment through on-demand CO_2 buffering and allowing continuous testing with flexible sampling times.

PLLA, PLGA, PLLA-*co*-PEG, and PDO all showed protective effectiveness, but PLLA and PLLA-*co*-PEG both showed the highest delay of Mg dilution monitored by a real-time photometric Mg assay. The formation of complex mixed crystal layers from SBF on the Mg surface under protective coatings was reproduced. However, due to the strong basic impact of Mg on pH, buffering with CO_2 is limited, as the system must be kept open and evaporation processes as well as saturation with carbonate influence the precipitation equilibria. The low solubility of magnesium salts coupled with medium volume loss due to the ventilated design requires additional interference in the experimental setup for long-term studies, e.g., media changes. Nevertheless, we believe that the presented method is valuable for evaluating the effectiveness of functional coatings in a biomedical context.

AUTHOR INFORMATION

Corresponding Author

Nicklas Fiedler − *Institute for Biomedical Engineering, Rostock University Medical Center, 18119 Rostock, Germany;*

https://doi.org/10.1021/acsbiomaterials.4c00835
ACS Biomater. Sci. Eng. 2024, 10, 5844−5855

orcid.org/0000-0002-4436-7010;
Email: Nicklas.fiedler@uni-rostock.de

Authors

Michael Teske − *Institute for Biomedical Engineering, Rostock University Medical Center, 18119 Rostock, Germany*
Sophie-Charlotte Nelz − *Institute for Biomedical Engineering, Rostock University Medical Center, 18119 Rostock, Germany*
Jonas Willem Flügge − *Institute for Biomedical Engineering, Rostock University Medical Center, 18119 Rostock, Germany*
Volkmar Senz − *Institute for Biomedical Engineering, Rostock University Medical Center, 18119 Rostock, Germany*
Dalibor Bajer − *Institute for Biomedical Engineering, Rostock University Medical Center, 18119 Rostock, Germany*
Niels Grabow − *Institute for Biomedical Engineering, Rostock University Medical Center, 18119 Rostock, Germany; Department Life, Light & Matter (LLM), University of Rostock, 18059 Rostock, Germany*
Stefan Oschatz − *Institute for Biomedical Engineering, Rostock University Medical Center, 18119 Rostock, Germany;* orcid.org/0000-0003-2339-456X

Complete contact information is available at: https://pubs.acs.org/10.1021/acsbiomaterials.4c00835

Author Contributions

Conceptualization: N.F. and S.O.; methodology: N.F., M.T., and S.O.; SEM imaging and EDX analysis: V.S.; sample preparation and spray coating: J.F and D.B.; *in vitro* degradation study: J.F. and C.N.; writing—original draft preparation: N.F. and S.O.; writing—review and editing: all; project administration: N.G.; funding acquisition: N.G. All authors have read and agreed to the published version of the manuscript.

Funding

Financial support by the European Regional Development Fund (ERDF) and the European Social Fund (ESF) within the collaborative research between economy and science of the state Mecklenburg-Vorpommern (TBI-V-1-095-VBW-033) is gratefully acknowledged.

Notes

The authors declare no competing financial interest.

■ ACKNOWLEDGMENTS

The authors thank Katja Hahn, Babette Hummel, Ingeborg Rühl, and Caroline Dudda for their expert technical assistance.

■ REFERENCES

(1) Zhang, S.; Zhang, X.; Zhao, C.; Li, J.; Song, Y.; Xie, C.; Tao, H.; Zhang, Y.; He, Y.; Jiang, Y.; Bian, Y. Research on an Mg-Zn Alloy as a Degradable Biomaterial. *Acta Biomater* **2010**, *6* (2), 626−640.
(2) Witte, F. Reprint Of: The History of Biodegradable Magnesium Implants: A Review. *Acta Biomater.* **2015**, *23 Suppl*, S28−S40.
(3) Hermawan, H. Updates on the Research and Development of Absorbable Metals for Biomedical Applications. *Prog. Biomater.* **2018**, *7* (2), 93−110.
(4) Luthringer, B. J. C.; Feyerabend, F.; Willumeit-Römer, R. Magnesium-Based Implants: A Mini-Review. *Magnes. Res.* **2014**, *27* (4), 142−154.
(5) Virtanen, S. Biodegradable Mg and Mg Alloys: Corrosion and Biocompatibility. *Mater. Sci. Eng., B* **2011**, *176* (20), 1600−1608.
(6) Walker, J.; Shadanbaz, S.; Woodfield, T. B. F.; Staiger, M. P.; Dias, G. J. Magnesium Biomaterials for Orthopedic Application: A Review From a Biological Perspective. *J. Biomed. Mater. Res. B: Appl. Biomater.* **2014**, *102* (6), 1316−1331.
(7) Kirkland, N. T.; Birbilis, N.; Staiger, M. P. Assessing the Corrosion of Biodegradable Magnesium Implants: A Critical Review of Current Methodologies and Their Limitations. *Acta Biomater.* **2012**, *8* (3), 925−936.
(8) Atrens, A.; Song, G.-L.; Cao, F.; Shi, Z.; Bowen, P. K. Advances in Mg Corrosion and Research Suggestions. *J. Magnes. Alloys* **2013**, *1* (3), 177−200.
(9) Saberi, A.; Bakhsheshi-Rad, H. R.; Abazari, S.; Ismail, A. F.; Sharif, S.; Ramakrishna, S.; Daroonparvar, M.; Berto, F. A Comprehensive Review on Surface Modifications of Biodegradable Magnesium-Based Implant Alloy: Polymer Coatings Opportunities and Challenges. *Coatings* **2021**, *11* (7), 747.
(10) Xin, Y.; Hu, T.; Chu, P. K. In Vitro Studies of Biomedical Magnesium Alloys in a Simulated Physiological Environment: A Review. *Acta Biomater.* **2011**, *7* (4), 1452−1459.
(11) Gonzalez, J.; Hou, R. Q.; Nidadavolu, E. P. S.; Willumeit-Römer, R.; Feyerabend, F. Magnesium Degradation Under Physiological Conditions − Best Practice. *Bioact. Mater.* **2018**, *3* (2), 174−185.
(12) Chen, L.; Sheng, Y.; Zhou, H.; Li, Z.; Wang, X.; Li, W. Influence of a MAO + PLGA Coating on Biocorrosion and Stress Corrosion Cracking Behavior of a Magnesium Alloy in a Physiological Environment. *Corros. Sci.* **2019**, *148*, 134−143.
(13) Erişen, D. E.; Zhang, Y.; Zhang, B.; Yang, K.; Chen, S.; Wang, X. Biosafety and Biodegradation Studies of AZ31B Magnesium Alloy Carotid Artery Stent In Vitro and In Vivo. *J. Biomed. Mater. Res. B: Appl. Biomater.* **2022**, *110*, 239.
(14) Jamel, M. M.; Jamel, M. M.; Lopez, H. F. Designing Advanced Biomedical Biodegradable Mg Alloys: A Review. *Metals* **2022**, *12* (1), 85.
(15) Chen, Y.; Dou, J.; Yu, H.; Chen, C. Degradable Magnesium-Based Alloys for Biomedical Applications: The Role of Critical Alloying Elements. *J. Biomater. Appl.* **2019**, *33* (10), 1348−1372.
(16) Han, L.; Zhang, Z.; Dai, J.; Li, X.; Bai, J.; Huang, Z.; Guo, C.; Xue, F.; Chu, C. The Influence of Alternating Cyclic Dynamic Loads With Different Low Frequencies on the Bio-Corrosion Behaviors of AZ31B Magnesium Alloy In Vitro. *Bioact. Mater.* **2022**, *7*, 263−274.
(17) Rajan, S. T.; Das, M.; Arockiarajan, A. Biocompatibility and Corrosion Evaluation of Niobium Oxide Coated AZ31B Alloy for Biodegradable Implants. *Colloids Surf., B* **2022**, *212*, No. 112342.
(18) Han, L.; Zhang, Z.; Dai, J.; Li, X.; Bai, J.; Huang, Z.; Guo, C.; Xue, F.; Chu, C. In Vitro Bio-Corrosion Behaviors of Biodegradable AZ31B Magnesium Alloy Under Static Stresses of Different Forms and Magnitudes. *J. Magnes. Alloys* **2023**, *11* (3), 1043−1056.
(19) Li, X.; Wang, Y.; Chu, C.; Han, L.; Bai, J.; Xue, F. A Study on Mg Wires/Poly-Lactic Acid Composite Degradation Under Dynamic Compression and Bending Load for Implant Applications. *J. Mech. Behav. Biomed. Mater.* **2020**, *105*, No. 103707.
(20) Zhang, Z.-Q.; Yang, Y.-X.; Li, J.-A.; Zeng, R.-C.; Guan, S.-K. Advances in Coatings on Magnesium Alloys for Cardiovascular Stents − a Review. *Bioact. Mater.* **2021**, *6* (12), 4729−4757.
(21) Zhang, D.; Peng, F.; Liu, X. Protection of Magnesium Alloys: From Physical Barrier Coating to Smart Self-Healing Coating. *J. Alloys Compd.* **2021**, *853*, No. 157010.
(22) Wagener, V.; Virtanen, S. Protective Layer Formation on Magnesium in Cell Culture Medium. *Mater. Sci. Eng. C: Mater. Biol. Appl.* **2016**, *63*, 341−351.
(23) Esmaily, M.; Svensson, J. E.; Fajardo, S.; Birbilis, N.; Frankel, G. S.; Virtanen, S.; Arrabal, R.; Thomas, S.; Johansson, L. G. Fundamentals and Advances in Magnesium Alloy Corrosion. *Prog. Mater. Sci.* **2017**, *89* (2169), 92−193.
(24) Kieke, M.; Feyerabend, F.; Lemaitre, J.; Behrens, P.; Willumeit-Römer, R. Degradation Rates and Products of Pure Magnesium Exposed to Different Aqueous Media Under Physiological Conditions. *BioNanoMaterials* **2016**, *17* (3−4), 2111.
(25) Arbeiter, D.; Eickner, T.; Oschatz, S.; Reske, T.; Specht, O.; Teske, M.; Senz, V.; Schmitz, K.-P.; Grabow, N. Physico chemical and phase separation characterization of high molecular PLLA blended with low molecular PCL obtained from solvent cast processes. *Mater. Res. Express* **2020**, *7* (9), 95302.

(26) Arbeiter, D.; Reske, T.; Teske, M.; Bajer, D.; Senz, V.; Schmitz, K.-P.; Grabow, N.; Oschatz, S. Influence of Drug Incorporation on the Physico-Chemical Properties of Poly(l-Lactide) Implant Coating Matrices-A Systematic Study. *Polymers* **2021**, *13* (2), 292.
(27) Mann, C. K.; Yoe, J. H. Spectrophotometric Determination of Magnesium With Sodium 1-Azo-2-Hydroxy-3-(2,4-Dimethylcarboxanilido)-Naphthalene-1′-(2-Hydroxybenzene-5-Sulfonate). *Anal. Chem.* **1956**, *28* (2), 202−205.
(28) Schinhammer, M.; Hofstetter, J.; Wegmann, C.; Moszner, F.; Löffler, J. F.; Uggowitzer, P. J. On the Immersion Testing of Degradable Implant Materials in Simulated Body Fluid: Active pH Regulation Using CO2. *Adv. Eng. Mater.* **2013**, *15* (6), 434−441.
(29) Wang, J.; Giridharan, V.; Shanov, V.; Xu, Z.; Collins, B.; White, L.; Jang, Y.; Sankar, J.; Huang, N.; Yun, Y. Flow-Induced Corrosion Behavior of Absorbable Magnesium-Based Stents. *Acta Biomater.* **2014**, *10* (12), 5213−5223.
(30) *Standard Practice for Laboratory Immersion Corrosion Testing of Metals*, 72nd ed.; ASTM International, 2004.
(31) Li, L.-Y.; Cui, L.-Y.; Zeng, R.-C.; Li, S.-Q.; Chen, X.-B.; Zheng, Y.; Kannan, M. B. Advances in Functionalized Polymer Coatings on Biodegradable Magnesium Alloys − A Review. *Acta Biomater.* **2018**, *79*, 23−36.
(32) Wei, Z.; Tian, P.; Liu, X.; Zhou, B. In vitro degradation, hemolysis, and cytocompatibility of PEO/PLLA composite coating on biodegradable AZ31 alloy. *J. Biomed. Mater. Res. B: Appl. Biomater.* **2015**, *103* (2), 342−354.
(33) Bakhsheshi-Rad, H. R.; Akbari, M.; Ismail, A. F.; Aziz, M.; Hadisi, Z.; Pagan, E.; Daroonparvar, M.; Chen, X. Coating Biodegradable Magnesium Alloys With Electrospun Poly-L-Lactic Acid-Åkermanite-Doxycycline Nanofibers for Enhanced Biocompatibility, Antibacterial Activity, and Corrosion Resistance. *Surf. Coat. Technol.* **2019**, *377*, No. 124898.
(34) Prajapati, S. K.; Jain, A.; Jain, A.; Jain, S. Biodegradable Polymers and Constructs: A Novel Approach in Drug Delivery. *Eur. Polym. J.* **2019**, *120* (2), No. 109191.
(35) Zhu, Y.; Liu, W.; Ngai, T. Polymer Coatings on Magnesium-Based Implants for Orthopedic Applications. *J. Polym. Sci.* **2022**, *60* (1), 32−51.
(36) De Rooij, J. F.; Heughebaert, J. C.; Nancollas, G. H. A ph study of calcium phosphate seeded precipitation. *J. Colloid Interface Sci.* **1984**, *100* (2), 350−358.
(37) Petersen, S.; Hussner, J.; Reske, T.; Grabow, N.; Senz, V.; Begunk, R.; Arbeiter, D.; Kroemer, H. K.; Schmitz, K.-P.; Meyer zu Schwabedissen, H. E.; Sternberg, K. In vitro study of dual drug-eluting stents with locally focused sirolimus and atorvastatin release. *J. Mater. Sci. Mater. Med.* **2013**, *24* (11), 2589−2600.
(38) *Standard Practice for Preparing, Cleaning, and Evaluating Corrosion Test Specimens*, 90th ed.; ASTM International, 2017.
(39) Yavuzyegit, B.; Karali, A.; Mori, A. de.; Smith, N.; Usov, S.; Shashkov, P.; Bonithon, R.; Blunn, G. Evaluation of Corrosion Performance of AZ31 Mg Alloy in Physiological and Highly Corrosive Solutions. *ACS Appl. Bio. Mater.* **2024**, *7* (3), 1735−1747.
(40) Qu, Q.; Ma, J.; Wang, L.; Li, L.; Bai, W.; Ding, Z. Corrosion behaviour of AZ31B magnesium alloy in NaCl solutions saturated with CO2. *Corros. Sci.* **2011**, *53* (4), 1186−1193.
(41) Oyane, A.; Kim, H.-M.; Furuya, T.; Kokubo, T.; Miyazaki, T.; Nakamura, T. Preparation and assessment of revised simulated body fluids. *J. Biomed. Mater. Res., Part A* **2003**, *65* (2), 188−195.
(42) Hayashi, M.; Yamamoto, A.; Aizawa, T.; Yusa, Y.; Shimizu, Y.; Imai, Y. In vitroanalysis of insoluble salt formation mechanism associated with Mg corrosion-variations depending on the diffusion environment in model tissue. *Biomed. Mater.* **2024**, *19* (2), 025010.
(43) Rapetto, C.; Leoncini, M. Magmaris: a new generation metallic sirolimus-eluting fully bioresorbable scaffold: present status and future perspectives. *J. Thorac. Dis.* **2017**, *9* (Suppl 9), S903−S913.
(44) Peron, M.; Bertolini, R.; Ghiotti, A.; Torgersen, J.; Bruschi, S.; Berto, F. Enhancement of stress corrosion cracking of AZ31 magnesium alloy in simulated body fluid thanks to cryogenic machining. *J. Mech. Behav. Biomed. Mater.* **2020**, *101*, No. 103429.
(45) Koo, Y.; Tiasha, T.; Shanov, V. N.; Yun, Y. Expandable Mg-Based Helical Stent Assessment Using Static, Dynamic, and Porcine Ex Vivo Models. *Sci. Rep.* **2017**, *7* (1), No. 1173.
(46) Ren, Y.; Huang, J.; Zhang, B.; Yang, K. Preliminary Study of Biodegradation of AZ31B Magnesium Alloy. *Front. Mater. Sci. China* **2007**, *1* (4), 401−404.
(47) Wang, Y.; Liang, W.; Liu, X.; Li, Q.; Xie, Y.; Jiang, Y. Osteogenesis and Degradation Behavior of Magnesium Alloy Plate In Vivo. *Eur. J. Inflamm.* **2021**, *19* (3), No. 205873922110340.
(48) Bowen, P. K.; Drelich, J.; Goldman, J. Magnesium in the Murine Artery: Probing the Products of Corrosion. *Acta Biomater.* **2014**, *10* (3), 1475−1483.
(49) Xu, L.; Yamamoto, A. Characteristics and Cytocompatibility of Biodegradable Polymer Film on Magnesium by Spin Coating. *Colloids Surf., B* **2012**, *93*, 67−74.
(50) Unocic, K. A.; Elsentriecy, H. H.; Brady, M. P.; Meyer, H. M.; Song, G. L.; Fayek, M.; Meisner, R. A.; Davis, B. Transmission Electron Microscopy Study of Aqueous Film Formation and Evolution on Magnesium Alloys. *J. Electrochem. Soc.* **2014**, *161* (6), C302−C311.

https://doi.org/10.1021/acsbiomaterials.4c00835
ACS Biomater. Sci. Eng. 2024, 10, 5844−5855

polymers

MDPI

Article

Influence of Drug Incorporation on the Physico-Chemical Properties of Poly(L-Lactide) Implant Coating Matrices—A Systematic Study

Daniela Arbeiter [1,*], Thomas Reske [2], Michael Teske [1], Dalibor Bajer [1], Volkmar Senz [1], Klaus-Peter Schmitz [1,2], Niels Grabow [1] and Stefan Oschatz [1]

[1] Institute for Biomedical Engineering, Rostock University Medical Center, Friedrich-Barnewitz-Straße 4, 18119 Rostock, Germany; michael.teske@uni-rostock.de (M.T.); dalibor.bajer@uni-rostock.de (D.B.); volkmar.senz@uni-rostock.de (V.S.); schmitz@iib-ev.de (K.-P.S.); niels.grabow@uni-rostock.de (N.G.); stefan.oschatz@uni-rostock.de (S.O.)

[2] Institute for Implant Technology and Biomaterials e.V., Friedrich-Barnewitz-Straße 4, 18119 Rostock, Germany; thomas.reske@uni-rostock.de

* Correspondence: daniela.arbeiter@uni-rostock.de; Tel.: +49-381-54345-554

Abstract: Local drug delivery has become indispensable in biomedical engineering with stents being ideal carrier platforms. While local drug release is superior to systemic administration in many fields, the incorporation of drugs into polymers may influence the physico-chemical properties of said matrix. This is of particular relevance as minimally invasive implantation is frequently accompanied by mechanical stresses on the implant and coating. Thus, drug incorporation into polymers may result in a susceptibility to potentially life-threatening implant failure. We investigated spray-coated poly-L-lactide (PLLA)/drug blends using thermal measurements (DSC) and tensile tests to determine the influence of selected drugs, namely sirolimus, paclitaxel, dexamethasone, and cyclosporine A, on the physico-chemical properties of the polymer. For all drugs and PLLA/drug ratios, an increase in tensile strength was observed. As for sirolimus and dexamethasone, PLLA/drug mixed phase systems were identified by shifted drug melting peaks at 200 °C and 240 °C, respectively, whereas paclitaxel and dexamethasone led to cold crystallization. Cyclosporine A did not affect matrix thermal properties. Altogether, our data provide a contribution towards an understanding of the complex interaction between PLLA and different drugs. Our results hold implications regarding the necessity of target-oriented thermal treatment to ensure the shelf life and performance of stent coatings.

Keywords: drug-eluting stent (DES); poly-L-lactide; drug delivery coatings; mechanical properties; thermal properties; surface morphology; paclitaxel; sirolimus; dexamethasone; cyclosporine A

check for updates

Citation: Arbeiter, D.; Reske, T.; Teske, M.; Bajer, D.; Senz, V.; Schmitz, K.-P.; Grabow, N.; Oschatz, S. Influence of Drug Incorporation on the Physico-Chemical Properties of Poly(L-Lactide) Implant Coating Matrices—A Systematic Study. *Polymers* **2021**, *13*, 292. https://doi.org/10.3390/polym13020292

Received: 23 December 2020
Accepted: 13 January 2021
Published: 18 January 2021

Publisher's Note: MDPI stays neutral with regard to jurisdictional claims in published maps and institutional affiliations.

Copyright: © 2021 by the authors. Licensee MDPI, Basel, Switzerland. This article is an open access article distributed under the terms and conditions of the Creative Commons Attribution (CC BY) license (https://creativecommons.org/licenses/by/4.0/).

1. Introduction

Drug-eluting stents (DES), in particular those of newer generations, are superior to bare metal stents in the treatment of coronary artery stenosis [1–5]. Among others, frequently used drugs are from the Limus family, especially sirolimus (SIR) [6–9], but also paclitaxel (PTX) [10], dexamethasone (DEX) [11,12], and cyclosporine A (CYCLO) [13,14]. SIR is mainly used for its immunosuppressant effects to inhibit organ transplant rejection, but also shows mammalian target of rapamycin (mTOR) inhibition, reducing cell proliferation and thus the risk of in-stent restenosis [15,16]. PTX is being applied directly to the target area with drug-eluting balloons or in polymer coatings of DES [3,17], however this has recently been questioned [18]. The mechanism of action for PTX is the inhibition of smooth muscle cell (SMC) migration and proliferation by suppression of spindle microtubule assembly during mitosis cycle [16,19]. Dexamethasone (DEX), a corticosteroid, is used for its immunosuppressive and anti-inflammatory properties [20]. Another active pharmaceutical ingredient (API) for potential DES application is CYCLO,

which blocks calcineurin-cyclophylin complexation and thus inhibits SMC proliferation and migration [21,22].

Besides polymer-free DES, one of the most common technologies is the drug incorporation into a polymer coating applied to the stent [23]. A wide range of polymers are in clinical use regarding drug carrying matrices for DES [24,25]. Alongside chemically inert polymers, such as fluorinated polymers, polylactide (PLA) and its derivatives are widely used as coating matrices due to the easy processability and their biodegradable nature [26]. Table 1 gives a brief overview about the state-of-the-art of available DES.

Table 1. Overview on selected commercially available DES (modified according to [25], drug loading data was taken from [27]).

Stent	Stent Material	Polymer	Absorption Time	Drug	Drug-Eluting Time	Manufacturer	Drug Loading
CYPHER	Stainless steel	PEVA/PBMA	Permanent	Sirolimus	90 days	Cordis	140 µg/cm^2
TAXUS EXPRESS	Stainless steel	SIBS	Permanent	Paclitaxel	>180 days	Boston Scientific	100 µg/cm^2
XIENCE ALPINE	CoCr	PVDF-HFP	Permanent	Everolimus	120 days	Abbott Laboratories	100 µg/cm^2
RESOLUTE INTEGRITY	CoNi with Pt-Ir	BioLinx	Permanent	Zotarolimus	180 days	Medtronic	-
ORSIRO	CoCr	PLLA	15 months	Sirolimus	100–120 days	Biotronik	1.4 µg/mm^2
ULTIMASTER	CoCr	PDLLA-PCL	3–4 months	Sirolimus	3–4 months	Terumo Interventional Systems	-
SYNERGY	PtCr	PLGA	3–4 months	Everolimus	3 months	Boston Scientific	38–179 µg/stent
NOBORI	Stainless steel	PDLLA	6–9 months	Biolimus	6–9 months	Terumo	15.6 µg/mm^2

PEVA = poly(ethylene-co-vinyl acetate); PBMA = poly(n-butyl methacrylate); SIBS = poly(styrene-*b*-isobutylene-*b*-styrene); PVDF-HFP = poly(vinylidene fluoride-co-hexafluoropropylene); BioLinx = blend of methacrylate and vinylpyrrolidone based polymers; PLLA = poly-L-lactide; PDLLA-PCL = poly(DL-lactide-co-caprolactone); PLGA = poly(lactic-co-glycolic acid); PDLLA = poly(DL-lactide).

In this context, effort has been taken, including work from our group, to understand and modify drug release behavior from polymer/drug matrices. Several reports regarding the release profile of PTX loaded PLA film coatings can be found in the literature [28–32]. Furthermore, in particular SIR loaded DES has been investigated to an extent [33–36]. Also, release profiles of DEX/PLLA [37] and CYCLO/PLLA [13] are well known from the literature.

As DES coatings usually possess a thickness in a range of only 10 µm for hemodynamic reasons, they are prone for fracturing or peeling off due to mechanical stress during implantation which is caused by stent insertion and dilatation [4,38]. Therefore, a drug containing coating does not only have to show appropriate release and biocompatibility, but furthermore a suitable mechanical performance paired with resilience against delamination and particle detachment, which is required e.g., in DIN EN ISO 25539-2 [39].

For relatively stiff and rigid polymers such as PLLA, blending with other polymers, e.g., PCL, is a frequently used technique to create suitable and sufficient ductile coatings [40–42]. In a recent work, we investigated the influence of PCL fraction on the mechanical, morphological and thermal behavior of high molecular weight (HMW) PLLA film materials [43]. Another way to modify the polymer properties is the use of small molecular additives. The fact that the incorporation of such additives into a polymer may lead to plasticizing or hardening effects by intermolecular interactions is well known [44–48]. As for that, Ljungberg and Wesslén reported on the influence of several additives on the mechanical and thermal properties of *PLA*. Triacetine and tributyl citrate proved to be effective plasticizers up to an extent of 25 w/w% where saturation occurred and the polymer-additive mixture showed phase separation upon heating, accompanied by an increase in PLA crystallinity due to enhanced molecular mobility [49].

However, even the incorporation of a drug alone, being a small molecule, the API may lead to the desired increase in flexibility and resilience against fracturing. Regarding the influence on the material properties of drugs incorporated into a polymer matrix, Siep-

mann, le Brun, and Siepmann reported on acrylic acid copolymers mixed with ibuprofen, chlorpheniramine maleate and metoprolol tartrate [50]. One of their findings was that by the addition of 20 w/w% ibuprofen, the glass transition temperature (T_g) of the polymer was decreased from 80 °C down to 20 °C accompanied by a strong increase of elongation at break. An innovative concept to overcome such effects, which are not always beneficial or even unwanted, is the encapsulation of the API in a hollow PLA nanoparticles, as reported by Lai's group [51,52]. Using DSC and IR measurements, they showed that this approach allows a physical separation between the drug and the carrier matrix, so that the drug does not interact with the polymer chains and matrix properties are not altered. Furthermore, due to the diffusion barrier, the encapsulation leads to a decreased burst release.

All those effects are of certain interest regarding a functional implant, especially in the field of stent devices, which have to be crimped and diluted and are even exposed to intense mechanical stress during the implantation process. Still, only little is known on how the integration of drugs as small molecules into the polymer matrix alters the physico-chemical and mechanical properties of a DDS coating in its entirety.

In the current literature, mostly release behavior of drug containing PLA has been addressed. Although it can be estimated, the influence a drug has on the matrix, such as a shift in T_g or changes in crystallinity, can differ greatly [53,54]. The present study addresses the outcome of the incorporation of selected drugs, SIR, PTX, DEX, and CYCLO, which are approved or under investigation for the local treatment regarding stent related complications, on the mechanical, thermal and morphological properties of PLLA thin films regarding the functionality as DES coatings.

The drug inclusion criterion for our study was to identify candidates with a high relevance in DES applications, but at the same time representing substantially different chemical base structures. While SIR is a macrocyclic lactone, PTX is a diterpene, DEX possesses a sterol backbone, and CYCLO is a cyclic peptide. Overall, the selected API cover a relevant range of different structural properties in terms of molecular weight, size, polarity, hydrophilicity or functional groups and therefore possible ways of interacting with the polymer matrix. Some indicators for these parameters are polar surface area (PSA) and partition coefficient (logP). Selected characteristics of SIR, PTX, DEX and CYCLO have been summarized in Table 2. To visualize how the drugs used differ in terms of molecular size and shape, structural formulas and space-filling model illustrations were included.

Table 2. An overview concerning the drugs used in this study for blending with PLLA and their selected properties.

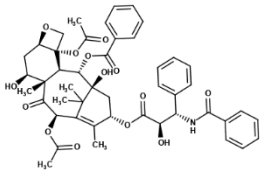
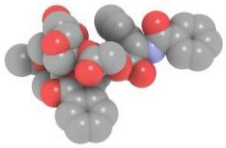
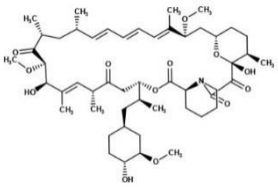
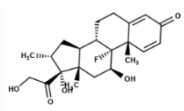
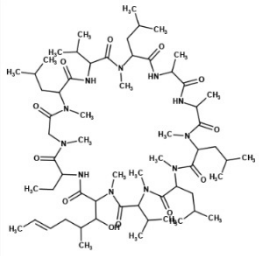
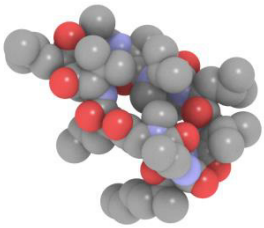
Drug	Structural Formula	Space Filling Model Illustration	PSA (in Å^2) [1]	logP	M_W (g/mol)
PACLITAXEL (PTX)			221	3 [18]	853.9
SIROLIMUS (SIR)			195	7.45 [55]	914.2
DEXAMETHASONE (DEX)			95	1.83 [56]	392.5

Table 2. *Cont.*

Drug	Structural Formula	Space Filling Model Illustration	PSA (in Å^2) [1]	logP	M_W (g/mol)
CYCLOSPORINE (CYCLO)			279	1.4 [57]	1202.6

[1] Polar surface area (PSA) values were taken from PubChem and calculated via CACTVS [58], according to the information on the website. MarvinSketch was used for molecular structure drawing (Marvin v.20.11, 2020, ChemAxon, Budapest, Hungary). Space filling models were created with QuteMol (v. 0.4.1) [59] using pdb-files created from MarvinSketch.

Our interest was to what extent blending PLLA with different drugs alone may influence or even have beneficial effects on the polymer properties. As shown in Table 1, commercially available DES vary in drug loading. This is both dependent on stent design, as well as on the incorporated API, as different drugs show different therapeutic windows. Thus, literature reports on incorporated drugs for DES technology range from 1 *w*/*w*% for PTX [60] up to 200 *w*/*w*% for DEX [37]. In order to generate comparable data for the selected drugs, we decided to investigate the alteration of polymer properties after incorporation of 10, 15, and 20 *w*/*w*% of drug in PLLA, knowing that certain drug coatings for clinical use may contain lower or higher drug amounts.

It must be noted that the topic of drug incorporation becomes even more complex when considering the effect of additives on polymer/drug matrices. There are several reports in the literature on how the addition of stabilizers or supporting molecules may enhance drug release, mechanical resilience or stability of the carrying matrix on a high level [61–63]. However, three or more component systems are a somewhat complex matter in respect to their physico-chemical properties as each part may interact with all the others alone and at once. Consequently, our focus was on binary systems formed by drug incorporation though the authors of this study are aware of the fact that several other compounds are of high interest regarding DES technology. To the best of our knowledge, the influence of commonly used drug molecules on the physico-chemical properties of matrix polymers, such as PLLA, against the background of DES coatings has not been systematically investigated. For this work, as one of the most widely used coating technique [64], especially in industrial application, drug loaded PLLA films were generated via airbrush spray-coating process.

In summary, our aim in the presented study was to analyze the effects of different drug candidates on the properties of the respective polymer/drug matrices from a biomedical engineering viewpoint. It addresses thermal and mechanical properties, long term stability, and phase behavior of PLLA/drug blends, which are parameters of crucial relevance to ensure shelf life and performance of stent coatings. In addition to the already comprehensive literature data concerning drug release behavior and biocompatibility, our results shall provide a complementary contribution towards an understanding of such drug coatings.

2. Materials and Methods

2.1. Chemicals

Chloroform and methanol were received from VWR international (Darmstadt, Germany) in technical grade quality.

HMW PLLA used was Resomer L 210 S, intrinsic viscosity in chloroform: 3.8 dL/g, M_w = 320 kDa (Evonik Industries AG, Essen, Germany). Drugs used were: Paclitaxel (Cfm Oskar Tropitzsch GmbH, Marktredwitz, Germany), sirolimus (Cfm Oskar Tropitzsch

GmbH, Marktredwitz, Germany), cyclosporine A (Synopharm GmbH & Co. KG, Glinde, Germany) and dexamethasone (Dr. Gerhard Mann Chem.-Pharm. Fabrik GmbH, Berlin, Germany).

All chemicals were used as received without further purification.

2.2. Preparation of Polymer Films via Spray Coating

Thin film specimens of PLLA with incorporated drugs were produced using airbrush spray coating process as was reported by our group before [35]. In brief, PLLA was dissolved in $CHCl_3$ and drug solution in MeOH (PTX, SIR, DEX) or $CHCl_3$ (CYCLO) was added. For each drug, a final ratio of 10 w/w%, 15 w/w% and 20 w/w% was adjusted with respect to the dissolved polymer. As reference, pure PLLA film was manufactured in the same manner without the addition of drugs.

Following to this, thin films of thicknesses of around 7 µm were generated using a custom-made airbrush device on rectangular glass slides as substrate (6.5 × 2.5 cm^2). Residual solvent from the process was removed from the coated glass slides under reduced pressure at 80 °C. A total amount of approximately 250 µg polymer film was formed and checked via weighing. Films were removed manually from the glass substrates using a scalpel to slightly lift the films, which led to easy detachment.

2.3. Raman Microscopy Imaging

Polymer films obtained via spray coating were investigated with regard to drug distrubution at the surface by means of Raman imaging. A WITec alpha 300 confocal Raman microscope (WITec GmbH, Ulm, Germany) with 10× magnification equipped with an input laser with a wavelength of ν = 532 nm was used. For Raman area scans, a 500 µm × 500 µm field with 50 dots per row and column was used, giving a resulting resolution of 10 μm^2. The area ratio of signals that are specific for the PLLA matrix ($\tilde{\nu}$ = 878 rel cm^{-1}) and the distinct drugs (PTX: $\tilde{\nu}$ = 1012 rel cm^{-1}, SIR: $\tilde{\nu}$ = 1642 rel cm^{-1}, DEX: $\tilde{\nu}$ = 1668 rel cm^{-1}) were chosen for visualizing drug distribution. The areas of distinct drug signals identified from preliminary measured reference spectra have been normalized to the area of the PLLA signal at $\tilde{\nu}$ = 883 rel cm^{-1}. The measurements have been performed for two separately manufactured drug containing PLLA films and the median of the quotients was formed. In the case of CYCLO incorporation, no distinct drug signal could be detected.

2.4. FTIR Measurements

FTIR-ATR-measurements were performed using a Bruker Vertex 70 IR-Spectrometer (Bruker, Leipzig, Germany) equipped with a DLaTGS-detector. Data were collected in the range of $\tilde{\nu}$ = 500 cm^{-1} to 4000 cm^{-1} with a resolution of $\tilde{\nu}$ = 4 cm^{-1} averaged over 100 scans in reflection mode using a Graseby Golden Gate Diamond ATR-unit. All spectra were subsequently baseline corrected and atmospheric compensation has been performed. Subsequently, the area of the CYCLO signal at $\tilde{\nu}$ = 1629 cm^{-1} has been compared to the area of PLLA signal at $\tilde{\nu}$ = 1749 cm^{-1}. The quotient formed from these areas in a similar manner as for Raman measurements can be found in Figure 1b.

2.5. SEM Imaging

Morphology of the polymer films was examined with scanning electron microscopy SEM QUANTA FEG 250 (FEI Company, Dreieich, Germany) operating in high vacuum and 10 kV, using an Everhart-Thornley secondary electron detector (ETD). The samples were fixed onto aluminum carriers using conductive carbon pads and Au sputter coated. The images were taken at magnification ×1000.

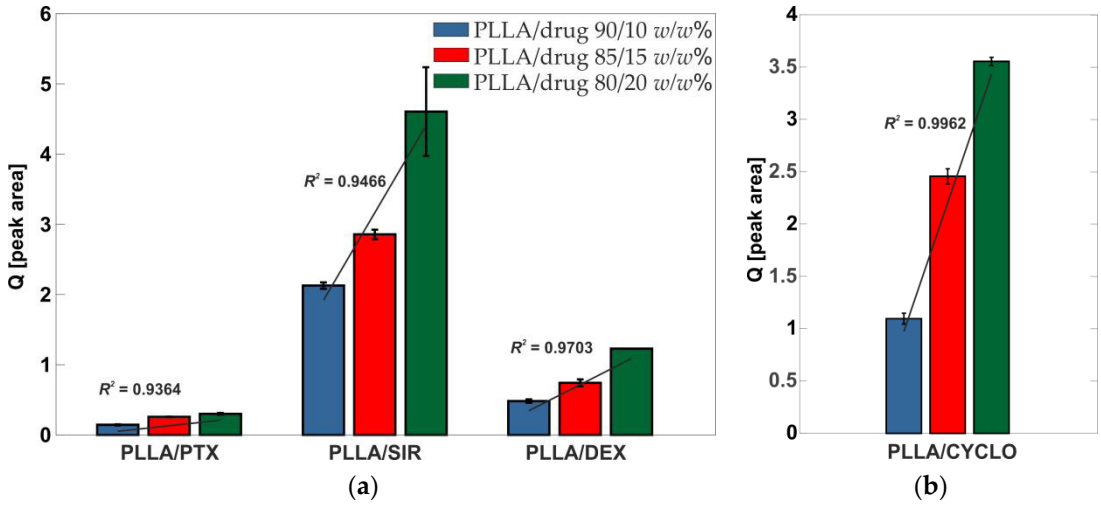


Figure 1. (**a**) Quotients of drug signal found in Raman spectroscopy (PTX: $\tilde{\nu}$ = 1012 rel cm^{-1}, SIR: $\tilde{\nu}$ = 1642 rel cm^{-1}, DEX: $\tilde{\nu}$ = 1668 rel cm^{-1}) compared to PLLA reference signal to ensure drug loading. (**b**) Quotient of the CYCLO signal at $\tilde{\nu}$ = 1629 cm^{-1} from FT-IR spectroscopy compared to PLLA reference signal. Linear regression of the means has been performed and R^2 values are given.

2.6. Contact Angle Measurements

Contact angle measurements have been performed using a mobile surface analyzer MSA (Krüss GmbH, Hamburg, Germany) equipped with a double pressure dosing unit at ambient conditions with 2 µL drop volume and 1 s equilibration time. As test liquids, deionized water and diiodomethane were used to calculate free surface energy. Contact angles have been determined in triplicate for each drug loaded polymer film using separate cutouts. Contact angles were calculated by averaging the values for both sides of the drops. To avoid bending of the test samples and to ensure a plain shape, the PLLA films have been mounted on pyrolytic graphite planchets.

2.7. Thermal Analysis

The DSC 1 system (Mettler-Toledo, Greifensee, Switzerland) was used to determine the thermal properties of drug-loaded PLLA spray-coated films using the conventional calibration methods with highly pure standards. The specimens were heated up from 25 °C at a rate of 10 K/min operating under nitrogen at atmospheric pressure. The end temperature was between 210 °C and 280 °C, depending on the incorporated drug. The sample weights were in the range of 0.3–2.5 mg. Samples were analyzed with respect to glass transition (T_g), crystallization temperature (T_c), melting temperature (T_m), and degree of crystallinity of PLLA (χ). The heats of fusion ΔH and crystallization χ were quantitatively evaluated by means of Equation (1)

$$\chi = 100\% \cdot \left[\frac{\Delta H_m}{\Delta H_{m0}} \right] \cdot \frac{1}{W} \quad (1)$$

where ΔH_{m0} is the enthalpy value of a pure crystalline material, ΔH_m is the enthalpy corresponding to the fusion process and W the amount of each component in the polymer/drug system. The reference value taken for ΔH_{m0} of PLLA was χ_{100} = 93.7 J/g [65]. All results were averaged over n = 5 samples.

2.8. Mechanical Testsing

Tensile tests were carried out using the uniaxial tensile test instrument Zwicki ZN 2.5 (Zwick/Roell, Ulm, Germany). Samples were cut into dumbbell shape specimens with effective dimensions of 12 mm × 2 mm according to DIN EN ISO 527-2 1BB standards [66]. Sample thickness was measured using SEM QUANTA FEG 250 (FEI Company, Dreieich,

Germany). It was determined using the reverse form of the dogbone sample. 10 mm samples directly neighboring the cutouts of the specimens for mechanical testing were mounted on the edge of the aluminum trays. The carrier was positioned vertically using a 90° adapter in the SEM to obtain a top view of the cutting edge. For each sample, at three distinct positions with n = 3, thickness values were determined.

Mechanical tests were conducted with a 10 N load cell and a crosshead speed of 25 mm/min. All tests were performed at room temperature (20 °C). The tensile force as a function of elongation was measured. Based on these data, the elastic modulus (E) was calculated in the linear elastic region. Furthermore, the tensile strength (σ_{max}) and elongation at break (ε_B) were determined for n = 5 samples. For statistical analysis, a twofold Nalimov's test has been performed and data were corrected for outliers.

2.9. Statistical Analysis

All data are given as mean ± standard deviation. For statistical analysis of contact angle, mechanical and DSC data, two tailed t-tests of the means versus PLLA reference have been performed. For statistical analysis, SigmaPlot software (V13.0, Systat Software, Inc., San Jose, CA, USA) has been used. Significances are given at a significance level of $p < 0.05$ and marked with an asterisk.

3. Results

3.1. Spectroscopical Analysis of Drug Loaded PLLA Films

Our first interest was whether drugs were homogeneous distributed into the PLLA films. Therefore, drug incorporation has been ensured by the use of Raman spectroscopy. The resulting quotient $Q = \left[\frac{A_{Drug}}{A_{PLLA}}\right]$ is given in Figure 1a. Raman spectra are given in the supporting information (Supplementary Figure S1).

From Raman data, a linear progression can be seen for all drugs leading to the assumption that no separation and precipitation from the solution during airbrush process occurred and that all drugs are distributed homogeneously in the polymer films. For CYCLO loaded PLLA films, no distinct Raman signal for the drug could be detected. To ensure the successful drug loading, FT-IR spectroscopy has been used. As for the drugs analyzed with Raman, linearity in the drug distribution was observed.

FTIR-ATR-measurements have been performed for all drug loaded PLLA films to investigate a potential polymer/drug interaction on a molecular level. Figure 2 shows IR spectra for 20 w/w% drug in PLLA, spectra for 10 w/w% and 15 w/w% can be found in the supporting information (Supplementary Figure S2). Characteristic IR bands of PLLA have been assigned according to [51] and are $\tilde{\nu}$ = 3001 cm^{-1} (CH stretch), $\tilde{\nu}$ = 1749 cm^{-1} (C=O stretch), $\tilde{\nu}$ = 1454 cm^{-1} (CH_3 bend), $\tilde{\nu}$ = 1359 cm^{-1} (C-H deformation), $\tilde{\nu}$ = 1180 cm^{-1} (C-O-C stretch), and $\tilde{\nu}$ = 1082 cm^{-1} (C-O-C stretch).

3.2. Influence of Drug Incorporation on the Surface Morphology and Drug Distribution

Changes in morphology due to the drug incorporation were investigated by means of macrophotography, scanning electron microscopy and Raman imaging. Image analysis of macro photography for drug containing PLLA films showed no significant changes compared to pure PLLA reference films such as phase separation or roughening. Macroscopic images are given in SI (Supplementary Figure S3). For a more detailed view, SEM imaging has been used to investigate the microscopic appearance of the drug loaded polymer films. At a magnification of 1000×, no such thing as microcrystals or other inhomogenities as well as changes in surface morphology could be observed for PTX and CYCLO. These drug containing films appeared smooth and comparable to the PLLA reference. The crater like shapes are most probably due to solvent evaporation. Regarding SIR and DEX, the surfaces show bumps in submicron range for all investigated concentrations, 10 w/w%, 15 w/w% and 20 w/w%. It must be noted that the side which was attached to the glass slid showed in all cases a plainer appearance. In Figure 3, exemplary SEM images for all PLLA/drug

combinations at the highest drug concentration of 20 w/w% at 1000× magnification are shown. SEM images for 10 w/w% and 15 w/w% can be found in Supplementary Figure S4.

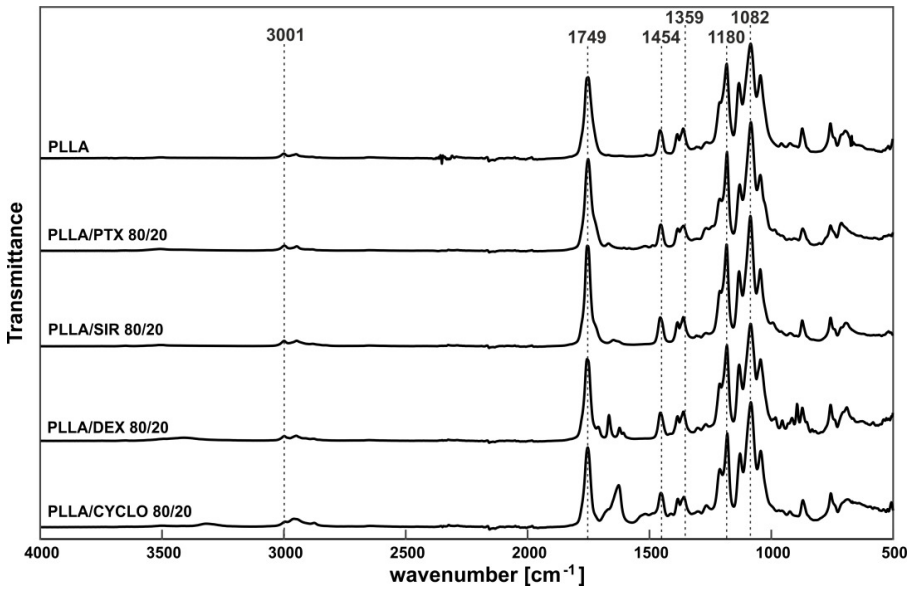


Figure 2. IR spectra of PLLA film and PLLA films with 20 w/w% incorporated drugs. IR bands of PLLA have been identified with reference to [51].

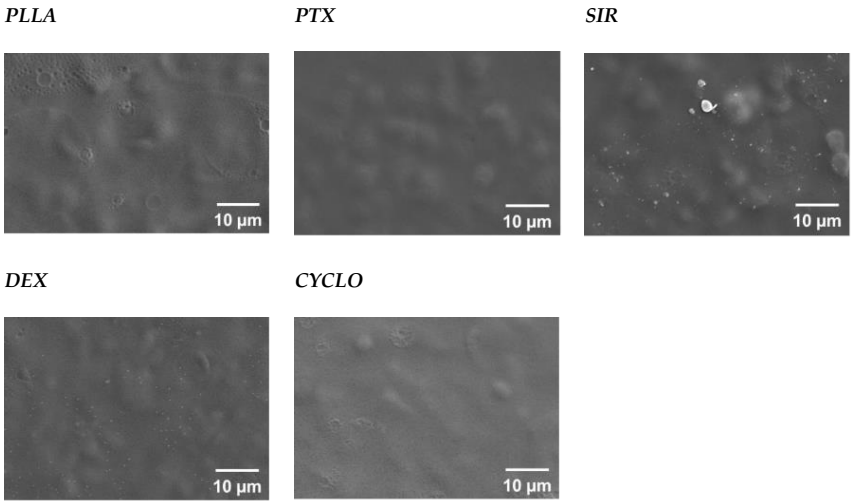


Figure 3. Exemplary SEM images for different drugs incorporated in PLLA samples (PLLA/drug 80/20 w/w%). Drugs used were paclitaxel (PTX), sirolimus (SIR), dexamethasone (DEX) and cislosporine (CYCLO).

As for Raman microscopy, distinct drug signals (PTX: $\tilde{\nu}$= 1012 rel cm^{-1}, SIR: $\tilde{\nu}$ = 1642 rel cm^{-1}, DEX: $\tilde{\nu}$= 1668 rel cm^{-1}, Supplementary Figure S1) were mapped in respect to their intensity. As mentioned before, CYCLO gave no measurable Raman signal when blended with PLLA and could therefore not be analyzed via Raman mapping. All drugs showed homogeneous distribution even at highest concentration of 20 w/w%, see Figure 4. No such things as macroscopic crystals, agglomerates or drug enriched phases were observed. Raman mapping images for 10 w/w% and 15 w/w% can be found in Supplementary Figure S5.

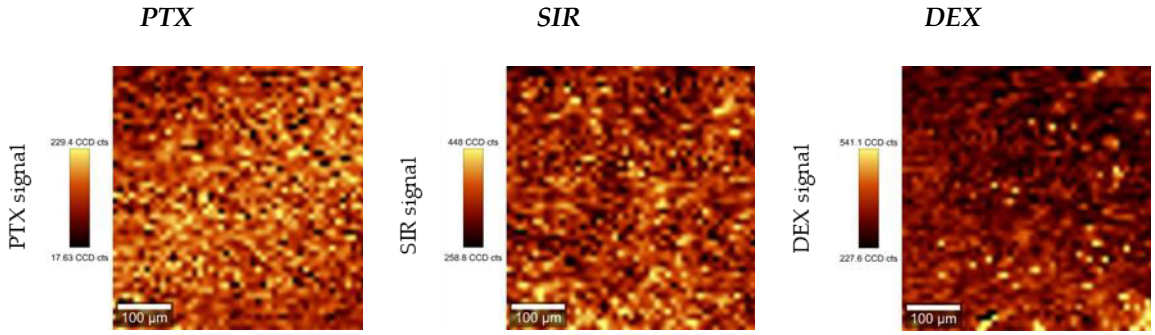


Figure 4. Exemplary Raman mapping images for different drugs incorporated in PLLA (PLLA/drug 20/80 *w*/*w*%). For CYCLO no distinct Raman signal could be detected.

3.3. Influence of Drug Incorporation on Surface Hydrophilicity

Figure 5 gives an overview on the contact angles for the polymer films addressed in this study. Exemplary images of the drops can be found in the Supplementary Figure S6. Compared to PLLA reference film, drug incorporation showed to have no effect on the surface wettability as all contact angles are in a range of 70–80°. Furthermore, surface free energy (SFE) calculated from contact angle data acquired from water and diiodomethane have been calculated. As can be seen, incorporation of the chosen drugs did not result in observable changes in SFE.

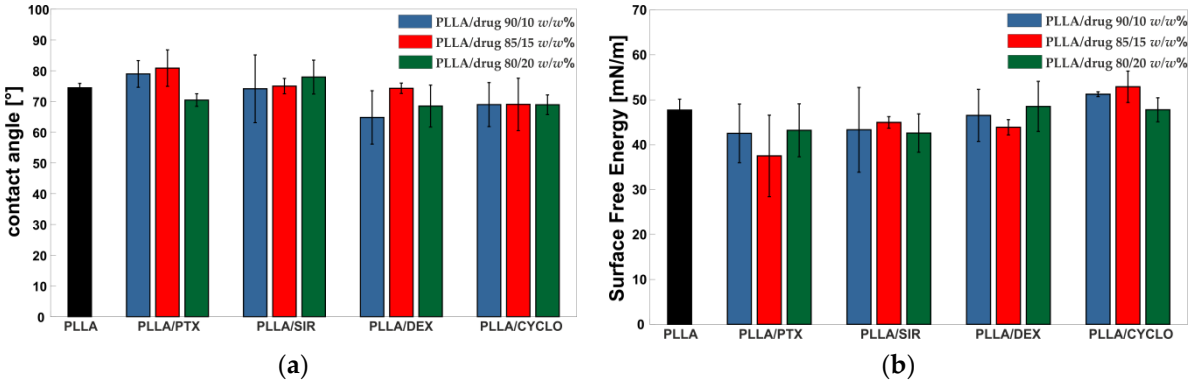


Figure 5. (**a**) Water contact angle and (**b**) surface free energy data for drug incorporated PLLA films (mean values for n = 3 with droplet angles taken each from both sides of the drops are shown). Statistical analysis (two-tailed *t*-test) did not show any significant differences ($p < 0.05$) of contact angle values and SFE values of drug incorporated PLLA films when compared to pure PLLA reference.

3.4. Influence of Drug Incorporation on the Thermal Properties—DSC

Figure 6 shows the first DSC heating curve of the spray coated films with the different drug ratios (90/10, 85/15, 80/20 *w*/*w*%) after thermal annealing. For reference, both the DSC curves of the pure polymer PLLA and the pure drug are included for each diagram.

The DSC heating curves of pure PLLA spray coated film exhibit a glass transition temperature at T_g = 72.8 °C. No exothermic peak, but an endothermic melting peak at 179 °C is observed, which is comparable to reported T_m data for HMW PLLA [67]. For 20 *w*/*w*% PTX, T_g of PLLA is shifted to lower temperatures, as shown in Table 3. Furthermore, an exothermic peak $T_{c,PLLA}$ is formed with increasing drug content, whose peak temperature is shifted to higher temperatures as the ratio increases (Figure 6a). The melting peak $T_{m,PLLA}$ is nearly identical at all concentrations. No other endothermic peak was identified that would be indicative of the presence of a pure PTX phase.

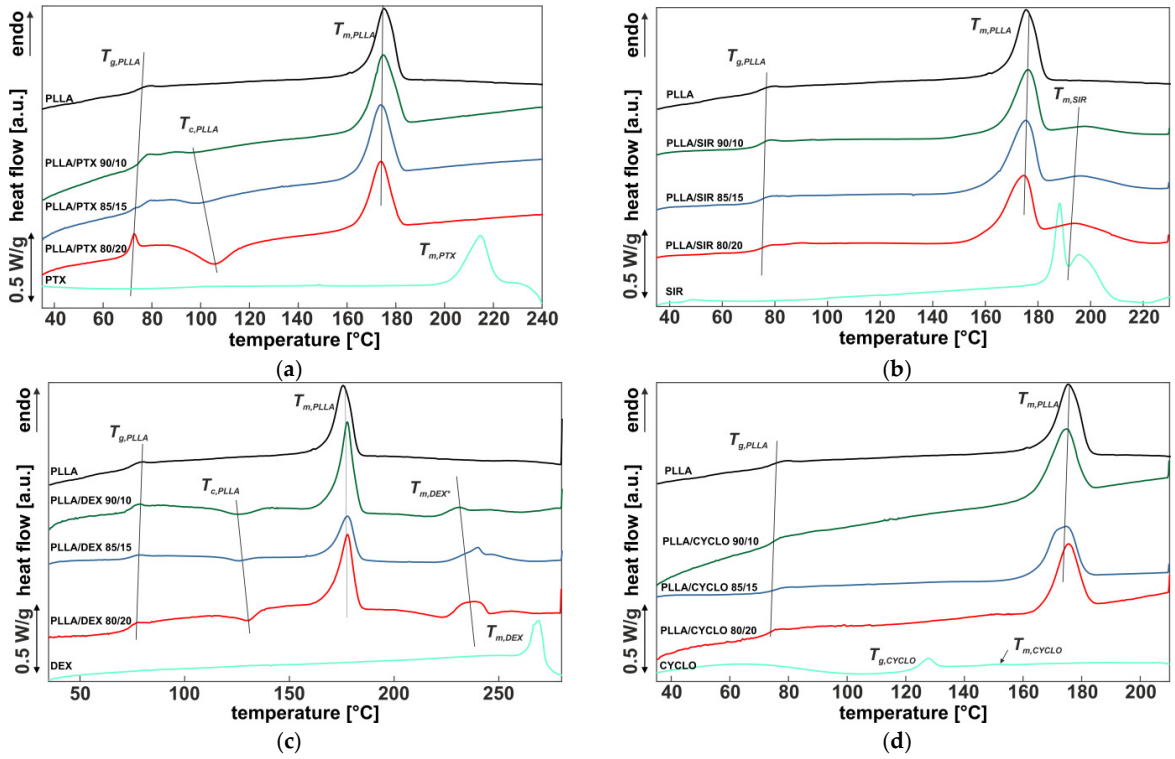


Figure 6. DSC thermograms of PLLA (black), drug (cyan) and PLLA/drug (**a**) PLLA/PTX, (**b**) PLLA/SIR, (**c**) PLLA/DEX and (**d**) PLLA/CYCLO) in different ratios (90/10, 85/15, 80/20 *w*/*w*%). The straight lines are guides for the eyes, only.

SIR incorporation into PLLA (Figure 6b) did not lead to distinct changes in $T_{g,PLLA}$ compared to pure PLLA. Even the endothermic melting peak $T_{m,PLLA}$ is kept constant. In addition, a further endothermic peak $T_{m,SIR}$ at 184 °C is observed, which can be related to the drug according to the reference measuring curve of the pure SIR material. There is no cold crystallization observed as in PTX.

PLLA/DEX DSC curves show no distinct shift in $T_{g,PLLA}$ (Table 3), but an exothermic peak $T_{c,PLLA}$ is formed with increasing drug content, whose peak temperature is shifted to higher temperatures as the drug content increases (Figure 6c). The PLLA melting peak $T_{m,PLLA}$ is almost identical at all concentrations. In addition, there is a further endothermic peak $T_{m,DEX}$ which can be identified from the measurement curve of the pure DEX material and which is shifted to higher temperatures and broadens as the drug ratio increases.

Thermograms of PLLA including CYCLO show no significant changes compared to pure PLLA (Figure 6d). As for that we conclude complete incorporation of the drug into the polymer matrix. However, as only little to no changes in $T_{g,PLLA}$ or $T_{m,PLLA}$ occur, low interaction of the polymer chains with the drug molecules can be assumed.

To evaluate the influence of drug incorporation on PLLA crystallinity, the percentage values as determined according to Equation (1) are plotted in Figure 7. The black bar refers to PLLA without drug content and with a value of $\chi = 37.8 \pm 1.9$ %, which is comparable with the literature for HMW PLLA [67]. With increasing PTX content, χ values of PLLA decreased from $\chi = 33 \pm 7$% down to $\chi = 11.3 \pm 1.7$%. In contrast, χ values of PLLA with SIR increased with increasing drug content. PLLA crystallinity including DEX or CYCLO show only little to no changes compared to pure PLLA. All χ values are given in Table 3.

Table 3. DSC results (glass transition (T_g), melting temperature (T_m) and degree of crystallinity (χ)) of PLLA/drug spray coated films in different ratios (90/10, 85/15, 80/20 *w*/*w*%) (n = 5 for each group). * in T_{m,DEX^*} indicates that shift in melting point occurs in comparison to pure drug.

PLLA/PTX	T_g (°C)	ΔH_{PLLA} (J/g)	χ (%)	$T_{m,PLLA}$ (°C)	ΔH_{PTX} (J/g)	$T_{m,PTX}$ (°C)
100/0	72.8 ± 0.5	35.4 ± 1.8	37.8 ± 1.9	177.08 ± 0.25	—	—
90/10	75.4 ± 0.4	31 ± 7	33 ± 7	174.72 ± 0.19	—	—
85/15	74.4 ± 2.6	26 ± 10	27 ± 10	173.84 ± 0.07	—	—
80/20	69.2 ± 0.8	10.6 ± 1.6	11.3 ± 1.7	173.78 ± 0.13	—	—
0/100	—	—	—	—	32.4 ± 1.2	213.48 ± 0.17
PLLA/SIR	**T_g (°C)**	**ΔH_{PLLA} (J/g)**	**χ (%)**	**$T_{m,PLLA}$ (°C)**	**ΔH_{SIR} (J/g)**	**$T_{m,SIR}$ (°C)**
100/0	72.8 ± 0.5	35.4 ± 1.8	37.8 ± 1.9	177.08 ± 0.25	—	—
90/10	73.45 ± 0.24	30 ± 5	32 ± 6	175.5 ± 0.5	43 ± 5	199.5 ± 0.6
85/15	74.9 ± 0.7	38 ± 8	41 ± 9	174.82 ± 0.28	45 ± 13	198.6 ± 0.6
80/20	73.9 ± 0.5	48.5 ± 2.9	52 ± 3	174.32 ± 0.07	49 ± 13	196.5 ± 0.5
0/100	—	—	—	—	64.9 ± 2.8	183.9 ± 0.5
PLLA/DEX	**T_g (°C)**	**ΔH_{PLLA} (J/g)**	**χ (%)**	**$T_{m,PLLA}$ (°C)**	**ΔH_{DEX} (J/g)**	**T_{m,DEX^*} (°C)**
100/0	72.8 ± 0.5	35.4 ± 1.8	37.8 ± 1.9	177.08 ± 0.25	—	—
90/10	74.3 ± 0.5	44.0 ± 2.4	46.9 ± 2.6	177.3 ± 0.3	1.9 ± 0.8	231.8 ± 1.5
85/15	71.7 ± 1.7	38 ± 6	40 ± 6	177.0 ± 0.5	19 ± 4	238.2 ± 0.9
80/20	74.9 ± 0.5	42 ± 10	45 ± 11	177.69 ± 0.15	8 ± 5	240.1 ± 1.4
0/100	—	—	—	—	15.2 ± 2.8	263.5 ± 0.8
PLLA/CYCLO	**T_g (°C)**	**ΔH_{PLLA} (J/g)**	**χ (%)**	**$T_{m,PLLA}$ (°C)**	**ΔH_{CYCLO} (J/g)**	**$T_{m,CYCLO}$ (°C)**
100/0	72.8 ± 0.5	35.4 ± 1.8	37.8 ± 1.9	177.08 ± 0.25	—	—
90/10	74.5 ± 0.7	43.1 ± 2.8	46 ± 3	174.51 ± 0.21	—	—
85/15	75.9 ± 2.0	40 ± 4	42 ± 4	174.61 ± 0.02	—	—
80/20	72.7 ± 2.4	36 ± 5	38 ± 6	173.7 ± 0.7	—	—
0/100	—	—	—	—	—	146.9 ± 0.7

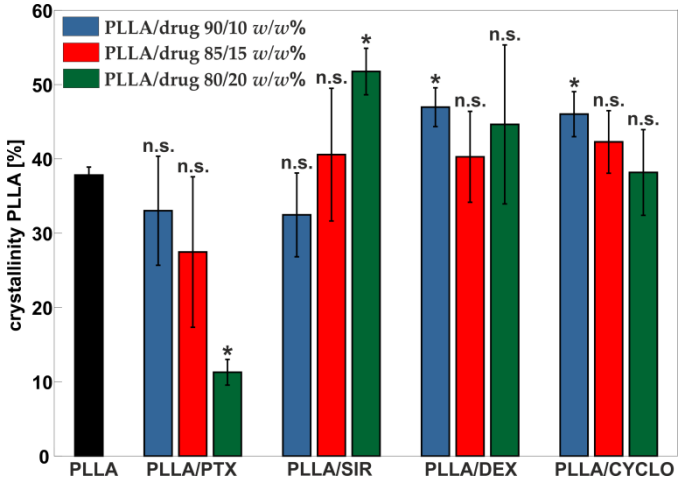


Figure 7. Crystallinity of PLLA in PLLA/drug spray coated films with different ratios (90/10, 85/15, 80/20 *w*/*w*%), determined from DSC measurements. Asterisks (*) mark significant differences of crystallinity data with $p < 0.05$ obtained by two-tailed *t*-test, each in comparison to PLLA reference. n.s. stands for not significant.

3.5. Coating Thickness Determination

For the calculation of mechanical parameters, adequately accurate thickness determination is necessary. A change in thickness accuracy of approximately ±1 µm would result in falsifying elastic modulus and tensile strength values of about 20 %. Consequently, as the films showed thicknesses in a range below 10 µm, thickness determination by the use of a dial indicator was not suitable.

To overcome this issue, film thickness has been determined using SEM imaging. Using a 90° adapter ensures precise sample characterization up to some few nanometers. However, measuring errors due to misalignment of the sample or manual setting of the scale bar have to be considered. As for that, a cutout close to the point of rupture of the strain samples has been threefold measured at three distinct points by SEM. A sample image for one of such measuring points is given in Figure 8a.

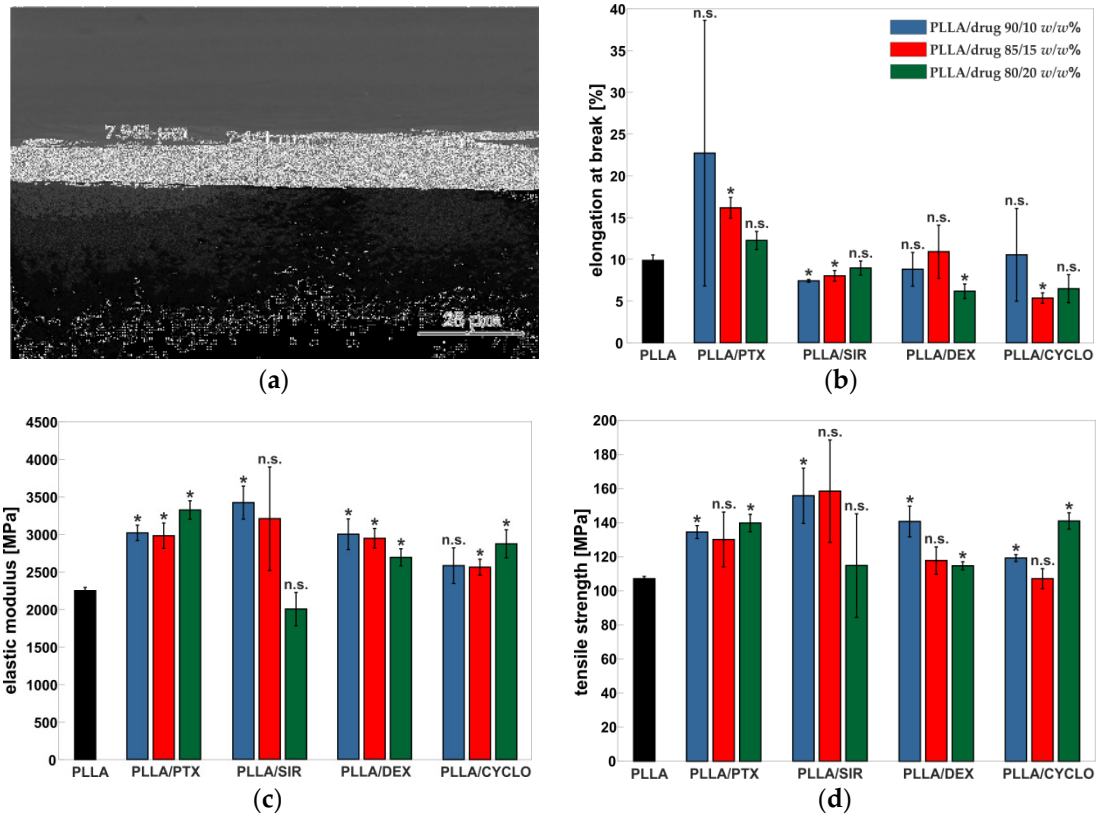


Figure 8. (**a**) Exemplary SEM image of PLLA reference film with determined thicknesses. (**b**–**d**) Mechanical properties ((**b**) elongation at break, (**c**) elastic modulus and (**d**) tensile strength), determined from uniaxial tensile tests of PLLA/drug spray coated films in different drug ratios (90/10, 85/15 and 80/20 *w*/*w*%). Asterisks (*) mark significant differences of the values with $p < 0.05$ obtained by two-tailed *t*-test, each in comparison to PLLA reference. n.s. stands for not significant.

3.6. Influence of Drug Incorporation on the Mechanical Properties

An overview on the mechanical parameters is given in Figure 8b–d. From tensile tests, elongation at break, elastic modulus and tensile strength have been calculated.

In general, drug incorporation results in an increase of elastic modulus up to 3420 ± 220 MPa for PLLA/SIR 90/10 compared to pure PLLA with a value of E = 2250 ± 40 MPa. Only SIR at 20/80 *w*/*w*% resulted in a decrease down to E = 2000 ± 220 MPa. Regarding the mechanical behavior, PTX leads to a high deviation for elongation at break values. SIR did not show to have any influence on the elongation at break. For DEX, a tendency to a decrease in elongation at break can be observed. Results for CYCLO also indicate a slight decrease in ε_B from 11 ± 6% (10 *w*/*w*%) to 6.4 ± 1.7% (20 *w*/*w*%) compared to PLLA at 9.9 ± 0.7%. All polymer/drug materials show higher tensile strength values up to 160 ± 30 MPa or comparable ones compared to pure PLLA with σ_{max} = 107.1 ± 1.3 MPa. Results of mechanical properties are given in Table 4 and the stress strain curves are given in Supplementary Figure S7.

Table 4. Mechanical properties (elastic modulus (E), tensile strength (σ_{max}), elongation at break (ε_B)), determined from uniaxial tensile tests of PLLA/drug spray coated films in different drug ratios (90/10, 85/15 and 80/20 w/w%).

PLLA/PTX	***E* (MPa)**	σ_{max} **(MPa)**	ε_B **(%)**
100/0	2250 ± 40	107.1 ± 1.3	9.9 ± 0.7
90/10	3020 ± 100	134 ± 4	23 ± 16
85/15	2980 ± 170	130 ± 16	16.1 ± 1.2
80/20	3320 ± 120	140 ± 5	12.3 ± 1.1
PLLA/SIR	***E* (MPa)**	σ_{max} **(MPa)**	ε_B **(%)**
100/0	2250 ± 40	107.1 ± 1.3	9.9 ± 0.7
90/10	3420 ± 220	156 ± 16	7.40 ± 0.17
85/15	3200 ± 700	160 ± 30	8.0 ± 0.7
80/20	2000 ± 220	115 ± 30	8.9 ± 0.8
PLLA/DEX	***E* (MPa)**	σ_{max} **(MPa)**	ε_B **(%)**
100/0	2250 ± 40	107.1 ± 1.3	9.9 ± 0.7
90/10	3000 ± 200	141 ± 9	8.8 ± 2.0
85/15	2940 ± 130	118 ± 8	11 ± 3
80/20	2690 ± 110	115 ± 2.4	6.1 ± 0.9
PLLA/CYCLO	***E* (MPa)**	σ_{max} **(MPa)**	ε_B **(%)**
100/0	2250 ± 40	107.1 ± 1.3	9.9 ± 0.7
90/10	2580 ± 240	119.2 ± 2.0	11 ± 6
85/15	2560 ± 110	107 ± 6	5.4 ± 0.7
80/20	2870 ± 190	141 ± 5	6.4 ± 1.7

4. Discussion

In this work, drug incorporated PLLA films were manufactured by spray-coating using PLLA/drug solutions, which is also the method of choice in industrial settings [64]. This technique allows the generation of homogeneous polymer coatings on complex structures, such as those represented by scaffolds for cardiovascular intervention in particular. Still, the removal of solvent residues remains crucial, as these, even in trace amounts, may show negative effects on biocompatibility as well as influence the mechanical and thermal properties of the coating. To investigate to what extend drugs influence the polymer matrix, rinsing protocols for solvent removal are unsuitable, as such treatments lead to washout of the drugs. For spray-coated thin films, however, thermal annealing above T_g under reduced pressure has shown to be sufficient to remove solvent residues, making rinsing steps unnecessary [35,68]. Nevertheless, thermal treatment may lead to further altering of the properties of the drug containing films, which must be taken into account.

Our initial interest was in macroscopic film morphology and drug distribution, whereas no macroscopic changes were observed. Raman and IR spectroscopy were used to prove the incorporation of drugs in the polymer films. For all drugs except for CYCLO, which was unmeasurable, Raman mapping showed a homogeneous distribution. Furthermore, contact angle and SFE measurements showed that drug incorporation did not result in significant changes even at a high concentration of 20 w/w%. This is interesting in a way such that the drugs addressed in this study exhibit very different logP values. Moreover, the observed phase separation and formation of microcrystals for DEX and SIR in accordance to DSC measurements appear to have no influence on surface wettability. This leads to the assumption that wettability of drug coating is not affected by drug addition, but remains comparable to the pure PLLA matrix.

The IR-spectra showed no distinct changes in IR bands but appear as overlapping spectra of PLLA and the incorporated drugs. As for that, we assume no chemical interaction of SIR, PTX, DEX, or CYCLO with the PLLA matrix as no shift in characteristic signals appears.

Regarding thermal analysis, the drugs showed a different behavior. CYCLO showed little to no influence on the polymer matrix and thus barely any effect on the thermal properties.

As for PTX, a slight shift of T_g of the polymer matrix was observed. In the literature, it has been reported that PTX is miscible with the amorphous domains of PLLA, in consequence softening the polymer matrix, leading to a decrease in T_g [69]. Furthermore, this also leads to the formation of an exothermic peak (T_c), which increases with increasing PTX amount, as the incorporated PTX decelerates polymer recrystallization [31,70]. Liggins and Burt explained it in a way that hydrogen bonding between PLLA and PTX lead to accumulation of PTX in the amorphous regions and therefore in a reduced rate of polymer chain diffusion and thus slowed crystallization [71]. In accordance to this, our results indicate a similar behavior for thin films accessible by spray coating. No PTX signal at around 217 °C was detected in the thermogram leading to the conclusion that PTX is completely blended into the polymer. However, the appearance of an exothermic peak at 104–107 °C for 20 w/w% PTX indicates that thermal annealing at 80 °C is not sufficient to achieve thermal equilibrium state and therefore may have an impact on long term properties in respect to biomedical application of such a drug containing matrix, e.g., shelf life.

For PLLA/SIR films, the presence of a SIR melting peak, up to 199.5 ± 0.6 °C, which is considerably higher than the T_m of the pure SIR component at 183.9 ± 0.5 °C, leads to the conclusion that SIR is not completely miscible with PLLA and phase separation occurs. This is underlined by means of the inhomogenities observed in SEM imaging. A similar observation has been made by Nukula for SIR in poly (butyl methacrylate)/poly(ethylene vinyl acetate) (PBMA/PEVA) [72]. They assumed from the broaden appearance of the SIR melting peak close to the melting peak of pure SIR in the thermogram that the drug is mainly encapsulated in an amorphous state with only little crystallinity. It is still unclear whether the SIR crystal formation is an effect due to immiscibility of PLLA or appeared when generating the test samples as SIR showed limited solubility in $CHCl_3$. To bypass this, the drug had been dissolved in MeOH, which has been added to the $CHCl_3$-polymer-solution. Precipitation may have been occurred at this point leading to micro crystals, though this has not been investigated in this study.

In the case of DEX incorporation, the shift of the endothermic peak $T_{m,DEX}$ from 231.8 ± 1.5 °C to 240.1 ± 1.4 °C indicates an interaction between DEX and PLLA. Consequently, a certain amount of DEX must have been incorporated into the PLLA matrix up to a threshold whereas phase separation occurs. Otherwise, we observed similar behavior as it has been reported for DEX containing PCL nanofibers by means of a drug melting signal [73]. As Martins et al. concluded, DEX precipitates from the polymer/drug solution during the manufacturing process in a similar way as for SIR. Also, the increased T_m of DEX leads to the conclusion that the drug exists in amorphous state in accumulated regions in the PLLA matrix. However, via Raman mapping, no DEX enriched areas could be detected. Both, for DEX and SIR, we assume that microcrystals have been formed which are below the resolution limit of the applied Raman mapping technique. As for area scans a 500 µm × 500 µm field with 50 dots per row and column was used, the resolution limit is ≥10 µm^2. As for SIR, SEM indicated the formation of submicron crystals when incorporating DEX in PLLA.

CYCLO resulted in a slight increase in crystallinity of PLLA. The absence of a distinct $T_{m,CYCLO}$ signal in comparison to the drug T_m for SIR or DEX showed complete blending of the drug with the polymer.

Altogether, our results point out complex phase transitioning processes during manufacturing. As a drug-polymer-solvent system is present, interaction of the three components in solution as well as during solvent evaporation and thus shifting of solubilities must been taken into account for manufacturing and application as it may alter crucial parameters such as drug release or mechanical resilience. Still, real time analysis of such processes remains challenging and technically sophisticated. Further research, e.g., by means of X-ray diffraction, may help to understand the drug PLLA interaction in combination with solvent influences.

Mechanical analysis of PLLA films containing PTX gave seemingly contradictory results regarding DSC analysis, especially crystallinity of the PLLA matrix. In this case, a decrease in crystallinity of approx. 13%, from 37.8 ± 1.9% down to 33 ± 7%, was observed which is accompanied by an approximate doubling of the elongation at break, from 9.9 ± 0.7% to 23 ± 16% yet an increase in the elastic modulus of up to 25%, from 2250 ± 40 MPa to 3020 ± 100 MPa was observed. The latter indicates a higher embrittlement. SIR incorporation leads to higher elastic modulus values of about 34%, from 2250 ± 40 MPa to 3420 ± 220 MPa, indicating a hardening effect. However, elastic modulus values decrease as drug content increases and approximate at 20 *w*/*w*% SIR the original PLLA value. DSC data show an increase of crystallinity of PLLA with increasing SIR amount. This, in addition to the formation of SIR crystallites, counteracts the elastic modulus increasing influence of SIR molecules interacting with the polymer chains. Therefore, we assume that SIR shows complex behavior in the polymer crystal lattice. The investigation of such interactions of PTX or SIR with PLLA may be of certain interest for future work in particular by means of crystal structure analysis, as the formation of multiple phases crucially alters properties highly relevant for biomedical applications such as drug release. In addition, such effects are in particular important regarding dilation behavior and drug carrying coating integrity after the exposure of mechanical stress as it appears at stent implantation.

DEX incorporation results in a tendency to lower elongation at break at high drug concentrations. Still, a decrease in elastic modulus of about 10%, from 3000 ± 200 MPa to 2690 ± 110 MPa, is observed. This may be due to the fact that on the one hand the drug interacts with the PLLA polymer chains on a molecular level, thus acting as plasticizer. However, on the other hand, the formation of aforementioned submicron crystals leads to the development of predetermined breaking points, therefore to a decrease in elongation at break of about 31%, from 8.8 ± 2.0% to 6.1 ± 0.9%. CYCLO shows with increasing drug ratio a reduction of elongation at break of ca. 40%, from 11 ± 6% to 6.4 ± 1.7% accompanied by an increase in elastic modulus and tensile strength of ca. 20%.

Regarding the mechanical analysis of PLLA/drug blends, it must be stated that handling of polymer films of a thickness of around 10 µm is challenging, as minimal defects or insufficient mounting in the testing device may drastically alter the results. However, the generation of thicker samples, e.g., by solvent casting process, may also be unsuitable as an increase in sample thickness leads to incomplete removal of residual solvent by evaporation. The remaining solvent may thus act as plasticizers, impairing the results on the drug influence. As for that, the literature and our DSC data for thin films obtained by spray-coating showed complete solvent removal after thermal annealing for which reason we decided to choose this manufacturing method for PLLA/drug films. Still, mechanical properties of such films, notably in the field of DES, are of particular interest. In the literature, some considerations about thermal analysis of drug incorporated polymers such as PLLA can be found. Yet, only limited data for mechanical investigations are available for reference. Consequently, further insight regarding the material properties of drug containing coatings is required.

5. Conclusions

Drug-eluting polymer coatings are an indispensable tool in biomedical device engineering, in particular for so-called combination products. Whereas drug release kinetics are clearly important and have been in the focus of extensive research, understanding the interaction of drugs with the drug-carrying polymer matrix is of great interest, especially in the field of drug-eluting stents.

In this study, PLLA/drug thin films have been investigated regarding the influence of the drug on thermal and mechanical properties of the polymer matrix. SIR, PTX, CYCLO and DEX were blended with HMW PLLA in ratios of 10, 15, and 20 *w*/*w*% with respect to the polymer. Our results showed that the selected drugs lead to an increase in tensile strength of the coating material. Regarding thermal properties, SIR and DEX

showed PLLA/drug phase separation. PTX and DEX incorporation resulted in thermal destabilization of the polymer, which is evident by the formation of exothermic peaks in the DSC thermograms. High amounts of PTX lead to a strong decrease in crystallinity of PLLA. CYCLO showed complete blending with the PLLA matrix and did only little affect the polymer properties.

Our aim was to contribute to the understanding of the complex interaction between PLLA and API. Different drugs possess crucially different chemical properties and ways of interacting when blended with polymers, and thus, the influence on the polymer matrix cannot be easily predicted. Advances in current established DES technology to overcome limitations and side effects, such as the risk of late stent thrombosis, inflammation and in stent-restenosis, demand for novel polymer/drug coatings. The present data underline that this in turn requires target-oriented thermal treatment to ensure shelf life and mechanical resilience.

Supplementary Materials: The following are available online at https://www.mdpi.com/2073-4360/13/2/292/s1, Figure S1: Raman spectra of PLLA and PLLA with incorporated drugs at a ratio of drug/PLLA = 10/90 *w*/*w*%. Figure S2: IR spectra of PLLA and PLLA with incorporated cyclosporine A at a ratio of CYCLO/PLLA = 10/90 *w*/*w*%. Figure S3: Macrophotographical images of polymer film cutouts of PLLA and drug loaded PLLA films. Figure S4: SEM images of pure PLLA film drug and loaded PLLA films obtained via spray-coating. Figure S5: Raman mapping of PLLA with incorporated drugs at given drug/PLLA ratios. Mapping has been performed for the drug signal intensity according to the signal in the related Raman spectra. Figure S6: Representative contact angle images for PLLA reference and SIR/PLLA = 10/90 *w*/*w*%. Given are images of the droplets of deionized water for CA determination and images of MeI_2 droplets for SFE calculation. Figure S7: Stress-strain curves of drug loaded PLLA films obtained via spray-coating.

Author Contributions: Conceptualization: D.A. and S.O.; methodology: D.A.; mechanical testing and DSC analysis: D.A.; SEM imaging: V.S.; Raman spectroscopy and mapping: T.R.; IR spectroscopy: M.T.; polymer film generation: D.B.; writing—original draft preparation: D.A. and S.O.; writing—review and editing: all; project administration: K.-P.S. and N.G.; funding acquisition: K.-P.S. and N.G. All authors have read and agreed to the published version of the manuscript.

Funding: Financial support by the Federal Ministry of Education and Research (BMBF) within RESPONSE "Partnership for Innovation in Implant Technology" and by the European Social Fund (ESF) within the excellence research program of the state Mecklenburg-Vorpommern Card-ii-Omics is gratefully acknowledged.

Institutional Review Board Statement: Not applicable.

Informed Consent Statement: Not applicable.

Data Availability Statement: The data presented in this study are available upon request from the corresponding author.

Acknowledgments: The authors thank Katja Hahn and Caroline Dudda for their expert technical assistance.

Conflicts of Interest: The authors declare no conflict of interest.

References

1. Seidlitz, A. Drug-Eluting Stents. In *In vitro Drug Release Testing of Special Dosage Forms*, 1st ed.; Fotaki, N., Klein, S., Eds.; Wiley: Hoboken, NJ, USA, 2020; pp. 87–117. ISBN 9781118341476.
2. Torii, S.; Jinnouchi, H.; Sakamoto, A.; Kutyna, M.; Cornelissen, A.; Kuntz, S.; Guo, L.; Mori, H.; Harari, E.; Paek, K.H.; et al. Drug-eluting coronary stents: Insights from preclinical and pathology studies. *Nat. Rev. Cardiol.* **2020**, *17*, 37–51. [CrossRef] [PubMed]
3. Ali, R.M.; Abdul Kader, M.; Wan Ahmad, W.A.; Ong, T.K.; Liew, H.B.; Omar, A.-F.; Mahmood Zuhdi, A.S.; Nuruddin, A.A.; Schnorr, B.; Scheller, B. Treatment of Coronary Drug-Eluting Stent Restenosis by a Sirolimus- or Paclitaxel-Coated Balloon. *JACC Cardiovasc. Interv.* **2019**, *12*, 558–566. [CrossRef] [PubMed]
4. Schmidt, W.; Lanzer, P.; Behrens, P.; Brandt-Wunderlich, C.; Öner, A.; Ince, H.; Schmitz, K.-P.; Grabow, N. Direct comparison of coronary bare metal vs. drug-eluting stents: Same platform, different mechanics? *Eur. J. Med. Res.* **2018**, *23*, 2. [CrossRef] [PubMed]

5. Wu, J.J.; Way, J.A.H.; Kritharides, L.; Brieger, D. Polymer-free versus durable polymer drug-eluting stents in patients with coronary artery disease: A meta-analysis. *Ann. Med. Surg. (Lond.)* **2019**, *38*, 13–21. [CrossRef] [PubMed]
6. Von Birgelen, C.; Buiten, R.A. Superiority of biodegradable polymer sirolimus-eluting stents in STEMI. *Lancet* **2019**, *394*, 1208–1210. [CrossRef]
7. Grubman, D.; Saito, Y.; Lansky, A. The Firehawk stent: A review of a novel abluminal groove-filled biodegradable polymer sirolimus-eluting stent. *Argentina de Cardioangiología Intervencionista* **2019**, *10*, 73–77. [CrossRef]
8. Yoshioka, G.; Nishihira, K.; Asada, Y.; Node, K. In-stent restenosis following third-generation sirolimus-eluting stent implantation: First report analysed from imaging modalities and histopathological findings. *Eur. Heart J.* **2020**, *17*, 1707. [CrossRef]
9. Bünger, C.M.; Grabow, N.; Sternberg, K.; Kröger, C.; Ketner, L.; Schmitz, K.-P.; Kreutzer, H.J.; Ince, H.; Nienaber, C.A.; Klar, E.; et al. Sirolimus-eluting biodegradable poly-L-lactide stent for peripheral vascular application: A preliminary study in porcine carotid arteries. *J. Surg. Res.* **2007**, *139*, 77–82. [CrossRef]
10. Stone, G.W.; Ellis, S.G.; Cox, D.A.; Hermiller, J.; O'Shaughnessy, C.; Mann, J.T.; Turco, M.; Caputo, R.; Bergin, P.; Greenberg, J.; et al. A polymer-based, paclitaxel-eluting stent in patients with coronary artery disease. *N. Engl. J. Med.* **2004**, *350*, 221–231. [CrossRef]
11. Razavi, M.K.; Donohoe, D.; D'Agostino, R.B.; Jaff, M.R.; Adams, G. Adventitial Drug Delivery of Dexamethasone to Improve Primary Patency in the Treatment of Superficial Femoral and Popliteal Artery Disease: 12-Month Results from the DANCE Clinical Trial. *JACC Cardiovasc. Interv.* **2018**, *11*, 921–931. [CrossRef]
12. König, A.; Leibig, M.; Rieber, J.; Schiele, T.M.; Theisen, K.; Siebert, U.; Gothe, R.M.; Klauss, V. Randomized comparison of dexamethasone-eluting stents with bare metal stent implantation in patients with acute coronary syndrome: Serial angiographic and sonographic analysis. *Am. Heart J.* **2007**, *153*, 979.e1–979.e8. [CrossRef] [PubMed]
13. Sternberg, K.; Kramer, S.; Nischan, C.; Grabow, N.; Langer, T.; Hennighausen, G.; Schmitz, K.-P. In vitro study of drug-eluting stent coatings based on poly(L-lactide) incorporating cyclosporine A—drug release, polymer degradation and mechanical integrity. *J. Mater. Sci. Mater. Med.* **2007**, *18*, 1423–1432. [CrossRef] [PubMed]
14. Majewska, P.; Oledzka, E.; Sobczak, M. Overview of the latest developments in the field of drug-eluting stent technology. *Biomater. Sci.* **2020**, *8*, 544–551. [CrossRef]
15. Wessely, R. New drug-eluting stent concepts. *Nat. Rev. Cardiol.* **2010**, *7*, 194–203. [CrossRef] [PubMed]
16. Wessely, R.; Schömig, A.; Kastrati, A. Sirolimus and Paclitaxel on polymer-based drug-eluting stents: Similar but different. *J. Am. Coll. Cardiol.* **2006**, *47*, 708–714. [CrossRef]
17. Vos, N.S.; Fagel, N.D.; Amoroso, G.; Herrman, J.-P.R.; Patterson, M.S.; Piers, L.H.; van der Schaaf, R.J.; Slagboom, T.; Vink, M.A. Paclitaxel-Coated Balloon Angioplasty versus Drug-Eluting Stent in Acute Myocardial Infarction: The Revelation Randomized Trial. *JACC Cardiovasc. Interv.* **2019**, *12*, 1691–1699. [CrossRef]
18. Dash, A.K. The dark side of paclitaxel. *Oncol. Rev.* **2010**, *4*, 71–72. [CrossRef]
19. Strohbach, A.; Busch, R. Polymers for Cardiovascular Stent Coatings. *Int. J. Polym. Sci.* **2015**, *2015*, 1–11. [CrossRef]
20. Liu, X.; de Scheerder, I.; Desmet, W. Dexamethasone-eluting stent: An anti-inflammatory approach to inhibit coronary restenosis. *Expert Rev. Cardiovasc. Ther.* **2004**, *2*, 653–660. [CrossRef]
21. Prunotto, M.; Bacchetta, M.; Jayaraman, S.; Galloni, M.; van Eys, G.; Gabbiani, G.; Bochaton-Piallat, M.-L. Cytostatic drugs differentially affect phenotypic features of porcine coronary artery smooth muscle cell populations. *FEBS Lett.* **2007**, *581*, 5847–5851. [CrossRef]
22. Jonasson, L.; Holm, J.; Hansson, G.K. Cyclosporin A inhibits smooth muscle proliferation in the vascular response to injury. *Proc. Natl. Acad. Sci. USA* **1988**, *85*, 2303–2306. [CrossRef] [PubMed]
23. Verdoia, M.; Kedhi, E.; Suryapranata, H.; Galasso, G.; Dudek, D.; de Luca, G. Polymer-Free vs. Polymer-Coated Drug-Eluting Stents for the Treatment of Coronary Artery Disease: A Meta-Analysis of 16 Randomized Trials. *Cardiovasc. Revasc. Med.* **2020**, *21*, 745–753. [CrossRef] [PubMed]
24. Parker, T.; Davé, V.; Falotico, R. Polymers for drug eluting stents. *Curr. Pharm. Des.* **2010**, *16*, 3978–3988. [CrossRef] [PubMed]
25. Lee, D.-H.; La Torre Hernandez, J.M.D. The newest generation of drug-eluting stents and beyond. *Eur. Cardiol. Rev.* **2018**, *13*, 54. [CrossRef]
26. Mokhena, T.C.; Mochane, M.J.; Sadiku, E.R.; Agboola, O.; John, M.J. Opportunities for PLA and Its Blends in Various Applications. In *Green Biopolymers and Their Nanocomposites*, 1st ed.; Gnanasekaran, D., Ed.; Springer: Singapore, 2019; pp. 55–81. ISBN 978-981-13-8063-1.
27. Hu, T.; Yang, J.; Cui, K.; Rao, Q.; Yin, T.; Tan, L.; Zhang, Y.; Li, Z.; Wang, G. Controlled Slow-Release Drug-Eluting Stents for the Prevention of Coronary Restenosis: Recent Progress and Future Prospects. *ACS Appl. Mater. Interfaces* **2015**, 11695–11712. [CrossRef]
28. Nguyen, K.T.; Shaikh, N.; Wawro, D.; Zhang, S.; Schwade, N.D.; Eberhart, R.C.; Tang, L. Molecular responses of vascular smooth muscle cells to paclitaxel-eluting bioresorbable stent materials. *J. Biomed. Mater. Res. A* **2004**, *69*, 513–524. [CrossRef]
29. Can, E.; Udenir, G.; Kanneci, A.I.; Kose, G.; Bucak, S. Investigation of PLLA/PCL blends and paclitaxel release profiles. *AAPS PharmSciTech* **2011**, *12*, 1442–1453. [CrossRef]
30. Steele, T.W.J.; Huang, C.L.; Widjaja, E.; Boey, F.Y.C.; Loo, J.S.C.; Venkatraman, S.S. The effect of polyethylene glycol structure on paclitaxel drug release and mechanical properties of PLGA thin films. *Acta Biomater.* **2011**, *7*, 1973–1983. [CrossRef]

31. Hobzova, R.; Hampejsova, Z.; Cerna, T.; Hrabeta, J.; Venclikova, K.; Jedelska, J.; Bakowsky, U.; Bosakova, Z.; Lhotka, M.; Vaculin, S.; et al. Poly(d,l-lactide)/polyethylene glycol micro/nanofiber mats as paclitaxel-eluting carriers: Preparation and characterization of fibers, in vitro drug release, antiangiogenic activity and tumor recurrence prevention. *Mater. Sci. Eng. C Mater. Biol. Appl.* **2019**, *98*, 982–993. [CrossRef]
32. Wulf, K.; Teske, M.; Matschegewski, C.; Arbeiter, D.; Bajer, D.; Eickner, T.; Schmitz, K.-P.; Grabow, N. Novel approach for a PTX/VEGF dual drug delivery system in cardiovascular applications-an innovative bulk and surface drug immobilization. *Drug Deliv. Transl. Res.* **2018**, *8*, 719–728. [CrossRef]
33. Seidlitz, A.; Schick, W.; Reske, T.; Senz, V.; Grabow, N.; Petersen, S.; Nagel, S.; Weitschies, W. In vitro study of sirolimus release from a drug-eluting stent: Comparison of the release profiles obtained using different test setups. *Eur. J. Pharm. Biopharm.* **2015**, *93*, 328–338. [CrossRef] [PubMed]
34. Venkatraman, S.; Boey, F. Release profiles in drug-eluting stents: Issues and uncertainties. *J. Control Release* **2007**, *120*, 149–160. [CrossRef] [PubMed]
35. Petersen, S.; Hussner, J.; Reske, T.; Grabow, N.; Senz, V.; Begunk, R.; Arbeiter, D.; Kroemer, H.K.; Schmitz, K.-P.; Meyer zu Schwabedissen, H.E.; et al. In vitro study of dual drug-eluting stents with locally focused sirolimus and atorvastatin release. *J. Mater. Sci. Mater. Med.* **2013**, *24*, 2589–2600. [CrossRef] [PubMed]
36. Grabow, N.; Bünger, C.M.; Kischkel, S.; Timmermann, J.H.; Reske, T.; Martin, D.P.; Williams, S.F.; Schareck, W.; Sternberg, K.; Schmitz, K.-P. Development of a sirolimus-eluting poly (L-lactide)/poly(4-hydroxybutyrate) absorbable stent for peripheral vascular intervention. *Biomed. Tech. (Berl.)* **2013**, *58*, 429–437. [CrossRef] [PubMed]
37. Lincoff, A.M.; Furst, J.G.; Ellis, S.G.; Tuch, R.J.; Topol, E.J. Sustained Local Delivery of Dexamethasone by a Novel Intravascular Eluting Stent to Prevent Restenosis in the Porcine Coronary Injury Model. *J. Am. Coll. Cardiol.* **1997**, *29*, 808–816. [CrossRef]
38. Wissgott, C.; Schmidt, W.; Brandt, C.; Behrens, P.; Andresen, R. Preliminary Clinical Results and Mechanical Behavior of a New Double-Layer Carotid Stent. *J. Endovasc. Ther.* **2015**, *22*, 634–639. [CrossRef]
39. *Cardiovascular Implants—Endovascular Devices. Part 2—Vascular Stents*; DIN EN ISO 25539-2:2019-07; Beuth Verlag GmbH: Berlin, Germany, 2019.
40. Wu, D.; Zhang, Y.; Yuan, L.; Zhang, M.; Zhou, W. Viscoelastic interfacial properties of compatibilized poly(ε-caprolactone)/polylactide blend. *J. Polym. Sci. B Polym. Phys.* **2010**, *48*, 756–765. [CrossRef]
41. Hilianen-Vainio, M.; Varpomaa, P. Modification of poly(L-lactides) by blending: Mechanical and hydrolytic behavior. *Macromol. Chem. Phys.* **1995**, *197*, 1503–1523. [CrossRef]
42. López-Rodríguez, N.; López-Arraiza, A.; Meaurio, E.; Sarasua, J.R. Crystallization, morphology, and mechanical behavior of polylactide/poly(ε-caprolactone) blends. *Polym. Eng. Sci.* **2006**, *46*, 1299–1308. [CrossRef]
43. Arbeiter, D.; Eickner, T.; Oschatz, S.; Reske, T.; Specht, O.; Teske, M.; Senz, V.; Schmitz, K.-P.; Grabow, N. Physico chemical and phase separation characterization of high molecular PLLA blended with low molecular PCL obtained from solvent cast processes. *Mater. Res. Express* **2020**, *7*, 95302. [CrossRef]
44. Darie-Niţă, R.N.; Vasile, C.; Irimia, A.; Lipşa, R.; Râpă, M. Evaluation of some eco-friendly plasticizers for PLA films processing. *J. Appl. Polym. Sci.* **2016**, *133*. [CrossRef]
45. Farah, S.; Anderson, D.G.; Langer, R. Physical and mechanical properties of PLA, and their functions in widespread applications—A comprehensive review. *Adv. Drug Deliv. Rev.* **2016**, *107*, 367–392. [CrossRef] [PubMed]
46. Jacobsen, S.; Fritz, H.G. Plasticizing polylactide?the effect of different plasticizers on the mechanical properties. *Polym. Eng. Sci.* **1999**, *39*, 1303–1310. [CrossRef]
47. Baiardo, M.; Frisoni, G.; Scandola, M.; Rimelen, M.; Lips, D.; Ruffieux, K.; Wintermantel, E. Thermal and mechanical properties of plasticized poly(L-lactic acid). *J. Appl. Polym. Sci.* **2003**, *90*, 1731–1738. [CrossRef]
48. Ozkoc, G.; Kemaloglu, S. Morphology, biodegradability, mechanical, and thermal properties of nanocomposite films based on PLA and plasticized PLA. *J. Appl. Polym. Sci.* **2009**, *114*, 2481–2487. [CrossRef]
49. Ljungberg, N.; Wesslén, B. The effects of plasticizers on the dynamic mechanical and thermal properties of poly(lactic acid). *J. Appl. Polym. Sci.* **2002**, *86*, 1227–1234. [CrossRef]
50. Siepmann, F.; Le Brun, V.; Siepmann, J. Drugs acting as plasticizers in polymeric systems: A quantitative treatment. *J. Control Release* **2006**, *115*, 298–306. [CrossRef] [PubMed]
51. Nguyen, D.D.; Luo, L.-J.; Lai, J.-Y. Effects of shell thickness of hollow poly(lactic acid) nanoparticles on sustained drug delivery for pharmacological treatment of glaucoma. *Acta Biomater.* **2020**, 302–315. [CrossRef]
52. Lee, C.-H.; Li, Y.-J.; Huang, C.-C.; Lai, J.-Y. Poly(ε-caprolactone) nanocapsule carriers with sustained drug release: Single dose for long-term glaucoma treatment. *Nanoscale* **2017**, *9*, 11754–11764. [CrossRef]
53. Wulf, K.; Arbeiter, D.; Matschegewski, C.; Teske, M.; Huling, J.; Schmitz, K.-P.; Grabow, N.; Kohse, S. Smart releasing electrospun nanofibers—Poly-L-lactide fibers as dual drug delivery system for biomedical application. *Biomed. Mater.* **2020**. [CrossRef]
54. Kunze, C.; Freier, T.; Kramer, S.; Schmitz, K.-P. Anti-inflammatory prodrugs as plasticizers for biodegradable implant materials based on poly(3-hydroxybutyrate). *J. Mater. Sci. Mater. Med.* **2002**, *13*, 1051–1055. [CrossRef] [PubMed]
55. Savla, R.; Browne, J.; Plassat, V.; Wasan, K.M.; Wasan, E.K. Review and analysis of FDA approved drugs using lipid-based formulations. *Drug Dev. Ind. Pharm.* **2017**, *43*, 1743–1758. [CrossRef] [PubMed]
56. Hansch, C.; Leo, A.; Hoekman, D. Exploring QSAR: Hydrophobic, Electronic, and Steric Constants. *J. Med. Chem.* **1996**, *39*, 1189–1190. [CrossRef]

57. Lallemand, F.; Schmitt, M.; Bourges, J.-L.; Gurny, R.; Benita, S.; Garrigue, J.-S. Cyclosporine A delivery to the eye: A comprehensive review of academic and industrial efforts. *Eur. J. Pharm. Biopharm.* **2017**, *117*, 14–28. [CrossRef] [PubMed]
58. Ihlenfeldt, W.D.; Takahashi, Y.; Abe, H.; Sasaki, S. Computation and management of chemical properties in CACTVS: An extensible networked approach toward modularity and compatibility. *J. Chem. Inf. Model.* **1994**, *34*, 109–116. [CrossRef]
59. Tarini, M.; Cignoni, P.; Montani, C. Ambient occlusion and edge cueing to enhance real time molecular visualization. *IEEE Trans. Vis. Comput. Graph.* **2006**, *12*, 1237–1244. [CrossRef]
60. Finkelstein, A.; McClean, D.; Kar, S.; Takizawa, K.; Varghese, K.; Baek, N.; Park, K.; Fishbein, M.C.; Makkar, R.; Litvack, F.; et al. Local drug delivery via a coronary stent with programmable release pharmacokinetics. *Circulation* **2003**, *107*, 777–784. [CrossRef]
61. Mochizuki, A.; Niikawa, T.; Omura, I.; Yamashita, S. Controlled release of argatroban from PLA film—Effect of hydroxylesters as additives on enhancement of drug release. *J. Appl. Polym. Sci.* **2008**, *108*, 3353–3360. [CrossRef]
62. Shi, W.; Gu, C.; Jiang, H.; Zhang, M.; Lang, M. Effects of amphiphilic chitosan-g-poly(ε-caprolactone) polymer additives on paclitaxel release from drug eluting implants. *Mater. Sci. Eng. C Mater. Biol. Appl.* **2014**, *45*, 502–509. [CrossRef]
63. Kim, S.M.; Park, S.-B.; Bedair, T.M.; Kim, M.-H.; Park, B.J.; Joung, Y.K.; Han, D.K. The effect of solvents and hydrophilic additive on stable coating and controllable sirolimus release system for drug-eluting stent. *Mater. Sci. Eng. C Mater. Biol. Appl.* **2017**, *78*, 39–46. [CrossRef]
64. Livingston, M.; Tan, A. Coating Techniques and Release Kinetics of Drug-Eluting Stents. *J. Med. Devices* **2019**, *10*. [CrossRef] [PubMed]
65. Fischer, E.W.; Sterzel, H.J.; Wegner, G. Investigation of the structure of solution grown crystals of lactide copolymers by means of chemical reactions. *Kolloid-Z. Z. Polym.* **1973**, *251*, 980–990. [CrossRef]
66. International Standard Organisation. *Plastics-Determination of Tensile Properties*; International Standard Organisation: Geneva, Switzerland, 2012.
67. Migliaresi, C.; de Lollis, A.; Fambri, L.; Cohn, D. The effect of thermal history on the crystallinity of different molecular weight PLLA biodegradable polymers. *Clin. Mater.* **1991**, *8*, 111–118. [CrossRef]
68. Freier, T.; Kunze, C.; Schmitz, K.-P. Solvent removal from solution-cast films of biodegradable polymers. *J. Mate. Sci. Lett.* **2001**, *20*, 1929–1931. [CrossRef]
69. Liggins, R.T.; Burt, H.M. Paclitaxel loaded poly(L-lactic acid) (PLLA) microspheres. II. The effect of processing parameters on microsphere morphology and drug release kinetics. *Int. J. Pharm.* **2004**, *281*, 103–106. [CrossRef] [PubMed]
70. Mandelkern, L. The crystallization kinetics of polymer-diluent mixtures: The temperature coefficient of the process. *Polymer* **1964**, *5*, 637–648. [CrossRef]
71. Liggins, R.T.; Burt, H.M. Paclitaxel-loaded poly(L-lactic acid) microspheres 3: Blending low and high molecular weight polymers to control morphology and drug release. *Int. J. Pharm.* **2004**, *282*, 61–71. [CrossRef]
72. Nukala, R.K.; Boyapally, H.; Slipper, I.J.; Mendham, A.P.; Douroumis, D. The application of electrostatic dry powder deposition technology to coat drug-eluting stents. *Pharm. Res.* **2010**, *27*, 72–81. [CrossRef]
73. Martins, A.; Duarte, A.R.C.; Faria, S.; Marques, A.P.; Reis, R.L.; Neves, N.M. Osteogenic induction of hBMSCs by electrospun scaffolds with dexamethasone release functionality. *Biomaterials* **2010**, *31*, 5875–5885. [CrossRef]

Biomaterials Science

ROYAL SOCIETY OF CHEMISTRY

PAPER

View Article Online
View Journal | View Issue

Check for updates

Cite this: *Biomater. Sci.*, 2023, **11**, 5240

Fetuin A functionalisation of biodegradable PLLA-*co*-PEG nonwovens towards enhanced biomineralisation and osteoblastic growth behaviour

Stefan Oschatz, *[a] Michael Teske, [a] Ulrike Burmeister,[b] Sabine Illner,[a] Volkmar Senz, [a] Hermann Lang,[b] Niels Grabow [a,c] and Jana Markhoff [a]

Therapy for large-scale bone defects remains a major challenge in regenerative medicine. In this context, biodegradable electrospun nonwovens are a promising material to be applied as a temporary implantable scaffold as their fibre diameters are in the micro- and nanometre range and possess a high surface-to-volume ratio paired with high porosity. In this work, *in vitro* assessment of biodegradable PLLA-*co*-PEG nonwovens with fetuin A covalently anchored to the surface has been performed in terms of biomineralisation and the influence on MG-63 osteoblast cell metabolic activity, biosynthesis of type I collagen propeptide and inflammatory potential. Our finding was that covalent fetuin A funtionalisation of the nonwoven material leads to a distinct increase in calcium affinity, thus enhancing biomineralisation while maintaining the distinct fibre morphology of the nonwoven. The cell seeding experiments showed that the fetuin A functionalised and subsequently *in vitro* biomineralised PLLA-*co*-PEG nonwovens did not show negative effects on MG-63 growth. Fetuin A funtionalisation and enhanced biomineralisation supported cell attachment, leading to improved cell morphology, spreading and infiltration into the material. Furthermore, no signs of increase in the inflammatory potential of the material have been detected by flow cytometry experiments. Overall, this study provides a contribution towards the development of artificial scaffolds for guided bone regeneration with the potential to enhance osteoinduction and osteogenesis.

Received 27th January 2023,
Accepted 26th May 2023

DOI: 10.1039/d3bm00141e

rsc.li/biomaterials-science

Published on 01 June 2023. Downloaded by University of Rostock on 6/5/2025 1:43:42 PM.

Introduction

Hard matrix defects represent a serious therapeutic issue, particularly in regenerative dentistry. There is the risk that the connective tissue and gingival epithelium will grow into and fill the bone defect, inhibiting autologous bone regeneration due to the increased proliferation rate compared to bone tissue.[1] This necessitates the use of a barrier layer to prevent infiltration of the gingival epithelium, but to support the formation of a bone cell matrix. Autogenous implants are naturally the material of choice for guided bone regeneration, but their availability is limited and harvesting is often associated with harvesting morbidities. Fully or partially synthetic materials are an attractive option, but are often insufficient in terms of osteoconduction, osteoinduction or osteoneogenesis.[2]

In this context, biomineralisation plays a fundamental role in intrinsic osteoinduction and osteogenesis. Formation of a biological apatite layer ensures binding of osteogenetic proteins such as collagen and also that hydroxyapatite (HA) surfaces cause upregulation of osteospecific genes in mesenchymal stem cells.[3] HA, although widely used, is difficult to handle due to its brittleness and fragility, in particular regarding patient-specific requirements. Thus, composite materials, *e.g.* the combination of biodegradable polymers with HA, are of great interest in bone regeneration research.[4,5] Regarding the osteogenic and osteoinductive potential of HA, Bohner *et al.* found that the equilibria between the release and consumption of Ca^{2+} and PO_4^{3-} ions by apatite formation and dissolution, in particular local Ca^{2+} and/or PO_4^{3-} ion concentration reduction, showed to be the promoter of intrinsic osteoinduction.[6] They concluded that a material is osteoinductive if, among other factors, Ca^{2+} and PO_4^{3-} ion contents are depleted in the surrounding blood supply. Accordingly, a material seeded with initiators for enhanced biomineralisation using Ca^{2+} and PO_4^{3-} ions from the surrounding media appears to be a very promising approach.

[a]*Institute for Biomedical Engineering, Rostock University Medical Center, Rostock, Germany. E-mail: stefan.oschatz@uni-rostock.de*
[b]*Department of Operative Dentistry and Periodontology, Rostock University Medical Center, Rostock, Germany*
[c]*Department Life, Light & Matter (LLM), University of Rostock, Rostock, Germany*

This journal is © The Royal Society of Chemistry 2023

Published on 01 June 2023. Downloaded by University of Rostock on 6/5/2025 1:43:42 PM.

As bone tissue is based on hierarchically organised fibrous structures, biomimetic nanofibre biomaterials are investigated for application in guided bone tissue regeneration.[7] In this context, nonwovens exhibit unique properties, as for instance an exceptionally high surface-to-volume ratio and a porous fibre interstice, mimicking biological extracellular matrix architecture.[8] The porous morphology supports cell infiltration and promotes new bone formation. The structural properties of the nonwovens allow for facile implantation and versatile application, as these materials are highly flexible and can easily adapt to the shape of complex hard tissue defects.[9]

A common approach is the use of electrospun poly(L-lactide) (PLLA) hybrid membranes loaded with hydroxyapatite (HA) microparticles as crystallisation nuclei to actively support bone regeneration.[10,11] However, the stability and homogeneity of the HA suspension before and during the manufacturing process are essential. In particular, phase separation of PLLA dissolved in $CHCl_3$ and HA particles in aqueous suspension is problematic and requires the addition of a surfactant.[12] Nevertheless, incorporation of HA into the PLLA-nonwovens leads to an increased growth of osteoblasts *in vitro*. Moreover, PLLA, albeit frequently used, may be disadvantageous for certain applications due to the rather long degradation time of 2–3 years.[13] PLLA-*co*-PEG copolymers, however, combine the mechanical properties of PLLA with a shorter degradation time due to the poly(ethylene glycol) (PEG) blocks, which, thanks to the capability to hydrate the PEG-backbone, enable transport of degraded chain fragments by the medium.[14] Furthermore, the degradation time can be adjusted, depending on the PEG content.[15]

In this work, biodegradable nonwovens were fabricated from commercially available PLLA-*co*-PEG triblock copolymers, which were subsequently functionalised with fetuin A, a vertebrate plasma protein, which exhibits a distinct calcium affinity.[16] In contrast to the established method of incorporating HA crystallisation nuclei into nonwoven membranes, the functionalization with fetuin A allows the material to absorb Ca^{2+} ions from the surrounding body fluids, which in turn initiate crystallisation, enabling the formation of a biogeneous CaP layer. Our aim was to investigate to what extent the superficially immobilised fetuin A influences the CaP binding capacity of the nonwovens and to evaluate the material regarding *in vitro* MG-63 osteoblast cell growth behaviour. The presented material combines the highly beneficial morphological properties of a nonwoven material with the enhanced capability of forming a biological apatite layer using surrounding physiological media within the implantation area. Compared to the use of HA-seeded materials, our approach shows promising *in vitro* results towards biomimetic guided bone regeneration.

Methods

If not stated otherwise, all chemicals were of technical grade and used as received without further treatment.

Nonwoven fabrication

Electrospinning was performed on a Contipro 4SPIN C4S LAB2 (Contipro, Dolní Dobrouč, Czech Republic). The used setup had an emitter-collector distance of 20 cm, 28 kV high voltage and a feed rate of 45 μL min^{-1} using a 6-fold multi jet feeder. Poly(L-lactide-*co*-PEG) triblock copolymer (Resomer LPt 46, Evonik, Essen, Germany) was dissolved in $CHCl_3$/TFE in a 1 : 4 ratio prior to spinning, giving 7.5 wt% polymer solution. The obtained nonwovens were annealed for 24 h at 80 °C under reduced pressure to remove the residual solvent. Nonwoven mats obtained by this process were of an overall thickness of 250 μm ± 13 μm as determined using a Mitutoyo 543-394B dial indicator (Mitutoyo Corporation, Kawasaki, Japan).

Mechanical testing

Uniaxial tensile testing was performed using a ZwickiLine ZN 2.5 testing machine (Zwick, Ulm, Germany). The tests were performed with a 10 N load cell, a preload of 0.005 N, and a crosshead speed of v = 25 mm min^{-1} with n = 5, as this crosshead speed was reported to be optimal for tensile testing of nonwoven specimens.[17] Tensile force was measured as a function of elongation. Young's modulus (E) was determined in the linear elastic region *via* linear regression. From the collected data, the elongation at break (ε_B) and ultimate tensile strength (σ_m) were extracted.

Water contact angle measurements

Water contact angle measurements were performed using a DSA25E drop shape analyser (Krüss GmbH, Hamburg, Germany) operating on Krüss Advance software (V.1.13) equipped with a pressure dosing unit under ambient conditions with a drop volume of 1.74 ± 0.077 μL and equilibration time of 1 s using deionized water as the test liquid. Contact angles have been determined by the sessile drop technique with n = 8 and were calculated by averaging the values for both sides of the drops.

Fetuin A functionalisation

Fetuin A was covalently linked to the surface of the fibres using common EDC/NHS coupling.[18] First, the nonwoven material underwent oxygen plasma treatment for the generation of superficially carboxyl groups under 0.3 mbar O_2 atmosphere for 30 s using a 60 W radio frequency plasma generator (Diener electronic GmbH & Co. KG, Ebhausen, Germany). then, human recombinant fetuin A (Sigma Aldrich, Darmstadt, Germany) was covalently linked to the nonwoven material using EDC/NHS as the crosslinker system. The oxygen-plasma activated nonwoven specimens (∅ = 6 mm) were incubated in 150 mM/100 mM EDC/NHS solution in 2-(*N*-morpholino)-ethanesulfonic acid buffer (MES, 50 mM, pH 5.0) for 1 h at room temperature and subsequently rinsed once with PBS and finally twice with deionised water (DW). Specimens were subsequently placed in 250 μL of 0.1 μg mL^{-1} fetuin A solution in PBS (0.08 M, pH = 7.6) for 1 h. Afterwards, specimens were placed in 2 mL of TRIS buffer at RT for 5 min.

Published on 01 June 2023. Downloaded by University of Rostock on 6/5/2025 1:43:42 PM.

In a final step, specimens were rinsed three times with washing buffer (1 PBS: 9 DW + 0.05% TWEEN 20) and DW and stored wet in a refrigerator until use in accelerated *in vitro* mineralisation and cell culture experiments. The maximum storage was for 1 week.

Quantification of fetuin A binding

Residual fetuin A in the supernatant after nonwoven functionalisation was quantified using a fetuin A sandwich ELISA kit (antibodies-online GmbH, Aachen, Germany) according to the manufacturer's instructions. Absorbance was determined at 450 nm using a Fluostar optima plate reader (BMG LABTECH, Ortenberg, Germany) and tetramethylbenzidine as the substrate and horseradish peroxidase labelled detection antibodies. Therefore, supernatants of PBS solutions from eight different fetuin A immobilisations were collected and pooled into 2 different samples that were quantified undiluted in duplicate. Calibration was performed using both fetuin A used for immobilisation and the kit's internal standard as reference.

In vitro mineralisation

Accelerated *in vitro* mineralisation was performed following the protocol as previously reported.[19] In summary, a metastable mineralisation medium consisting of $CaCl_2$ and K_2HPO_4 in HEPES buffer at pH = 7.6 with an ion product of 9 mM^2 and a Ca/P ratio of 1.64 was used. Nonwoven specimens have been treated with the mineralisation medium at pH = 7.4 and 22 °C under shaking conditions for 3 days and were superficially rinsed with deionised water before further use for cell culture experiments. For quantitative Ca^{2+}-analysis, calcium phosphate precipitates on samples (∅ = 6 mm) were hydrolysed by the addition of 1 mL of 0.1 M HCl and shaking for 30 min (n = 6). 15 μL of the resulting solution was added to 1 mL of 0.2 mM Arsenazo III-solution buffered with 75 mM imidazole, vortexed and the Ca^{2+}-concentration was determined *via* UV/Vis spectroscopy using a BioMate 3S UV-Visible spectrometer (Thermo Scientific, Waltham, MA, USA) at 650 nm.

SEM imaging and EDX

SEM imaging was performed using a SEM QUANTA FEG 250 (FEI Company, Germany) operating in high vacuum and 10 kV, equipped with an Everhart–Thornley secondary electron detector (ETD). The samples were fixed onto aluminium carriers using pyrolytic graphite planchets and Au sputter coated. The images were taken at magnifications ×250, ×500 and ×1000. Energy-dispersive X-ray spectroscopic analysis (EDX) was performed using an EDAX microanalysis system. Fibre analysis was performed according to the literature.[20,21]

Cell biological testing

Cell cultivation was carried out in an incubator Memmert ICO240med (Memmert GmbH, Schwabach, Germany) under simulated *in vivo* conditions at 5% CO_2, 21% O_2, and 37 °C. Tissue culture polystyrene (TCPS) served as a common surface for growth control and is named as negative control (NC) throughout this article. A positive control group (PC) was treated with a cytotoxic concentration of 10^{-4} M disulfiram/tetraethylthiuram disulfide (TETD). For the *in vitro* tests, the commercially available human bone cell line MG-63 was used (ATCC® CRL1427™, LGC Standards GmbH, Wesel, Germany).

MG-63 is an established cell line and was isolated from osteosarcoma in a 14-year old Caucasian male patient. MG-63 cells were cultured in modified Eagle's medium (MEM) (with 2 mM L-glutamine and 1.5 g L^{-1} $NaHCO_3$) with 10% fetal calf serum (FCS) and 1% penicillin/streptomycin (all: PAN Biotech GmbH, Aidenbach, Germany). Cells were harvested from the culture flask using trypsin. The test samples (∅ 6 mm) were weighed down using PTFE rings and directly seeded with MG-63 cells at a density of 10 000 cells per 96 well (~29 500 cells per cm^2) in 200 μL of culture medium in six parallel wells for every material configuration, respectively. Three independent experiments were conducted. Cultivation was carried out over 48 h without any medium changes.

The metabolic activity of cells was determined *via* CellQuanti-Blue assay (BioAssay Systems, Biotrend Chemicals GmbH, Cologne, Germany) after 48 h (six wells per test in duplicates, n = 3). The non-fluorescent resazurin is transformed into high-fluorescent resorufin by cellular reductases from metabolically active cells. The fluorescence, which is directly proportional to the metabolic cell activity, was measured at an emission wavelength of 590 nm with an excitation wavelength of 544 nm using a microplate reader (FLUOstar OPTIMA, BMG Labtech, Offenburg, Germany). Values were normalized to PLLA-*co*-PEG nonwoven reference set as 100%.

Cell morphology was analysed by fluorescence staining of cells using phalloidin (AlexaFluor™ 488 phalloidin) for actin filaments as well as DAPI (NucBlue™ Fixed Cell ReadyProbes™) for cell nuclei (both: Invitrogen/Thermo Fisher, Dreieich, Germany), respectively. Therefore, cells were fixed by formalin, washed with PBS and afterwards stained using one drop of staining solution per ml of PBS, respectively and 100 μL per well. Incubation was carried out for 30 min in the dark at room temperature. For imaging at 5× magnification, the Olympus BX53M microscope (Olympus, Hamburg, Germany) was used.

Cell fixation for scanning electron microscopy was carried out using 2.5% glutaraldehyde (Merck, Darmstadt, Germany), with subsequent dehydration by an ethanol exchange series, and dried at room temperature.

Type I collagen propeptide quantification

ELISA was used to verify protein synthesis in the culture supernatants after 48 h of cultivation. Supernatants of six wells were pooled per configuration in an experiment. Supernatants of three independent tests were measured in duplicate. For quantitative measurement of C-terminal propeptide in type I collagen (Metra C1CP EIA Kit, Quidel, Buende, Germany), controls and diluted samples were placed in 96-well plates coated with mouse anti-CICP monoclonal antibodies and incubated for 2 h at room temperature (RT). After washing steps to remove unbound antigens, rabbit polyclonal anti-CICP antibodies were added followed by incubation for 50 min at RT.

 This journal is © The Royal Society of Chemistry 2023

Published on 01 June 2023. Downloaded by University of Rostock on 6/5/2025 1:43:42 PM.

Additional lyophilised IgG goat antibodies against rabbit in conjugate with alkaline phosphatase was used and incubation was done at RT for further 50 min. Then, substrate solution (35 min, RT, in the dark) and stop solution were added before absorbance measurement at 405 nm with a plate reader. A 4-parameter calibration curve fitting equation was used to verify the protein content based on the standard curve. The C-terminal pro-peptide of pro-collagen was considered to correlate with collagen expression. Data were set in relation to the metabolic cell viability.

Flow cytometry

Potential synthesis of inflammation markers after 48 h of cell cultivation on PLLA-*co*-PEG nonwovens was evaluated *via* flow cytometry (MACSQuant Analyzer 10, Miltenyi Biotec, Bergisch-Gladbach, Germany) using the MACSPlex human cytokine 12 kit according to the manufacturer's instructions (Miltenyi Biotec, Bergisch-Gladbach, Germany). Supernatants of six wells were pooled per configuration in each experiment. Supernatants of three independent tests have been measured within the cytokine assay according to the protocol. In brief, cell culture supernatants were incubated with antibody-coated MACSPlex beads for granulocyte-macrophage colony-stimulating factor (GM CSF), interferon-α (IFN-α), IFN-γ, interleukins 2 (IL-2), IL-4, IL-5, IL-6, IL-9, IL-10, IL-12p70, IL-17A, and tumour necrosis factor α (TNF α) in the MACSPlex filter plate for 2 hours. After the washing steps, the MACSPlex cytokine 12 detection reagent including APC-conjugated antibodies was added and incubated for 1 hour. Incubation steps were carried out in the dark at 450 rpm and RT. The analysis with the MACSPlex cytokine 12 kit was conducted using blue and red lasers of the flow cytometer to detect FITC, PE and APC. The median of the APC fluorescence of each captured bead population gives the concentration of each cytokine in the sample. Measured standards of known quantities are used for the quantification of the concentrations of analytes in the supernatants by means of MACSQuantify software (Miltenyi Biotec, Bergisch-Gladbach, Germany).

Statistical analysis of cell biological experiments

The statistical significance was calculated using IBM® SPSS® Statistics version 25 (IBM Corp., New York, NY, USA). Data were tested for outliers using the formulae according to Nalimov. Normal distribution of data was evaluated with Shapiro–Wilk test and Kruskal–Wallis tests for independent samples was used to determine statistical significance. Data are shown as mean values ± standard deviation (SD). Values of $p < 0.05$ were set to be significant.

Results and discussion

Electrospinning of PLLA-*co*-PEG

PLLA-*co*-PEG nonwovens obtained by electrospinning exhibited homogeneous fibre distribution. Average fibre diameter was determined from two 1000× SEM overview images using the GIFT macro for ImageJ developed by our group.[20,21] Fibre diameters determined in this way were about d = 0.763 µm ± 0.005 µm, showing no signs of beading or other defects in morphology (Fig. 1).

From mechanical testing, averaged characteristics were Young's modulus E = 7.3 ± 2.4 MPa, yield strength of σ_m = 4.78 ± 0.1 MPa and elongation at break of ε_B = 275.7 ± 24%. Minimum elongation at break as shown in the averaged stress–strain curve (Fig. 2) was $\varepsilon_{B,min}$ = 242%.

Contact angle measurements using deionized water showed that the PLLA-*co*-PEG nonwoven exhibits hydrophobic properties, giving a water contact angle of θ = 121.2° ± 7.35°. Free surface energy using diiodomethane as the second test liquid was not accessible as the MeI_2 immediately interacted with the nonwoven material, thus no contact angle for MeI_2 was measurable.

Fetuin A functionalisation and *in vitro* mineralisation

Fetuin A was covalently linked to the nonwoven surface by EDC/NHS coupling, as shown in Fig. 3. Superficial functional

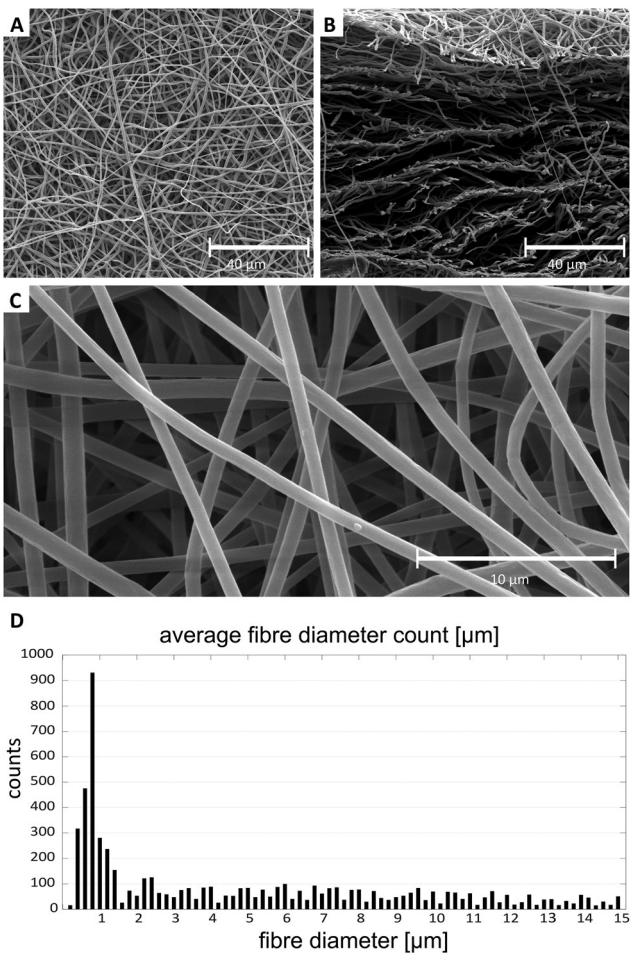


Fig. 1 Overview (A) and cross-sectional (B) SEM image of PLLA-*co*-PEG nonwoven (each at 1000× magnification), overview of PLLA-*co*-PEG nonwoven at 4000× magnification (C) and histogram of fibre diameter evaluation by using the GIFT macro for ImageJ (D).

Published on 01 June 2023. Downloaded by University of Rostock on 6/5/2025 1:43:42 PM.

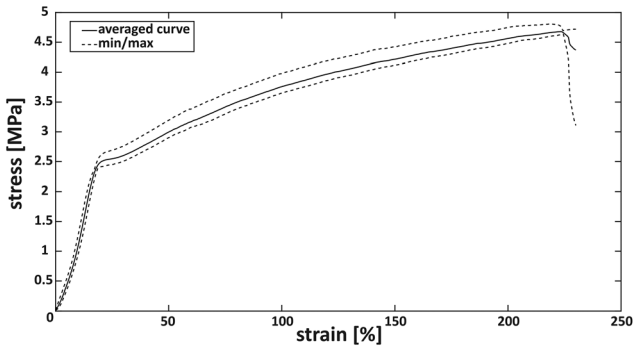


Fig. 2 Averaged stress strain curve of PLLA-*co*-PEG nonwoven obtained from quasi-static tensile testing. Deviation is indicated by dashed lines.

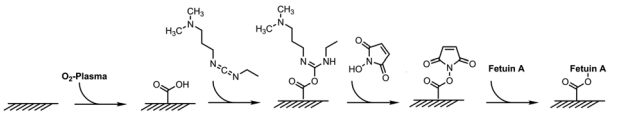


Fig. 3 Schematic of the EDC/NHS coupling of fetuin A on the nonwoven surface after O_2-plasma treatment for the generation of superficial carboxyl groups.

carboxyl groups for subsequent protein binding were generated using low-pressure oxygen plasma.

The plasma process did not seem to affect fibre surface morphology and no signs of fibre cracks could be observed in SEM after plasma treatment compared to the untreated nonwoven (Fig. 4B). Also, EDC/NHS linking of fetuin A did not show any effect on the fibre morphology of the PLLA-*co*-PEG samples (Fig. 4B and C).

ELISA data of the binding solution showed residual fetuin A in the supernatant of 0.73 ng mL^{-1} ± 0.076 ng mL^{-1}, yielding a calculated fetuin A load of 99.3 ng mm^{-2} on the nonwoven material. This results in immobilisation of 99.3% ± 0.1% of the used fetuin A. However, this does not allow any conclusion as to whether the total amount of fetuin A is covalently bound or merely adsorbed/incorporated by the nonwoven due to the high porosity. Considering the observed effect of fetuin A on biomineralisation and cell growth behaviour, however, we assume that the majority of the protein is covalently bound to the surface and thus not easily washed out.

Fetuin A exhibits a distinct Ca^{2+} affinity, thus enabling the material to bind Ca^{2+} from the surrounding medium, leading to biogeneous CaP mineralisation without adding further crystallisation nuclei. To assess the mineralisation potential of the fetuin A functionalised nonwovens, the described material was subsequently treated with an accelerated *in vitro* mineralisation protocol using an oversaturated $CaHPO_3$ solution. Untreated PLLA-*co*-PEG nonwoven and PLLA-*co*-PEG nonwoven which underwent O_2-plasma treatment serve as reference. The Ca^{2+} load was measured after incubation of 3 days using a photometric Ca-Arsenazo III assay after hydrolysis. Our results show that Ca^{2+} load was *circa* 5× higher compared to that in the PLLA-*co*-PEG base material (Fig. 5A). To verify that this observation was not solely resulting from the increased surface polarity due to the O_2-plasma process, control experiment was

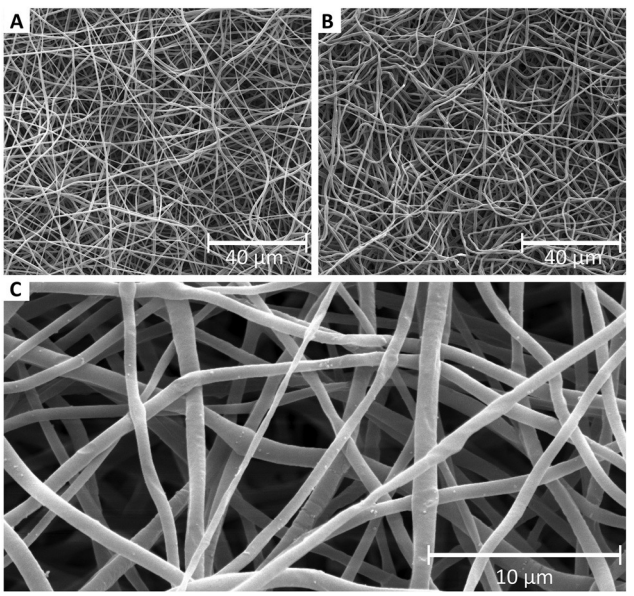


Fig. 4 Overview SEM image of PLLA-*co*-PEG nonwoven after O_2-plasma treatment (A, 500× magnification) and after fetuin A coupling (B and C; 500× and 4000× magnification).

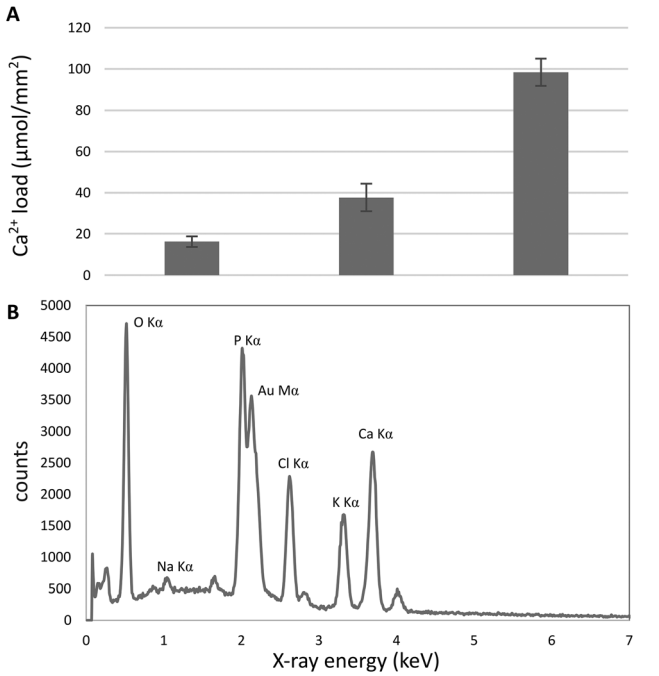


Fig. 5 Ca^{2+} load on the surface of PLLA-*co*-PEG nonwoven in µmol per mm^2 after accelerated *in vitro* mineralisation for 3 days as determined by photometric quantification using Ca^{2+}-Arsenazo III-complex after hydrolysis of CaP precipitates using 0.1 M HCl (n = 6) (A). EDX spectrum and elemental composition of CaP crystallites (B).

 This journal is © The Royal Society of Chemistry 2023

Published on 01 June 2023. Downloaded by University of Rostock on 6/5/2025 1:43:42 PM.

performed using this intermediate material. Despite O_2-functionalisation leading to a *circa* two-fold increase in the Ca^{2+} load, the increased CaP load cannot be attributed to the polarity changes from O_2-plasma treatment alone. In fact, immobilised fetuin A showed binding to calcium ions from the surrounding medium, which in turn act as crystallisation nuclei, initialising biomimetic CaP crystallite mineralisation. Analysis of the stoichiometric composition of the crystallites by means of EDX gave a Ca : P ratio of 1.33, whereas Ca : P ratio of hydroxyl apatite is 1.67 (Fig. 5B). This may be derived from the mixed crystal formation from the oversaturated mineralisation medium. However, the formation of CaP is indicated.

This becomes even more obvious when the microstructure of the mineralised samples is considered (Fig. 6). As can be seen in SEM imaging, the CaP load of untreated samples comes from loosely attached CaP crystallites (Fig. 6A and B), which precipitated from the metastable mineralisation medium. In contrast, fetuin A functionalisation leads to large scale crystallite growth on the surface, so that the fibres are encapsulated by CaP and the fibre morphology of the nonwovens is preserved (Fig. 6C–F). Thus, a distinct effect of the superficially linked fetuin A on the mineralisation capabilities of the material can be concluded.

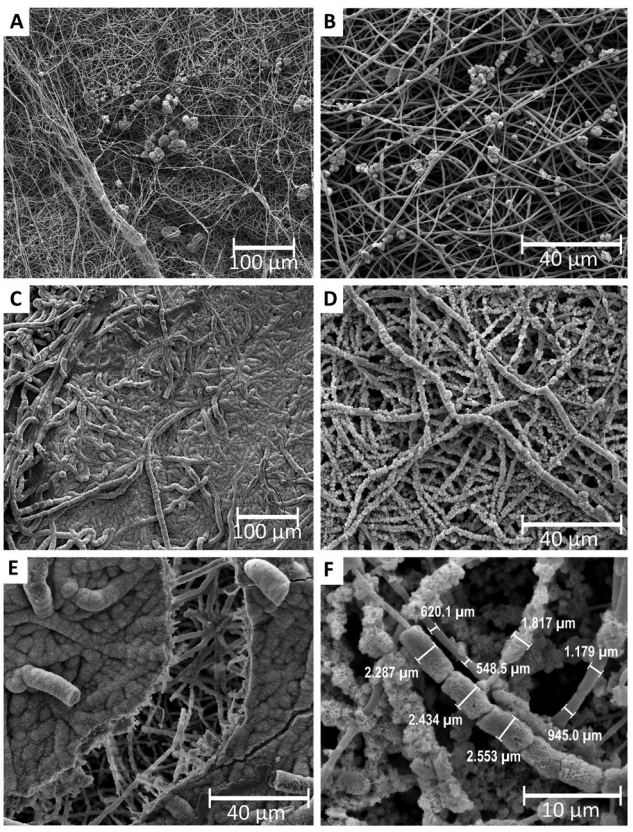


Fig. 6 SEM image of PLLA-*co*-PEG nonwoven without further functionalisation (A and B; 250× and 1000× magnification) and with fetuin A functionalisation (C–F; 250×, 1000×, 1000× and 4000× magnification) after accelerated *in vitro* mineralisation.

SEM imaging shows that fetuin A functionalisation leads to homogeneously distributed CaP formation over the entire surface of the functionalised nonwoven. The entire nonwoven fibres are enclosed by a CaP layer, also in deeper layers, maintaining the fibrous morphology of the nonwoven, which is very promising with regard to the specific microenvironment requirements for osteoinduction and osteogenesis.

Cell culture experiments

To investigate the influence of fetuin A functionalisation of PLLA-*co*-PEG nonwovens on cell growth behaviour, human MG-63 osteoblasts were directly seeded on PLLA-*co*-PEG nonwovens with different modifications. From this, it was observed that metabolic cell activity on oxygen treated nonwovens was significantly reduced (2.8 ± 2.3%) compared to that of other groups (Fig. 7).

Fetuin A functionalisation of the nonwoven resulted in slightly decreased metabolic activity (86 ± 22.4%) compared to the reference group (100 ± 26.7%), whereas fetuin A functionalisation of PLLA-*co*-PEG nonwoven followed by *in vitro* biomineralisation led to an increase in cell activity (112.3 ± 27.3%).

Being the most abundant globular plasma protein in calf serum, fetuin A is commonly used as an additive in cell culture medium.[22,23] When in solution, fetuin A has shown to promote cell differentiation, adhesion, and proliferation of various cell types.[24]

The copolymer we used in this study consisted of 96% PLLA blocks. Thus, due to no available cell related data for PLLA-*co*-PEG nonwovens, we relate our findings to pure PLLA nonwovens under the assumption that the effect of the PEG blocks is small in overall cell behaviour. For nanofibre guided bone regeneration, common approaches are the use of calcium phosphate[23,25,26] and hydroxylapatite[22,26,27] loaded nonwovens, being promising composites for mineralisation and showing improved differentiation, viability and activity of (pre-)osteoblasts,[24,28,29] fibroblasts[30] and mesenchymal stem cells.[22,27] Apatite coated electrospun PLLA scaffolds with varying pore size and porosity have been shown to lead to

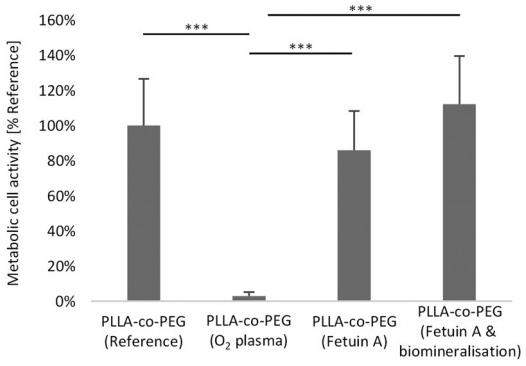


Fig. 7 Metabolic cell activity of human MG-63 osteoblast cells on PLLA-*co*-PEG nonwovens after 48 h of incubation, CellQuanti Blue Assay, mean + SD, n = 3 with six parallel wells, respectively. Kruskal–Wallis test with ***$p \leq 0.001$.

Published on 01 June 2023. Downloaded by University of Rostock on 6/5/2025 1:43:42 PM.

increased alkaline phosphatase activity and cell-mediated mineralisation in pre-osteoblasts.[31] Furthermore, it was shown that fetuin A bound to CaP nanoparticles enabled a reduction of the particle toxicity on human vascular smooth muscle cells.[32] Nevertheless, serum fetuin A is known to inhibit osteoblast apoptosis in cell culture experiments.[33] Patterned nano sized electrospun nonwovens obtained by plasma treatment resulted in significant increased cell attachment and proliferation of MG-63 osteoblast cells.[34] However, PLLA nonwovens with varying microscale roughness have been shown to decrease osteoblast proliferation.[35]

In this work, fluorescence staining of human MG-63 osteoblast cells on PLLA-*co*-PEG nonwovens revealed differences in cell density and morphology for the different modification steps in accordance with metabolic cell activity data. Cells grown on reference nonwovens were mainly round-shaped and aggregated (Fig. 8A).

After oxygen treatment, no cell nuclei or actin filaments of cells were visible (Fig. 8B). In contrast to this, cell elongation and spreading were positively influenced by fetuin A functionalisation (Fig. 8C) and even more by fetuin A functionalisation followed by *in vitro* biomineralisation (Fig. 8D).

For further investigation of cell morphology and to confirm fluorescence staining image interpretation, SEM imaging of the modified PLLA-*co*-PEG materials was performed (Fig. 9).

MG-63 osteoblast cells on the reference nonwoven appeared to be slightly elongated and primarily round-shaped (Fig. 9A), whereas O_2-plasma treated nonwovens resulted in apoptotic cells (Fig. 9B). Both fetuin A functionalised (Fig. 9C) PLLA-*co*-PEG nonwovens and fetuin A functionalised nonwovens after accelerated *in vitro* biomineralisation (Fig. 9D) showed

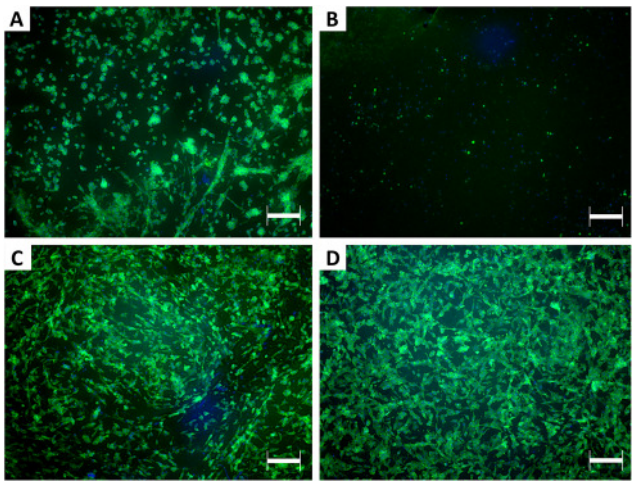


Fig. 8 Exemplary fluorescence images of human MG-63 osteoblast cells on PLLA-*co*-PEG nonwovens after 48 h: PLLA-*co*-PEG reference (A), PLLA-*co*-PEG after O_2-plasma functionalisation (B), PLLA-*co*-PEG after covalent fetuin A functionalisation (C) and fetuin A functionalised PLLA-*co*-PEG nonwoven after accelerated *in vitro* biomineralisation (D); green – actin filaments, blue – cell nuclei, images taken at 5× magnification, scale bar refers to 400 µm.

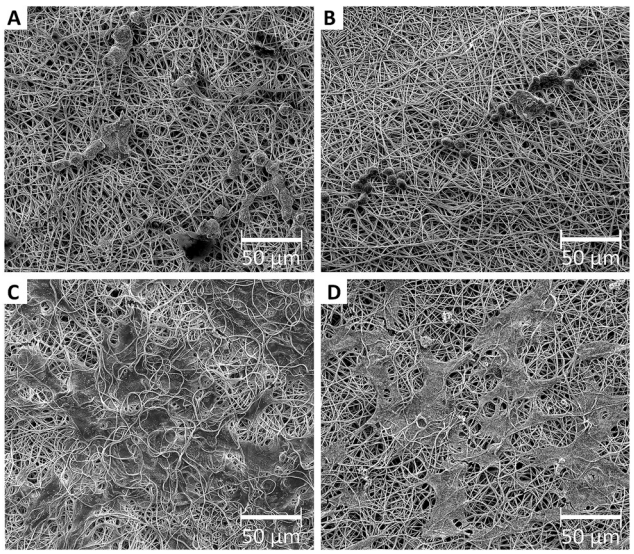


Fig. 9 (A) Exemplary SEM images of human MG-63 osteoblast cells on PLLA-*co*-PEG nonwovens after 48 h incubation: PLLA-*co*-PEG after O_2-plasma functionalisation (B), PLLA-*co*-PEG after covalent fetuin A functionalisation (C) and fetuin A functionalised PLLA-*co*-PEG nonwoven after accelerated *in vitro* biomineralisation (D), all images taken at 500× magnification.

improved cell adhesion, spreading and even infiltration of osteoblasts into the material.

This is according to the literature, as similar results have been published for pre-osteoblasts on HA-loaded nonwovens[29,36] as well as osteoblasts on β-tricalcium phosphate-incorporated ones[25] indicating improved osteoblastic size, adhesion, spreading and migration into the highly porous membranes. Increased affinity to adhesion and attachment to HA-loaded nonwovens has also been shown for fibroblasts.[30] Human MG-63 osteoblast cells showed distinct adhesion and infiltration in PLLA/PEG nonwovens.[37] Fetuin A coating on HA did not further alter osteoblastic actin cytoskeletal morphology, which was already improved compared to TCPS.[23]

Following cell morphology and metabolic activity experiments, procollagen I synthesis of MG-63 was evaluated. Collagen type I precursors were detected *via* ELISA from the supernatants of human MG-63 osteoblast cells grown on PLLA-*co*-PEG nonwovens after 48 h of incubation. A slight decrease of procollagen I was observed on both fetuin A functionalised nonwovens being more distinct on the calcified surface (Fig. 10), but without significant differences to the control group.

According to the literature, PLLA is known to increase collagen production.[38] Yet, our finding was a reduced amount of collagen I precursor in the supernatant in comparison with unmodified PLLA-*co*-PEG nonwovens. Since fetuin A promotes intrafibrillar mineralisation of collagen *in vitro*,[39] we assume that synthesised collagen precursors have been bound to fetuin A on the modified nonwovens, resulting in a reduced

 This journal is © The Royal Society of Chemistry 2023

Published on 01 June 2023. Downloaded by University of Rostock on 6/5/2025 1:43:42 PM.

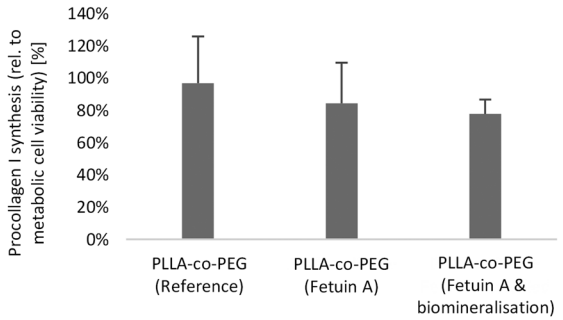


Fig. 10 Pro-collagen I synthesis of human MG-63 osteoblast cells on PLLA-*co*-PEG nonwovens after 48 h of incubation, pro-collagen type I synthesis related to metabolic cell viability, mean + SD, $n = 3$ with duplicates, respectively. Kruskal–Wallis test with $*p \leq 0.05$.

collagen I precursor concentration in the supernatants. However, so far no comparable studies, even for HA, have been published, making comparison difficult. Binding of collagen precursors to fetuin A on the nonwovens have to be evaluated in follow-up studies.

Fetuin A in serum acts as a carrier for lipids, which may influence inflammation and apoptosis.[22] Furthermore, fetuin A itself is divergently regulated by different proinflammatory mediators and described as anti-inflammatory protein due to its structural similarity to other proteins.[40,41] Nevertheless, so far there are no studies dealing with the inflammatory potential of nonwoven-bound fetuin A. In this study, synthesis of inflammation markers was assessed using flow cytometry (Fig. 11).

Overall, IFN-γ, IL-5, IL-6, IL-9, IL-12p70 and TNF-α have been below the detection limit for all tested materials. As for GM-CS, IFN-a, IL-2, IL-4, IL-10 and IL-17, no significant differences between the groups were observed, indicating no changes in inflammatory potential of fetuin A functionalised PLLA-*co*-PEG nonwovens. However, levels of IFN-α (~5 pg mL^{-1}), IL-2 (~12 pg mL^{-1}) and IL-4 (~18 pg mL^{-1}) were slightly increased in general. In studies with similar approaches using hydroxyapatite or CaP on nonwovens, inflammatory potential was barely investigated, especially when using osteoblasts. Electrospun hydroxyapatite nanofibers do not provoke cytokine production at least in macrophages.[42] Subcutaneously tested in rats, hydroxyapatite nanocrystal-coated PLLA fabrics showed reduced inflammatory response compared to the uncoated material.[43] To have a more detailed look at the inflammatory reactions *in vivo* studies need to be conducted. However, from our data it could be shown that none of our process steps resulted in an increase in inflammatory markers.

To evaluate the barrier function of the fetuin A functionalised PLLA-*co*-PEG nonwoven, additional cell seeding experiments for 96 hours were carried out. After fixation, cell penetration was examined by cross-sectional SEM imaging (Fig. 12). First, after 96 hours, a confluent cell layer can be seen on fetuin A functionalised PLLA-*co*-PEG nonwoven after accelerated *in vitro* biomineralisation. In contrast, even after 96 hours of cultivation, cells on the unmodified material did not result in the formation of a confluent cell layer, showing scattered cell patches. Cross sectional images of fetuin A functionalised PLLA-*co*-PEG nonwovens after accelerated *in vitro* biomineralisation

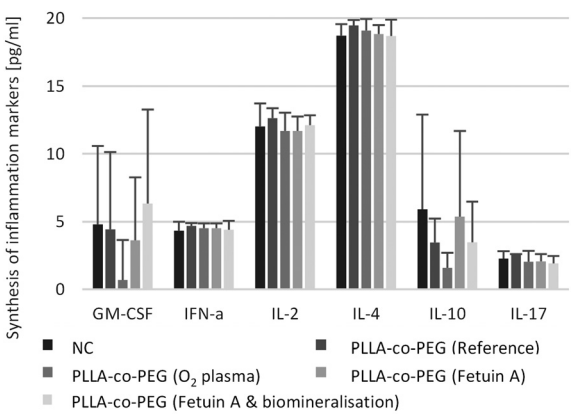


Fig. 11 Synthesised inflammation markers of MG-63 osteoblast cells on PLLA-*co*-PEG nonwovens after 48 h of incubation, mean + SD, $n = 3$.

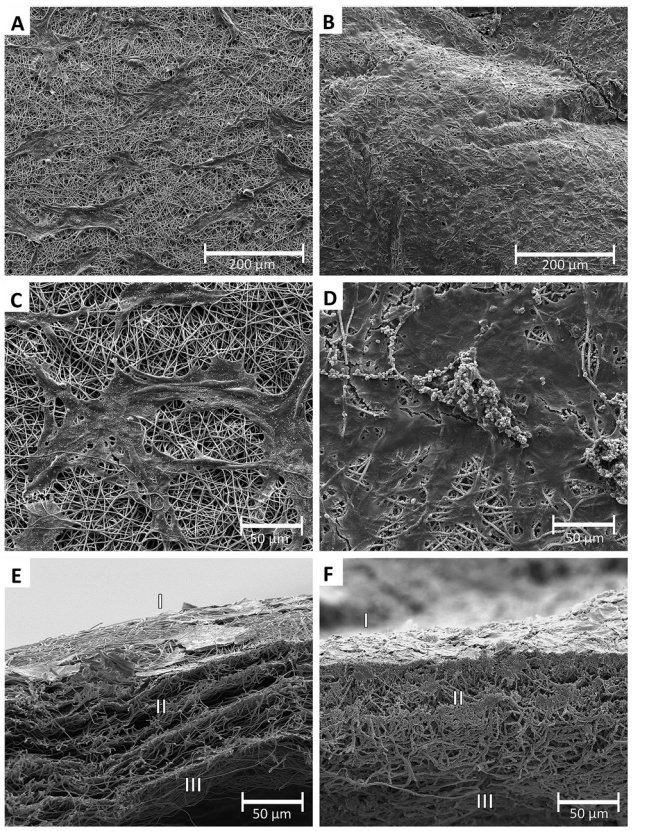


Fig. 12 SEM images of PLLA-*co*-PEG nonwoven (overview images A) at 200× and (C) 500× and cross section image (E) at 500× magnification and fetuin A functionalised PLLA-*co*-PEG nonwovens after *in vitro* biomineralisation (overview images B) at 200× and (D) 500× and cross section image (F) at 500× magnification after 96 h of incubation with MG-63 cells. For both cross section images, top side with cell layer (I), cutting edge (II) and bottom side (III) are indicated.

Published on 01 June 2023. Downloaded by University of Rostock on 6/5/2025 1:43:42 PM.

sation first revealed a comparable mineralisation pattern of the bulk of the nonwoven, as already shown in SEM overview images. Moreover, from overview and cross sectional images, a dense confluent cell layer could be observed on the top side of the fetuin A functionalised PLLA-*co*-PEG nonwoven after *in vitro* biomineralisation. In addition, all materials revealed that no cells were able to penetrate into the material, as no cells were visible in the cutting area and on the bottom side of the material, showing successful barrier function of the membrane.

Conclusion

In this work, we showed that fetuin A modification of biodegradable nonwovens appears to be a novel and feasible approach towards enhanced biomineralisation of rather non-polar polymer-based biomaterials. Our initial functionalisation results indicate a distinct enabling of CaP crystal growth on the material surface, as well as in the material bulk under *in vitro* conditions, compared to the untreated nonwoven. Fetuin A functionalised nonwovens show promising properties and the potential for application in oral and maxillofacial bone regeneration, or for the use on osteosynthesis implants to improve osteogenesis and healing of critical bone defects associated with fractures.

Microscopic evaluation of cell culture experiments using human MG-63 osteoblast cells showed an improved attachment and spreading of cells on fetuin A functionalised PLLA-*co*-PEG nonwovens, although no significantly increased metabolic cell activity and pro-collagen I synthesis could be detected in comparison to the unfunctionalised nonwoven. Furthermore, none of the nonwovens resulted in the increased synthesis of inflammatory markers by osteoblasts.

The presented approach has the potential to be used as a novel scaffold material in bone regenerative medicine, as nonwovens are easy to handle and can conveniently be adapted to various shapes, addressing individual sites of application.

Author contributions

Stefan Oschatz: conceptualisation, investigation, methodology, and writing – original draft; Jana Markhoff: conceptualisation, investigation, methodology, and writing – original draft; Michael Teske: methodology, investigation, and writing – original draft; Sabine Illner: resources and writing – review and editing; Ulrike Burmeister: clinical expertise and writing – review and editing; Hermann Lang: clinical expertise and writing – review and editing; Volkmar Senz: SEM imaging and evaluation; Niels Grabow: supervision and writing – review and editing.

Conflicts of interest

The authors have a patent pending concerning the topic of the manuscript.

Acknowledgements

The skilful work and excellent technical assistance of Caroline Dudda, Babette Hummel, Katja Hahn, Gabriele Karsten, Martina Nerger and Jonathan Ortelt are gratefully acknowledged. Financial support by Rostock University Medical Center within the FORUN program is gratefully acknowledged.

References

1 F. Yang, S. K. Both, X. Yang, X. F. Walboomers and J. A. Jansen, Development of an electrospun nano-apatite/PCL composite membrane for GTR/GBR application, *Acta Biomater.*, 2009, **5**, 3295–3304.
2 X. Cheng and F. Yang, More Than Just a Barrier—Challenges in the Development of Guided Bone Regeneration Membranes, *Matter*, 2019, **1**, 558–560.
3 L. Lin, K. L. Chow and Y. Leng, Study of hydroxyapatite osteoinductivity with an osteogenic differentiation of mesenchymal stem cells, *J. Biomed. Mater. Res., Part A*, 2009, **89**, 326–335.
4 I. S. Deschamps, G. L. Magrin, R. S. Magini, M. C. Fredel, C. A. M. Benfatti and J. C. M. Souza, On the synthesis and characterization of β-tricalcium phosphate scaffolds coated with collagen or poly (D, L-lactic acid) for alveolar bone augmentation, *Eur. J. Dent.*, 2017, **11**, 496–502.
5 F. J. Martínez-Vázquez, P. Miranda, F. Guiberteau and A. Pajares, Reinforcing bioceramic scaffolds with in situ synthesized ε-polycaprolactone coatings, *J. Biomed. Mater. Res., Part A*, 2013, **101**, 3551–3559.
6 M. Bohner and R. J. Miron, A proposed mechanism for material-induced heterotopic ossification, *Mater. Today*, 2019, **22**, 132–141.
7 L. Zhu, D. Luo and Y. Liu, Effect of the nano/microscale structure of biomaterial scaffolds on bone regeneration, *Int. J. Oral Sci.*, 2020, **12**, 6.
8 A. Majchrowicz, A. Roguska, A. Krawczyńska, M. Lewandowska, J. Martí-Muñoz, E. Engel and O. Castano, In vitro evaluation of degradable electrospun polylactic acid/bioactive calcium phosphate ormoglass scaffolds, *Archiv. Civ. Mech. Eng.*, 2020, **20**, 1–11.
9 M. Baranowski, M. Wasyłeczko, A. Kosowska, A. Plichta, S. Kowalczyk, A. Chwojnowski, W. Bielecki and J. Czubak, Regeneration of Articular Cartilage Using Membranes of Polyester Scaffolds in a Rabbit Model, *Pharmaceutics*, 2022, **14**, 1016.
10 A. J. Nathanael and T. H. Oh, Encapsulation of Calcium Phosphates on Electrospun Nanofibers for Tissue Engineering Applications, *Crystals*, 2021, **11**, 199.
11 M. P. Bernardo, B. C. R. Da Silva, A. E. I. Hamouda, M. A. S. de Toledo, C. Schalla, S. Rütten, R. Goetzke, L. H. C. Mattoso, M. Zenke and A. Sechi, PLA/Hydroxyapatite scaffolds exhibit in vitro immunological inertness and promote robust osteogenic differentiation of

 This journal is © The Royal Society of Chemistry 2023

Published on 01 June 2023. Downloaded by University of Rostock on 6/5/2025 1:43:42 PM.

human mesenchymal stem cells without osteogenic stimuli, *Sci. Rep.*, 2022, **12**, 2333.
12 H.-W. Kim, H.-H. Lee and J. C. Knowles, Electrospinning biomedical nanocomposite fibers of hydroxyapatite/poly (lactic acid) for bone regeneration, *J. Biomed. Mater. Res., Part A*, 2006, **79**, 643–649.
13 D. Arbeiter, K. Lebahn, T. Reske, V. Senz, T. Eickner, K.-P. Schmitz, N. Grabow and S. Oschatz, Comparison of accelerated and enzyme-associated real-time degradation of HMW PLLA and HMW P3HB films, *Polym. Test.*, 2022, **107**, 107471.
14 Q. Breche, G. Chagnon, G. Machado, E. Girard, B. Nottelet, X. Garric and D. Favier, Mechanical behaviour's evolution of a PLA-b-PEG-b-PLA triblock copolymer during hydrolytic degradation, *J. Mech. Behav. Biomed. Mater.*, 2016, **60**, 288–300.
15 M. Penco, S. Marcioni, P. Ferruti, S. D'Antone and R. Deghenghi, Degradation behaviour of block copolymers containing poly(lactic-glycolic acid) and poly(ethylene glycol) segments, *Biomaterials*, 1996, **17**, 1583–1590.
16 E. S. Vasquez, J. L. Cunningham, J. B. McMahan, C. L. Simpson and K. B. Walters, Fetuin-A adsorption and stabilization of calcium carbonate nanoparticles in a simulated body fluid, *J. Mater. Chem. B*, 2015, **3**, 6411–6419.
17 L. Lou, J. Wang and S. Ramkumar, Optimization of testing parameters for tensile property evaluation of poly(vinyl alcohol) nanofibers webs, *J. Appl. Polym. Sci.*, 2019, **136**, 47159.
18 K. Wulf, D. Arbeiter, C. Matschegewski, M. Teske, J. Huling, K.-P. Schmitz, N. Grabow and S. Kohse, Smart releasing electrospun nanofibers-poly: L.lactide fibers as dual drug delivery system for biomedical application, *Biomed. Mater.*, 2020, **16**, 15022.
19 S. Oschatz, S. Kohse, V. Senz, T. Eickner, K.-P. Schmitz and N. Grabow, Accelerated in vitro-calcification of potential urethane based heart valve replacement materials, *Curr. Dir. Biomed. Eng.*, 2018, **4**, 221–224.
20 A. Götz, V. Senz, W. Schmidt, J. Huling, N. Grabow and S. Illner, General image fiber tool: A concept for automated evaluation of fiber diameters in SEM images, *Measurement*, 2021, **177**, 109265.
21 J. Huling, A. Götz, N. Grabow and S. Illner, GIFT: An ImageJ macro for automated fiber diameter quantification, *PLoS One*, 2022, **17**, e0275528.
22 L. Brylka and W. Jahnen-Dechent, The role of fetuin-A in physiological and pathological mineralization, *Calcif. Tissue Int.*, 2013, **93**, 355–364.
23 J. Xie, M. J. Baumann and L. R. McCabe, Adsorption of serum fetuin to hydroxylapatite does not contribute to osteoblast phenotype modifications, *J. Biomed. Mater. Res., Part A*, 2005, **73**, 39–47.
24 M. Demetriou, C. Binkert, B. Sukhu, H. C. Tenenbaum and J. W. Dennis, Fetuin/alpha2-HS glycoprotein is a transforming growth factor-beta type II receptor mimic and cytokine antagonist, *J. Biol. Chem.*, 1996, **271**, 12755–12761.
25 V. I. dos Santos, C. Merlini, Á. Aragones, K. Cesca and M. C. Fredel, Influence of calcium phosphates incorporation into poly(lactic-co-glycolic acid) electrospun membranes for guided bone regeneration, *Polym. Degrad. Stab.*, 2020, **179**, 109253.
26 Z. Nie, Fetuin: its enigmatic property of growth promotion, *Am. J. Physiol.*, 1992, **263**, C551–C562.
27 J. W. Lim, K.-J. Jang, H. Son, S. Park, J. E. Kim, H. B. Kim, H. Seonwoo, Y.-H. Choung, M. C. Lee and J. H. Chung, Aligned Nanofiber-Guided Bone Regeneration Barrier Incorporated with Equine Bone-Derived Hydroxyapatite for Alveolar Bone Regeneration, *Polymers*, 2020, **13**, 60.
28 N. Johari, M. Fathi, Z. Fereshteh, S. Kargozar and A. Samadikuchaksaraei, The electrospun poly(ε–caprolactone)/fluoridated hydroxyapatite nanocomposite for bone tissue engineering, *Polym. Adv. Technol.*, 2020, **31**, 1019–1026.
29 C. Fu, H. Bai, J. Zhu, Z. Niu, Y. Wang, J. Li, X. Yang and Y. Bai, Enhanced cell proliferation and osteogenic differentiation in electrospun PLGA/hydroxyapatite nanofibre scaffolds incorporated with graphene oxide, *PLoS One*, 2017, **12**, e0188352.
30 F. Keivani, P. Shokrollahi, M. Zandi, S. Irani, F. Shokrolahi and S. C. Khorasani, Engineered electrospun poly(caprolactone)/polycaprolactone-g-hydroxyapatite nano-fibrous scaffold promotes human fibroblasts adhesion and proliferation, *Mater. Sci. Eng., C*, 2016, **68**, 78–88.
31 B. M. Whited, J. R. Whitney, M. C. Hofmann, Y. Xu and M. N. Rylander, Pre-osteoblast infiltration and differentiation in highly porous apatite-coated PLLA electrospun scaffolds, *Biomaterials*, 2011, **32**, 2294–2304.
32 Y. Dautova, D. Kozlova, J. N. Skepper, M. Epple, M. D. Bootman and D. Proudfoot, Fetuin-A and albumin alter cytotoxic effects of calcium phosphate nanoparticles on human vascular smooth muscle cells, *PLoS One*, 2014, **9**, e97565.
33 M. M. X. Cai, E. R. Smith and S. G. Holt, The role of fetuin-A in mineral trafficking and deposition, *BoneKEy Rep.*, 2015, **4**, 672.
34 H. J. Jeon, H. Lee and G. H. Kim, Nano-Sized Surface Patterns on Electrospun Microfibers Fabricated Using a Modified Plasma Process for Enhancing Initial Cellular Activities, *Plasma Processes Polym.*, 2014, **11**, 142–148.
35 C. Ribeiro, V. Sencadas, A. C. Areias, F. M. Gama and S. Lanceros-Méndez, Surface roughness dependent osteoblast and fibroblast response on poly(L-lactide) films and electrospun membranes, *J. Biomed. Mater. Res., Part A*, 2015, **103**, 2260–2268.
36 H. Li, C. Huang, X. Jin and Q. Ke, An electrospun poly(ε-caprolactone) nanocomposite fibrous mat with a high content of hydroxyapatite to promote cell infiltration, *RSC Adv.*, 2018, **8**, 25228–25235.
37 M. Spasova, O. Stoilova, N. Manolova, I. Rashkov and G. Altankov, Preparation of PLLA/PEG Nanofibers by Electrospinning and Potential Applications, *J. Bioact. Compat. Polym.*, 2007, **22**, 62–76.

Published on 01 June 2023. Downloaded by University of Rostock on 6/5/2025 1:43:42 PM.

38 S. Ray, H. Adelnia and H. T. Ta, Collagen and the effect of poly-l-lactic acid based materials on its synthesis, *Biomater. Sci.*, 2021, **9**, 5714–5731.
39 F. Nudelman, A. J. Lausch, N. A. J. M. Sommerdijk and E. D. Sone, In vitro models of collagen biomineralization, *J. Struct. Biol.*, 2013, **183**, 258–269.
40 H. Wang and A. E. Sama, Anti-inflammatory role of fetuin-A in injury and infection, *Curr. Mol. Med.*, 2012, **12**, 625–633.
41 E. Chekol Abebe, Z. Tilahun Muche, A. Behaile T/Mariam, T. Mengie Ayele, M. Mekonnen Agidew, M. Teshome Azezew, E. Abebe Zewde, T. Asmamaw Dejenie and M. Asmamaw Mengstie, The structure, biosynthesis, and biological roles of fetuin-A: A review, *Front. Cell Dev. Biol.*, 2022, **10**, 945287.
42 J. Pasuri, J. Holopainen, H. Kokkonen, M. Persson, K. Kauppinen, P. Lehenkari, E. Santala, M. Ritala and J. Tuukkanen, Osteoclasts in the interface with electrospun hydroxyapatite, *Colloids Surf., B*, 2015, **135**, 774–783.
43 H. Yanagida, M. Okada, M. Masuda, M. Ueki, I. Narama, S. Kitao, Y. Koyama, T. Furuzono and K. Takakuda, Cell adhesion and tissue response to hydroxyapatite nanocrystal-coated poly(L-lactic acid) fabric, *J. Biosci. Bioeng.*, 2009, **108**, 235–243.

 This journal is © The Royal Society of Chemistry 2023